

Dissertation zur Erlangung des Doktorgrades  
der Fakultät für Chemie und Pharmazie  
der Ludwig-Maximilians-Universität München

**Theoretical description of magnetic Compton scattering  
and magnetic properties of Cr-chalcogenide compounds**

Diana Benea

aus

Klausenburg, Rumänien

2004



### Erklärung

Diese Dissertation wurde im Sinne von §13 Abs. 3 bzw. 4 der Promotionsordnung vom 29. Januar 1998 von Prof. Dr. H. Ebert betreut.

### Ehrenwörtliche Versicherung

Diese Dissertation wurde selbstständig, ohne unerlaubte Hilfe erarbeitet.

München, 17. 04. 2004

Diana Benea

Dissertation eingereicht am 17. 04. 2004

1. Gutachter: Prof. Dr. H. Ebert
2. Gutachter: Prof. Dr. W. Bensch

Mündliche Prüfung am 10. 12. 2004



# Contents

<b>1</b>	<b>Introduction</b>	<b>13</b>
1.1	Compton effect . . . . .	14
1.2	Positron annihilation . . . . .	15
1.3	Cr-chalcogenide systems . . . . .	15
1.4	Scope of the work . . . . .	16
<b>2</b>	<b>Theory</b>	<b>19</b>
2.1	Density Functional Theory . . . . .	19
2.1.1	Non-relativistic Density Functional Theory . . . . .	20
2.1.2	Relativistic Density Functional Theory . . . . .	29
2.2	Korringa-Kohn-Rostoker Green's Function Method . . . . .	34
2.2.1	Green's Function . . . . .	35
2.2.2	The Calculation of Observables . . . . .	36
2.2.3	The single-site scattering . . . . .	39
2.2.4	The single-site Green's function . . . . .	44
2.2.5	Multiple scattering . . . . .	46
2.2.6	Multiple Scattering Green's function . . . . .	48
2.3	Treatment of Disordered Alloys . . . . .	52
2.3.1	The Coherent Potential Approximation Method . . . . .	52
2.4	Conclusions . . . . .	58
<b>3</b>	<b>Compton scattering</b>	<b>59</b>
3.1	Compton scattering cross section . . . . .	60
3.2	Magnetic Compton Scattering (MCS) . . . . .	61
3.3	The expression for the magnetic Compton profile . . . . .	64

3.4	Application to the transition metals Fe and Ni . . . . .	68
3.4.1	Three-dimensional spin momentum density . . . . .	73
3.5	Application to disordered alloys . . . . .	75
3.5.1	Compton anisotropic profiles in $\text{Ni}_x\text{Co}_{1-x}$ alloy . . . . .	75
3.5.2	Magnetic Compton profiles in $\text{Fe}_3\text{Pt}$ Invar alloy and ordered compound . . . . .	78
3.6	Magnetic Compton profiles for rare earth systems . . . . .	85
3.6.1	Magnetic Compton profile of Gd . . . . .	85
3.6.2	Magnetic Compton profile of $\text{Y}_{0.38}\text{Gd}_{0.62}$ alloy . . . . .	88
3.7	Magnetic Compton profile of $\text{UFe}_2$ . . . . .	90
3.7.1	The orbital polarization . . . . .	91
3.7.2	Influence of spin-orbit coupling and orbital polarization on the MCP of $\text{UFe}_2$ . . . . .	93
3.7.3	Individual atomic-type contributions on the magnetic Compton profile of $\text{UFe}_2$ . . . . .	94
3.8	Conclusions . . . . .	96
<b>4</b>	<b>Positron annihilation</b> . . . . .	<b>99</b>
4.1	Introduction to positron annihilation . . . . .	99
4.2	The electron-positron momentum density . . . . .	101
4.3	Electron-positron momentum density of V . . . . .	105
4.4	Comparison with Compton scattering . . . . .	108
4.5	Conclusions . . . . .	110
<b>5</b>	<b>Ground-state properties of Cr-chalcogenide systems</b> . . . . .	<b>111</b>
5.1	Structural properties of binary $\text{CrX}$ ( $X = \text{S}, \text{Se}, \text{Te}$ ) compounds . . . . .	114
5.2	Band-structure calculations of $\text{CrX}$ ( $X = \text{S}, \text{Se}, \text{Te}$ ) systems . . . . .	115
5.2.1	Density of states . . . . .	116
5.2.2	Phase stability . . . . .	118
5.2.3	Magnetic moments . . . . .	119
5.3	Non-collinear spin structures . . . . .	120
5.3.1	Non-collinear spin structure in CrSe system . . . . .	121
5.3.2	Non-collinear spin structure in CrTe system . . . . .	124

5.4	Band-structure calculations for the system $\text{CrTe}_{1-x}\text{Se}_x$ . . . . .	126
5.4.1	Magnetic moments . . . . .	126
5.4.2	Magnetic ground state . . . . .	127
5.5	Band-structure calculations for $\text{Cr}_{1+x}(\text{Te}_{1-y}\text{Se}_y)_2$ systems . . . . .	130
5.5.1	Structural properties of $\text{Cr}_{1+x}(\text{Te}_{1-y}\text{Se}_y)_2$ compounds . . . . .	130
5.5.2	Preferential site occupation . . . . .	131
5.5.3	Density of states and magnetic moments . . . . .	132
5.6	Band-structure calculations for $(\text{Cr}_x\text{Ti}_{1-x})_5\text{Te}_8$ systems . . . . .	135
5.6.1	Structural properties of $(\text{Cr}_x\text{Ti}_{1-x})_5\text{Te}_8$ compounds . . . . .	136
5.6.2	Preferential site occupation . . . . .	137
5.6.3	Density of states and magnetic moments . . . . .	139
5.7	Conclusions . . . . .	144
<b>6</b>	<b>Summary</b>	<b>145</b>
<b>A</b>	<b>Green's function in momentum representation (Compton)</b>	<b>147</b>
<b>B</b>	<b>Matrix elements (Compton)</b>	<b>151</b>
<b>C</b>	<b>Green's function in momentum representation (Positron Annihilation)</b>	<b>155</b>
C.1	Site-diagonal contribution . . . . .	155
C.2	Site-off-diagonal contribution . . . . .	158
C.3	Lattice sum . . . . .	160
<b>D</b>	<b>Matrix elements (Positron Annihilation)</b>	<b>163</b>





# List of Tables

3.1	Spin magnetic moments per formula unit in $\text{Fe}_3\text{Pt}$ compound. Results are quoted as $\mu_B$ per formula unit of $\text{Fe}_{0.75}\text{Pt}_{0.25}$ . The MCS (magnetic Compton scattering) and VSM (vibrating sample magnetometer) experimental data stem from Taylor et al. [1]. . . . .	79
3.2	Spin magnetic moments per Fe atom in $\text{Fe}_3\text{Pt}$ compound. . . . .	80
3.3	The theoretical spin magnetic moments in Gd . The SPR-KKR calculated magnetic moments are compared with FLAPW results of Kubo and Asano [2] respectively with LMTO magnetic moments of Duffy et al. [3]. . . . .	85
3.4	LMTO [4] and SPR-KKR magnetic moments of $\text{Y}_{0.38}\text{Gd}_{0.62}$ alloy. The SPR-KKR spin magnetic moments are presented in parenthesis. . . . .	88
3.5	Magnetic moments of U and Fe in $\text{UFe}_2$ compound. . . . .	92
5.1	The experimental [5, 6, 7] lattice parameters for $\text{CrX}$ ( $X = \text{S, Se, Te}$ ) systems. .	115
5.2	The interatomic distances in the NiAs structure for $\text{CrX}$ ( $X = \text{S, Se, Te}$ ) systems. N is the number of neighbours and $c$ and $ab$ distinguish Cr-neighbours along the $c$ -axis and within the $ab$ plane. . . . .	115
5.3	The exchange-splitting of the Cr(3d) states of $\text{CrX}$ ( $X = \text{S, Se, Te}$ ) systems in KKR and ASW calculations (Dijkstra et al. [8]). . . . .	116
5.4	Total energy difference $E_{FM} - E_{AF}$ (mRy) in $\text{CrX}$ ( $X = \text{S, Se, Te}$ ) systems from SPR-KKR calculations. . . . .	118
5.5	Magnetic moments in $\text{CrX}$ ( $X = \text{S, Se, Te}$ ) compounds resulting from SPR-KKR, LMTO [9] and ASW [8] calculations. . . . .	119
5.6	Magnetic moments of Cr in $\text{CrX}$ ( $X = \text{S, Se, Te}$ ) compounds resulted from FM/AF SPR-KKR calculations. . . . .	120
5.7	The SPR-KKR-LSDA equilibrium lattice parameters of $\text{CrTe}_{0.30}\text{Se}_{0.70}$ system for AF and FM, compared with the experimental values ([5, 6, 7]). . . . .	127
5.8	The SPR-KKR-GGA equilibrium lattice parameters of $\text{CrTe}_{0.30}\text{Se}_{0.70}$ system for AF and FM, compared with the experimental values ([5, 6, 7]). . . . .	129

5.9	The lattice parameters for $\text{Cr}_{1+x}(\text{Se}/\text{Te})_2$ non-stoichiometric trigonal compounds [10]. . . . .	130
5.10	Magnetic moments in trigonal $\text{Cr}_{1+x}(\text{Te}_{0.88}\text{Se}_{0.12})_2$ non-stoichiometric compounds (in $\mu_B$ ). . . . .	132
5.11	Magnetic moments in trigonal $\text{Cr}_{1.26}(\text{Te}_{0.88}\text{Se}_{0.12})_2$ and $\text{Cr}_{1.26}(\text{Te}_{0.75}\text{Se}_{0.25})_2$ non-stoichiometric compounds (in $\mu_B$ ). . . . .	134
5.12	The lattice parameters for $(\text{Cr}_x\text{Ti}_{1-x})_{1.25}\text{Te}_2$ systems measured by Bensch et al. [10]. The value of $z$ is given in units of $c$ . . . . .	137
5.13	The average interatomic distances in $(\text{Cr}_x\text{Ti}_{1-x})_{1.25}\text{Te}_2$ systems. The Cr/Ti atoms are denoted by M. . . . .	137
5.14	The exchange splitting of Cr 3d in $(\text{Cr}_x\text{Ti}_{1-x})_{1.25}\text{Te}_2$ compounds. Cr(a) and Cr(b) denote the two crystallographic sites of Cr in $P\bar{3}m1$ trigonal symmetry. . . . .	142
5.15	The SPR-KKR calculated magnetic moments in $(\text{Cr}_x\text{Ti}_{1-x})_{1.25}\text{Te}_2$ compounds. . . . .	143

# List of Figures

2.1	The schematic representation of the CPA condition. Label 'c' stands for 'effective atoms' of the coherent medium and the sites labelled 'A' and 'B' are occupied by the constituent atoms A or B with relative probability $x = x_A$ and respectively $1 - x = x_B$ . . . . .	53
3.1	The Compton scattering geometry. . . . .	63
3.2	Magnetic Compton profiles for Fe along the [001] direction (left) and [110] direction (right). Experimental data of Collins et al. (circles), APW calculations of Wakoh et al. (dotted line) and KKR calculations (full line). . . . .	69
3.3	The SPR-KKR s, p and d- contribution to the magnetic Compton profile of Fe along the [001] direction. . . . .	70
3.4	The MCP for Fe along the [111] direction. The momentum resolution of experimental data (Cooper et al.) is 0.7 a.u. (left) and 0.2 a.u. (McCarthy) (right). Both KKR and FLAPW calculations have been convoluted with a Gaussian of FWHM equal with the experimental momentum resolution. . . . .	71
3.5	The MCP profiles of Ni along the [001] direction. The FLAPW calculations of Kubo and Asano [11], the LMTO-LSDA/GGA calculations of Dixon et al. and the KKR calculations (full line) have been convoluted with a Gaussian of 0.43 a.u. FWHM., according to the experimental resolution of Dixon et al.'s data [12]. . . . .	72
3.6	The MCP profile of Ni along [111] direction (left) and [110] direction (right). The FLAPW calculations of Kubo and Asano [11] and the KKR calculations (full line) have been convoluted with a Gaussian of 0.43 a.u. FWHM to fit the experimental data of Dixon et al. [12]. . . . .	73
3.7	A two-dimensional projection of the spin momentum density: KKR calculations (up), FLAPW calculations [13] (middle) and experiment (down) [13]. . . . .	74
3.8	The anisotropic Compton profiles of $\text{Ni}_{0.75}\text{Co}_{0.25}$ . Our SPR-KKR calculations (full line) are compared with experimental data and KKR calculations of Bansil et al. [14]. . . . .	76

3.9	The anisotropic Compton [110]-[001] profiles of $\text{Ni}_{0.75}\text{Co}_{0.25}$ and pure Ni obtained by the SPR-KKR calculations. . . . .	76
3.10	The anisotropic [110]-[001] spin-up (left) and spin-down (right) profiles of $\text{Ni}_{0.75}\text{Co}_{0.25}$ and pure Ni obtained by the SPR-KKR. . . . .	77
3.11	The $\text{Cu}_3\text{Au}$ structure. . . . .	79
3.12	Left: The [001] directional MCP of $\text{Fe}_3\text{Pt}$ . The experimental profile was measured at 305 K (Srajer et al. [15]) and normalized to the corresponding total spin moment. The SPR-KKR and FLAPW (Srajer et al. [15]) profiles have been broadened with a Gaussian of 0.8 a.u. FWHM. Right: The unbroadened [001] directional MCP of $\text{Fe}_3\text{Pt}$ derived from SPR-KKR and FLAPW GGA (Wakoh et al. [16]) calculations, respectively. . . . .	80
3.13	The SPR-KKR MCP along the [001] direction of $\text{Fe}_3\text{Pt}$ decomposed into atomic type contributions (left). The d orbitals contributions at the MCP along the [001] direction of $\text{Fe}_3\text{Pt}$ , decomposed into atomic type contributions (right), by SPR-KKR calculations. . . . .	81
3.14	The [110] (left) and [111] (right) directional MCP of $\text{Fe}_3\text{Pt}$ . The SPR-KKR profile (full line), the LMTO [1] and FLAPW [16] calculations are compared with experimental data [1]. . . . .	83
3.15	The [110] (left) and [111] (right) directional MCP for disordered $\text{Fe}_{0.75}\text{Pt}_{0.25}$ alloy. The SPR-KKR calculations (full line) are compared with KKR-CPA calculations of Major et al. and experimental data [1]. Both KKR-CPA calculations have been broadened with a Gaussian of 0.4. a.u. FWHM, in accordance with the experimental momentum resolution. . . . .	83
3.16	The unbroadened [110] (left) and [111] (right) directional MCP of $\text{Fe}_3\text{Pt}$ . The SRR-KKR calculations for ordered and disordered compounds, respectively FLAPW-GGA calculations (Wakoh et al. [16]) are presented. . . . .	84
3.17	Magnetic Compton profile of Gd. Theoretical calculations are broadened with a Gaussian of FWHM 0.44 a.u.. The fully relativistic SPR-KKR profiles are compared with FLAPW [2], LMTO [3] MCP and experimental data [3]. . . .	86
3.18	Theoretical predictions on the magnetic Compton scattering of Gd. Left: The SPR-KKR calculations (full line) together with FLAPW calculations of Kubo and Asano [2] and respectively LMTO calculations of Duffy et al. [3]. The gray line is the equivalent free-atom profile for Gd 4f, normalized to 7 electrons. Right: The effect of the spin-orbit coupling on the SPR-KKR MCP of Gd. . . . .	87
3.19	Magnetic Compton profile of $\text{Y}_{0.38}\text{Gd}_{0.62}$ alloy. SPR-KKR profiles have been broadened with a Gaussian of FWHM 0.44 a.u. and normalized according to the 4f moment to be compared with experimental data of Duffy et al. [4]. . . .	89

3.20	Magnetic Compton profiles of $Y_{0.38}Gd_{0.62}$ and $Gd_{0.50}Y_{0.50}$ alloys. The SPR-KKR profiles have been normalized to free atom-like 4f contribution. . . . .	90
3.21	Influence of the spin orbit coupling (left) and orbital polarization (right) on the magnetic Compton profile of $UFe_2$ . The theoretical spectra have been convoluted with a Gaussian of FWHM 0.78 a.u. to fit the experimental data of Lawson et al. [17]. . . . .	93
3.22	The theoretical magnetic Compton profile of $UFe_2$ . The SOC = 0 labels the scalar-relativistic calculation and SOC labels the fully relativistic calculation. OP denotes the SPR-KKR calculation with orbital polarization included. . . . .	94
3.23	The magnetic Compton profile of $UFe_2$ (full line) decomposed into U (dotted line), Fe (dashed line) and interference term (U-Fe) contribution (dashed-dotted line). The profiles have been broadened with a Gaussian of FWHM = 0.78 a.u., according to the experimental momentum resolution. The experimental data of Lawson et al. [17] are represented by circles. . . . .	95
3.24	The partial components: U (circles), Fe (squares) and interference term (triangles) resulting from the SPR-KKR decomposition of the magnetic Compton profile, together with the 'Fe-3d' (full line), 'U-5f' (dotted line) and the 'spd' (dashed line) term used by Lawson et al. [17] to compose the best fit of the experimental data. . . . .	95
4.1	Positron annihilation in the solid gives rise to the $\gamma$ -rays detected by experimental measurements. . . . .	100
4.2	2D-ACAR for V perpendicular to the [001] direction: SPR-KKR calculations (top), LMTO calculations [18] (middle), experiment [18] (bottom). . . . .	106
4.3	2D-ACAR for V perpendicular to the [210] direction: SPR-KKR calculations (top), LMTO calculations [18] (middle) and experiment [18] (bottom). . . . .	107
4.4	Left: The SPR-KKR and LMTO [18] calculated magnetic Compton profile $J_{mag}(p_z)$ of Fe along the [001] (left) and the [110] direction (right) is compared with the positron annihilation spectra $J_{mag}^{2\gamma}(p_z)$ . . . . .	109
4.5	The SPR-KKR s, p and d- contribution to the positron annihilation spectra $J_{mag}^{2\gamma}(p_z)$ of Fe along the [001] direction (left) compared with the decomposition of the corresponding magnetic Compton profile (right). . . . .	110
5.1	The magnetic phase diagram of $CrTe_{1-x}Se_x$ [19] deduced from temperature dependence of magnetisation (crosses), neutron scattering measurements (triangles) and resistivity measurements (circles). The magnetic ordering (ferro-, antiferromagnetic and non-collinear) is indicated by arrows. . . . .	113
5.2	The NiAs structure for the CrX (X = S, Se, Te) systems. . . . .	114
5.3	The spin-resolved KKR density of states of CrS. . . . .	116

5.4	The spin-resolved KKR density of states of CrSe. . . . .	117
5.5	The spin-resolved KKR density of states of CrTe. . . . .	117
5.6	The spin configuration for ferromagnetic/antiferromagnetic calculation. . . . .	118
5.7	Non-collinear spin configuration in CrSe system. The spin orientation is shown for Cr atoms. . . . .	121
5.8	The exchange coupling parameters $J_{ij}$ for ferromagnetic spin configuration in the system CrSe [20]. . . . .	122
5.9	The exchange coupling parameters $J_{ij}$ for antiferromagnetic spin configuration in the system CrSe [20]. . . . .	122
5.10	The total energy vs. $\theta$ angle for the spin configuration from Fig. 5.7. SPR-KKR calculations for CrSe system. . . . .	123
5.11	The exchange coupling parameters $J_{ij}$ for ferromagnetic spin configuration in the system CrTe [20]. . . . .	125
5.12	The exchange coupling parameters $J_{ij}$ for antiferromagnetic spin configuration in the system CrTe [20]. . . . .	125
5.13	The total energy vs. tilt angle $\theta$ for the spin configuration from Fig. 5.7. SPR-KKR calculations for the CrTe system. . . . .	126
5.14	The behaviour of the magnetic moments in $\text{CrTe}_{1-x}\text{Se}_x$ system with increasing Se concentration, as resulted from SPR-KKR calculations. . . . .	127
5.15	The total energy of the system $\text{CrTe}_{0.30}\text{Se}_{0.70}$ as a function of lattice parameters, as resulted from SPR-KKR calculations, using LSDA to describe the exchange-correlation potential. . . . .	128
5.16	The total energy of the system $\text{CrTe}_{0.30}\text{Se}_{0.70}$ as a function of lattice parameters, as resulted from SPR-KKR calculations using the GGA to describe the exchange-correlation potential. . . . .	128
5.17	The structure of the non-stoichiometric $\text{Cr}_{1+x}\text{Q}_2$ (Q=Te/Se) compounds (left). The crystal structure of $\text{Cr}_{5+x}\text{Te}_8$ (right) [10]. . . . .	131
5.18	The SPR-KKR total energy variation of the system $\text{Cr}_{1.28}(\text{Te}_{0.88}\text{Se}_{0.12})_2$ as a function of Cr concentration $x$ moved from site $a$ to site $b$ , according to the scheme: $\text{Cr}_{1.0}\text{Cr}_{0.28}(\text{Te}_{0.88}\text{Se}_{0.12})_2 \rightarrow \text{Cr}_{1-x}^a\text{Cr}_{x+0.28}^b(\text{Te}_{0.88}\text{Se}_{0.12})_2$ . . . . .	132
5.19	Spin-resolved DOS of the system $\text{Cr}_{1.23}(\text{Te}_{0.88}\text{Se}_{0.12})_2$ obtained by SPR-KKR calculations. . . . .	133
5.20	Spin-resolved DOS of the system $\text{Cr}_{1.28}(\text{Te}_{0.88}\text{Se}_{0.12})_2$ obtained by SPR-KKR calculations. . . . .	133
5.21	Spin-resolved DOS of the system $\text{Cr}_{1.28}(\text{Te}_{0.75}\text{Se}_{0.25})_2$ obtained by SPR-KKR calculations. . . . .	134

5.22	The SPR-KKR total energy variation of the system $\text{Cr}_{1.25}\text{Te}_2$ as a function of Cr concentration $x$ moved from site $a$ to site $b$ , according to the scheme: $\text{Cr}_{1.25}\text{Te}_2 \rightarrow \text{Cr}_{1-x}^a \text{Cr}_{x+0.25}^b \text{Te}_2$ . . . . .	138
5.23	The SPR-KKR total energy variation of the system $(\text{Cr}_{0.4}\text{Ti}_{0.6})_{1.25}\text{Te}_2$ as a function of Cr concentration $\delta$ moved from site $b$ to site $a$ , according to the scheme: $(\text{Cr}_{0.4}\text{Ti}_{0.6})^a (\text{Cr}_{0.1}\text{Ti}_{0.15})^b \text{Te}_2 \rightarrow (\text{Cr}_{0.4+\delta}\text{Ti}_{0.6-\delta})^a (\text{Cr}_{0.1-\delta}\text{Ti}_{0.15+\delta})^b \text{Te}_2$ . . . . .	139
5.24	The spin-resolved KKR density of states of $\text{Cr}_{1.25}\text{Te}_2$ . . . . .	140
5.25	The spin-resolved KKR density of states of $(\text{Cr}_{0.6}\text{Ti}_{0.4})_{1.25}\text{Te}_2$ . . . . .	140
5.26	The spin-resolved KKR density of states of $(\text{Cr}_{0.4}\text{Ti}_{0.6})_{1.25}\text{Te}_2$ . . . . .	141
5.27	The spin-resolved KKR density of states of $(\text{Cr}_{0.2}\text{Ti}_{0.8})_{1.25}\text{Te}_2$ . . . . .	141
A.1	The vectorial configuration for the Green's function formula A.1 . . . . .	148





# Chapter 1

## Introduction

*Motto: The real voyage of discovery consists not in seeking new landscapes, but in having new eyes.*  
(M. Proust)

The magnetic properties of condensed matter is a subject which has been studied for nearly three thousand years. Lodestone, a natural ferric ferrite ( $\text{Fe}_3\text{O}_4$ ) attracted the attention of greek philosophers being mentioned by Thales who believed lodestone to possess a soul. The chinese were the first to understand and exploit the directive properties of lodestone. From about 100 AD there are references in chinese texts to a 'south-pointer', which was a lodestone spoon mounted on a top of an earthplate, permitting the rotation upon its bowl in response to magnetic torque. The result of the study on the lodestone's properties was one of the first technological product: the navigational magnetic compass. Although the compass was certainly used in West Europe by the twelfth century (references to it are dated 1175) only in the 16<sup>th</sup> century came the first prove that the earth itself is a magnet. William Gilbert (1544-1603), physicist at the Queen's Elisabeth court, wrote '*De magnete*' giving the first rational explanation to the mysterious ability of the compass needle to point north-south. This work opened the serial of scientific description of magnetic properties of the matter.

The progress in the following centuries has been more rapid and two major achievements have emerged which connect magnetism with other physical phenomena. Firstly, in 1820 Hans Christian Oersted showed that a magnetic needle rotates if it is placed near an electric circuit, demonstrating the inextricably link between magnetism and electricity. Later Michael Faraday [21, 22] demonstrated the link between light and magnetism, the magneto-optic Faraday effect which bears his name. These capital discoveries were unified in four equations, the laws of Ampère, Faraday, Biot-Savart and Laplace by Maxwell. These four equations epitomize the electromagnetic revolution. Richard Feymann claimed that '*ten thousand years from now, there can be little doubt that the most significant event of the 19<sup>th</sup> century will be judged as Maxwell's discovery of the laws of electrodynamics*'.

With Maxwell's equations the classical electromagnetism was complete, but ferromagnetism remained a mystery. It was in 1907 when Peter Weiss produced a theory of ferromagnetism

based on the assumption that the interaction between magnetic molecules can be described by an internal 'molecular field'. Combining the molecular field with the theory by Langevin of paramagnetic solids gave a description of the phase transition at the Curie temperature where a ferromagnet loses its magnetisation and becomes paramagnetic.

The existence of this 'molecular field' produced a strong conflict between classical theory of magnetism and experiment, the solution being given by quantum mechanics. Bohr postulated that the angular momentum of electrons is quantized and the orbital magnetic moments are associated with the orbiting electron currents. In 1922 a famous experiment by Stern and Gerlach proved beyond all doubts that the magnetic moments have a quantized character. Compton suggested in 1921 that the electron possessed also a magnetic moment associated with an intrinsic spin angular momentum and this was discovered by Goudsmit and Uhlenbeck in 1925. In 1928 Dirac [23, 24] explained the existence of spins by writing down a relativistically invariant extension of Schrödinger's equation where the electron spin came naturally out of the calculation. The Weiss field was shown by Dirac and Heisenberg to arise from the Pauli principle that no two electrons could occupy the same state.

We mentioned here just few moments in the history of the magnetism. However it is the magnetism in condensed matter systems, including ferromagnets, spin glasses and low-dimensional systems, which is still of great interest today. Macroscopic systems exhibit magnetic properties which are fundamental different from those of atoms and molecules, despite the fact that they are composed of the same basic constituents. This arises because magnetism is a collective phenomenon, involving the mutual cooperation of enormous number of particles, and in this sense similar to the superconductivity and superfluidity.

The technological drive to find new materials for use in permanent magnets, sensors or in recording applications runs in parallel with the effort to explain theoretically the existent properties of materials. All new achievements need a strong theoretical support and accordingly the KKR band structure method in its relativistic version is a valuable tool in the ground state properties of the condensed matter.

The scope of the present thesis is to give an insight into different aspects of magnetism: Compton magnetic scattering and positron annihilation in the metallic systems and the magnetic properties in Cr-chalcogenide systems, for which a theoretical description is presented.

## 1.1 Compton effect

The Compton effect was discovered at the beginning of the 20th century, when it was observed that the scattering process affects to some extent the energy spectrum of the radiation. This revelation arise from experiments with scattered  $\gamma$ -rays, which indicates not only that the secondary radiation beam was softer than the primary beam, but also that the softening depends on the scattering angle.

A few years later, Arthur Compton carried out a famous set of measurements with X-rays (Compton 1923 [25, 26]). Using a recently developed wavelength analyser, he determined

for the first time numerically the softening of the scattered radiation. The scattering of the light on a metallic target was described as an interaction between the photons and individual electrons which behave as free particles. In classical physics, electromagnetic waves possess no momentum. To assign a momentum to an electromagnetic wave was a revolutionary idea at that time and so, Compton scattering emerged as one of the direct manifestations of the quantum nature of light.

Soon later it was realized that the Compton scattered line is broadened. Jauncey (1925) [27] was the first who linked the motion of the target electrons to a Doppler broadening of the Compton scattered beam. Unfortunately he chose to base his calculations on the Bohr-Sommerfeld orbital model and, not surprisingly, his predicted lineshapes were unrealistic. Du Mond (1929) [28, 29] had more success when he used the novel Fermi-Dirac distribution function to predict the lineshape; indeed, his result on beryllium possibly represents the earliest direct evidence for the validity of Fermi-Dirac as opposed to Maxwell-Boltzmann statistics for the electron gas.

Nowadays, most of physicists connect the Compton effect with the early vindication of quantum ideas whereas many would associate it with the high-energy physics, but only very few of them would link the phenomenon to studies on the electron momentum density distributions.

Despite this situation, the Compton scattering is still a subject of interest for the solid state physicists, Compton-scattering studies providing access to the electron momentum distribution of the target (Cooper 1985 [30], Schülke 1991 [31]). A part of the present work is an attempt to make the connection between electron momentum density and experimentally accessible Compton profiles more transparent.

## 1.2 Positron annihilation

Positrons entering a solid annihilate mainly by emitting two  $\gamma$  rays in nearly opposite directions. The 2D-ACAR (two-dimensional angular correlation of the annihilation radiation) measurements consist in detecting simultaneously the direction of the two  $\gamma$  photons. The 2D-ACAR spectrum is proportional to the two-dimensional projection of the electron-positron momentum density  $n_{2\gamma}(\vec{r})$ . Thus a 2D-ACAR measurement contains information on the electron and the positron wave functions, and on the positron-electron and electron-electron correlations. Also, the positron annihilation is a successful method for Fermi surface measurement in metallic systems.

## 1.3 Cr-chalcogenide systems

The system Cr-chalcogenide is a class of materials possessing metallic, half-metallic or semi-conducting character dependent on the anion and on the ratio between Cr and chalcogen

atoms. Also, Cr-chalcogenides may have ferromagnetic, antiferromagnetic or non-collinear spin structure for different structures and compositions. The substitution of Ti or V for Cr enlarge this class of materials and enable new properties, as spin-glass behaviour for Ti substituted  $\text{Cr}_5\text{Te}_8$ . Also, the Te substitution for Se within an isostructural series leads to a significant change of interatomic distances between metal atoms. As a consequence, the magnetic interaction between metal neighbours is weaker.

All these structural and compositional modifications for the Cr-chalcogenide systems in discussion within this thesis have been very precisely characterized by experimental measurements performed by the group of Prof. W. Bensch from University of Kiel. The theoretical investigations performed by us comes to support the interpretation of the experimental results and to enable the understanding of the different magnetic properties of individual Cr-chalcogenide systems.

## 1.4 Scope of the work

First-principles investigations are performed in the framework of density functional theory (DFT) within the local density approximation as implemented in the spin polarized relativistic version of the Korringa-Kohn-Rostoker (SPR-KKR) band structure method. The fundamentals of the density functional theory (DFT) which represent the basis of the self-consistent band structure calculations, as well as the method to solve the Kohn-Sham-Dirac equation based on the multiple scattering theory treating spin-orbit coupling and spin polarisation on an equal footing are presented in detail in Chapter 2. The coherent potential approximation (CPA) used to deal with random substitutional alloys is presented also in Chapter 2.

The basics of the theoretical approach of the magnetic Compton profile is presented in Chapter 3. The calculations of the directional magnetic Compton profile for the pure transitional metals (Fe and Ni) is compared with the experimental data. The decomposition of the Fe spectra into s, p and d-like contribution is accomplished. The anisotropic Compton profile for the disordered alloy Ni-Co is calculated and the effect of the disorder in  $\text{Fe}_3\text{Pt}$  systems is discussed. The influence of spin-orbit coupling on the magnetic Compton profiles of Gd and Y-Gd alloys is considered. Finally, the influence of the spin-orbit coupling and orbital polarisation on the magnetic Compton profile of  $\text{UFe}_2$  is discussed in detail.

The theoretical approach for the electron-positron momentum density and the formalism for calculating the two-dimensional angular correlation of the annihilation radiation (2D-ACAR) is presented in Chapter 4. 2D-ACAR spectra for a pure transitional metal (V) is compared with the experimental data and with LMTO calculations.

In Chapter 5, the connection between the composition, structural characteristics and magnetic properties in Cr-chalcogenide systems is discussed. Ground state band structure SPR-KKR calculations have been performed in order to establish the magnetic moments and magnetic phase stability for binary  $\text{CrX}$  ( $X = \text{S}, \text{Se}, \text{Te}$ ) compounds and for  $\text{CrSe}_x\text{Te}_{1-x}$  alloys. The magnetic moments and density of states in the non-stoichiometric  $\text{Cr}_{1+x}(\text{Te/Se})_2$

compounds have been calculated. The preference of Cr for one crystallographic site in the trigonal structure of the space group  $P\bar{3}m1$  is explained using energetic arguments. The influence of Ti substitution for Cr into  $\text{Cr}_5\text{Te}_8$  on the structure and the magnetic properties is discussed. The preferential site occupation of the metal atoms Ti and Cr is determined.



# Chapter 2

## Theory

### 2.1 Density Functional Theory

In the last 30 years, many theoretical techniques were developed to describe the electronic structure of condensed material using self-consistent first principles quantum-mechanical methods.

One of the difficulties for a successful theoretical description of a given material arise from electron-electron interaction. If one decides to ignore the effects of electron-electron interaction, then the motion of each electron is described by a single-particle wave function. Thus the ground state of the system could be written (Hartree Fock Theory) as a antisymmetric product of one-electron wave functions. However in this way the properties of the condensed material cannot be described correctly. Therefore, one should include the effects of the interaction between the electrons making some sensible approximations to enable one to successfully model such a system.

Density Functional Theory (DFT) is a general theoretical framework which enable us to calculate the ground state energy  $E_g$  of any condensed matter system consisting of electrons in some external potential.

DFT was introduced in 1964 by Hohenberg and Kohn [32]. It is a theoretical tool that provides a general framework for the calculation of the ground state of an ensemble of atoms, whose nuclei are fixed at specified positions, using the electronic density as a basic variable of the total energy functional, which is written  $E[n(\vec{r})]$ . The square brackets are the standard way to indicate that a function depends on a function rather than a variable; in this case energy is a function of electronic density  $n(\vec{r})$  which vary with respect to  $\vec{r}$ .

DFT differs from Hartree Fock theory, as it uses the electronic density rather than wave functions as basic quantities to describe the properties of a material. DFT also includes both exchange and correlation effects in a mean field sense, whereas Hartree Fock theory includes exchange, but ignores correlation effects. DFT has also the advantage that it can be used efficiently for calculating the properties of systems that contains hundreds of particles - one would not attempt to solve such a problem using Hartree-Fock-like methods.

### 2.1.1 Non-relativistic Density Functional Theory

The development of the DFT enable a wide variety of systems to be described correctly by this theory including systems with degenerate ground states, spin-polarised systems and many others.

The Hamiltonian for a system of N interacting electrons can be written as:

$$\hat{H} = \hat{T} + \hat{U} + \hat{V} = \hat{H}_0 + \hat{V} . \quad (2.1)$$

In this equation,  $\hat{T}$  represents the kinetic energy of the electrons,  $\hat{U}$  represents their Coulomb repulsion and  $\hat{V}$  is their interaction with an external field.

The ground state energy of the electronic system is:

$$E_g = \langle \Psi | \hat{H}_0 + \hat{V} | \Psi \rangle . \quad (2.2)$$

The electronic density is written as:

$$n(\vec{r}) = \langle \Psi | \hat{n}(\vec{r}) | \Psi \rangle \quad (2.3)$$

where  $\Psi$  is the many-electron wave function representing the whole system. The operator  $\hat{n}(\vec{r})$  represents the electronic density at point  $\vec{r}$ . In terms of field operators for creation and annihilation of particles this operator reads:

$$\hat{n}(\vec{r}) = \sum_{\sigma} \Phi_{\sigma}^{\dagger}(\vec{r}) \Phi_{\sigma}(\vec{r}) , \quad (2.4)$$

where we sum over the particle spin  $\sigma$ . We can also write down the expression for the operators in Eq. (2.1) in terms of field operators:

$$\hat{U} = \frac{1}{2} \frac{e^2}{4\pi\epsilon_0} \sum_{\sigma, \sigma'} \int \int \Phi_{\sigma}^{\dagger}(\vec{r}) \Phi_{\sigma'}^{\dagger}(\vec{r}') \frac{1}{|\vec{r} - \vec{r}'|} \Phi_{\sigma'}(\vec{r}') \Phi_{\sigma}(\vec{r}) d^3r d^3r' \quad (2.5)$$

$$\hat{V} = \sum_{\sigma} \int v^{ext}(\vec{r}) \Phi_{\sigma}^{\dagger}(\vec{r}) \Phi_{\sigma}(\vec{r}) d^3r \quad (2.6)$$



$$\hat{T} = -\frac{\hbar^2}{2m} \sum_{\sigma} \int \nabla \Phi_{\sigma}^{\dagger}(\vec{r}) \nabla \Phi_{\sigma}(\vec{r}) d^3 r . \quad (2.7)$$

Eq. (2.5) represents the Coulomb repulsion between the electrons, the factor  $\frac{1}{2}$  outside occurs because the summation for each pair is done twice. Eq. (2.6) represents the effect of the external potential  $v^{ext}$  and (2.7) is the kinetic energy operator.

Nonrelativistic DFT is based on two statements, that were derived by Hohenberg and Kohn [32] and that form the basic theorems for DFT:

1. *All ground state properties of a system of N interacting electrons acted on by the same well defined external potential  $v^{ext}(\vec{r})$  can be expressed as a unique functional of the density distribution  $n(\vec{r})$ . In particular one has for the ground state energy:*

$$E_g[n(\vec{r})] = \int v^{ext}(\vec{r}) n(\vec{r}) d^3 r + F[n(\vec{r})] . \quad (2.8)$$

This first term in Eq. (2.8) describes the energy due to the interaction of the electrons with the external potential  $v^{ext}$  and the second term describes the rest of the energy contributions of the system. The energy functional  $F[n(\vec{r})]$  is actually defined as the ground state expectation value of the Hamiltonian  $\hat{H}_0$ , where  $\hat{H}_0 = \hat{T} + \hat{U}$ , with  $\hat{T}$  describing the kinetic energy of electrons and  $\hat{U}$  describing the interactions between electrons, respectively.

It should be mentioned that the energy functional  $F[n(\vec{r})]$  is a universal functional and this implies that  $F[n(\vec{r})]$  does not refer solely to a particular system, but is valid for any number of particles in the system and for any external potential  $v^{ext}(\vec{r})$ .

It is convenient to separate the functional  $F[n(\vec{r})]$  into two parts. The first term is the Hartree energy  $E_H[n(\vec{r})]$  and the second is the unknown functional  $G[n(\vec{r})]$ , which is a universal functional in the same manner as  $F[n(\vec{r})]$ .

$$F[n(\vec{r})] = E_H[n(\vec{r})] + G[n(\vec{r})] \quad (2.9)$$

Furthermore, one may make the definition

$$G[n(\vec{r})] = T_0[n(\vec{r})] + E_{xc}[n(\vec{r})] \quad (2.10)$$

where  $T_0[n(\vec{r})]$  is the kinetic energy of a system of non-interacting electrons in the ground state with density distribution  $n(\vec{r})$  and the only unknown is the so-called exchange -correlation energy  $E_{xc}[n(\vec{r})]$  and thus an approximation for this has to be made. The exchange-correlation energy is defined as the part of energy  $F[n(\vec{r})]$  not included in  $E_H[n(\vec{r})]$  nor in  $T_0[n(\vec{r})]$ . The physical origin for this term is the fact that electrons tend to avoid each other

as a consequence of the Pauli exclusion principle and Coulomb repulsion.

Under the previous suppositions, the expression for the ground state energy reads as :

$$\begin{aligned}
 E_g[n(\vec{r})] &= \int v^{ext}(\vec{r})n(\vec{r})d^3r + E_H[n(\vec{r})] + T_0[n(\vec{r})] + E_{xc}[n(\vec{r})] \\
 &= \int v^{ext}(\vec{r})n(\vec{r})d^3r + \frac{1}{2} \frac{e^2}{4\pi\epsilon_0} \int \int \frac{n(\vec{r})n(\vec{r}')}{|\vec{r} - \vec{r}'|} d^3r d^3r' \\
 &\quad + T_0[n(\vec{r})] + E_{xc}[n(\vec{r})] .
 \end{aligned} \tag{2.11}$$

To deal with this expression for the ground state energy one can make use of the second theorem of DFT:

2. *The ground state energy associated with a given external potential is found by minimizing the total energy functional with respect to changes in the electron density while the number of particles is held fixed. The density that yields the minimum total energy is the ground state density.*

Next we need to perform the minimization of the total energy. The number of electrons  $N$  in our system does not change and we can write:

$$K[n(\vec{r})] = \int n(\vec{r})d^3r = N . \tag{2.12}$$

To solve the minimization problem the Lagrange multiplier method is used. According to this method,  $K[n(\vec{r})]$  is multiplied by the unknown Lagrange multiplier  $\mu$  (which must have the unit of energy) and subtracts it from the total energy functional. The result is written as:

$$\begin{aligned}
 E[n(\vec{r})] - \mu K[n(\vec{r})] &= T_0[n(\vec{r})] + \frac{1}{2} \frac{e^2}{4\pi\epsilon_0} \int \int \frac{n(\vec{r})n(\vec{r}')}{|\vec{r} - \vec{r}'|} d^3r d^3r' + \int n(\vec{r})v^{ext}(\vec{r})d^3r + \\
 &\quad E_{xc}[n(\vec{r})] - \mu \int n(\vec{r})d^3r .
 \end{aligned} \tag{2.13}$$

Minimizing this functional with respect to the electronic density distribution  $n(\vec{r})$ , one is now able to determine  $\mu$  from the conservation of particles constraint,  $K[n(\vec{r})]$ , for a given electron density distribution. Taking an infinitesimal variation of Eq. (2.8) and setting the resultant expression equal to zero, we end up with:

$$\int \delta n(\vec{r}) \left[ v^{ext}(\vec{r}) + \frac{\delta T_0[n(\vec{r})]}{\delta n(\vec{r})} + \frac{1}{2} \frac{e^2}{4\pi\epsilon_0} \int \frac{n(\vec{r}')}{|\vec{r} - \vec{r}'|} d^3r' + \frac{\delta E_{xc}[n(\vec{r})]}{\delta n(\vec{r})} - \mu \right] d^3r = 0 . \tag{2.14}$$

Eq. (2.14) should be valid for an arbitrary variation in density  $\delta n(\vec{r})$  and this can only be true if the expression between the brackets is zero. The extremal  $n_{GS}$ , which is the ground state density for the energy functional is obtained when:

$$\mu = v^{ext}(\vec{r}) + \frac{\delta T_0[n(\vec{r})]}{\delta n(\vec{r})} + \frac{1}{2} \frac{e^2}{4\pi\epsilon_0} \int \frac{n(\vec{r}')}{|\vec{r} - \vec{r}'|} d^3r' + \frac{\delta E_{xc}[n(\vec{r})]}{\delta n(\vec{r})}. \quad (2.15)$$

This Euler equation for an interacting system of electrons seems to be not very helpful to get  $n_{GS}(\vec{r})$ , because of the unknown quantities  $\mu$  and  $E_{xc}(\vec{r})$ . To solve the problem, one make the following supposition using quantum mechanical theory: for a non-interacting electronic system,  $E_H[n(\vec{r})] = E_{xc}[n(\vec{r})] = 0$ , so Eq. (2.15) becomes:

$$v^{ext}(\vec{r}) + \frac{\delta T_0[n(\vec{r})]}{\delta n(\vec{r})} = \mu \quad (2.16)$$

If we use the notation:

$$v^{eff}(\vec{r}) = v^{ext}(\vec{r}) + \frac{1}{2} \frac{e^2}{4\pi\epsilon_0} \int \frac{n(\vec{r}')}{|\vec{r} - \vec{r}'|} d^3r' + \frac{\delta E_{xc}[n(\vec{r})]}{\delta n(\vec{r})} \quad (2.17)$$

we get

$$v^{eff}(\vec{r}) + \frac{\delta T_0[n(\vec{r})]}{\delta n(\vec{r})} = \mu \quad (2.18)$$

and one can notice that the Euler equations for an interacting system and that of a non-interacting gas are formally identical. Assuming that there is a method to obtain the effective potential  $v^{eff}(\vec{r})$ , one is now able to determine the ground state of an interacting system using similar techniques to that for determining the ground state of a non-interacting system acted on by the external potential  $v^{ext}(\vec{r})$ .

For this system, the many body Schrödinger equation can be reduced by separation of variables to N single-particle Schrödinger equations and the many body wave function is a product of single-particle wave functions. Accordingly we can write the Schrödinger equation for each electron individually:

$$\left[ -\frac{\hbar^2}{2m} \nabla^2 + v^{ext}(\vec{r}) \right] \Psi_i = \epsilon_i \Psi_i. \quad (2.19)$$

Using the defined effective potential from Eq. (2.17), the Schrödinger equation for our interacting electronic system is formally identical:

$$\left[ -\frac{\hbar^2}{2m} \nabla^2 + v^{eff}(\vec{r}) \right] \Psi_i = \epsilon_i \Psi_i. \quad (2.20)$$

The Schrödinger-like equation containing  $v^{eff}$  is the so-called the Kohn-Sham equation and  $\Psi_i$  are Kohn-Sham orbitals.  $\Psi_i$  and  $\epsilon_i$  are not the wave function and the corresponding energy for real electrons and because of this they don't have any physical meaning.  $\Psi_i$  and  $\epsilon_i$  are simply auxiliary quantities for calculating  $n(\vec{r})$  and the total energy using the expression:

$$n(\vec{r}) = \sum_{i=1}^N |\Psi_i(\vec{r})|^2 . \quad (2.21)$$

The eigenvalues  $\epsilon_i$  can also be used to express the total energy associated with the set of one-electron equations (see Eq. (2.20)):

$$\begin{aligned} \sum_{i=1}^N \epsilon_i &= T_0[n(\vec{r})] + \int v^{eff}(\vec{r})n(\vec{r})d^3r \\ &= T_0[n(\vec{r})] + \int v^{ext}(\vec{r})n(\vec{r})d^3r + \frac{e^2}{4\pi\epsilon_0} \int \int \frac{n(\vec{r})n(\vec{r}')}{|\vec{r} - \vec{r}'|} d^3r d^3r' \\ &\quad + \int \frac{\delta E_{xc}[n(\vec{r})]}{\delta n(\vec{r})} n(\vec{r})d^3r . \end{aligned} \quad (2.22)$$

If we substitute  $T[n(\vec{r})]$  from Eq. (2.22) into Eq. (2.11) we get:

$$E_g[n(\vec{r})] = \sum_{i=1}^N \epsilon_i - \frac{1}{2} \frac{e^2}{4\pi\epsilon_0} \int \int \frac{n(\vec{r})n(\vec{r}')}{|\vec{r} - \vec{r}'|} d^3r d^3r' - \int \frac{\delta E_{xc}[n(\vec{r})]}{\delta n(\vec{r})} n(\vec{r})d^3r + E_{xc}[n(\vec{r})] . \quad (2.23)$$

Let's assume we have an adequate approximation for  $E_{xc}$ . Then we have a set of self consistent equations to solve. The starting point is to make a guess for the effective potential in Eq. (2.17). Using this effective potential one can solve the Kohn Sham Eq. (2.20) using standard single-particle theory (see refs. [33], [34]). The resulting  $\Psi_i$  is used to calculate  $n(\vec{r})$  by Eq. (2.21). The density  $n(\vec{r})$  is re-used to calculate, by Eq. (2.17), the potential  $v^{eff}$ . We continue going round this loop until the potential at one iteration is the same (within a required accuracy) with the potential coming from the previous iteration and we get at the final  $v^{eff}$ . The eigenfunctions  $\epsilon_i$  obtained solving the Kohn-Sham Eq. (2.20) with this effective potential are used to calculate the total energy  $E_g[n(\vec{r})]$  from Eq. (2.23).

This formalism is equally applicable to bosons and fermions, the exchange-correlation energy is that which takes the statistics into account.

In the formalism presented above, all the terms except the exchange-correlation energy are treated exactly. The critical problem of DFT is to use an appropriate approximation for the exchange-correlation energy, because for solid state systems, except for the case of a uniform electron gas, the explicit form is not known. Due to the Coulomb repulsion, one may

think that there is a region of depleted charge surrounding each electron. At a given point  $\vec{r}'$  the density depletion associated with the electron located at  $\vec{r}$  is  $n^h(\vec{r}, \vec{r}')$ . The exchange-correlation hole must contain a unit charge, i.e., the sum-rule

$$\int n^h(\vec{r}, \vec{r}') d^3 r' = -1 \quad (2.24)$$

must be satisfied.

The derivation of the exchange-correlation energy  $E_{xc}[n(\vec{r})]$  can be done using a method known as adiabatic connection [35, 36, 37]. The basic concept is that while keeping the density fixed, the non-interacting system is connected to the interacting system via a coupling constant  $\lambda$ , which represent the strength of the electron-electron interaction.  $\lambda = 0$  implies the non-interacting system and  $\lambda = 1$  is the fully interacting system. Using this method, the exchange-correlation functional can be written as:

$$E_{xc}[n(\vec{r})] = \frac{1}{2} \frac{e^2}{4\pi\epsilon_0} \int n(\vec{r}) d^3 r \int \frac{n^h(\vec{r}, \vec{r}')}{|\vec{r} - \vec{r}'|} d^3 r'. \quad (2.25)$$

The exchange-correlation hole  $n^h(\vec{r}, \vec{r}')$  is actually averaged over a coupling constant dependent hole  $n_\lambda^h(\vec{r}, \vec{r}')$ :

$$n^h(\vec{r}, \vec{r}') = \int_0^1 n_\lambda^h(\vec{r}, \vec{r}') d\lambda. \quad (2.26)$$

A useful quantity to define from Eq. (2.25) is the exchange-correlation energy per particle  $\epsilon_{xc}(n(\vec{r}))$ , otherwise known as energy density:

$$\epsilon_{xc}(n(\vec{r})) = \frac{1}{2} \int \frac{n^h(\vec{r}, \vec{r}')}{|\vec{r} - \vec{r}'|} d^3 \vec{r}'. \quad (2.27)$$

Simply said, the electronic many body problem would be solved if  $n^h(\vec{r}, \vec{r}')$  were known exactly in analytic form.

Because of the isotropic nature of the Coulomb interaction, the exchange-correlation function can be evaluated using exact wave functions and it can be shown that, although the hole may be strongly non-spherical, the only contributing parts to the total exchange-correlation energy are the spherical ones, due to the fact that the non-spherical terms average out to zero.

The most used approximation method to calculate the exchange-correlation energy is called Local Density Approximation (LDA). In LDA, a slowly varying electron density distribution is supposed. The exchange-correlation energy of an electronic system is constructed by assuming that the exchange-correlation energy per electron at a point  $\vec{r}$  in the electron gas,

is equal to the exchange-correlation energy per electron in a homogeneous electron gas that has the same electron density at the point  $\vec{r}$ . It follows that

$$E_{xc}[n(\vec{r})] \approx \int n(\vec{r}) \epsilon_{xc}(n(\vec{r})) d^3r . \quad (2.28)$$

The physical meaning of this formula is the following: in performing an integral we divide the volume up into infinitesimal volumes and sum all their contribution to the integral. Here the assumption is made that in each infinitesimal volume the density is constant and hence the exchange-correlation energy will approximately take on the value for the homogeneous electron gas in that infinitesimal volume.

The LDA approximation is exact for two extreme cases: slowly varying charge densities and high electron densities, but in spite of some famous failures, it was found that the LDA produces surprisingly good results for a wide class of systems with rapidly varying densities. If the spin degrees of freedom are taken into account, von Barth and Hedin [38] established a straightforward generalization of the Hohenberg-Kohn theorem, founding so-called spin-density functional theory (SDFT). Within this approach it was assumed that the external field couples only to the spin degree of freedom which leads to the additional potential term in the Hamiltonian

$$\mu_B \int \vec{B}_{ext}(\vec{r}) \hat{m}(\vec{r}) d^3r \quad (2.29)$$

with  $B_{ext}$ , the external magnetic field and  $\hat{m}(\vec{r})$  the spin density operator

$$\hat{m}(\vec{r}) = \sum_{\alpha, \beta} \Phi_{\alpha}^{+}(\vec{r}) \vec{\sigma}_{\alpha\beta} \Phi_{\beta}(\vec{r}) \quad (2.30)$$

and  $\vec{\sigma}_{\alpha\beta}$ , the vector of Pauli matrices.

The energy functional depends now not only on the particle density  $n(\vec{r})$  but also on the spin density  $\vec{m}(\vec{r})$ . If the external magnetic field  $B_{ext}$  and the quantization axis point along the z direction everywhere, one has to consider only the z projection  $m_z$  of the spin density and the particle density  $n$  as independent variables in the energy functional

$$E_g[n(\vec{r}), m_z(\vec{r})] = F[n(\vec{r}), m_z(\vec{r})] + \int [v^{ext}(\vec{r})n(\vec{r}) - \mu_B B_z(\vec{r})m_z(\vec{r})] d^3r . \quad (2.31)$$

Using the notation  $n^{+}$  and  $n^{-}$  for the spin-projected particle densities, we can write the spin and particle densities as

$$m(\vec{r}) = n^{+}(\vec{r}) - n^{-}(\vec{r}) \quad (2.32)$$

$$n(\vec{r}) = n^{+}(\vec{r}) + n^{-}(\vec{r}) \quad (2.33)$$

and one can generalize the Kohn-Sham Eq. (2.20) for each spin  $\sigma$  in the following way:

$$(-\vec{\nabla}^2 + V^\sigma(\vec{r}))\Phi_i^\sigma(\vec{r}) = \epsilon_i^\sigma(\vec{r}). \quad (2.34)$$

The effective spin-dependent potential used in this equation is

$$V^\sigma = V_{ext} + V_H + V_{xc}^\sigma + \sigma B_{ext}, \quad (2.35)$$

with the exchange-correlation potential

$$V_{xc}^\sigma(\vec{r}) = \frac{\partial E_{xc}[n^+, n^-]}{\partial n^\sigma(\vec{r})}. \quad (2.36)$$

Doing some transformations, one can set up the new independent potentials:

$$V_{xc}(\vec{r}) = \frac{1}{2}(V_{xc}^+(\vec{r}) + V_{xc}^-(\vec{r})) = \frac{\partial E_{xc}[n, m]}{\partial n(\vec{r})} \quad (2.37)$$

$$B_{xc}(\vec{r}) = \frac{1}{2}(V_{xc}^+(\vec{r}) - V_{xc}^-(\vec{r})) = \frac{\partial E_{xc}[n, m]}{\partial m(\vec{r})} \quad (2.38)$$

and re-write the spin-dependent potential as:

$$V^\sigma = V_{ext} + V_H + V_{xc} + \sigma B_{eff} \quad (2.39)$$

with  $B_{eff} = B_{ext} + B_{xc}$ . Clearly, due to the definition of  $B_{eff}$ , there may exist a magnetic solution for zero external field strength. If such a solution exists, it may have a lower energy than the non-magnetic case and the theory may predict magnetic ordering.

Similar with the DFT, a crucial point in SDFT is to supply a reasonable approximation for the exchange-correlation energy. Using the same justification like in the case of LDA, the most used approximation in the spin-dependent case has the form:

$$E_{xc}[n(\vec{r}), m_z(\vec{r})] = \int n(\vec{r})\epsilon_{xc}[n, m]d\vec{r}, \quad (2.40)$$

where  $\epsilon_{xc}[n, m]$  is the correlation energy of a homogeneous spin polarized electron gas.

Parametrizations for  $\epsilon_{xc}[n, m]$  can be found in the work of v. Barth and Hedin [38], Gunnarsson and Lundqvist [39], Vosko, Wilk and Nusair [40], Perdew and Zunger [41], respectively. The LSDA provides a realistic description of the structural properties, elastic and vibrational properties for both solids and molecules, but for certain systems the LSDA has a strong tendency to over-binding.

The Generalized Gradient Approximation (GGA) for the exchange-correlation energy improved upon the Local Spin Density Approximation (LSDA) description of atoms, molecules

and solids ([42, 43, 44, 45, 46]). In the Generalized Gradient Approximation (GGA) the gradient is included as a new variable and one tries to determine the best scheme that fulfills the relation:

$$E_{xc}^{GGA}[n(\vec{r})] = \int d^3r f(n^+, n^-, \nabla n^+, \nabla n^-) n(\vec{r}) . \quad (2.41)$$

There are many parametrizations for the exchange and correlation functionals, among the most known one should mention the PW91 [47, 48] exchange and correlation functional, which was constructed by introducing a real-space cut-off of the spurious long-range part of the density-gradient expansion for the exchange-correlation hole. The cut-off procedure was designed in such a way that as many as possible of the known features of the exact exchange and correlation energy were obeyed.

It has later been discovered that there are some unphysical wiggles in the PW91 exchange-correlation potential for small and large reduced density gradients. There are also quite many parameters in the PW91 functional, and it has been found that more features of the exchange-correlation energy exist than those satisfied by the PW91 parametrization.

To remedy the weakness of the PW91 functional the Perdew-Burke-Ernzerhof (PBE) functional has been constructed [49, 50]. This is today the most used GGA functional. The second order expansion for slowly varying or small density variations is fulfilled, as in the case of PW91, but this constraint has been relaxed in the PBE functional to give a better description of the linear response limit.

In the GGA, the appropriate exchange energy form for slowly varying densities is

$$E_x^{GGA}[n(\vec{r})] \approx \int n(\vec{r}) \epsilon_x^{GGA}(n(\vec{r}), s(\vec{r})) d^3r \approx \int n(\vec{r}) \epsilon_x^{LDA}(n(\vec{r})) F_x^{GGA}(s(\vec{r})) \quad (2.42)$$

where the variable  $s$  is the reduced density gradient, given by the formula:

$$s(n(\vec{r})) = \frac{\nabla n(\vec{r})}{2k_F n(\vec{r})} \quad (2.43)$$

and  $k_F$  is defined by  $n(\vec{r}) = \frac{k_F^3}{3\pi^2}$ .

The functional present in Eq. (2.41),  $F_x^{GGA}(s(\vec{r}))$ , is the exchange enhancement function of the GGA and in the case of PBE it is given by

$$F_x^{PBE} = 1 + \kappa - \frac{\kappa}{1 + \mu s^2 / \kappa} \quad (2.44)$$

where, as before,  $s$  is the reduced density gradient and the constants  $\mu = 0.2195$  and  $\kappa = 0.804$  are chosen in such a way, that the gradient expansion around  $s = 0$  should give the



correct linear response of the homogeneous electron gas, and the local Lieb-Oxford bound [51]:

$$\begin{aligned} E_x^{PBE}[n^+, n^-] &\geq E_{xc}[n^+, n^-] \\ &\geq -1.679e^2 \int d^3r n(\vec{r})^{4/3} \end{aligned} \quad (2.45)$$

should be satisfied.

The PBE functional is often called as a 'first principles' functional, because it is constructed from known limits of the homogeneous electron gas and scaling relations. Furthermore, it doesn't contain any parameters, which are not either fundamental constants or determined to satisfy some specific quantum mechanical boundary conditions. It should however be noted that except for the high and low gradient constraints (linear response of homogeneous electron gas and Lieb-Oxford bound) the exchange enhancement function is not restricted. The GGA has the same problems as LDA in calculating properties like densities of states (DOS), band structures or photo-emission spectra. Even the correct density functional will not describe these properties exactly. It is beyond the DFT to calculate properties other than ground state energy and (spin polarized) charge density. In practice LDA gives reasonably good optical spectra and band structures are looking as expected in many cases, but there are exceptions. For example, the strongly correlated system  $\text{La}_2\text{CuO}_4$  is predicted to be a metal while in reality it is an insulator. Also in line with this, band-gaps calculated with GGA or LDA are smaller than the observed values.

## 2.1.2 Relativistic Density Functional Theory

In the previous section, an explicit form of the Hamiltonian was not specified, so this means that relativistic effects can be included through various correction terms, like the inclusion of the rest mass effect or spin-orbit coupling, in this formalism.

Nevertheless, not all the phenomena can get this way an appropriate treatment. Many phenomena appearing in magnetic materials are intrinsically of relativistic origin and because of that, they require an adapted fully relativistic version of DFT.

The first of such a description was made by Rajagopal and Callaway [52]. They generalized the Kohn-Hohenberg-Sham description for the non-relativistic inhomogeneous fermion gas, with spin effects included. A further development of this model was done later by Rajagopal (1978) [53], Ramana and Rajagopal (1979) [54] and separately, by McDonald and Vosko (1979) [55].

The interaction of the external magnetic field  $\vec{B}_{ext}(\vec{r}) = \vec{\nabla} \times \vec{A}_{ext}$  with the electronic system is included in the Hamiltonian through the coupling of the Dirac current to the vector potential  $\vec{A}_{ext}$ :

$$\hat{H} = \hat{T} + \hat{U} + \hat{V} - e \int \hat{J}(\vec{r}) \vec{A}_{ext}(\vec{r}) d^3r . \quad (2.46)$$

Here the Dirac electronic system is described using four-vector notation, so the scalar potential and the vector potential are combined to get the following expression for the external potential:

$$A_{ext}^\mu(\vec{r}) = \left( \frac{1}{ec} v^{ext}, \vec{A}_{ext}(\vec{r}) \right). \quad (2.47)$$

The four-current electron density distribution has the expression:

$$J^\mu(\vec{r}) = (cn(\vec{r}), \vec{J}(\vec{r})). \quad (2.48)$$

These four components of  $J^\mu(\vec{r})$  must satisfy the continuity equation, ensuring that the charge within the system is conserved, so the four components of the vector are not all independent of one other:

$$\frac{\delta J^\mu(\vec{r})}{\partial x_\mu} = 0 = \nabla \cdot \vec{J}(\vec{r}) + \frac{\delta n(\vec{r})}{\partial t}. \quad (2.49)$$

The operatorial form of this vector is:

$$\vec{J}(\vec{r}) = c\varphi^\dagger(\vec{r})\vec{\alpha}\varphi(\vec{r}), \quad (2.50)$$

where  $c$  is the speed of light,  $\varphi^\dagger(\vec{r})$  and  $\varphi(\vec{r})$  are Dirac field operators and  $\vec{\alpha}$  is the 4x4 Dirac matrix

$$\vec{\alpha} = \begin{pmatrix} 0 & \vec{\sigma} \\ \vec{\sigma} & 0 \end{pmatrix}. \quad (2.51)$$

The energy operators which enter in the Eq. (2.46) are similar with those used in the non-relativistic version of DFT ( Eqs. (2.5), (2.6) and (2.7))

$$\hat{U} = \frac{1}{2} \frac{e^2}{4\pi\epsilon_0} \int \int \varphi^\dagger(\vec{r})\varphi^\dagger(\vec{r}') \frac{1}{|\vec{r} - \vec{r}'|} \varphi(\vec{r}')\varphi(\vec{r}) d^3r d^3r' \quad (2.52)$$

$$\hat{V} = \int v^{ext}(\vec{r})\varphi^\dagger(\vec{r})\varphi(\vec{r}) d^3r \quad (2.53)$$

$$\hat{T} = \int \varphi^\dagger(\vec{r})(c\vec{\alpha}\vec{p} + \beta mc^2)\varphi(\vec{r}) d^3r \quad (2.54)$$

where  $\beta$  is a 4x4 Dirac matrix ( $I_2$  -the 2x2 identity matrix):

$$\beta = \begin{pmatrix} I_2 & 0 \\ 0 & -I_2 \end{pmatrix}. \quad (2.55)$$

The Kohn Hohenberg theorems were changed to describe the properties of the total energy functional  $W[J^\mu(\vec{r})]$  of a system of relativistic electrons:

- The total energy per unit volume of a system described by Hamiltonian from Eq. (2.46) can be written as a functional of the expectation value of the four-current density

$$W[J^\mu(\vec{r})] = T[J^\mu(\vec{r})] + G[J^\mu(\vec{r})] + e \int J^\mu(\vec{r}) A^\mu(\vec{r}) d^3r . \quad (2.56)$$

Here  $T[J^\mu(\vec{r})] = \langle \Phi | \hat{T} | \Phi \rangle$  is the relativistic kinetic energy of a system of non-interacting electrons, with the rest mass energy included and  $G[J^\mu(\vec{r})] = \langle \Phi | \hat{U} | \Phi \rangle$  is the internal potential energy of the system. Making use of the Lagrange multiplier method one can get

$$\delta W[J^\mu(\vec{r})] = \int \delta J^\mu(\vec{r}) \left[ \frac{\delta T(\vec{r})}{\delta J^\mu(\vec{r})} + \frac{\delta G(\vec{r})}{\delta J^\mu(\vec{r})} + e A_{ext}^\mu - \omega_\mu \right] d^3r = 0 . \quad (2.57)$$

$\delta J^\mu(\vec{r})$  is an arbitrary small change in  $J^\mu(\vec{r})$  so the quantity between the brackets must be zero to fulfill this condition:

$$\frac{\delta T(\vec{r})}{\delta J^\mu(\vec{r})} + \frac{\delta G(\vec{r})}{\delta J^\mu(\vec{r})} + e A_{ext}^\mu = \omega_\mu . \quad (2.58)$$

Furthermore, this relation can be arranged in such a way to look similar with that for non-interacting electronic system, introducing the effective potential:

$$A_{eff}^\mu[J^\mu(\vec{r})] = e A_{ext}^\mu + \frac{1}{e} \frac{\delta G(\vec{r})}{\delta J^\mu(\vec{r})} , \quad (2.59)$$

which can be split into effective scalar and vectorial potentials:

$$v_{eff} = v^{ext} + \frac{\delta G(\vec{r})}{\delta n(\vec{r})} \quad (2.60)$$

and

$$\vec{A}_{eff} = \vec{A}_{ext} + \frac{1}{e} \frac{\delta G(\vec{r})}{\delta \vec{J}(\vec{r})} . \quad (2.61)$$

For getting the effective potential, the following internal energy functional expression is used:

$$G[J^\mu(\vec{r})] = \frac{1}{2} \frac{e^2}{4\pi\epsilon_0} \int \int \frac{n(\vec{r})n(\vec{r}')}{|\vec{r} - \vec{r}'|} d^3r d^3r' - \frac{1}{2} \frac{e^2}{4\pi\epsilon_0 c^2} \int \int \frac{J(\vec{r})J(\vec{r}')}{|\vec{r} - \vec{r}'|} d^3r d^3r' + E_{xc}[J^\mu(\vec{r})] \quad (2.62)$$

Now one can make use of the second Kohn-Hohenberg statement, adapted for the relativistic case:

• *The non-degenerate ground state of an inhomogeneous interacting system of  $N$  relativistic electrons can be described by a set of  $N$  single particle effective Dirac equations with a suitable defined single particle-like scalar and vector potential.*

The effective single-particle Kohn-Sham-Dirac equation obtained looks as:

$$\left( c\alpha(\hat{p} - e\vec{A}_{eff}(\vec{r})) + \beta mc^2 + v_{eff}(\vec{r}) \right) \Psi_i(\vec{r}) = w_i \Psi_i(\vec{r}). \quad (2.63)$$

One needs to start with a reasonable guess for the exchange-correlation energy  $E_{xc}[n(\vec{r}), \vec{J}(\vec{r})]$  which is evaluated by means of relativistic quantum Monte-Carlo calculations. The second step is to get the effective potentials (using Eq. (2.62) and then Eqs. (2.60) and (2.61)) which will be inserted in the Kohn-Sham-Dirac equation. Solving this equation and getting  $w_i$  and  $\Psi_i$  will enable us to calculate the new electronic and current densities:

$$n(\vec{r}) = \sum_{i=1}^N \Psi_i^\dagger(\vec{r}) \Psi_i(\vec{r}) \quad (2.64)$$

and

$$\vec{J}(\vec{r}) = c \sum_{i=1}^N \Psi_i^\dagger(\vec{r}) \alpha \Psi_i(\vec{r}) \quad (2.65)$$

respectively, which will enter in the next loop. One ends up this loop with a self-consistent determined effective potential and electronic current densities. Those will be used to determine the total energy through the formula:

$$\begin{aligned} W[n(\vec{r}), \vec{J}(\vec{r})] &= \sum_{i=1}^N w_i - \frac{1}{2} \frac{e^2}{4\pi\epsilon_0} \int \int \frac{n(\vec{r})n(\vec{r}')}{|\vec{r} - \vec{r}'|} d^3r d^3r' + E_{xc}[J^\mu(\vec{r})] \\ &\quad - \frac{1}{2} \frac{e^2}{4\pi\epsilon_0 c^2} \int \int \frac{J(\vec{r})J(\vec{r}')}{|\vec{r} - \vec{r}'|} d^3r d^3r' - \int \frac{\delta E_{xc}[n(\vec{r}), \vec{J}(\vec{r})]}{\delta n(\vec{r})} n(\vec{r}) d^3r \\ &\quad - \int \frac{\delta E_{xc}[n(\vec{r}), \vec{J}(\vec{r})]}{\delta \vec{J}(\vec{r})} \vec{J}(\vec{r}) d^3r. \end{aligned} \quad (2.66)$$

It should be emphasized that this equation doesn't contain the vector potential  $\vec{A}$  and the current density  $\vec{J}$  has no explicitly dependence on the vector potential.

The exchange-correlation energy poses the most severe problem as this term include the current-current interactions. The relativistic exchange-correlation functional,  $E_{xc}[J_\mu(\vec{r})]$  has to include all the magnetic exchange-correlation effects which are intrinsically relativistic in nature, like the retardation of the Coulomb interaction between electrons and the magnetic

interaction between moving electrons, through its dependence on the spatial components of current. In principle, the exchange-correlation energy can be calculated from the solution of the self-consistent set of Kohn-Sham equations together with the expression for the total energy functional but in practice this implementation is done using several approximations, not unlike the non-relativistic Local Density Approximation (see [37]).

Such an alternative method of taking relativistic effects into account in DFT has been developed by Rajagopal and Callaway(1973) [52] and emphasized by MacDonald and Vosko (1979) [55]. Using this approach, one is able to derive equations that look more like the familiar non-relativistic DFT for magnetic systems.

Performing a Gordon decomposition of the current density, one is able to separate its orbital and spin parts, leading to a fully relativistic version of SDFT described above. Ignoring the diamagnetic effects, i.e. neglecting the terms in  $\vec{A}_{ext}(\vec{r})$  and assuming that the orbital currents are also negligible, the coupling of the spin part of the current to the vector potential  $\vec{A}_{ext}(\vec{r})$  can be described by a term analogous to that in Eq. (2.31)

$$\mu_B \vec{m}(\vec{r}) \cdot \vec{B}_{eff}(\vec{r}) \quad (2.67)$$

with the spin magnetisation defined by:

$$\vec{m}(\vec{r}) = \sum_i \Phi_i^\dagger(\vec{r}) \beta \vec{\sigma} \Phi_i(\vec{r}) . \quad (2.68)$$

As in the SDFT, the quantization axis is chosen to be the z direction. Under these suppositions, one gets the approximate Kohn-Sham-Dirac equation

$$\left[ i\hbar \vec{\alpha} \nabla + \beta m c^2 + v_{eff} + \mu_B \sigma_z B_{eff}(\vec{r}) \right] \Phi_i(\vec{r}) = w_i \Phi_i(\vec{r}) \quad (2.69)$$

with the effective scalar potential  $v_{eff}(\vec{r})$  and the effective magnetic field  $B_{eff}(\vec{r})$  given by the following expressions:

$$v_{eff}(\vec{r}) = v^{ext}(\vec{r}) + \frac{e^2}{4\pi\epsilon_0} \int \frac{n(\vec{r}')}{|\vec{r} - \vec{r}'|} + \frac{\delta E_{xc}[n(\vec{r}), m(\vec{r})]}{\delta n(\vec{r})} \quad (2.70)$$

$$B_{eff} = B_{ext} + \frac{\delta E_{xc}[n(\vec{r}), m(\vec{r})]}{\delta m(\vec{r})} . \quad (2.71)$$

In this way, ignoring the orbital current density contribution, one arrives at a Kohn-Sham-Dirac equation completely analogous to the non-relativistic SDFT Schrödinger equation (2.31). It should be emphasized that this relativistic DFT approach is derived as a first principle framework to calculate the properties of condensed mater with internal magnetic effects. However, the implementation of this theory is a complex problem. An adequate method for this implementation will be presented in the following.

## 2.2 Korrington-Kohn-Rostoker Green's Function Method

In the previous chapter it was shown how the many-body problem can be reduced using DFT to that of single particles moving independently in an effective field that describes all the interactions with the surrounding electrons and nuclei. One has to choose now an appropriate numerical band-structure method in order to perform a quantitative *ab-initio* description of the electronic structure of the crystal on the basis of the Kohn-Sham scheme. The basis of all calculations done within this thesis is multiple scattering theory. When applied to ordered solids, multiple scattering theory leads to the so-called Korrington-Kohn-Rostoker band theory method. This theory was first derived by Korrington [56, 57] and, independently, a bit later by Kohn and Rostoker [58]. Unlike most other methods, the KKR aims to calculate the so-called 'single-particle Green's function(GF)' instead of the electronic wave functions and energy eigenvalues of the crystal. As will be shown later, knowledge of the Green's function is enough to calculate all single-particle expectation values of a crystal like particle densities or other quantities important in condensed matter physics, such as densities of states and magnetic moments.

It should also be emphasized that the KKR method produces equations that can be used for the first-principle calculations in a manner that is very efficient from a computational point of view and it has the very appealing advantage that it can be easily generalized to deal with disordered alloys as well as periodic solids.

Between those who brought important contributions to the KKR-GF method, should be mentioned Faulkner [59, 60], Faulkner and Stocks [61], Györffy and Stocks [62], Stocks, Temmerman and Györffy [63], Gonis [64, 65, 66], Dederichs et al. [67] and for relativistic treatment, Strange et al. [68], Weinberger [69], Strange [37] and Ebert [70, 71, 72, 73].

The basic idea of KKR is that an incident wave function to any given site is a superposition of the outgoing ones from all the other sites. In order to determine the Green's function of the system at a fixed energy, the first task is to determine the wave functions and the so-called t-matrix which describes the scattering on each individual atomic scatterer characterized by non-overlapping, spatially bounded potentials. Further one has to construct the so-called T-matrix in order to reproduce the scattering in the whole crystal. Using the appropriate Dyson equation, the atomic t-matrices and the structure constants  $G$  which depend only on the crystal structure can be combined to construct the so-called scattering path operator  $\tau$ . This scattering path operator describes all possible scattering events for a single electron on its way between two individual scattering centers and because of this is a central quantity to construct the Green's function for the whole system.

Because much of the scattering theory is written in terms of the Green's function, the following section will be devoted to introduce this very useful mathematical instrument and to indicate some of its most characteristic features and uses.

### 2.2.1 Green's Function

Let's consider the following eigenvalue problem, where  $\hat{H}_0(\vec{r})$  is a general Hermitian operator:

$$\hat{H}_0(\vec{r})\Phi(\vec{r}) = E\Phi(\vec{r}) . \quad (2.72)$$

The Green's function associated to this Hamiltonian equation is defined by

$$[E - \hat{H}_0(\vec{r})]G_0(\vec{r}, \vec{r}', E) = \delta(\vec{r} - \vec{r}') . \quad (2.73)$$

Here it must be noticed that  $G(\vec{r}, \vec{r}', E)$  must fulfill the same boundary conditions as the solution of Eq. (2.72),  $\Phi(\vec{r})$ .

The Green's function can be expressed through the eigenvalues  $E_n$  and eigenfunctions  $\Phi_n(\vec{r})$  of the Hamiltonian  $\hat{H}_0(\vec{r})$ . Assuming a complete set of orthonormal wavefunctions with the property

$$\sum_n \Phi_n(\vec{r})\Phi_n^\dagger(\vec{r}') = \delta(\vec{r} - \vec{r}') \quad (2.74)$$

the spectral representation of the Green's function is given by:

$$G_0(\vec{r}, \vec{r}', E) = \sum_n \frac{\Phi_n(\vec{r})\Phi_n^\dagger(\vec{r}')}{E - E_n} . \quad (2.75)$$

One has to notice that the energy integral of the Green's function is not defined at real energies because of the singularities at  $E_n$  and has to be evaluated as a contour integral. In order to define the Green's operator for each real energy, it is necessary to specify a limiting procedure for the parameter E. For this reason, the so-called retarded (-) and advanced (+) Green's functions are introduced:

$$G^\pm(\vec{r}, \vec{r}', E) = \lim_{\epsilon \rightarrow 0} \sum_n \frac{\Phi_n(\vec{r})\Phi_n^\dagger(\vec{r}')}{E - E_n \pm i\epsilon} . \quad (2.76)$$

Those two operators are connected through the following relation:

$$G^+(\vec{r}, \vec{r}', E) = G^-(\vec{r}', \vec{r}, E)^\dagger \quad (2.77)$$

The Green's function is used in scattering theory as a method of solving inhomogeneous differential equations. The solution of the equation:

$$(\hat{H}_0(\vec{r}) + V(\vec{r}))\Psi(\vec{r}) = E\Psi(\vec{r}) \quad (2.78)$$

where  $E$  is an eigenvalue of the Hamiltonian  $\hat{H}_0(\vec{r})$ , can be written as

$$\Psi(\vec{r}, E) = \Phi(\vec{r}, E) + \int G_0(\vec{r}, \vec{r}', E) V(\vec{r}') \Psi(\vec{r}', E) d^3 r' . \quad (2.79)$$

This equation is called Lippman-Schwinger equation and  $\Phi(\vec{r}, E)$  is an eigenvector of the operator  $\hat{H}_0$ . Analogously, the Green's function of a perturbed system is connected to the Green's function of the unperturbed system by the so-called Dyson equation:

$$G(\vec{r}, \vec{r}', E) = G_0(\vec{r}, \vec{r}', E) + \int G_0(\vec{r}, \vec{r}'', E) V(\vec{r}'') G(\vec{r}'', \vec{r}', E) d^3 r'' . \quad (2.80)$$

We can use this equation to approximate the Green function for the perturbed system, substituting  $G(\vec{r}'', \vec{r}', E)$  back into this equation and keeping only the  $n$  first terms. This kind of approximation is called Born approximation of  $n$ th order.

A very useful quantity defined in scattering theory is the so-called T-operator. The matrix of this operator is defined in many ways. Two equivalent definitions are:

$$V(\vec{r}) G(\vec{r}, \vec{r}', E) = \int T(\vec{r}, \vec{r}_2, E) G_0(\vec{r}_2, \vec{r}', E) d^3 r_2 \quad (2.81)$$

$$G(\vec{r}, \vec{r}', E) V(\vec{r}') = \int G_0(\vec{r}, \vec{r}_2, E) T(\vec{r}_2, \vec{r}', E) d^3 r_2 \quad (2.82)$$

Substitution of the first of these expressions into the Dyson equation gives:

$$G(\vec{r}, \vec{r}', E) = G_0(\vec{r}, \vec{r}', E) + \int \int G_0(\vec{r}, \vec{r}_1, E) T(\vec{r}_1, \vec{r}_2, E) G_0(\vec{r}_2, \vec{r}', E) d^3 r_1 d^3 r_2 \quad (2.83)$$

This equation connect via the T-operator the free-particle Green's function to the full scattering Green's function and describes all possible scattering in the system. The Dyson-type equation for the T-matrix can be written also as follows:

$$T(\vec{r}, \vec{r}', E) = V(\vec{r}) \delta(\vec{r} - \vec{r}') + \int V(\vec{r}) G_0(\vec{r}, \vec{r}_1, E) T(\vec{r}_1, \vec{r}', E) d^3 r_1 . \quad (2.84)$$

## 2.2.2 The Calculation of Observables

The Green's function contains all physical relevant informations about an electronic system and can be used directly to calculate many observable quantities straightforwardly. We will show in this section how the density of states, charge density or magnetic moments can be calculated.

The starting point will be the retarded Green's function formula (2.76), where  $\Phi_n$  and  $E_n$  are



the eigenfunction and eigenvalues of the Hamiltonian. If one can let  $\vec{r}$  and  $\vec{r}'$  to be in the same atomic cell, one has the site-diagonal Green's function. Taking the trace of both sides of the formula and integrating over  $\vec{r}$  we have:

$$\int TrG^+(\vec{r}, \vec{r}', E)d^3r = \lim_{\epsilon \rightarrow 0} \sum_n \frac{1}{E - E_n + i\epsilon} \quad (2.85)$$

where the normalization condition

$$\int \Phi_n^\dagger(\vec{r})\Phi_n(\vec{r})d^3r = 1 \quad (2.86)$$

was taken into account. Making use now on the following identity

$$\lim_{\epsilon \rightarrow 0} \frac{1}{x - a + i\epsilon} = \frac{1}{x - a} - i\pi\delta(x - a) \quad (2.87)$$

we can write

$$-\frac{1}{\pi}\Im \int TrG^+(\vec{r}, \vec{r}', E)d^3r = \sum_n \delta(E - E_n) . \quad (2.88)$$

The right side of the previous equation is clearly the density of states, because

$$\int_E^{E+\Delta E} \sum_n \delta(E - E_n)dE = N , \quad (2.89)$$

where N is the number of states between  $E$  and  $E + \Delta E$ . Therefore we can write the following simple expression for the density of states in terms of the Green's function:

$$n(E) = -\frac{1}{\pi}\Im \int TrG^+(\vec{r}, \vec{r}', E)d^3r \quad (2.90)$$

and the number of states below energy  $E_{max}$  as

$$N(E_{max}) = -\frac{1}{\pi}\Im \int_{-\infty}^{E_{max}} \int TrG^+(\vec{r}, \vec{r}', E)d^3r . \quad (2.91)$$

To calculate the charge density, we consider the following expression for this quantity:

$$\rho(\vec{r}) = e \sum_n^{occ} \Phi_n^\dagger(\vec{r})\Phi_n(\vec{r}) \quad (2.92)$$

where the summation extends over all occupied states. Combining this expression with retarded Green's function expression (2.76), putting then  $\vec{r} = \vec{r}'$  and integrating over the energy up to the highest occupied state at the Fermi level  $E_F$ , gives

$$\begin{aligned}
\int_{-\infty}^{E_F} Tr G^+(\vec{r}, \vec{r}', E) dE &= \lim_{\epsilon \rightarrow 0} \sum_n \int_{-\infty}^{E_F} Tr \frac{\Phi_n(\vec{r}) \Phi_n^\dagger(\vec{r}')}{E - E_n + i\epsilon} dE \\
&= \lim_{\epsilon \rightarrow 0} \sum_n Tr \{ \Phi_n(\vec{r}) \Phi_n^\dagger(\vec{r}') \} \int_{-\infty}^{E_F} \frac{1}{E - E_n + i\epsilon} dE \\
&= \sum_n \Phi_n(\vec{r}) \Phi_n^\dagger(\vec{r}') \int_{-\infty}^{E_F} \left( \frac{1}{E - E_n} - i\pi \delta(E - E_n) \right) dE \quad (2.93)
\end{aligned}$$

where under the trace, the order of  $\Phi_n$  and  $\Phi_n^\dagger$  can be reversed. If we take the imaginary part of each side and take into account the integration of the  $\delta$ -function over the specified range change the summation of all states to all occupied states, we can write the final expression for the charge density as follows:

$$\rho(\vec{r}) = -\frac{e}{\pi} \Im \int_{-\infty}^{E_F} Tr G^+(\vec{r}, \vec{r}, E) dE . \quad (2.94)$$

Another quantity of interest is the spin magnetization density, given by:

$$\vec{m}(\vec{r}) = - \sum_n^{occ} \Phi_n(\vec{r}) \beta \vec{\sigma} \Phi_n^\dagger(\vec{r}) . \quad (2.95)$$

Similar to the previous derivation, we obtain the following expression for this quantity:

$$\vec{m}(\vec{r}) = \frac{1}{\pi} \Im \int_{-\infty}^{E_F} Tr \beta \vec{\sigma} G(\vec{r}, \vec{r}, E) dE , \quad (2.96)$$

where the trace includes the spin. One can get the spin magnetic moment performing the integral over  $\vec{r}$ :

$$m_{spin} = \frac{1}{\pi} \Im Tr \int_{-\infty}^{E_F} dE \int_{\Omega} \beta \hat{\sigma}_z G(\vec{r}, \vec{r}, E) d^3r \quad (2.97)$$

The magnetic moment at a site, coming from the orbital motion of electrons, the so called orbital magnetic moment, can be expressed in an analogous way as

$$m_{orb} = \frac{1}{\pi} \Im Tr \int_{-\infty}^{E_F} dE \int_{\Omega} \beta \hat{l}_z G(\vec{r}, \vec{r}, E) d^3r . \quad (2.98)$$

The probability that an electron in the solid will have a momentum  $\vec{p}$  and an energy  $E$  is given by the spectral density function,

$$A(E, \vec{p}) = -\frac{1}{\pi} \int_{-\infty}^{E_F} \Im G(\vec{p}, \vec{p}, E) dE . \quad (2.99)$$

The function  $G(\vec{p}, \vec{p}', E)$  that appears in this expression is the double Fourier transform of  $G(\vec{r}, \vec{r}', E)$ , written as

$$G(\vec{p}, \vec{p}', E) = \frac{1}{N\Omega} \int \int \exp(i(\vec{p}\vec{r} - \vec{p}'\vec{r}')) G(\vec{r}, \vec{r}', E) d^3r d^3r' . \quad (2.100)$$

The spectral density  $A(E, \vec{p})$  is very useful for interpreting the results of positron annihilation experiments, but can also be connected with momentum densities, constructed from magnetic Compton scattering experiments.

### 2.2.3 The single-site scattering

The first step in a first-principles study of magnetic and relativistic effects in metals and alloys using the KKR-GF method is to get the solutions of the Kohn-Sham-Dirac equations for an individual scattering center. For that purpose Strange et al. [74] investigated the associated Lippman-Schwinger equation and derived a set of radial differential equations for the single-site solutions.

Before one begins to delve into the details of scattering theory, it is useful to examine the physical properties of the scattering potential. The overall potential of the material can be thought of as being composed of individual smoothly varying single-site potentials centred on each lattice site. As one is dealing with close packed systems, it is reasonable to assume that the potential centred on each individual lattice site can be taken to be spherical symmetric around this lattice point. This assumption allowed us to use the so-called muffin-tin construction for the effective potential: the space is divided into non-overlapping at most touching spheres centered at each atom-site. The potential is supposed to be symmetric inside this so-called muffin-tin sphere and to have a constant value between the bounding spheres. For convenience, this constant value of the potential in the so-called interstitial region is often chosen to be the origin of the energy scale. The expression of the potential can be written as:

$$V_n(\vec{r} - \vec{R}_n) = V_n(\vec{r}_n) = \begin{cases} V_n(r_n) & \text{if } |\vec{r}_n| < r_{mt}^n \\ 0 & \text{otherwise} \end{cases} \quad (2.101)$$

For a system which is subject to a magnetic field, one will consider the motion of an electron in a spherically symmetric potential and an effective magnetic field, for simplicity chosen to

point along the z axis:  $\vec{B}(\vec{r}) = B(r)\hat{e}_z$ . The corresponding Dirac equation has the following expression:

$$[i\gamma_5\sigma_r c\left(\frac{\partial}{\partial r} + \frac{1}{r} - \frac{\beta}{r}\vec{K}\right) + V + \beta\sigma_z B + (\beta - 1)\frac{c^2}{2} - E]\Psi_\nu = 0. \quad (2.102)$$

Here  $\sigma_r = \hat{r} \cdot \vec{\sigma}$  and the matrix  $\gamma_5$  is given by:

$$\gamma_5 = \begin{pmatrix} 0 & -I_2 \\ -I_2 & 0 \end{pmatrix}. \quad (2.103)$$

The spin-orbit operator is defined by:

$$\hat{K} = \beta(\vec{\sigma} \cdot \vec{l} + 1). \quad (2.104)$$

To solve the Dirac equation, one makes the ansatz:

$$\Psi_\nu = \sum_{\Lambda} \Psi_{\Lambda\nu} \quad (2.105)$$

where  $\Psi_{\Lambda\nu}$  have the same form as the linearly independent solutions for a spherical symmetric potential:

$$\Psi_{\Lambda}(\vec{r}, E) = \begin{pmatrix} g_{\kappa}(r, E)\chi_{\Lambda}(\hat{r}) \\ if_{\kappa}(r, E)\chi_{-\Lambda}(\hat{r}) \end{pmatrix}. \quad (2.106)$$

Here  $g_{\kappa}$  and  $f_{\kappa}$  are the large, and respectively the small component of the radial wave function and  $\chi_{\pm\Lambda}$  are the spin angular functions. The spin-orbit quantum number  $\kappa$  and magnetic quantum number  $\mu$  were combined in the symbol  $\Lambda = (\kappa, \mu)$  and  $-\Lambda = (-\kappa, \mu)$ . The spin-angular functions  $\chi_{\Lambda}$  can be expanded further, using the Clebsch-Gordon coefficients  $C(l\frac{1}{2}j; m_l, m_s)$ , the complex spherical harmonics  $Y_l^{m_l}$  and the Pauli-spinors  $\chi_{m_s}$  in the following expression:

$$\chi_{\Lambda} = \sum_{m_s=\pm 1/2} C(l\frac{1}{2}j; \mu - m_s, m_s)Y_l^{\mu - m_s}(\hat{r})\chi_{m_s}. \quad (2.107)$$

The spin-angular functions  $\chi_{\Lambda}(\hat{r})$  are simultaneous eigenfunction of the operators  $j^2$ ,  $j_z$  and  $\hat{K}$ , with  $\vec{j} = \vec{l} + \frac{1}{2}\vec{\sigma}$ . The eigenvalues of these operators can be connected by the following relations:

$$\kappa = \begin{cases} -l - 1 & \text{for } j = l + \frac{1}{2} \\ l & \text{for } j = l - \frac{1}{2} \end{cases} \quad (2.108)$$

$$j = |\kappa| - \frac{1}{2} \quad (2.109)$$

$$-j \leq \mu \leq +j \quad (2.110)$$

$$\bar{l} = l - S_\kappa. \quad (2.111)$$

Here  $S_\kappa = \kappa/|\kappa|$  is the sign of  $\kappa$  and  $\bar{l}$  is the orbital angular momentum quantum number corresponding to  $\chi_{-\Lambda}$ . If one inserts the ansatz (2.106) into the single-site Dirac equation (2.102) and integrates over the angles, the following radial differential equation are obtained:

$$P'_{\Lambda\nu} = -\frac{\kappa}{r}P_{\Lambda\nu} + \left[ \frac{E - \nu}{c^2} + 1 \right] Q_{\Lambda\nu} + \frac{B}{c^2} \sum_{\Lambda'} \langle \chi_{-\Lambda} | \sigma_z | \chi_{-\Lambda'} \rangle Q_{\Lambda'\nu} \quad (2.112)$$

$$Q'_{\Lambda\nu} = \frac{\kappa}{r}Q_{\Lambda\nu} - [E - \nu]P_{\Lambda\nu} + B \sum_{\Lambda'} \langle \chi_{\Lambda} | \sigma_z | \chi_{\Lambda'} \rangle P_{\Lambda'\nu}. \quad (2.113)$$

Here  $P_{\Lambda\nu} = r g_{\Lambda\nu}$ ,  $Q_{\Lambda\nu} = c r f_{\Lambda\nu}$  and the coupling coefficients are given by

$$\langle \chi_{\Lambda} | \sigma_z | \chi_{\Lambda'} \rangle = \delta_{\mu\mu'} \begin{cases} -\frac{\mu}{\kappa+1/2} & \text{if } \kappa = \kappa' \\ -\sqrt{1 - \left(\frac{\mu}{\kappa+1/2}\right)^2} & \text{for } \kappa = -\kappa' - 1 \\ 0 & \text{otherwise} \end{cases} \quad (2.114)$$

The selection rules derived from the properties of the angular matrix elements lead to a coupling between the partial waves with the same  $\mu$ , i.e.  $\mu$  is still a good quantum number. Also, for two coupled partial waves with angular momentum  $l$  and  $l'$  one has the restriction  $l - l' = 0, \pm 2, \dots$ , i.e. only waves with the same parity are coupled. Even with these restrictions, there are an infinite number of partial waves coupled, but in practice all coupling terms for which  $l - l' = \pm 2$  are ignored. Feder et al. [75] justify this restriction showing that the error introduced by this approximation is of the order  $1/c^2$ . On the other hand, Jenkins and Strange [76] showed that one has to retain the coupling in  $\kappa$  (up to  $l = 5, 6$ ) if the calculated quantities are very small on the energy scale, such as the magnetocrystalline anisotropy energy, for example. For the present calculations, only  $l - l' = 0$  coupling was kept, restricting the number of terms in Eq. (2.112) and (2.113) to 2, if  $|\mu| < j$ . For the case  $\mu = j$ , there is no coupling at all and one can say that the solutions  $\Psi_\nu$  have pure spin-angular character  $\Lambda$ .

Obviously, the Eqs. (2.112) and (2.113) has to be solved numerically. In order to solve these equations, inside the muffin-tin sphere one has to set a limit for the angular momentum expansion  $l_{max}$ . Accordingly a set of  $2(l_{max} + 1)^2$  linear independent regular solutions  $\Psi_\nu$  can be created solving the Dirac equation (2.102) numerically. Because near the nucleus ( $r \rightarrow 0$ )

the magnetic part of the effective potential can be neglected, one can initialize the outward integration with a well-defined spin angular character as follows:

$$\Psi_\nu = \sum_{\Lambda'} \Psi_{\Lambda'\nu}(\vec{r}, E) \xrightarrow{r \rightarrow 0} \Psi_{\Lambda\nu}(\vec{r}, E) . \quad (2.115)$$

Going away from the nucleus, the coupling introduced by the magnetic field has to be considered and a possible choice for the index of regular solution is to identify  $\nu$  with  $\Lambda$ , giving the asymptotic behaviour for  $r \rightarrow 0$ :

$$\Psi_\Lambda(\vec{r}, E) = \sum_{\Lambda'} \Psi_{\Lambda'\Lambda}(\vec{r}, E) . \quad (2.116)$$

The radial Dirac equation for the free particle has two linearly independent solutions, regular and irregular at the origin. These solutions can be written in terms of spherical Bessel functions  $j_l(x)$  (the incoming regular solution) and the spherical Hankel function  $h_l(x)$  (the outgoing regular solution), as follows:

$$j_\Lambda(\vec{r}, E) = \sqrt{1 + \frac{E}{c^2}} \begin{pmatrix} j_l(pr) \chi_\Lambda(\hat{r}) \\ \frac{icpS_\kappa}{E+c^2} j_l(pr) \chi_{-\Lambda}(\hat{r}) \end{pmatrix} \quad (2.117)$$

$$j_l^\times(\vec{r}, E) = \sqrt{1 + \frac{E}{c^2}} \begin{pmatrix} j_l(pr) \chi_\Lambda^*(\hat{r}) \\ \frac{-icpS_\kappa}{E+c^2} j_l(pr) \chi_{-\Lambda}^*(\hat{r}) \end{pmatrix}^T \quad (2.118)$$

$$h_\Lambda^+(\vec{r}, E) = \sqrt{1 + \frac{E}{c^2}} \begin{pmatrix} h_l^+(pr) \chi_\Lambda(\hat{r}) \\ \frac{icpS_\kappa}{E+c^2} h_l^+(pr) \chi_{-\Lambda}(\hat{r}) \end{pmatrix} \quad (2.119)$$

$$h_\Lambda^{+\times}(\vec{r}, E) = \sqrt{1 + \frac{E}{c^2}} \begin{pmatrix} h_l^+(pr) \chi_\Lambda^*(\hat{r}) \\ \frac{-icpS_\kappa}{E+c^2} h_l^+(pr) \chi_{-\Lambda}^*(\hat{r}) \end{pmatrix}^T , \quad (2.120)$$

where  $p = \sqrt{E(1 + E/c^2)}$  is the relativistic electronic momentum. The row spinor functions in Eqs. (2.118) and (2.120) signed by a "  $\times$  " denote left hand side eigenfunctions of  $\hat{H}_0$ , i.e. they obey the left-hand side free-particle Dirac equation:

$$\langle \Psi^\times | (E - \hat{H}_0) = 0 . \quad (2.121)$$

The left-hand-side solution  $\langle \Psi^\times |$  can be understood as the Hermitian conjugate of the right-hand-side solution of the adjoint equation

$$(E^* - \hat{H}_0^\dagger) | \Psi^{\times\dagger} \rangle = 0 \quad (2.122)$$

Here  $E^*$  is the complex conjugated energy including the rest mass energy and  $\hat{H}_0^\dagger = \hat{H}_0$  for free particles [77].

With the functions (2.117) and (2.119) one can construct the regular wave function at the boundary of the muffin-tin sphere as a combination of the incoming and outgoing waves:

$$R_\Lambda(\vec{r}, E) = j_\Lambda(\vec{r}, E) - ip \sum_{\Lambda'} h_{\Lambda'}^+(\vec{r}, E) t_{\Lambda\Lambda'}(E), \quad (2.123)$$

which is the asymptotic solution of the Eqs. (2.112) and (2.113). Here  $t_{\Lambda\Lambda'}$  defines the elements of the single-site scattering matrix  $t$ . By definition, the single-site t-matrix operator generates the scattered wave by a single-site muffin-tin potential.

A procedure to determine the t-matrix elements  $t_{\Lambda\Lambda'}(E)$  was introduced by Ebert and Györfy [78]. They defined two auxiliary functions  $f^\pm(\vec{r}, E)$  with the boundary conditions given by the Hankel functions

$$f^\pm(\vec{r}, E) = h^\pm(\vec{r}, E) \quad \text{if} \quad \vec{r} \geq \vec{r}_{mt}. \quad (2.124)$$

Because these functions are a complete set of eigenfunctions of Dirac Hamiltonian, they can be used to express the set of independent solutions  $\Psi_\Lambda(\vec{r}, E)$  as:

$$\Psi_\Lambda(\vec{r}, E) = \sum_{\Lambda'} \Psi_{\Lambda'\Lambda}(\vec{r}, E) = \frac{1}{2} \sum_{\Lambda'} (a_{\Lambda'\Lambda}(E) f_{\Lambda'}^+(\vec{r}, E) + b_{\Lambda'\Lambda}(E) f_{\Lambda'}^-(\vec{r}, E)) \quad (2.125)$$

where  $a(E)$  and  $b(E)$  are auxiliary matrices given by

$$\begin{aligned} a_{\Lambda\Lambda'}(E) &= -ipr^2 [h_\Lambda^-(pr), \Phi_{\Lambda\Lambda'}(\vec{r}, E)]_r \\ b_{\Lambda\Lambda'}(E) &= ipr^2 [h_\Lambda^+(pr), \Phi_{\Lambda\Lambda'}(\vec{r}, E)]_r. \end{aligned} \quad (2.126)$$

Here  $[\dots]$  denotes the relativistic form of the Wronskian

$$[h_\Lambda^+, \Phi_{\Lambda\Lambda'}]_r = h_l^+ c f_{\Lambda\Lambda'} - \frac{p}{1 + E/c^2} S_\kappa h_l^+ g_{\Lambda\Lambda'}. \quad (2.127)$$

Outside the muffin-tin sphere, one has  $V_{eff} = 0$  and  $B_{eff} = 0$ . Thus the Dirac equation has free-particle-like solutions. The solutions given by Eq. (2.123), valid for  $\vec{r} \geq r_{mt}$  and Eq. (2.125), valid for  $\vec{r} \leq r_{mt}$  have to match at the muffin-tin boundary. This condition enables us to determine the t-matrix elements, for which one can find the following expression:

$$t(E) = \frac{i}{2p} (a(E) - b(E)) b^{-1}(E). \quad (2.128)$$

An alternative set of linearly independent regular solutions for the Dirac equation, allowed by the t-matrix symmetry properties, can be obtained by superposition of the wave functions  $\Phi_\Lambda$  according to the boundary conditions

$$\begin{aligned} Z_\Lambda(\vec{r}, E) &= \sum_{\Lambda'} R_\Lambda(\vec{r}, E) t_{\Lambda'\Lambda}^{-1}(E) \\ &= \sum_{\Lambda'} j_{\Lambda'}(\vec{r}, E) t_{\Lambda'\Lambda}^{-1}(E) - ip h_\Lambda^+(\vec{r}, E). \end{aligned} \quad (2.129)$$

These functions are normalized according to the convention of Faulkner and Stocks [61] and allow straightforwardly to set up the electronic Green's function. The irregular solutions are fixed by the boundary condition:

$$J_\Lambda(\vec{r}, E) \xrightarrow{r \rightarrow r_{mt}} j_\Lambda(\vec{r}, E) \quad (2.130)$$

and can be obtained just by inward integration. The solutions of the Dirac equation,  $Z_\Lambda$  and  $J_\Lambda$ , outside the potential well can be continued into the sphere in such a way that they represent the solutions to the Dirac equation in the whole space. The special advantage for using those free particle solutions is that these functions are real for real energies, if the cell potential satisfies some very common symmetry properties.

## 2.2.4 The single-site Green's function

In order to get the single-site Green's function, one has to start with the free-particle Green's function, which is a solution of the equation:

$$(\alpha \hat{p} + \beta m c^2 - E) G_0(\vec{r}, \vec{r}') = -\delta(\vec{r} - \vec{r}') \tilde{I} \quad (2.131)$$

Introducing  $\vec{R} = \vec{r} - \vec{r}'$  (with  $R = |\vec{R}|$ ), the solution can be written as

$$G_0(\vec{r}, \vec{r}', E) = -(\alpha \hat{p} + \beta m c^2 - E) \frac{e^{ipR}}{4\pi R} \tilde{I}_4. \quad (2.132)$$

Here we should note that  $G_0$  is a 4x4 matrix and  $E$  is the electron energy with the rest mass  $mc^2$  included. Using the plane-wave expansion

$$\frac{e^{ipR}}{4\pi R} = ip \sum_{\Lambda} j_l(pr_{<}) h_l^+(pr_{>}) \chi_\Lambda(\hat{r}) \chi_\Lambda^\dagger(\hat{r}'), \quad (2.133)$$

where  $r_{<} = \min\{\vec{r}, \vec{r}'\}$  and  $r_{>} = \max\{\vec{r}, \vec{r}'\}$ , together with the Eq. (2.132), one can get the free-electron relativistic Green's function:

$$G_0(\vec{r}, \vec{r}', E) = -ip \sum_{\Lambda'} [j_\Lambda(p\vec{r}) h_\Lambda^{+\times}(p\vec{r}') \Theta(\vec{r}' - \vec{r}) + h_\Lambda^+(p\vec{r}) j_\Lambda^\times(p\vec{r}') \Theta(\vec{r} - \vec{r}')], \quad (2.134)$$



where  $\theta(\vec{r})$  is the well-known step-function. Here the left-hand side solutions of the free particle Dirac equation appear,  $j_{\Lambda}^{\times}(p\vec{r})$  and  $h_{\Lambda}^{\times}(p\vec{r})$ , given by the relations (2.118) and (2.120). The regular and irregular solutions of the Dirac equation,  $j_{\Lambda}(p\vec{r})$  and  $h_{\Lambda}(p\vec{r})$  are given by the relations (2.117) and (2.119). The single-site Green's function is now easy to obtain, inserting the free electron Green's function into the Dyson equation (2.80):

$$G_{ss}(\vec{r}, \vec{r}', E) = G_0(\vec{r}, \vec{r}', E) + \int \int d^3r_1 d^3r_2 G_0(\vec{r}, \vec{r}_1, E) t(\vec{r}_1, \vec{r}_2, E) G_0(\vec{r}_2, \vec{r}', E) . \quad (2.135)$$

In order to obtain the single-site t-matrix elements (see Eq. 2.128), one can make use of the Lippman-Schwinger equation. If one consider for the single-site scattering the asymptotic solution  $R_{\Lambda}(\vec{r}, E)$  given by the relation (2.123) and  $j_{\Lambda}(\vec{r}, E)$  as free electron solution, the Lippman-Schwinger equation reads:

$$R_{\Lambda}(\vec{r}, E) = j_{\Lambda}(\vec{r}, E) + \int \int d^3r' d^3r'' G_0(\vec{r}, \vec{r}', E) t^n(\vec{r}', \vec{r}'', E) j_{\Lambda}(\vec{r}'', E) . \quad (2.136)$$

Substituting the expression for  $G_0$  into this equation and comparing with the expression for  $R_{\Lambda}(\vec{r}, E)$  from Eq. (2.123), one can find the single-site t-matrix elements in the angular momentum representation:

$$t_{\Lambda\Lambda'}^n(E) = \int \int d^3r d^3r' j_{\Lambda}^+(\vec{r}, E) t^n(\vec{r}, \vec{r}', E) j_{\Lambda'}(\vec{r}', E) . \quad (2.137)$$

Now, going back with this expression for the single-site t-matrix into the Dyson equation (2.135), we arrive at the following expression for the single-site Green's function:

$$\begin{aligned} G_{ss}(\vec{r}, \vec{r}', E) &= \sum_{\Lambda\Lambda'} Z_{\Lambda}^n(\vec{r}, E) t_{\Lambda\Lambda'}^n(E) Z_{\Lambda'}^{n\times}(\vec{r}', E) \\ &\quad - \sum_{\Lambda} Z_{\Lambda}^n(\vec{r}, E) J_{\Lambda}^{n\times}(\vec{r}', E) \Theta(\vec{r}' - \vec{r}) \\ &\quad - \sum_{\Lambda} J_{\Lambda}^{n\times}(\vec{r}, E) Z_{\Lambda}^n(\vec{r}', E) \Theta(\vec{r} - \vec{r}') , \end{aligned} \quad (2.138)$$

where the right and left hand-side solutions of free-particle Dirac equation,  $Z_{\Lambda}$  and respectively  $Z_{\Lambda}^{\times}$  are defined by:

$$Z_{\Lambda}(\vec{r}, E) = \sum_{\Lambda'} j_{\Lambda'}(p\vec{r}) t_{\Lambda\Lambda'}^{-1}(E) - ip h_{\Lambda}^+(\vec{r}, E) \quad (2.139)$$

$$Z_{\Lambda}^{\times}(\vec{r}, E) = \sum_{\Lambda'} j_{\Lambda'}^{\times}(p\vec{r}) t_{\Lambda\Lambda'}^{-1\times}(E) - ip h_{\Lambda}^{+\times}(\vec{r}, E) , \quad (2.140)$$

where  $t^\times = t^T$  is the left hand side t-matrix. One has to note that the left-hand-side solutions of Dirac equation are obtained from the same differential equations as the conventional right-hand-side solutions  $Z_\Lambda$  and  $J_\Lambda$ . For highly symmetric systems  $Z_\Lambda^\times$  and  $J_\Lambda^\times$  are obtained from  $Z_\Lambda$  and  $J_\Lambda$  by simple complex conjugation and transposition:

$$Z_\Lambda^\times(\vec{r}, E) = \sum_{\Lambda'} (g_{\Lambda'\Lambda}(\vec{r}, E)\chi_{\Lambda'}^\dagger(\hat{r}); -if_{\Lambda'\Lambda}(\vec{r}, E)\chi_{\Lambda'}^\dagger(\hat{r})) \quad (2.141)$$

and

$$J_\Lambda^\times(\vec{r}, E) = \sum_{\Lambda'} (\tilde{g}_{\Lambda'\Lambda}(\vec{r}, E)\chi_{\Lambda'}^\dagger(\hat{r}); -i\tilde{f}_{\Lambda'\Lambda}(\vec{r}, E)\chi_{\Lambda'}^\dagger(\hat{r})) \quad (2.142)$$

since the left and right hand solutions are identical with respect to their radial parts.

## 2.2.5 Multiple scattering

In order to describe the multiple scattering of electrons by a distribution of scatterers, our aim is to calculate the Green's function and the T-matrix of the whole system starting from the single-site scattering on the  $n$ th site potential. First, we have to construct the potential function:

$$V(\vec{r}) = \sum_{i=1}^N V_i(\vec{r}_i) \quad (2.143)$$

that is a sum of potential wells centered on a set of  $N$  sites whose locations are at the points  $\vec{R}_i$ . The vectors  $\vec{r}_i$  are defined by  $\vec{r}_i = \vec{r} - \vec{R}_i$  and it will be supposed that each potential is zero outside a bounding sphere of radius  $S_i$ ,  $V_i = 0$  if  $r_i > S_i$  and that the bounding spheres do not overlap each other.

Making use of this potential function, the T-matrix equation (2.84) in operator form will read:

$$T(E) = V + VG_0(E)T(E) = \sum_{i=1}^N (V_i + V_iG_0(E)T(E)) = \sum_{i=1}^N P_i(E) \quad (2.144)$$

where

$$P_i(E) = V_i + V_iG_0(E)T(E) = V_i + V_iG_0(E)P_i + V_iG_0(E) \sum_{j \neq i} P_j(E) \quad (2.145)$$

$$P_i(E) = \frac{V_i}{1 - V_iG_0(E)} \left( 1 + \sum_{i \neq j} G_0(E)P_j(E) \right) \quad (2.146)$$

Let's consider now a single site scattering on a potential well centered at  $\vec{R}_i$ . The t-matrix reads as:

$$\begin{aligned} t^i(E) &= V_i + V_i G_0(E) t^i(E) \\ t^i(E) &= \frac{V_i}{1 - V_i G_0(E)} \end{aligned} \quad (2.147)$$

This expression can be substituted in equation (2.145) to give

$$P_i(E) = t^i(E) + \sum_{i \neq j} t^i(E) G_0(E) P_j(E) \quad (2.148)$$

If we introduce now the new quantity

$$\tau^{ij}(E) = t^i(E) \delta_{ij} + \sum_{k \neq i} t^i(E) G_0(E) \tau^{kj}(E) \quad (2.149)$$

it can be shown that the T-matrix of the system has the form:

$$T(E) = \sum_{i,j=1}^N \tau^{ij}(E) \quad (2.150)$$

The quantities  $\tau^{ij}(E)$  is known as scattering path operators and were first introduced by Görffy and Stott (1972) [79]. They will help us to write down the solution of multiple scattering problem in terms of the solution of the single-site scattering problem.

As we have already seen, the single-site t-matrix generates the scattered wave due to a single potential. In multiple scattering,  $T(E)$  gives the scattered wave due to a distribution of scatterers. The scattering path operator  $\tau^{ij}$  gives the scattered wave from site  $j$  due to a wave incident upon site  $i$  with all scatterings in between (Györffy and Stocks, 1980 [62]) and this can be seen easier expanding the previous expression in Born series:

$$\tau^{ij} = t^i(E) \delta_{ij} + \sum_{k \neq j} t^i G_0 t^k \delta_{kj} + \sum_{k \neq i} \sum_{l \neq k} t^i G_0(E) t^k G_0(E) t^l \delta_{lj} + \dots \quad (2.151)$$

We have seen how to solve the Kohn-Sham-Dirac equation for scattering an electron from a single site. The scattering path operator allows us to write the solution to the multiple-scattering problem in terms of the single-site scattering t-matrix.

## 2.2.6 Multiple Scattering Green's function

In order to obtain the Green's function, it can be considered that our reference system consists in a single scatterer at position  $n$ , surrounded by vacuum. One can consider as perturbation all the rest of the scattering centers. In this way, for a crystal system, the perturbation will be the whole crystal with one atom at site  $n$  missing. It is not usual to have the perturbation bigger than the system, but this approach suggested by Faulkner and Stocks [61] was remarkably successful.

We write the Green's function for the whole system in terms of the Green's function for the single-site scattering as:

$$G(\vec{r}, \vec{r}', E) = \vec{G}_n(\vec{r}, \vec{r}', E) + \int \int G_n(\vec{r}, \vec{r}_1, E) T_{nn}(\vec{r}_1, \vec{r}_2, E) G_n(\vec{r}_2, \vec{r}', E) d^3r_1 d^3r_2 \quad (2.152)$$

where  $r_1 > r$  and  $r_2 > r'$ . The quantity  $T_{nn}$  is the scattering matrix for the system of all scatterers except the  $n$ th:

$$T_{nn}(E) = \sum_{i \neq n} \sum_{j \neq n} \tau^{ij}(E). \quad (2.153)$$

We suppose that  $\vec{r}$  is in the  $n$ th and  $\vec{r}'$  is in the  $m$ th bounding sphere, so we can write  $\vec{r} = \vec{r}_n + \vec{R}_n$  and  $\vec{r}' = \vec{r}_m + \vec{R}_m$ . In analogy with Eq. (2.137) we define the spin-angular matrix elements of  $\tau^{ij}$  as following:

$$\tau_{\Lambda\Lambda'}^{ij}(E) = \int_{\Omega_i} d^3r \int_{\Omega_j} d^3r' j_{\Lambda}^{\times}(p(\vec{r} - \vec{R}_i)) \tau^{ij}(\vec{r}, \vec{r}', E) j_{\Lambda'}(p(\vec{r}' - R_j)) \quad (2.154)$$

where the integration volume for  $\vec{r}$  and  $\vec{r}'$  is confined to the volume  $\Omega_i$  and  $\Omega_j$  of the cells  $i$  and respectively  $j$ . Replacing the single-site Green's function, together with the  $\tau^{ij}$  spin-angular matrix elements into Eq. (2.152), we get the following expression for the multiple scattering Green's function:

$$\begin{aligned} G(\vec{r}_n + \vec{R}_n, \vec{r}_m + \vec{R}_m, E) &= \sum_{\Lambda\Lambda'} Z_{\Lambda}^n(\vec{r}_n, E) \tau_{\Lambda\Lambda'}^{nm}(E) Z_{\Lambda'}^{m\times}(\vec{r}_m, E) \\ &\quad - \delta_{mn} \sum_{\Lambda} [Z_{\Lambda}^n(\vec{r}_n, E) J_{\Lambda}^{n\times}(\vec{r}'_n, E) \theta(\vec{r}'_n - \vec{r}_n) \\ &\quad + J_{\Lambda}^n(\vec{r}_n, E) Z_{\Lambda}^{n\times}(\vec{r}'_n, E) \theta(\vec{r}_n - \vec{r}'_n)]. \end{aligned} \quad (2.155)$$

Concerning this expression we have to note first that we have not made any supposition upon the array of scatterers, so is it valid for any array of non-overlapping potential functions. Secondly, the multiple scattering information (in  $\tau^{nm}$ ) is completely separated from the wave function information (in  $Z^n$  and  $J^n$ ).

The last task is now to determine the scattering operator for the whole system. We start putting the operator-equation (2.149) in the coordinate representation:

$$\tau^{ij}(\vec{r}, \vec{r}', E) = \delta_{ij} t^i(\vec{r}, \vec{r}', E) + \sum_{k \neq i} \int \int d^3 r_1 d^3 r_2 t^i(\vec{r}, \vec{r}_1, E) G_0(\vec{r}_1, \vec{r}_2, E) \tau^{kj}(\vec{r}_2, \vec{r}') . \quad (2.156)$$

One has to note that  $t^i$  is non-zero just inside the  $i$ th sphere. The free-particle Green's function  $G_0(\vec{r}_1, \vec{r}_2, E)$  describes the propagation from site  $k$  to site  $i$ , so  $\vec{r}_1$  is in the  $i$ th and  $\vec{r}_2$  is in the  $k$ th bounding sphere. Because of this, we can write  $\vec{r}_1 = \vec{R}_i + \vec{r}_i$  and  $\vec{r}_2 = \vec{R}_k + \vec{r}_k$ . Due to the translational symmetry of the Green's function, we have

$$G_0(\vec{r}_1, \vec{r}_2, E) = G_0(\vec{r}_i, \vec{R}_k - \vec{R}_i + \vec{r}_k, E) . \quad (2.157)$$

The following expression for  $G_0$  will be used, according to Eq. (2.134):

$$G_0(\vec{r}_i, \vec{R}_k - \vec{R}_i + \vec{r}_k, E) = -ip \sum_{\Lambda} j_{\Lambda}(\vec{r}_i, E) h_{\Lambda}^{+\times}(\vec{R}_k - \vec{R}_i + \vec{r}_k, E) . \quad (2.158)$$

The spherical Hankel function  $h_{\Lambda}^{+\times}$  diverges at  $\vec{R}_i$  but is regular at all other points, so another expansion, around  $\vec{R}_i$ , can be used

$$-iph^{+\times}(\vec{R}_k - \vec{R}_i + \vec{r}_k, E) = \sum_{\Lambda'} G_{\Lambda\Lambda'}^{ij}(E) j_{\Lambda'}^{\times}(\vec{r}_k, E) \quad (2.159)$$

and we finally get for the free-particle Green's function the expression:

$$G_0(\vec{r}, \vec{r}') = \sum_{\Lambda\Lambda'} j_{\Lambda}(\vec{r}_i, E) G_{\Lambda\Lambda'}^{ij}(E) j_{\Lambda'}^{\times}(\vec{r}_k, E) . \quad (2.160)$$

The expansion coefficients  $G_{\Lambda\Lambda'}^{ij}(E)$  are called structure constants because they don't depend on the potentials  $V_i$ , but only on the relative positions of the scatterers  $i$  and  $j$ . In the relativistic theory they have the expression:

$$G_{\Lambda\Lambda'}^{ij}(E) = -4\pi ip \sum_{m_s} \sum_{\Lambda''} i^{l-l'-l''} C_{\Lambda}^{m_s} C_{\Lambda'}^{m_s} h_{l''}^{+}(pR_{ij}) C_{\Lambda\Lambda'\Lambda''} \quad (2.161)$$

with  $R_{ij} = |\vec{R}_j - \vec{R}_i|$ ,  $C_{\Lambda}^{m_s} = C(l\frac{1}{2}j; \mu - m_s, m_s)$  and the Gaunt coefficients

$$C_{\Lambda\Lambda'\Lambda''} = \int d\Omega Y_l^{\mu-m_s*}(\hat{r}) Y_{l'}^{\mu'-m_s}(\hat{r}) Y_{l''}^{\mu''-m_s}(\hat{r}) \quad (2.162)$$

Using the angular representation of the scattering path operator (2.154) we can now write for the scattering path operator the following expression

$$\tau_{\Lambda\Lambda'}^{ij}(E) = \delta_{ij} t_{\Lambda\Lambda'}^i(E) + \sum_{\Lambda''\Lambda'''} t_{\Lambda\Lambda''}^i(E) \sum_{k \neq i} G_{\Lambda''\Lambda'''}^{ij}(E) \tau_{\Lambda'''\Lambda'}^{jk}(E). \quad (2.163)$$

In the super-matrix notation, the equation of motion for the  $\tau$ -matrix is

$$\begin{aligned} \underline{\tau}^{ij} &= \underline{t}^i \delta_{ij} + \underline{t}^i \sum_{k \neq i} \underline{G}^{ik} \underline{\tau}^{kj} \\ &= \underline{t}^i \delta_{ij} + \sum_{k \neq i} \underline{\tau}^{ik} \underline{G}^{ik} \underline{t}^i, \end{aligned} \quad (2.164)$$

where the underline indicates a matrix with respect to  $\Lambda = (\kappa, \mu)$ . Here the single site  $t$ -matrix  $\underline{t}^i$  is fixed by the solutions to the single-site Dirac equation for site  $i$ . Furthermore,  $\underline{G}^{ij}$  is the relativistic real space Green's function or structure constants matrix that represents the propagation of free electron between sites  $i$  and  $j$ . It is related to its non-relativistic counterparts  $G_{\mathcal{L}\mathcal{L}'}^{ij} = G_{LL'}^{ij} \delta_{m_s m'_s}$  by the relation

$$G_{\Lambda\Lambda'}^{ij} = (1 + E/c^2) \sum_{\mathcal{L}\mathcal{L}'} S_{\Lambda\mathcal{L}}^+ G_{\mathcal{L}\mathcal{L}'}^{ij} S_{\mathcal{L}'\Lambda'}, \quad (2.165)$$

where  $\mathcal{L}$  and  $L$  stand for the sets  $(l, m_l, m_s)$  and  $(l, m_l)$ , respectively, of non-relativistic quantum numbers. The elements of the unitary transformation matrix  $\underline{S}$  in Eq. (2.165) are given by the Clebsch Gordan coefficients  $C(l \frac{1}{2} j, \mu - m_s, m_s)$ . Furthermore one can write

$$\underline{\tau}^{ij} = t^i \delta_{ij} + t^i \sum_k \underline{G}^{ik} \underline{\tau}^{kj} \quad (2.166)$$

$$t^{i-1} \underline{\tau}^{ij} - \sum_k \underline{G}^{ik} \underline{\tau}^{kj} = \delta_{ij} \quad (2.167)$$

$$\sum_k \delta_{ik} t^{i-1} \underline{\tau}^{ik} - \underline{G}^{ik} \underline{\tau}^{kj} = \delta_{ij} \quad (2.168)$$

$$\sum_k [\delta_{ik} t^{i-1} - \underline{G}^{ik}] \underline{\tau}^{kj} = \delta_{ij} \quad (2.169)$$

$$(2.170)$$

where  $\sum_{k \neq i} G^{ik} \dots$  has been replaced by  $\sum_k G^{ik} \dots$  by defining  $G^{ii} = 0$ . Finally the  $\underline{\tau}$  matrix reads as :

$$\underline{\tau} = [\underline{t}^{-1} - \underline{G}]^{-1} \quad (2.171)$$

where each element of the supermatrix is

$$\underline{\tau}^{ij} = \{ [\underline{t}^{-1} - \underline{G}]^{-1} \}_{ij} . \quad (2.172)$$

If we have  $N$  scattering centers and angular momentum expansion going up to  $l^{max}$ , the dimension of the  $\underline{\tau}$  matrix will be  $2N \sum_{l=0}^{l^{max}} (2l+1) = 2N(L_{max} + 1)^2$ .

In the calculations we will use the spin polarized relativistic (SPR) KKR program to solve the Kohn-Sham-Dirac equations, we deal with infinite crystals, so one can make use of the periodicity of such an ordered infinite system. Using the Fourier transformation, we can write:

$$\tau_{\Lambda\Lambda'}(\vec{k}, E) = \frac{1}{N} \sum_{ij} e^{-i\vec{k}(\vec{R}_i - \vec{R}_j)} \tau_{\Lambda\Lambda'}^{ij}(E) \quad (2.173)$$

and

$$G_{\Lambda\Lambda'}(\vec{k}, E) = \frac{1}{N} \sum_{ij} e^{-i\vec{k}(\vec{R}_i - \vec{R}_j)} G_{0\Lambda\Lambda'}^{ij}(\vec{R}_i - \vec{R}_j, E) . \quad (2.174)$$

If we assume the t-matrix is the same at every lattice site, we find that

$$\underline{\tau}(\vec{k}, E) = [\underline{t}^{-1}(E) - \underline{G}(\vec{k}, E)]^{-1} \quad (2.175)$$

The scattering path operator can be obtained through a Brillouin-zone integration of the form:

$$\tau_{\Lambda\Lambda'}^{ij} = \frac{1}{V_{BZ}} \int_{V_{BZ}} d\vec{k} \left[ \underline{t}^{-1}(E) - \underline{G}(\vec{k}, E) \right]_{\Lambda\Lambda'}^{-1} e^{i\vec{k}(\vec{R}_i - \vec{R}_j)} . \quad (2.176)$$

As usual, one can make use of group theory to restrict the integration in Eq. (2.176) to the irreducible part of the Brillouin-zone, that depends on the orientation of the magnetization. Clearly, the scattering path operator in Eq. (2.174) will be singular when

$$|\underline{t}^{-1}(E) - \underline{G}(\vec{k}, E)| = 0 . \quad (2.177)$$

This is known as the KKR determinant, after Korringa (1947) and Kohn and Rostoker (1954) who introduced the method. When Eq. (2.177) is satisfied, the scattering path operator has a singularity which corresponds to a pole in the Green's function, and poles in the Green's function occur at the same energies as the eigenvalues of the Hamiltonian. Hence, finding the zeros of the KKR determinant is a method to find electronic energy levels or equivalently, the band structure.

## 2.3 Treatment of Disordered Alloys

In order to be able to describe disordered alloys, the theoretical methods presented so far have to be reconsidered, because they were directly relevant only to ordered stoichiometric systems. In practice there are many types of disordered systems with technological applicability, that's why it was necessary to develop theoretical methods to describe such systems. The type of disorder considered within this thesis, is that of a random substitutional binary alloy. Such a material is assumed to possess structural order, and so has a clear underlying crystalline lattice structure. However, due to the random distribution of its constituent atoms, such a material is not translational invariant. Density Functional theory is not affected by the translational invariance, and because of this will play a central role in the description of random substitutional alloys. The difficulty which arises due to the random distribution of the constituent atoms is that Bloch's theorem cannot be applied directly.

A viable idea to evade this problem and to be able to solve the Kohm-Sham-Dirac equations is to replace the disordered system by an ordered one, consisting of effective 'atoms'. In this way it is possible to regain the translational invariance and one has to solve further the relevant equations for an ordered system of effective 'atoms'. This approach is known as 'effective medium theory' and, depending on the assumptions made about the properties of effective 'atoms', can describe successfully the disordered systems.

The calculations done within this thesis in order to describe disordered systems use the so-called Coherent Potential Approximation (CPA) method. This approach, in combination with KKR method turned out to be a reliable tool to study the electronic structure of random substitutional binary alloys (see the contributions of Bansil et al.(1975) [80], Temmerman et al. (1978) [81], Györffy and Stocks (1980) [62], J. S. Faulkner (1982) [82] and Faulkner and Stocks (1980) [61]).

### 2.3.1 The Coherent Potential Approximation Method

The aim of the Coherent Potential approximation is to calculate configurationally averaged properties of a random material in a self consistent way. Essentially one can describe the random metallic alloy by a lattice of effective potentials in such a way that the average motion of an electron through the effective medium is approximatively the same like through the actual material. This means that if one wishes to describe the system using an(periodic) coherent potential  $V^{CPA}$ , the Green's function corresponding to this coherent potential should be equivalent to the true ensemble-averaged Green's function of the alloy.

The Coherent Potential approximation (CPA) was introduced simultaneously by Soven [83] in connexion with disordered electronic systems, and by Taylor [84] in connection with the lattice dynamics of mass disordered alloys. The CPA belongs to the class of mean-field theories, in which the properties of the entire material are determined from the behaviour at a localized region, usually taken to be a single site (cell) in the material. In order to create the configuration of the random substitutional binary alloy of composition  $A_xB_{1-x}$  it is as-



sumed that the site occupancies are uncorrelated and that the probability that a particular lattice site  $i$  is occupied by element A is  $x_A = x$  and likewise for B is  $x_B = 1 - x$ . For this disordered system, one may assume that there are only two distinct types of potential,  $V^A$  and  $V^B$ , corresponding to the two elements A and B of the material.

This coherent potential  $V^{CPA}$  (which in general is a complex energy-dependent quantity) is constructed by replacing at any single site in the effective medium the individual constituent potentials of the alloy, given as  $V^A$  or  $V^B$ , in such a way that no further scattering is produced on average.

This medium can be chosen in some physically and intuitively reasonable manner in such a way that averages over the occupation of a site embedded in the effective medium should yield quantities indistinguishable from those associated with a site of the medium itself. Because a translational invariant medium produces no scattering of a wave, it is assumed that the scattering off of a real atom embedded in the CPA medium must vanish on the average. This condition, schematic presented in Fig. 2.1 has the following mathematical expression:

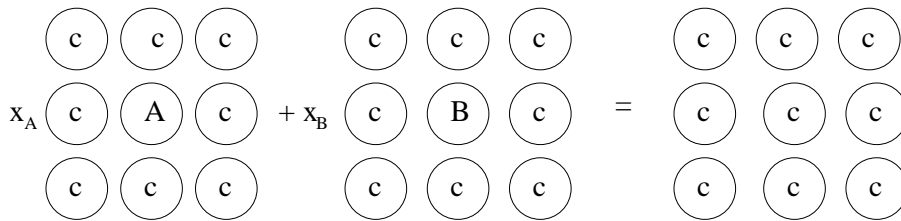


Figure 2.1: The schematic representation of the CPA condition. Label 'c' stands for 'effective atoms' of the coherent medium and the sites labelled 'A' and 'B' are occupied by the constituent atoms A or B with relative probability  $x = x_A$  and respectively  $1 - x = x_B$ .

$$\underline{\mathcal{T}}^C = x_A \underline{\mathcal{T}}^A + x_B \underline{\mathcal{T}}^B, \tag{2.178}$$

where  $\underline{\mathcal{T}}^c$  is the scattering path operator corresponding to this hypothetical ordered CPA medium and  $\underline{\mathcal{T}}^A$  or  $\underline{\mathcal{T}}^B$  describes the total scattering due to a single atom of type A or B, respectively, which is embedded in the effective coherent-potential medium. Equivalently, the site-diagonal part of the Green's function of a real atom embedded in the CPA medium, averaged over the possible occupations of a single site, should be equal with the corresponding Green's function of the medium itself.

The averages one performs in the CPA involve only the occupation of a single site and consequently the CPA is a single-site (SS) approximation, this averaging procedure neglects scattering off of clusters of atoms, which may be important in some cases.

Our first aim is to obtain approximations for the average  $\langle G \rangle$  over the previously described configuration. As has been shown in the previous chapter, the Green's function

$G(E, \vec{r}, \vec{r}')$  for an electron moving in the field of a collection of muffin-tin scatterers can be written in the form (see also Eq. (2.155)) :

$$G(\vec{r}, \vec{r}', E) = \sum_{\Lambda\Lambda'} Z_{\Lambda}^i(\vec{r}_i, E) \tau_{\Lambda\Lambda'}^{ii}(E) Z_{\Lambda'}^{i\times}(\vec{r}'_i, E) - \sum_{\Lambda} Z_{\Lambda}^i(\vec{r}_{i<}, E) J_{\Lambda}^{i\times}(\vec{r}'_{i>}, E) \quad (2.179)$$

when  $\vec{r}$  and  $\vec{r}'$  are both in the neighbourhood of the  $i$ th scatterer, so the vectors  $\vec{r}$  and  $\vec{r}'$  may fall inside the  $i$ th muffin-tin sphere, but they must not be in any other sphere.  $Z^i$  and  $J^i$  are the regular and irregular solutions of the Dirac equation for single-site potential  $V^i$  (see also Eqs. (2.129) and (2.130)). We will refer to Eq. (2.179) as the site-diagonal (SD) expression of the Green's function.

If the vector  $\vec{r}$  is in the neighbourhood of the  $i$ th scatterer and  $\vec{r}'$  is in the neighbourhood of the  $j$ th scatterer, the Green's function may be written in the form:

$$G(\vec{r}, \vec{r}', E) = \sum_{\Lambda\Lambda'} Z_{\Lambda}^i(\vec{r}_i, E) \tau_{\Lambda\Lambda'}^{ij}(E) Z_{\Lambda'}^{j\times}(\vec{r}'_j, E). \quad (2.180)$$

This equation (2.180) is the non-site-diagonal (NSD) Green's function expression. Doing the following step in the CPA description, is now needed to calculate the average of such a Green's functions, the averaging being over the ensemble of all alloy configurations that can be formed by distributing  $x_A N$  atoms of type A and  $x_B N$  atoms of type B over the lattice sites.

The ensemble average of the site-diagonal (SD) Green's function can be written as:

$$\begin{aligned} \langle G(\vec{r}, \vec{r}', E) \rangle &= x_A \sum_{\Lambda\Lambda'} Z_{\Lambda}^{i,A}(\vec{r}_i, E) \langle \tau_{\Lambda\Lambda'}^{ii,A}(E) \rangle Z_{\Lambda'}^{i,A\times}(\vec{r}'_i, E) \\ &+ x_B \sum_{\Lambda\Lambda'} Z_{\Lambda}^{i,B}(\vec{r}_i, E) \langle \tau_{\Lambda\Lambda'}^{ii,B}(E) \rangle Z_{\Lambda'}^{i,B\times}(\vec{r}'_i, E) \\ &- \sum_{\Lambda} [x_A Z_{\Lambda}^{i,A}(\vec{r}_{i<}, E) J_{\Lambda}^{i,A\times}(\vec{r}'_{i>}, E) \\ &- x_B Z_{\Lambda}^{i,B}(\vec{r}_{i<}, E) J_{\Lambda}^{i,B\times}(\vec{r}'_{i>}, E)] , \end{aligned} \quad (2.181)$$

where  $Z_{\Lambda}^{i,\alpha}(E, \vec{r}_i)$ , respectively  $J_{\Lambda}^{i,\alpha}(E, \vec{r}_i)$ , are the wave functions for the case when  $\vec{r}_i$  is in the  $i$ th muffin-tin sphere and an  $\alpha$  atom is in that site,  $\alpha$  being A or B.  $\langle \tau_{\Lambda\Lambda'}^{ii,\alpha}(E) \rangle$  is the average over the subset of the ensemble for which the atom of type  $\alpha$  (A or B) is definitely known to be on the  $i$ th site. A similar average can be done for the non-site-diagonal (NDS) Green's function and the result of averaging looks like:

$$\begin{aligned} \langle G(\vec{r}, \vec{r}', E) \rangle &= x_A^2 \sum_{\Lambda\Lambda'} Z_{\Lambda}^{i,A}(\vec{r}_i, E) \langle \tau_{\Lambda\Lambda'}^{ij,AA}(E) \rangle Z_{\Lambda'}^{j,A\times}(\vec{r}'_j, E) \\ &+ x_B^2 \sum_{\Lambda\Lambda'} Z_{\Lambda}^{i,B}(\vec{r}_i, E) \langle \tau_{\Lambda\Lambda'}^{ij,BB}(E) \rangle Z_{\Lambda'}^{j,B\times}(\vec{r}'_j, E) \end{aligned}$$

$$\begin{aligned}
& + x_A x_B \sum_{\Lambda\Lambda'} Z_{\Lambda}^{i,A}(\vec{r}_i, E) \langle \tau_{\Lambda\Lambda'}^{ij,AB}(E) \rangle Z_{\Lambda}^{j,B\times}(\vec{r}'_j, E) \\
& + x_B x_A \sum_{\Lambda\Lambda'} Z_{\Lambda}^{i,B}(\vec{r}_i, E) \langle \tau_{\Lambda\Lambda'}^{ij,BA}(E) \rangle Z_{\Lambda}^{j,A\times}(\vec{r}'_j, E) .
\end{aligned} \tag{2.182}$$

Here there is another kind of average for the scattering path operator, namely  $\langle \tau_{\Lambda\Lambda'}^{ij,\alpha\beta}(E) \rangle$ , which is the restricted average over the subset of ensemble for which an atom of type  $\alpha$  (A or B) is known to be on the  $i$ th site and another atom of type  $\beta$  (B or A) is known to be on the  $j$ th site. The next step is now to calculate those ensemble averages for the scattering path operators. For this purpose, we will make use of the so-called single-site approximation, which means that, if we calculate for example  $\langle \tau_{\Lambda\Lambda'}^{ii,\alpha}(E) \rangle$  we presume that the effective scattering matrix  $\underline{t}^C(E)$  appears on every site except the  $i$ th site and  $\underline{t}^{\alpha}(E)$  appears there. Equations (2.181) and (2.182) are exact, but they can be greatly simplified invoking the single-site approximation. This derivation ends up with the following result:

$$\langle \tau^{ii,\alpha}(E) \rangle = \underline{D}_{\alpha}^{ii} \underline{\mathcal{I}}_C^{ii}, \tag{2.183}$$

where

$$\underline{D}_{\alpha}^{ii} = \{ \underline{I} + \underline{\mathcal{I}}_C^{ii} [\underline{t}_{\alpha}^{-1} - \underline{t}_C^{-1}] \}^{-1} \tag{2.184}$$

and

$$\underline{\mathcal{I}}_C^{ii} = \frac{\Omega}{(2\pi)^3} \int \underline{\mathcal{I}}_C(E, \vec{k}) d^3 k . \tag{2.185}$$

$\underline{\mathcal{I}}_C(E, \vec{k})$  is given by the matrix inversion:

$$\underline{\mathcal{I}}_C(E, \vec{k}) = \left[ (\underline{t}^C)^{-1} - \underline{G}(E, \vec{k}) \right]^{-1} . \tag{2.186}$$

We have to note that the average  $\langle \tau^{ii,\alpha}(E) \rangle$  is independent on the site index  $i$  and that's why we can name it  $\langle \tau^{00,\alpha}(E) \rangle$ . For the same reason, the matrix  $\underline{D}_{\alpha}^{ii}$  will be named further simpler, namely  $\underline{D}_{\alpha}^{00}$ .

In order to obtain the average  $\langle \tau^{ij,\alpha\beta}(E) \rangle$ , one has to put  $\underline{t}^{\alpha}(E)$  on the  $i$ th site,  $\underline{t}^{\beta}(E)$  on the  $j$ th site and  $\underline{t}^C(E)$  on all the others. The result is

$$\langle \tau^{ij,\alpha\beta}(E) \rangle = \underline{D}_{\alpha}^{00} \underline{\mathcal{I}}_C^{ij} \tilde{\underline{D}}_{\beta}^{00} \tag{2.187}$$

where the matrix  $\underline{D}_{\alpha}^{00}$  is defined in Eq. (2.184) and  $\tilde{\underline{D}}_{\beta}^{00}$  is given by:

$$\tilde{\underline{D}}_{\beta}^{00} = \{ \underline{I} + [\underline{t}_{\beta}^{-1} - \underline{t}_C^{-1}] \underline{\mathcal{I}}_C^{ii} \}^{-1} \tag{2.188}$$

The matrix  $\underline{\mathcal{T}}_C^{ij}$  is given by the expression:

$$\underline{\mathcal{T}}_C^{ij} = \frac{\Omega}{(2\pi)^3} \int e^{i\vec{k}\vec{R}_{ij}} \underline{\mathcal{T}}_C(E, \vec{k}) d^3k \quad (2.189)$$

The  $\underline{\mathcal{T}}_C^{ij}$  is the same for the  $i$ - $j$  pairs of sites separated by a vector  $\vec{R}_{ij} = \vec{R}_j - \vec{R}_i$  of the same magnitude and direction.

In order to obtain the ensemble averaged Green's function within the single-site approximation,  $G_c(E, \vec{r}, \vec{r}') = \langle G(E, \vec{r}, \vec{r}') \rangle$ , the ensemble averages  $\langle \tau^{00,\alpha}(E) \rangle$  and  $\langle \tau^{ij,\alpha\beta}(E) \rangle$  have to be substituted into Eqs. (2.181) and (2.182). The site-diagonal (SD) and non-site-diagonal ensemble average Green's functions are needed for most calculations of electronic properties in alloys.

It can be seen from the defining equations that  $G_c(\vec{r}, \vec{r}', E)$  describes a periodic system in the sense that

$$G_c(\vec{r} + \vec{R}_n, \vec{r}' + \vec{R}_n, E) = G_c(\vec{r}, \vec{r}', E) . \quad (2.190)$$

No statement has been made so far in this derivation concerning the way that the effective scattering matrix  $\underline{t}^C$  is defined. One has to note that the most remarkable feature of  $G_c(\vec{r}, \vec{r}', E)$  is that the effective wave function for each site is different for the SD and NSD cases. The theory for electronic states in an alloy has been designed to arrive at an effective Green's function rather than to get an effective wave function because every property of an alloy can be calculated using  $G_c(\vec{r}, \vec{r}', E)$ . In the following section it will be shown how one can calculate electronic properties of alloys. Let's consider first the average density of states for a random substitutional alloy, in the single-site approximation. This can be expressed in the formula:

$$\rho_C(E) = -\frac{1}{\pi} \Im \int_{\Omega} G_c(\vec{r}, \vec{r}, E) d^3r \quad (2.191)$$

Because only values of  $G_c(\vec{r}, \vec{r}', E)$  for which  $\vec{r} = \vec{r}'$  enters in the expression, only the SD form of Green's function is needed. Inserting Eq. (2.181), with the average scattering path operator given by Eq. (2.183) into this expression, leads to

$$\rho_C(E) = -\frac{1}{\pi} \sum_{\alpha=A,B} x_{\alpha} \sum_{\Lambda\Lambda'} \Im \langle \tau_{\Lambda\Lambda'}^{00,\alpha}(E) \rangle \int_{\Omega} Z_{\Lambda}^{\alpha}(\vec{r}, E) Z_{\Lambda'}^{\alpha\times}(\vec{r}, E) d^3r , \quad (2.192)$$

where  $\alpha = A$  or  $B$  indicates that the site in question is occupied by an atom of type  $A$  or  $B$ . If we use the notation

$$\underline{F}_{\Lambda\Lambda'}^{\alpha\alpha}(E) = \int_{\Omega} Z_{\Lambda}^{\alpha}(\vec{r}, E) Z_{\Lambda'}^{\alpha\times}(\vec{r}, E) d^3r \quad (2.193)$$

where the underline means a matrix with respect to  $\Lambda = \{\kappa, \mu\}$ , one may express  $\rho_C(E)$  as

$$\rho_C(E) = -\frac{1}{\pi} \sum_{\alpha=A,B} x_\alpha \Im Tr \underline{F}^{\alpha\alpha}(E) \underline{D}_\alpha^{00}(E) \underline{I}_C^{00}(E). \quad (2.194)$$

From the expression given for the average density of states (2.194) it is clear that one may resolve the total density of states  $\rho_C(E)$  into components  $\rho_A(E)$  and  $\rho_B(E)$ . These quantities may be thought of as the average density of states (per atomic cell) on an A- or B-type site in the alloy. Consequently the total density of states may be written as the sum of the concentration weighted component density of states thus

$$\rho_C(E) = x_A \rho_A(E) + x_B \rho_B(E), \quad (2.195)$$

where the component density of states can be identified as

$$\rho_\alpha(E) = -\frac{1}{\pi} \Im Tr [\underline{F}^{\alpha\alpha}(E) \underline{D}_\alpha^{00}(E) \underline{I}_C^{00}(E)] \quad (2.196)$$

with  $\alpha = A$  or  $B$ . The expressions for the total and component densities of states, which are identical to those derived by Faulkner and Stocks [61], are given in a completely general form such that they can be used for both relativistic or non-relativistic calculations.

The charge densities  $\rho_A(\vec{r})$  and  $\rho_B(\vec{r})$  associated with a given atomic type can be obtained through a energy integration up to the Fermi energy, as follows:

$$\rho_\alpha(\vec{r}) = -\frac{1}{\pi} \int_{-\infty}^{E_F} \Im Tr [\underline{F}^{\alpha\alpha}(\vec{r}, \vec{r}, E) \underline{D}_\alpha^{00}(E) \underline{I}_C^{00}(E)] dE \quad (2.197)$$

where

$$\underline{F}_{\Lambda\Lambda'}^{\alpha\alpha}(E, \vec{r}, \vec{r}') = Z_\Lambda^\alpha(\vec{r}, E) Z_{\Lambda'}^{\alpha\times}(\vec{r}', E). \quad (2.198)$$

Another quantity, used by Györfy et al. [62] in order to formulate theories for soft X-ray emission, electron-photon interaction and other phenomena is so called density matrix, defined as

$$\rho(\vec{r}, \vec{r}', E) = x_A \rho_A(\vec{r}, \vec{r}', E) + x_B \rho_B(\vec{r}, \vec{r}', E). \quad (2.199)$$

The components of density matrix are ( $\alpha$  is A or B):

$$\rho_\alpha(\vec{r}, \vec{r}', E) = -\frac{1}{\pi} \Im Tr [\underline{F}^{\alpha\alpha}(\vec{r}, \vec{r}') \underline{D}_\alpha^{00} \underline{I}_C^{00}]. \quad (2.200)$$

With the formulas for  $G_c(\vec{r}, \vec{r}', E)$  available, the comparison with experimental data for density of states for example, is straightforward (see [82] and [61]). The CPA is regarded as one

of the best single-site theories for the description of random substitutional binary alloys. On the other hand, multiple-site scattering effects are implicitly included within the theory as the single-site approximation is based on the idea of a single scattering site immersed in an average 'effective' medium. Consequently, it is appropriate to proceed developing calculations combining the CPA with the KKR theory. The calculations done in this thesis use this approach in order to investigate the properties of random substitutional alloys.

## 2.4 Conclusions

This chapter presented the theoretical framework used within this thesis in order to describe the electronic structure of condensed matter.

As the description of any solid is in essence a many body problem, it has been presented how the use of the DFT can reduce and hence simplify considerably such a many body problem to that of a single electron moving independently of all other electrons in a effective field created by surrounding electrons and nuclei.

The multiple scattering KKR theory is used to solve the previously simplified problem and to obtain the full description of the electronic structure of the condensed matter systems under investigation.

On the basis of the underlying band structure, one is able to calculate important properties of materials. Such a class of materials which will be investigated in the following is the Cr-chalcogenides system with different transitional metals substituting partially the Cr atoms. In addition, the formalism presented above will be extended in order to calculate spectroscopic properties, namely the magnetic Compton profile for pure metallic systems and for random substitutional alloys respectively.

## Chapter 3

# Compton scattering

The purpose of a Compton scattering experiment is to determine the momenta, or momentum distribution of the target electrons. Typically, one employs a primary beam of a known photon energy  $E$ , and measures the spectrum of secondary photon energies  $E'$  after scattering from the sample through a known angle  $\theta$ . When radiation is Compton scattered, the emerging beam is Doppler broadened because of the motion of the target electrons. The analysis of this broadened spectra, the so-called Compton profile, provides informations about the electron momentum distribution of the scatterers.

Compared with other experimental techniques, Compton scattering offers several advantages. Compton scattering is an inelastic process, in which a high energy photon collides with a single electron and imparts energy to it. Since the scattering is from a single-electron and (to a good approximation) occurs at a single point in space, the process must be incoherent. Incoherent scattering, as opposed to coherent Bragg scattering, occurs when there is no phase relationship between the waves scattered by different atoms in a sample. The incoherent nature of Compton scattering means that the process can only be sensitive to bulk properties- that it is, an average over real space.

Due to these features, Compton scattering is directly related to the electronic ground state, whereas other spectroscopic methods (e.g. photoemission spectroscopy) involve excited states. Since theoretical methods (like density functional theory) are tailored to give predictions of the ground state, Compton scattering allows for a rather fundamental test of these theories. Also, Compton scattering has the advantage that is not much sensitive to the sample purity, lattice defects or to the surface, so the Compton experiment samples the electrons in the crystal uniformly.

A limiting factor have been the poor momentum resolution achieved in experiments, but the utilization of solid-state detectors since 1970's, and subsequently the employment of high-resolution crystal spectrometers at modern synchrotron radiation sources since the 1980's have revived this field.

The interpretation of standard Compton profiles is far from trivial, because the directly accessible quantity is a projection of the momentum density  $n(\vec{p})$  onto the scattering vector and some features of  $n(\vec{p})$  are lost because of projection. There is a complementary experimental

technique, the 2D-ACAR (2D angular correlation of the annihilation radiation) which can resolve these details. It gives the 2D projection of the 3D electronic momentum density along the direction perpendicular to the detector plane, while the Compton scattering gives the momentum density  $n(\vec{p})$  integrated over the perpendicular plane to the scattering vector. Obviously, first-principles prediction within the conventional band theory model can facilitate the interpretation of Compton data a lot.

### 3.1 Compton scattering cross section

Many of the important features of Compton scattering can be explained analysing the kinematics of this process. In the scattering experiment the total flux reaching the detector can be measured and the differential scattering cross section  $\frac{d\sigma}{d\Omega}$  deduced. When inelastic processes are involved, the spectral distribution can be plotted and the double differential scattering cross section  $\frac{d^2\sigma}{d\Omega d\omega}$  can be obtained ( $\omega = \omega_1 - \omega_2$  is the energy transfer). In the past, many expressions for the scattering cross section were developed, starting with the non-relativistic Thomson cross-section for unpolarized photons:

$$\frac{d\sigma}{d\Omega} = \frac{r_e^2}{2}(1 + \cos^2 \theta), \quad (3.1)$$

where  $r_e = e^2/mc^2$  is the classical electron radius. However, soon it was found that high energy radiation doesn't obey this formula (the total cross-section was lower than predicted) and other approaches were developed. Klein and Nishina (1929) performed a quantum electrodynamical calculation of the Compton scattering cross-section obtaining the following formula [85]:

$$\frac{d\sigma}{d\Omega} = \frac{r_e^2}{2} \left(\frac{E'}{E}\right)^2 \left\{ (1 + \cos^2 \theta) + \frac{E - E'}{mc^2} (1 - \cos \theta) \right\} \quad (3.2)$$

valid for a free electron initially at rest and for any photon energy. This formula explains the puzzling asymmetry between forward and back scattering and it contains no parameter specific to the scatterer.

At low photon energies,  $E \sim E'$  and the Klein-Nishina cross section reduces to the classical form, as one would expect. When the incident photon energy becomes an appreciable fraction of  $mc^2$ , the departure from the Thomson formula becomes prominent.

With very high energy photons, the role of the electron spin starts to be important in the interaction and the scattering becomes sensitive to the magnetic properties of the sample for incident circularly polarized radiation. A term depending on the electron spin in the scattering cross section was first derived by Lipps and Tolhoek (1954) [86] and an extension to electrons in molecules and solids was done by Platzman and Tzoar (1970) [87]. This term



is a first order correction which couples the electron spin orientation to the photon circular polarization:

$$\frac{d\sigma}{d\Omega} = \frac{r_e^2}{2} [(1 + \cos^2 \theta + P_3 \sin^2 \theta) - 2P_2\tau(1 - \cos \theta) \langle \vec{S} \rangle \cdot (\hat{\mathbf{q}} \cos \theta - \hat{\mathbf{q}}')], \quad (3.3)$$

where  $P_2$  and  $P_3$  are the Stokes parameters for circular, respectively linear polarization,  $\vec{S}$  is the electron spin vector and  $\hat{\mathbf{q}}$  and  $\hat{\mathbf{q}}'$  are the directions of the primary and secondary photon beams, respectively.

The term proportional to  $P_2$  can be viewed as an interference between charge and magnetic amplitude, so this term is sensitive to the momentum space spin polarization in a magnetically ordered material. The prefactor  $\tau = E/m_0c^2$  ( $E$  is the incident photon energy and  $m_0c^2$  is the rest mass energy of the electron) makes this term typically about 1 % of the charge cross section [13]. If the magnitude and angular variation of the magnetic scattering is compared with the unpolarized scattering, appreciable differences will be observed at high scattering angles for short wavelengths.

Starting from the supposition enclosed in the previous formula, many ferromagnetic systems have been studied using magnetic Compton scattering, providing valuable informations about their spin momentum density, as will be seen in the next sections. In addition, many theoretical studies have been done in this field and one should mention among others the work of Wakoh and Kubo (1977) [88], Williams (1977) [89], Mills (1987) [90], Collins et al. [91], Sakurai et al. [92], Kubo and Asano [11], Y Tanaka et al. [13], Cooper et al. [93], Cardwell and Cooper (1989) [94] and Dixon et al. [12].

An important role in the development of the Compton scattering cross-section measurements played the radiation sources, spectrometers and photons detectors. While the first observations of the Compton scattering were made using radioactive sources, the majority of the Compton scattering experiments use today synchrotron radiation sources. In particular, magnetic Compton scattering is included in the research program of every third generation synchrotron facility.

## 3.2 Magnetic Compton Scattering (MCS)

Conventional Compton scattering studies did not involve magnetic properties of the scatterers. However, as has been indicated above, the magnetic term in the scattering cross section derived first by Lipps and Tolkoek made it possible to investigate the magnetic properties of the scatterers.

This type of experiment became feasible with the advent of the high energy synchrotron radiation sources, in spite of inherently small cross section involved. Compared to the charge scattering contribution, the magnetic term is smaller by a factor of  $\hbar\omega/m_0c^2$ , where  $m_0c^2$  is the rest mass energy of the electron and  $\hbar\omega$  is the incident photon energy. Therefore, these experiments must be performed with powerful photon sources, in order to maximize the

signal connected with the cross section for magnetic scattering.

By alternately measuring the standard Compton profiles with opposite sample magnetization (or photon helicity), magnetic Compton scattering (MCS) provides a measure of the momentum distribution of the difference between the spin-up and spin-down electrons. To be sensitive to the magnetic electrons, MCS require circularly polarized photons that couple according to that term in the incoherent scattering cross section which arises from the charge and magnetic scattering interference.

The first magnetic Compton profile measurements were performed by Sakai and Ono [95] who obtained circularly polarized gamma rays from the cryogenically oriented radioactive source of  $^{57}\text{Co}$ . Although this pioneering experiment suffered from a low count rate, the result clearly demonstrated the existence of the magnetic effect predicted theoretically by Platzman and Tzoar [87].

The interpretation of the measured Compton scattering cross section is in most cases made within the so-called impulse approximation (IA). In this approximation it is assumed that the electrons involved in the scattering can be treated like free and their binding can be only seen in the spread of their momenta. The physical meaning of this approximation can be seen as follows: the time the photon spends probing the electron distribution ( $\sim \hbar/\omega$ ) is so short that the other electrons of the sample cannot relax to take into account the hole created by the recoiling electron until it has completely escaped from the system so that the scattering is essentially from single electrons which can be thought as free electrons. The potential energy of the electron distribution  $V(r)$  is considered constant for the duration of the collision and thus cancels out in the energy conservation equation.

The deviation from the impulse approximation has been the subject of several theoretical studies. Ribberfors [96] and Holm and Ribberfors [97] made thorough calculations using the incident photon energy, the atomic number and the scattering angle as parameters to find a possible deviation from the IA. It turned out that the IA works surprisingly well. Eisenberg and Platzman [98] studied the influence of the potential to the observed spectrum and expressed the errors in terms of  $(\frac{E_B}{E_r})^2$ , where  $E_B$  is the binding energy and  $E_r$  is the recoil energy of the photons. For small ratio, as it is the case for most experiments, the IA works well again.

Within this approximation, if one considers an incident photon with wave vector  $\vec{k}_0$  and a scattered photon with the wave vector  $\vec{k}'$  (see Fig. 3.1), the magnetic Compton cross section for a solid can be written as:

$$\left[ \frac{d^2\sigma}{d\Omega dp_z} \right]_{\uparrow} - \left[ \frac{d^2\sigma}{d\Omega dp_z} \right]_{\downarrow} \equiv \left[ \frac{d^2\sigma}{d\Omega dp_z} \right]_{\Delta} = P_c r_0^2 \left( \frac{k'^2}{k_0^2} \right) \Psi_2(\sigma) J_{mag}(p_z), \quad (3.4)$$

where  $P_c$  is the degree of circular polarization and  $r_0$  is the classical electron radius and  $\Psi_2$  is a geometrical factor, defined as:

$$\Psi_2 = \pm \sigma (k_0 \cos \alpha \cos \varphi - k' \cos(\alpha - \varphi)) (\cos \varphi - 1) \frac{\hbar c}{m_0 c^2}. \quad (3.5)$$

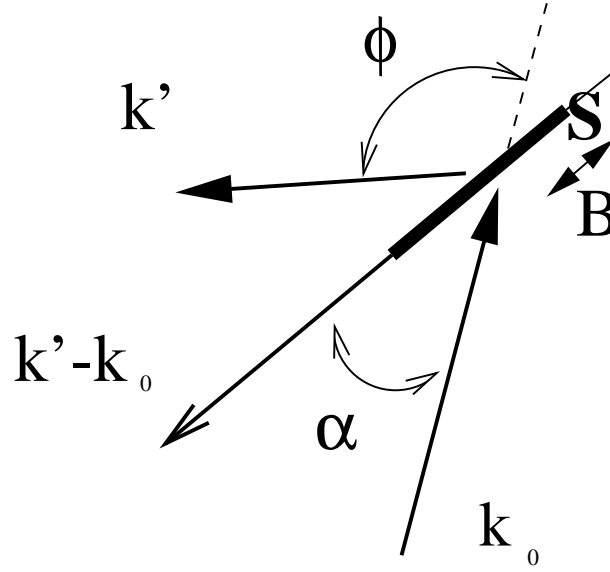


Figure 3.1: The Compton scattering geometry.

In this formula,  $\sigma$  is the electron spin ( $\pm 1$ ),  $\alpha$  is the angle between the incident photon ( $\vec{k}_0$ ) and the magnetization direction ( $\vec{B}$ ) and  $\varphi$  is the scattering angle. As can be seen from Eqs. (3.4) and (3.5), the magnetic cross-section can be increased by making the angle  $\alpha$  smaller and  $\phi$  larger.  $J_{mag}$  is the momentum distribution of the unpaired electrons projected along the scattering vector ( $p_z$ ), also known as the magnetic Compton profile:

$$J_{mag}(p_z) = \int \int (n^\uparrow(\vec{p}) - n^\downarrow(\vec{p})) dp_x dp_y . \quad (3.6)$$

Here the electron momentum density for a given spin orientation is given by  $n^{\uparrow(\downarrow)}(\vec{p})$ . By constraining the sample magnetisation and the incident and scattered wave vector to be coplanar (see Fig. 3.1), the measured profile depends only upon the electron's spin. The traditional Compton scattering samples a projection of the electron momentum density, where the integrated area under the Compton profile obtained is proportional to the total number of electrons. The Compton profile is a one-dimensional projection of the electron momentum density  $n(\vec{p})$  along the scattering vector  $p_z$ :

$$J(p_z) = \int \int n(\vec{p}) dp_x dp_y . \quad (3.7)$$

The area under the profile is equal with the number of electrons in the Wigner-Seitz cell, i.e.

$$\int J(p_z) dp_z = Z . \quad (3.8)$$

In the magnetic scattering, we are interested only on those electrons which contribute to the spin moment, and which are, therefore, unpaired. If we consider the total electron momentum density to be composed of spin-up and spin-down electrons, we can write

$$n(\vec{p}) = n^\uparrow(\vec{p}) + n^\downarrow(\vec{p}) . \quad (3.9)$$

If a spin moment exists, this is given by the difference in occupancy of the spin-up and spin-down bands:

$$\mu_{spin} = \int [n^\uparrow(\vec{p}) - n^\downarrow(\vec{p})] d^3p . \quad (3.10)$$

This difference can be measured in a magnetic Compton experiment due to the spin dependent term in the scattering cross section. The area under the magnetic Compton profile is equal to the spin moment per Wigner-Seitz cell:

$$\int_{-\infty}^{+\infty} J_{mag}(p_z) dp_z = \mu_{spin} . \quad (3.11)$$

On the basis of this derivation, we can consider the magnetic Compton scattering as an established technique for probing the spin-dependent momentum densities and band-structures of magnetic solids. The orbital momentum is not measured, the magnetic Compton profile is solely sensitive to the spin moments of the scatterers [99, 90, 89, 87, 100] .

The shape of the magnetic Compton profile carries information about the localization of the electronic moment. This is a useful asset, as the localization of the moment and its interaction with the surrounding conduction electrons, e.g. via the s-d interaction, is the mechanism which drives the magnetic ordering.

The experiments of spin-polarized positron angular correlation also probe the spin density, but in this case the positron-electron correlation effects have to be considered. The positron doesn't sample electrons from all states equally, whilst De Haas-van Alphen measurements are only sensitive to the electrons from the Fermi surface. Compared to these techniques, the value of the magnetic Compton scattering stems from its uniform sensitivity to the whole of electron momentum distribution.

### 3.3 The expression for the magnetic Compton profile

Our aim is to calculate the magnetic Compton profile  $J_{mag}(p_z)$  including all relativistic effects. Starting from the expression of  $J_{mag}(p_z)$  from Eq. (3.7), one needs a method to obtain the momentum density  $n(\vec{p})$ . It has been shown in the previous chapters how the Green's function  $G(\vec{r}, \vec{r}', E)$  for a system can be calculated and how certain quantities describing a system can be connected to the Green's function of that system. In this case, the quantity

involved is defined in the momentum space. As a consequence, a change of representation is required for the Green's function, according to the formula:

$$G_{m_s m'_s}(\vec{p}, \vec{p}', E) = \frac{1}{N\Omega} \int d^3r \int d^3r' \Phi_{\vec{p}m_s}^\times(\vec{r}) \Im G^+(\vec{r}, \vec{r}', E) \Phi_{\vec{p}'m'_s}(\vec{r}'). \quad (3.12)$$

Here  $\Omega$  is the volume of the unit cell and  $\Phi_{\vec{p}m_s}$  are the eigenfunctions of the momentum operator, which can be written as  $\Phi_{\vec{p}m_s} = U(\vec{p})e^{i\vec{p}\vec{r}} = U_{\vec{p}m_s}e^{i\vec{p}\vec{r}}$ , where  $U(\vec{p})$  is a four-component spinor satisfying the equation:

$$(c\vec{\alpha}\vec{p} + \beta mc^2)U_{\vec{p}m_s} = E_p U_{\vec{p}m_s}. \quad (3.13)$$

One may write  $\vec{r} = \vec{R}_n + \vec{r}_{0n}$  where  $\vec{R}_n$  is the origin of the  $n$ th cell and  $\vec{r}_{0n}$  is included into this cell. In addition, one may consider the real-space integration  $\int d^3r$  as a summation over the cell-integrals  $\int d^3r = \sum_n \int d^3r_{0n}$ . Consequently, the expression for the Green's function reads:

$$\begin{aligned} G_{m_s m'_s}(\vec{p}, \vec{p}', E) &= \frac{1}{N\Omega} \sum_n \int d^3r_0 \int d^3r' \\ &\quad \times \phi_{\vec{p}m_s}^\times(\vec{R}_n + \vec{r}_0) \Im G^+(\vec{R}_n + \vec{r}_0, \vec{r}', E) \phi_{\vec{p}'m'_s}(\vec{r}') \\ &= \frac{1}{N\Omega} \sum_n \int d^3r_0 \int d^3r' \\ &\quad \times U_{\vec{p}m_s}^\times e^{-i\vec{p}(\vec{R}_n + \vec{r}_0)} \Im G^+(\vec{R}_n + \vec{r}_0, \vec{R}_n + \vec{r}', E) U_{\vec{p}'m'_s} e^{i\vec{p}'(\vec{R}_n + \vec{r}')} . \end{aligned} \quad (3.14)$$

If the translational invariance property of the Green's function is taken into account (see Eq. (2.190)) and the Bloch theorem is applied for  $\Phi_{\vec{p}m_s}$ , one gets:

$$\begin{aligned} G_{m_s m'_s}(\vec{p}, \vec{p}', E) &= \frac{1}{\Omega} \int d^3r_0 \int d^3r' U_{\vec{p}m_s}^\times e^{-i\vec{p}\vec{r}_0} \Im G^+(\vec{r}_0, \vec{r}', E) U_{\vec{p}'m'_s} e^{i\vec{p}'\vec{r}'} \frac{1}{N} \sum_n e^{i(-\vec{p} + \vec{p}')\vec{R}_n} \\ &= \frac{1}{\Omega} \int d^3r_0 \int d^3r' U_{\vec{p}m_s}^\times e^{-i\vec{p}\vec{r}_0} \Im G^+(\vec{r}_0, \vec{r}', E) U_{\vec{p}'m'_s} e^{i\vec{p}'\vec{r}'} \Delta(-\vec{p} + \vec{p}') \end{aligned} \quad (3.15)$$

and finally, the result is

$$G_{m_s m'_s}(\vec{p}, \vec{p}', E) = G_{m_s}(\vec{p}, \vec{p}', E) \delta_{m_s m'_s} \delta_{\vec{p}\vec{p}'} . \quad (3.16)$$

This property is very useful for our purpose, because performing an energy integration up to the Fermi level, one gets the spin-projected momentum density, according to the formula:

$$n^{m_s}(\vec{p}) = -\frac{1}{\pi} \int_0^{E_F} \Im G_{m_s}(\vec{p}, \vec{p}, E) dE . \quad (3.17)$$

This is a quantity depending on the momentum vector which has to be projected on the scattering vector direction through integration in a plane perpendicular to it. A two-dimensional integration in the  $(p_x, p_y)$  plane is the final step to calculate the magnetic Compton profile by the formula:

$$J_{mag}(p_z) = \int \int (n^\uparrow - n^\downarrow) dp_x dp_y . \quad (3.18)$$

The problem is still unsolved; in order to make our formalism applicable, we have to get a general formula for  $G_{m_s}(\vec{p}, \vec{p}, E)$ , equally valid for systems with many atoms per unit cell, pure systems and for substitutional disordered alloys.

We will start our calculation from the following formula for momentum's representation eigenfunctions:

$$\Phi_{\vec{p}m_s} = \left( \frac{E_p + c^2}{2E_p + c^2} \right)^{\frac{1}{2}} \left( \begin{array}{c} \chi_{m_s} \\ \frac{c\vec{\sigma}\vec{p}}{E_p + c^2} \chi_{m_s} \end{array} \right) e^{i\vec{p}\vec{r}} , \quad (3.19)$$

where

$$E_p = \frac{c^2}{2} \left( \sqrt{1 + \frac{p^2}{c^2}} - 1 \right) \quad (3.20)$$

is the electron's total energy,  $\chi_{m_s}$  are the Pauli spinors and  $m_s$  is the spin quantum number. Using the expansion (see Rose [101])

$$\chi_{m_s} e^{i\vec{p}\vec{r}} = 4\pi \sum_{\Lambda} i^l C_{\Lambda}^{m_s} Y_l^{\mu - m_s*}(\vec{p}) j_l(pr) \chi_{\Lambda} \quad (3.21)$$

and the properties of the operator  $\vec{\sigma}\vec{p}$ , these functions are rewritten as:

$$\Phi_{\vec{p}m_s} = 4\pi \left( \frac{E_p + c^2}{2E_p + c^2} \right)^{\frac{1}{2}} \sum_{\Lambda} i^l C_{\Lambda}^{m_s} Y_l^{\mu - m_s*}(\vec{p}) \left( \begin{array}{c} j_l(pr) \chi_{\Lambda}(\hat{r}) \\ \frac{icS_k}{E_p + c^2} j_l(pr) \chi_{-\Lambda}(\hat{r}) \end{array} \right) , \quad (3.22)$$

where  $C_{\Lambda}^{m_s}$  are the Clebsch-Gordan coefficients,  $Y_l^{m_l}$  are the complex spherical harmonics,  $\chi_{\Lambda}(\hat{r})$  are the spin-angular functions and  $j_l(pr)$  are the spherical Bessel functions.

Introducing this expression of the momentum operator eigenfunctions into the Green's function expression (3.12), together with the site-diagonal (SD) (Eq. (2.179)) and site-nondiagonal

(NSD) expressions (Eq. (2.180)) of the Green's function in the coordinate representation, one gets:

$$\begin{aligned}
G_{m_s}(\vec{p}, \vec{p}, E) &= \frac{1}{\Omega} \int d^3 r_{0q} \int d^3 r'_{0q} U_{\vec{p}m_s}^\times e^{-i\vec{p}(\vec{r}_{0q} + \vec{R}_q)} \\
&\Im \left[ \sum_{\alpha} x_{q\alpha} \sum_{\Lambda\Lambda'} Z_{\Lambda}^{q\alpha}(\vec{r}_{0q}, E) \tau_{\Lambda\Lambda'}^{0q0q,\alpha}(E) Z_{\Lambda'}^{q\alpha\times}(\vec{r}'_{0q}, E) \right. \\
&\quad \left. - \sum_{\Lambda} Z_{\Lambda}^{q\alpha}(\vec{r}_{nq<}, E) J_{\Lambda}^{q\alpha\times}(\vec{r}_{nq>}, E) \right] U_{\vec{p}m_s} e^{i\vec{p}(\vec{r}'_{0q} + \vec{R}_q)} \\
&+ \frac{1}{\Omega} \sum_q \sum_{n'q'} \int d^3 r_{0q} \int d^3 r'_{n'q'} U_{\vec{p}m_s}^\times e^{-i\vec{p}(\vec{r}_{0q} + \vec{R}_q)} \\
&\Im \left[ \sum_{\alpha\beta} x_{q\alpha} x_{q'\beta} \sum_{\Lambda\Lambda'} Z_{\Lambda}^{nq\alpha}(\vec{r}_{nq}, E) \tau_{\Lambda\Lambda'}^{nq\alpha n'q'\beta}(E) Z_{\Lambda'}^{n'q'\beta\times}(\vec{r}'_{n'q'}, E) \right] \\
&\times U_{\vec{p}m_s} e^{i\vec{p}(\vec{r}'_{n'q'} + \vec{R}_{n'} + \vec{R}_{q'})} .
\end{aligned} \tag{3.23}$$

The details of the calculations are presented in the Appendix A. The quantities  $M_{m_s\Lambda}^{q\alpha}$  and  $\tilde{M}_{m_s\Lambda m'_s}^{q\alpha}$  are the following matrix elements (see Appendix B) of the regular and irregular solutions of the Dirac equation:

$$\begin{aligned}
M_{m_s\Lambda} &= M_{m_s\Lambda}(\vec{p}, E) \\
&= \langle \phi_{\vec{p}m_s} | Z_{\Lambda} \rangle
\end{aligned} \tag{3.24}$$

and

$$\begin{aligned}
M_{m_s\Lambda''m'_s} &= M_{m_s\Lambda''m'_s}(\vec{p}, E) \\
&= \langle \phi_{\vec{p}m_s}(\vec{r}) | \left( Z_{\Lambda''}(\vec{r}) J_{\Lambda''}^\times(\vec{r}') \Theta(r' - r) \right. \\
&\quad \left. J_{\Lambda''}(\vec{r}) Z_{\Lambda''}^\times(\vec{r}') \Theta(r - r') \right) | \phi_{\vec{p}m'_s}(\vec{r}') \rangle .
\end{aligned} \tag{3.25}$$

From this, the following expression for the momentum representation Green's function is derived (see Appendix A):

$$\begin{aligned}
G_{m_s m'_s}(\vec{p}, \vec{p}, E) &= \frac{1}{\Omega} \Im \sum_q \sum_{\alpha} x_{q\alpha} \left[ \sum_{\Lambda\Lambda'} M_{m_s\Lambda}^{q\alpha} t_{\Lambda\Lambda'}^{q\alpha} M_{m'_s\Lambda'}^{q\alpha*} - \sum_{\Lambda} \tilde{M}_{m_s\Lambda m'_s}^{q\alpha} \right] \\
&+ \frac{1}{\Omega} \Im \sum_q \sum_{\alpha} x_{q\alpha} \sum_{\Lambda\Lambda'} M_{m_s\Lambda}^{q\alpha} \left( D^{q\alpha} \tau^{0q0qCPA} - t^{q\alpha} \right)_{\Lambda\Lambda'} M_{m'_s\Lambda'}^{q\alpha*}
\end{aligned}$$

$$\begin{aligned}
& -\frac{1}{\Omega} \Im \sum_q \sum_{\alpha\beta} x_{q\alpha} x_{q\alpha} \sum_{\Lambda\Lambda'} M_{m_s\Lambda}^{q\alpha} \left( D^{q\alpha} \tau^{0q0qCPA} \tilde{D}^{q\alpha} \right)_{\Lambda\Lambda'} M_{m'_s\Lambda'}^{q\alpha*} \\
& + \frac{1}{\Omega} \Im \sum_q \sum_{q'} e^{-i\vec{p}(\vec{R}_q - \vec{R}_{q'})} \sum_{\alpha\beta} x_{q\alpha} x_{q'\beta} \\
& \quad \sum_{\Lambda\Lambda'} M_{m_s\Lambda}^{q\alpha} \left( D^{q\alpha} \tau^{qq'CPA}(\vec{p}) \tilde{D}^{q'\beta} \right)_{\Lambda\Lambda'} M_{m'_s\Lambda'}^{q'\beta*}. \tag{3.26}
\end{aligned}$$

The first term in this formula is the single-site part, with the single-site t-matrix elements given by Eq. (2.137). For the energy-integration of this term, a path along the real axis will be used; in this way, the matrices  $M_{m_s\Lambda m'_s\Lambda'}^{q\alpha}$  can be ignored, because they contain the irregular solutions of the Dirac equations which can be ignored for real energies because only the imaginary part has to be considered.

The second term is the so-called backscattering term and can be evaluated through an energy integration in the complex plane, along an arc-like contour path with only few energy mesh points. The scattering path operator  $\tau^{0q0qCPA}$  is given by the CPA equation (2.183) and the matrix  $D^{q\alpha}$  is defined in Eq. (2.184). The third term prevents a double-counting coming from the same site in the non-site diagonal expression of the Green's function, which is present in the fourth term. The scattering path operator which appears in the fourth term was already defined in the CPA theory for disordered alloys and is given in Eq. (2.189).

One should emphasize that this formula enables us to treat pure systems as well. In this case the matrix  $D^{q\alpha}$  is the identity matrix,  $x_{q\alpha} = 1$  and the  $\tau^{0q0qCPA}$  is replaced by the supermatrix (2.171) defined in the multiple scattering section. Also, the systems with many atoms per unit cell and substitutional disordered alloys are successfully described by this formalism, as will be shown in the next sections.

### 3.4 Application to the transition metals Fe and Ni

A first test of the formalism presented before has been done for the transition metals Fe and Ni. Ferromagnetic iron has been a very popular material for many magnetic measurements, mainly because of its large (spin) magnetic moment at room temperature which maximize the magnetic Compton cross-section. From a theoretical point of view, Fe is relatively simple system to model, and several band-structure techniques have been adapted to calculate magnetic Compton profiles. Because of these reasons, there are several studies on the MCP in Fe, first of them published in 1976 by Sakai and Ono [95]. The resolution of the experimental data is rather poor in this early study, so we convoluted our calculated profiles with a Gaussian having a full width at half maximum (FWHM) equal to the experimental momentum resolution.

The experimental profiles we used for comparison are already normalized with the area under the profile equal with the spin magnetic moment and we didn't perform a further normalization.



The magnetic Compton profiles along the scattering directions  $[001]$ ,  $[110]$  and  $[111]$  are calculated by applying the SPR-KKR package to perform electronic structure calculations based on the Vosko, Wilk and Nusair parametrization for the exchange-correlation energy. The calculation routine allows to have the magnetic moments rotated away from the global  $z$ -axis. This means that the band-structure problem is solved in a local frame of reference having the scattering vector direction as  $z$ -axis. The integration in the  $(p_x, p_y)$  plane is done up to  $p_{x,max} = p_{y,max} = 10$  a.u. in a rectangular grid which consists of  $50 \times 50$  grid points. The test calculations we have done to check the validity of this approach showed that any increasing of the number of grid points or the maximum value of the  $p_x$  or  $p_y$  momentum doesn't change the shape of the calculated profiles. The energy integration splits into an arc-like path of 30 points in the complex energy plane and a path parallel to the real energy axis which consists of 50 energy-points.

The directional profiles for Fe are presented in Figs. 3.2 and 3.4. The experimental data of

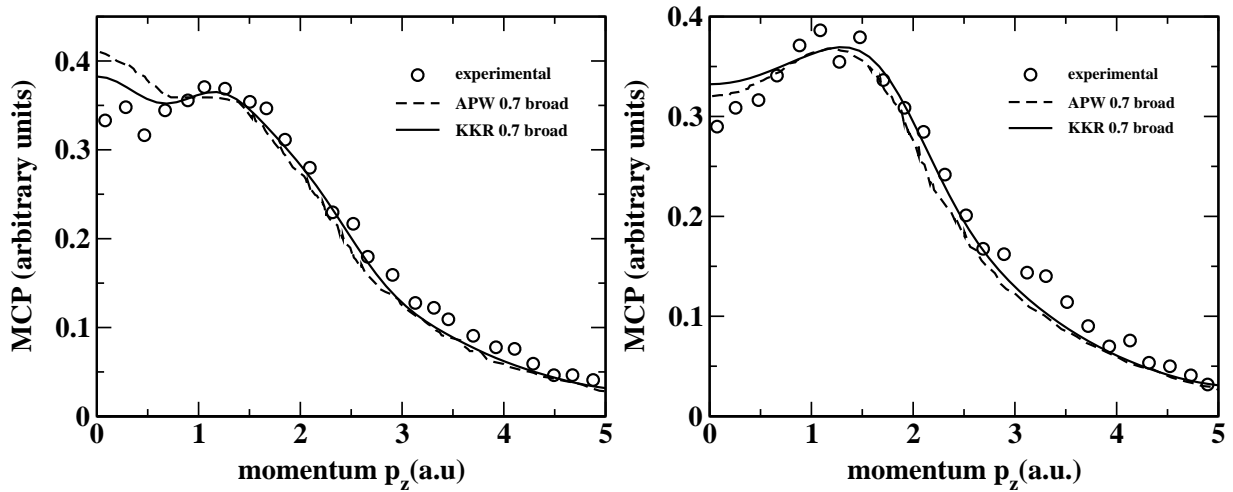


Figure 3.2: Magnetic Compton profiles for Fe along the  $[001]$  direction (left) and  $[110]$  direction (right). Experimental data of Collins et al. (circles), APW calculations of Wakoh et al. (dotted line) and KKR calculations (full line).

directional magnetic profiles in  $bcc$  Fe have been measured by Collins et al. [91] using circularly polarised 60 keV synchrotron radiation with a circular polarisation degree of 0.45 %. The total momentum resolution of the spectrometer is 0.7 atomic units. The profiles have been normalised to an area in the momentum range  $-8$  to  $+8$  a.u. equal with the spin magnetic moment of Fe ( $2.2\mu_B$ ).

The APW data of Wakoh et al. [91] and our SPR-KKR calculations have been convoluted with a Gaussian of FWHM 0.70 a.u. to match the experimental resolution. As can be seen in Figs. 3.2 and 3.4, the KKR Compton profiles are in good agreement with the experimental data and with the APW calculations. The differences appear primarily in the low momentum region, where all the directional profiles are characterized by a central dip. This dip is due to the existence of regions in the momentum space where the momentum density of the

majority band  $n^\uparrow(\vec{p})$  is decreased compared with that of the minority band,  $n^\downarrow(\vec{p})$ .

In general, magnetism arises from more than one orbital in a solid state material. Commonly, the moments are spatially concentrated around the atomic sites, but with polarized band electrons playing a crucial role in the exchange interaction responsible for magnetic ordering. The negative polarization at low momentum is therefore supposed to occur (see [91, 11, 93]) because the s-p bands have opposite polarisation to that of 3d bands. The s-p states are spread out in real space and therefore are more localized in momentum space contributing mainly to the low momentum region near the center of the profile.

We checked this supposition, calculating the s-p and d-states contributions to the magnetic Compton profile for Fe along the [001] direction. According to formula (3.26), we can isolate the different s-p or d-like contributions if we restrict to the appropriate  $\Lambda = (\kappa, \mu)$  for the calculation of the matrix elements  $M_{m_s\Lambda}^{q\alpha}$ . The s-p and d contributions to the MCP are presented in Fig. 3.3. As can be seen, for  $p_z \leq 1.0$  a.u. the negative s-p contribution plays an important role. This result confirms once more the previous theoretical predictions [91, 11, 93].

Due to the broadening, the fine structure of the spectra disappears but a discrepancy is still

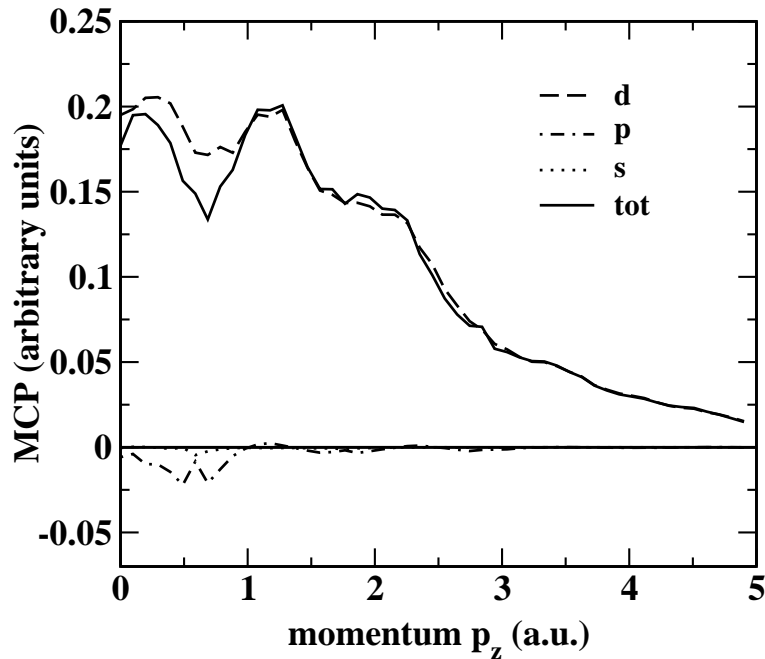


Figure 3.3: The SPR-KKR s, p and d- contribution to the magnetic Compton profile of Fe along the [001] direction.

visible between theory and experiment at low momentum in Fig. 3.2. Both APW and KKR calculations did not reproduce correctly the behaviour for  $p_z < 1$  a.u. in any scattering direction, and because of this we considered the more accurate experimental data of McCarthy along [111] direction [102] with 0.2 a.u. momentum resolution to check the agreement. In addition, the FLAPW results of Kubo and Asano [11] convoluted with a 0.2 a.u. FWHM

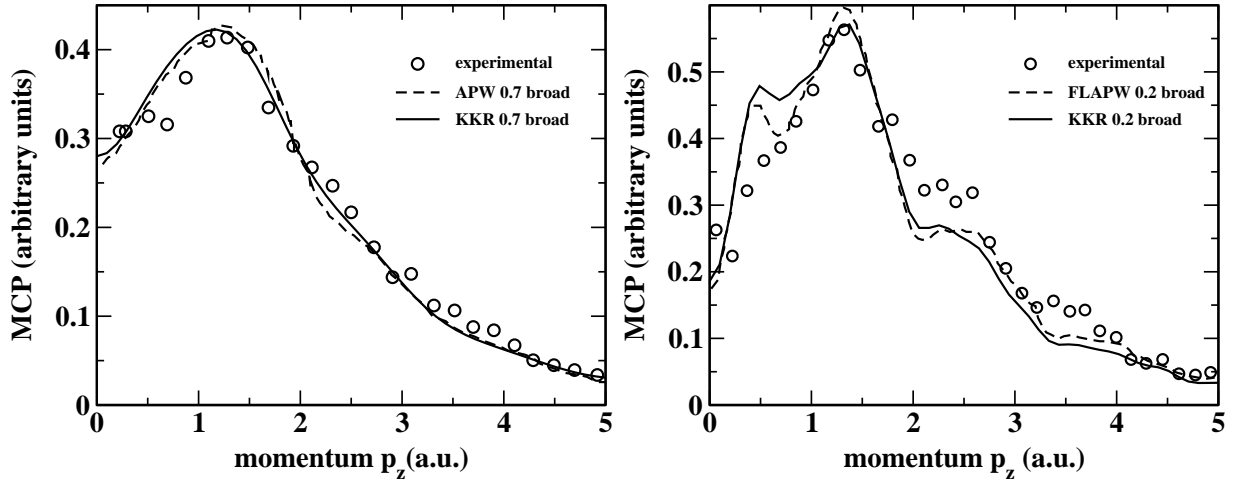


Figure 3.4: The MCP for Fe along the [111] direction. The momentum resolution of experimental data (Cooper et al.) is 0.7 a.u. (left) and 0.2 a.u. (McCarthy) (right). Both KKR and FLAPW calculations have been convoluted with a Gaussian of FWHM equal with the experimental momentum resolution.

parameter have been plotted in Fig. 3.4. Again the discrepancy between theory and experiment is located mostly in the first Brillouin zone and the fully relativistic KKR approach doesn't improve too much the agreement. Both theoretical description predict a local peak at  $p_z \simeq 0.5$  a.u. which is absent in the experimental profile. The fine structure shows some additional peaks at  $p_z \simeq 1.5, 2.5$  and  $3.5$  a.u. which are, according to Cooper et al. [102], the so-called 'umklapp' features of the predicted peak at  $p_z \simeq 0.5$  a.u. in the first Brillouin zone. They point out that for momenta greater than those of the first Brillouin zone boundaries, all features are due to higher moment components of the structure present in the first Brillouin zone. These arise because electrons with a given  $\vec{k}$  contribute to the momentum density at  $\vec{p} = \vec{k} + n\vec{G}$ , where  $\vec{G}$  is the reciprocal lattice vector and  $n = 0, 1, 2, \dots$ . Thus some features in the momentum density propagates according to reciprocal lattice vectors from those in the first zone.

Unfortunately, the system with one of the highest magnetic effect, Fe, is not necessarily the most interesting. The fine structure predicted from calculations on Fe has far less structure than is found for example in the case of Ni which will be discussed in the following. In its ferromagnetic phase, it has a magnetic moment of  $0.61 \mu_B$  to which its spin part contributes  $0.56 \mu_B$ . This net moment is caused by the exchange-splitting of the 3d band and includes, as in the Fe case, a negative polarisation of the s- and p-like electrons.

The most recent MCP experimental profiles with the best resolution (0.43 a.u.) have been measured by Dixon et al. [12] at the high-energy X-Ray beamline (ID15) at the ESRF. Even if powerful sources are available, such a good resolution is difficult to achieve because of the small magnetic moment of Ni. The experimental profiles have been normalized to the spin magnetic moment ( $0.56 \mu_B$ ). Our calculations and other theoretical profiles presented here

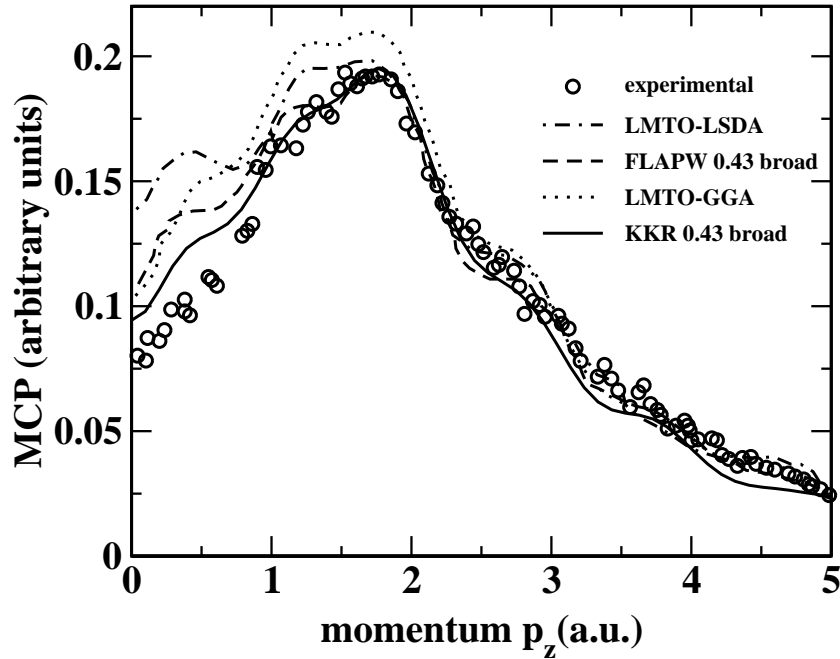


Figure 3.5: The MCP profiles of Ni along the [001] direction. The FLAPW calculations of Kubo and Asano [11], the LMTO-LSDA/GGA calculations of Dixon et al. and the KKR calculations (full line) have been convoluted with a Gaussian of 0.43 a.u. FWHM., according to the experimental resolution of Dixon et al.'s data [12].

have not been normalized to this value. The scaling of the KKR profile was adjusted to give the best fit of the experimental profile.

In Fig. (3.5) we present our KKR magnetic Compton profile along the [001] direction, together with the experimental data of Dixon et al., the FLAPW calculations of Kubo and Asano [11] and LMTO-LSDA/GGA calculations of Dixon et al. [12]. The KKR, FLAPW and LMTO calculated profiles have been broadened using a Gaussian with FWHM of 0.43 a.u., according to the experimental resolution.

All the theoretical results fit the data at high momenta, but they all predict spin moments which are too large. At low momenta, all theoretical MCP are predicting a local peak at  $\simeq 0.5$  a.u., which is absent in the experimental spectra. This is a common failure of the theories thought to be most likely due to a failure of the description of the exchange and correlation effects [102, 103]. This result is similar to Fe: although the magnetic profile has less structure, the major discrepancy between theory and experiment is again in the first Brillouin zone.

Due to the lower resolutions, the 'umklapp' features are not very prominent at higher momenta, but still visible at  $\simeq 1.2, 1.7, 2.7$  and  $3.7$  a.u.. While LMTO overestimates the 1.2 and 1.7 a.u. peaks, the features at 2.7 and 3.7 a.u. are good reproduced by all calculations.

Our calculations gives the best fit along the [001] scattering direction, but this does not hold for all geometries, as can be seen in Fig. 3.6. Because the LMTO calculations are far from the

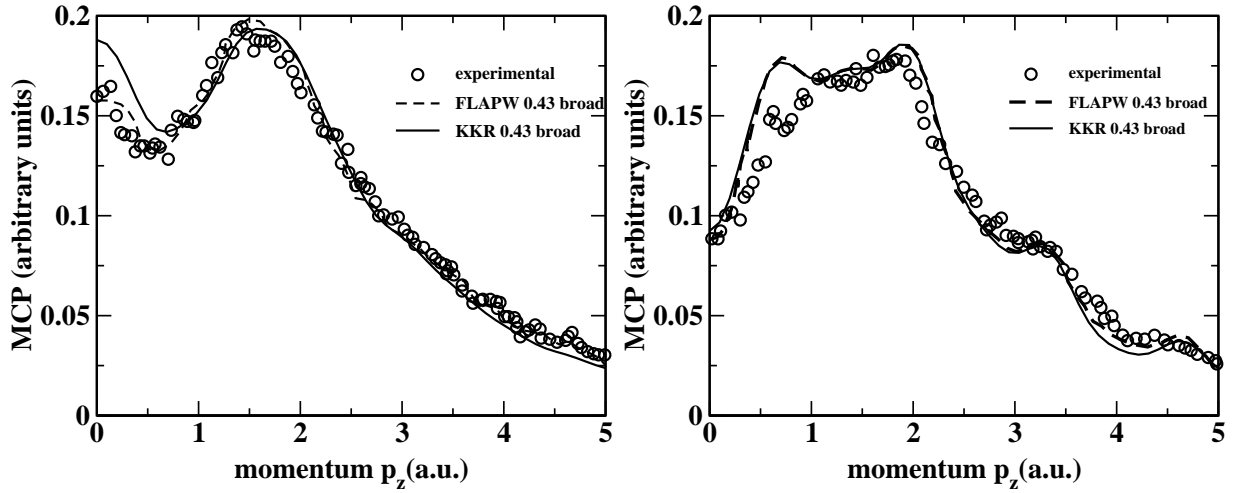


Figure 3.6: The MCP profile of Ni along [111] direction (left) and [110] direction (right). The FLAPW calculations of Kubo and Asano [11] and the KKR calculations (full line) have been convoluted with a Gaussian of 0.43 a.u. FWHM to fit the experimental data of Dixon et al. [12].

experiment, they have not been reproduced in this figure.

Along the [110] direction, the KKR and FLAPW results are almost identical, both predict a peak at  $\simeq 0.7$  a.u. which is absent in the experimental data but reproduce well the features at  $\simeq 2.0, 3.3$  and  $4.6$  a.u.. Also, the fit at 0 a.u. is quite satisfying for both calculations.

Along the [111] direction, the peak at  $p_z = 0$  a.u. is overestimated by our calculations and better reproduced by the FLAPW results. Also, the dip at  $\simeq 0.6$  a.u. in the experimental data, better reproduced by FLAPW, is shifted by our KKR calculations at  $\simeq 0.8$  a.u..

In conclusion, our KKR fully relativistic calculations of the MCP for pure metallic systems Fe and Ni are in reasonable agreement with the experimental data and with other non-relativistic theoretical results. One should note that relativistic effects are small for these systems and a noteworthy improvement of the agreement with experimental data by fully relativistic calculations is difficult to see.

### 3.4.1 Three-dimensional spin momentum density

The first three-dimensional spin momentum density was reconstructed for Fe from 14 separate magnetic Compton profiles by Tanaka et al. [13] using a Fourier transform technique. The surface perpendicular to the [001] direction crossing the  $\Gamma$  point has a deep minimum around the  $\Gamma$  point and four peaks at  $p_x = \pm 1.8$  a.u. and  $p_y = \pm 1.8$  a.u.. The experimental two-dimensional projection normal to the [001] direction of the spin momentum density is correctly reproduced by the FLAPW band calculations of Kubo [13]. Because the full three-

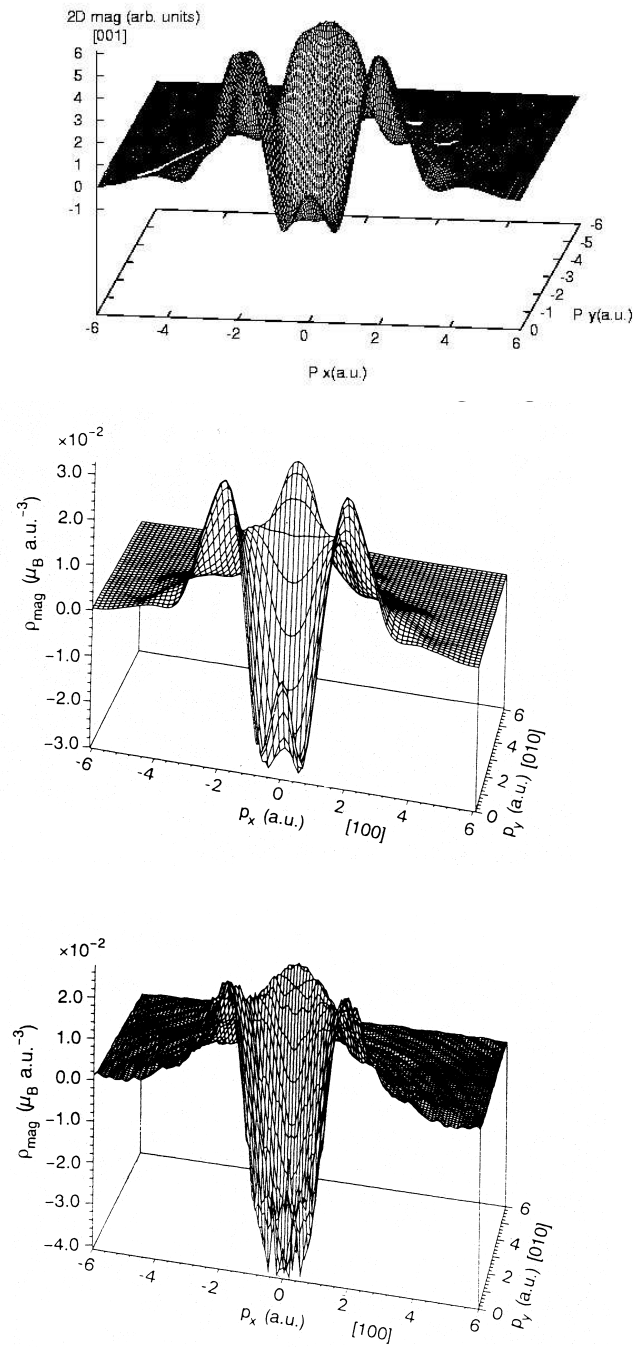


Figure 3.7: A two-dimensional projection of the spin momentum density: KKR calculations (up), FLAPW calculations [13] (middle) and experiment (down) [13].

dimensional momentum density offers an excellent opportunity to test theoretical models, this was the next application for our KKR method. The result of our calculations, namely the two-dimensional projection normal to the [001] direction (convoluted with the experimental resolution expressed by a Gaussian of FWHM 0.76 a.u.) is shown in the Fig. 3.7. The agreement between the KKR two-dimensional projection and experimental, respectively FLAPW calculated two dimensional projection of the spin momentum density is good, demonstrating the reliability of MCP calculation using the KKR method. This encouraged us to develop our code in order to describe momentum densities of more complex compounds and in disordered alloys, which will be treated in the next section.

## 3.5 Application to disordered alloys

### 3.5.1 Compton anisotropic profiles in $\text{Ni}_x\text{Co}_{1-x}$ alloy

The Compton profiles along the [001], [110] and [111] directions for  $\text{Ni}_{0.75}\text{Co}_{0.25}$  disordered alloy were calculated using the KKR method within the CPA and the atomic sphere approximation. The exchange-correlation part of the potential was described, as before, in the local spin-density (LSDA) approximation. The *fcc* structure was used with the experimental lattice parameters of 6.6694 for the alloy and 6.6518 atomic units [104] for pure nickel. The parameters for the energy and momentum integration given in the previous section were used.

The motivation of considering this alloy was the idea that the electronic structure of  $\text{Ni}_{0.75}\text{Co}_{0.25}$  and of pure Ni may differ substantially. If one starts to add Co in the Ni-system, the average moment of the alloy will increase because of the open d-shell of Co. Also, the number of electrons in the unit cell will decrease because Co has less electrons in the d-shell. The KKR band structure calculations show that each Ni atom in the alloy carries a spin moment of  $0.59 \mu_B$ , while the Co atoms carried a spin moment of  $1.62 \mu_B$  giving a net moment of  $0.85 \mu_B$  per formula unit. The spin and orbital magnetic moment was  $0.63 \mu_B$  on Ni atom and  $1.69 \mu_B$  on Co atom. These values are in agreement with the KKR-CPA computed values of Bansil et al. [14] ( $0.64 \mu_B$  on Ni atom and  $1.63 \mu_B$  on Co atom).

Because the results for the MCP in Ni and  $\text{Ni}_{0.75}\text{Co}_{0.25}$  alloy are quite similar, it is interesting to analyse the fine structure of the spectra. For this purpose, the theoretical charge (spin up + spin down) profiles for  $\text{Ni}_{0.75}\text{Co}_{0.25}$  along the high-symmetry were subtracted two by two, in order to obtain the so-called anisotropic profiles. In Fig. 3.8 the  $\Delta J_{[110]-[001]}$  and  $\Delta J_{[111]-[110]}$  anisotropic profiles are presented, together with the experimental data and the KKR-CPA calculations of Bansil et al. [14]. The experimental data were produced using a  $^{137}\text{Cs}$   $\gamma$ -ray source within a total momentum resolution of 0.4 atomic units.

The theoretical profiles were convoluted with a Gaussian of FWHM 0.4 a.u. in order to simulate the experimental resolution and thus to allow a direct comparison with the experiment.

As can be seen, our calculations are consistent with the experimental data and with the KKR-CPA calculations of Bansil et al.. The shape of the oscillations are similar, but for  $p_z > 3$

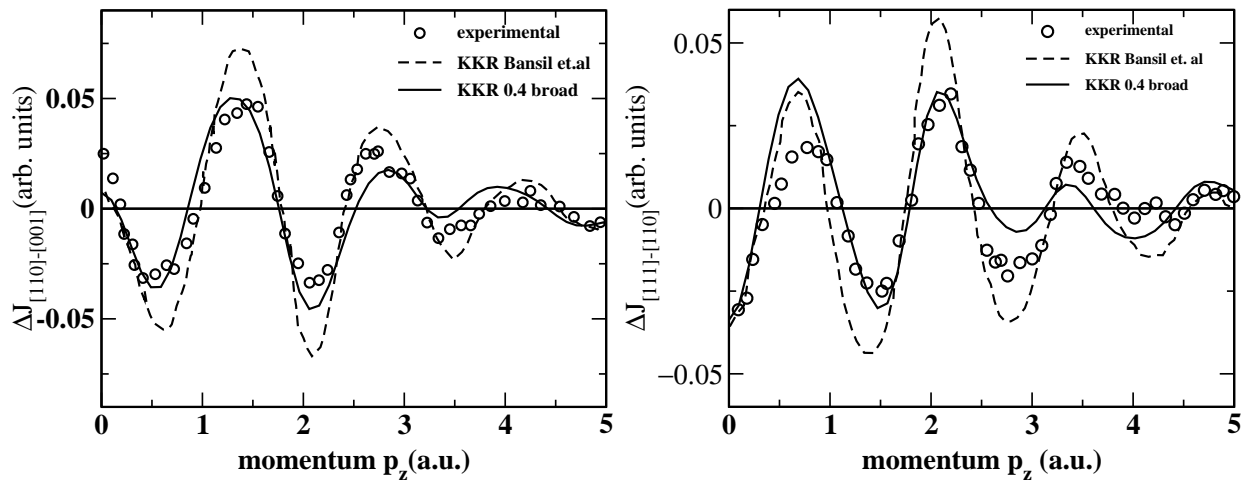


Figure 3.8: The anisotropic Compton profiles of  $\text{Ni}_{0.75}\text{Co}_{0.25}$ . Our SPR-KKR calculations (full line) are compared with experimental data and KKR calculations of Bansil et al. [14].

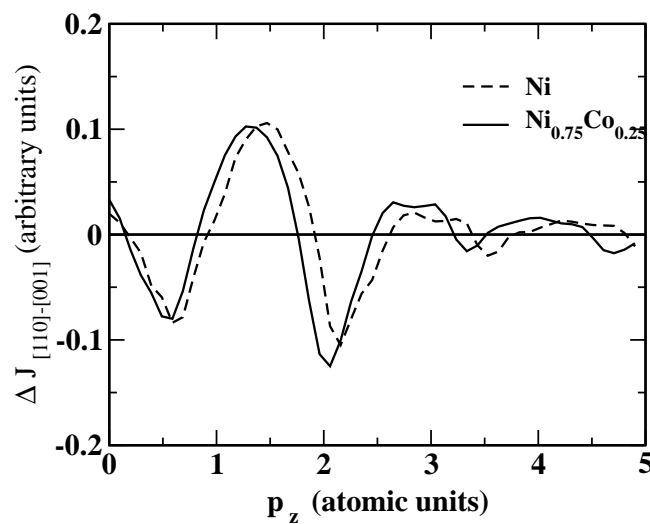


Figure 3.9: The anisotropic Compton [110]-[001] profiles of  $\text{Ni}_{0.75}\text{Co}_{0.25}$  and pure Ni obtained by the SPR-KKR calculations.



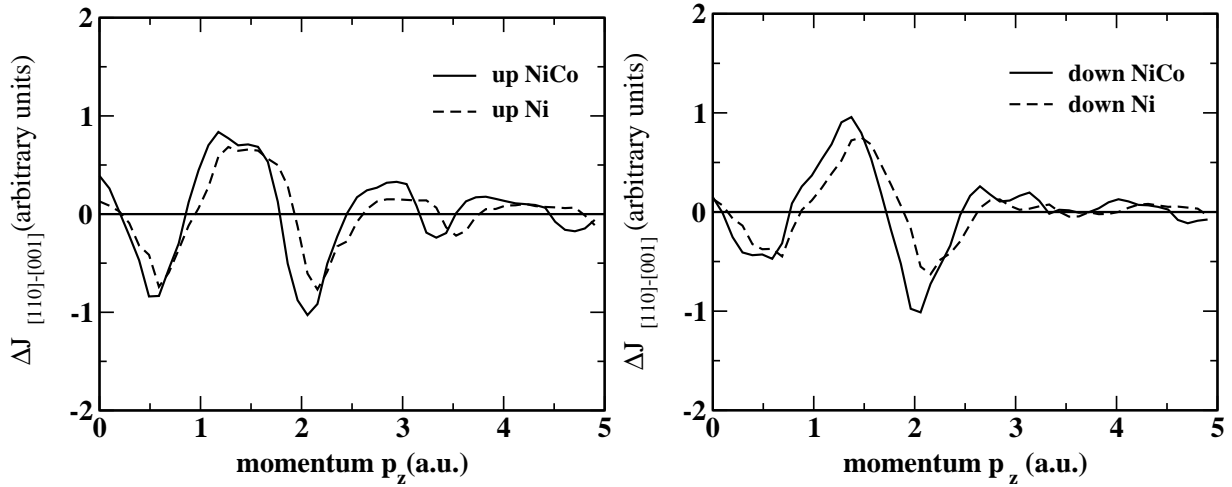


Figure 3.10: The anisotropic [110]-[001] spin-up (left) and spin-down (right) profiles of  $\text{Ni}_{0.75}\text{Co}_{0.25}$  and pure Ni obtained by the SPR-KKR.

a.u. our calculations doesn't reproduce correctly the position of the maxima and minima. A small shift towards smaller momenta is visible in our [110]-[001] calculated profile, the maximum at  $\simeq 4.2$  a.u. in the experimental spectra is given by our calculations at  $\simeq 4.0$  a.u.. Also, for  $p_z > 3$  a.u. the amplitude of the minimum at  $\simeq 3.5$  a.u. is underestimated.

In the [111]-[110] anisotropic profile, our calculations describe the minima and maxima positions better, but the amplitude of the spectrum is overestimated at  $p_z < 2.5$  a.u. and underestimated for higher momenta. Also, the shift towards smaller momenta is still present in this spectra for  $p_z > 3$  a.u.. Both theoretical calculations show a deviation from the experimental spectra at  $p_z = 0$  in the [110]-[001] profile. There are differences also between our KKR calculations and those of Bansil et al., supposed to appear due to the different exchange-correlation parametrizations within the LSDA. Nevertheless, the agreement between both calculation and experiment is reasonable. Our fully relativistic KKR calculation doesn't improve substantially the agreement with experiment because the relativistic effects in the 3d transition metals are small. The achieved agreement allows us to use our calculations for Ni and  $\text{Ni}_{0.75}\text{Co}_{0.25}$  alloy to investigate possible changes in the anisotropic profile due to alloying.

The anisotropic profiles for Ni and  $\text{Ni}_{0.75}\text{Co}_{0.25}$  alloy are represented in Figs. 3.9 and 3.10. As can be seen, the similarity of the profiles makes a identification of Co specific features very difficult. According to our calculations, the similarity remains when the spin up, respectively spin-down anisotropic profiles are discussed, so we cannot conclude that the spectral changes in the alloy are limited mainly to the minority-spin states, as it was concluded by Bansil et al. [14]. The slight shift towards smaller momenta of the alloy's spectra may have several reasons. A study of the behaviour of this shift with respect to the alloy's concentration or exchange-correlation parametrization would be required before one may allow for a reasonable conclusion.

### 3.5.2 Magnetic Compton profiles in Fe<sub>3</sub>Pt Invar alloy and ordered compound

In 1897 Guillaume discovered that face-centred cubic alloys of Fe and Ni with Ni concentration around 35 % exhibit anomalously low (almost zero) thermal expansion over a wide temperature range. This effect, known as the Invar effect, has since been found in various ordered and random alloys and even in amorphous materials. One of those systems is Fe<sub>1-x</sub>Pt<sub>x</sub>, which exhibits the invar effect around the ordered crystallographic phase Fe<sub>3</sub>Pt. It was found that also other physical properties of invar systems, such as the atomic volume, elastic modulus, heat capacity, magnetization and Curie (Néel) temperature show an anomalous behaviour [105].

There is much theoretical work undertaken on the invar problem, but the mechanism responsible for it is still subject of debates. The first theoretical model, proposed by Weiss [106], postulates that  $\gamma$ -Fe (*fcc*) has two different nearly-degenerate magnetic states: a high spin (HS) state with a moment of  $\sim 2.8 \mu_B/\text{atom}$  and a larger atomic volume and a low spin (LS) state with a moment of  $\sim 0.5 \mu_B/\text{atom}$  and small atomic volume. The relative populations of these states depends upon the system temperature in such a way as to create a large volume magnetostriction that opposes the thermal expansion of the lattice.

Until now, there has not been an experimental evidence that conclusively supports the two state model. The neutron scattering experiments [107] studying the temperature dependence of the form factor shows no evidence for a charge transfer in the material. Also, the photoemission data [108] are not conclusive concerning a possible charge transfer.

Recent theoretical studies [105] suggest that the invar ground state is a non-collinear-one, but the experiment [109] doesn't prove this hypothesis and the invar compound is thought to have a collinear magnetic structure.

The first studies of magnetic Compton profiles on Fe<sub>3</sub>Pt compound were done by Srajer et al. [15]. They determined the [001] MCP profile experimentally at 305 K and 490 K and calculated the profile using the FLAPW method with a LSDA potential, showing that the charge transfer between HS and LS states may exist. Their MCP studies were continued by Taylor et al. [1] and Major et al. [110], who measured the [110] and [111] profiles and found no temperature-dependence of the profile shapes. In addition, the LMTO and KKR calculations together with the experimental data show that disorder doesn't play a major role concerning the profile's shape.

The FLAPW-GGA calculations of Wakoh et al. [16] seems to fit the experimental data better than the LMTO calculations, although they didn't take the disorder into account.

Our work on ordered and disordered Fe<sub>3</sub>Pt continue the combined efforts to determine the shape of the MCP profiles and to find a hint to elucidate the invar mechanism.

Self-consistent potentials of ferromagnetic Fe<sub>3</sub>Pt were determined by the SPR-KKR within the atomic sphere approximation (ASA). The Coherent Potential Approximation (CPA) was used for the treatment of the disordered alloy. The Cu<sub>3</sub>Au structure was used for the ordered compound with a lattice parameter  $a = 7.088$  a.u.. The same lattice parameter was kept for the disordered *fcc*-Fe<sub>0.75</sub>Pt<sub>0.25</sub> alloy. With these parameters, each Fe atom carried a

spin moment of  $2.59\mu_B$  while the spin moment induced on Pt was  $0.27\mu_B$  per atom in the ordered compound. The net magnetic moment was  $2.085\mu_B/\text{FU}$ , while the spin contribu-

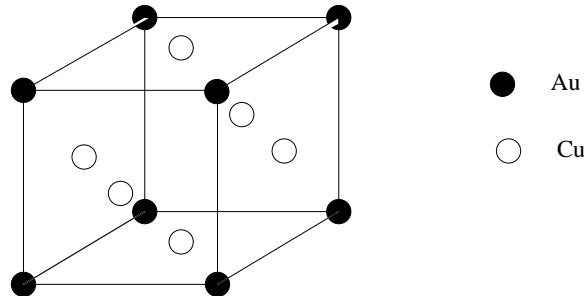


Figure 3.11: The  $\text{Cu}_3\text{Au}$  structure.

	Ordered sample	Disordered sample
15K MCS experiment [1]	$1.85 \pm 0.02$	$1.64 \pm 0.02$
300K MCS experiment [1]	$1.54 \pm 0.02$	$1.47 \pm 0.02$
300K VSM experiment [1]	1.61	
KKR-CPA(Major) [110]	2.136	2.156
SPR-KKR(present work)	2.009	2.132
LMTO [1]	2.096	
FLAPW [16]	2.169	

Table 3.1: Spin magnetic moments per formula unit in  $\text{Fe}_3\text{Pt}$  compound. Results are quoted as  $\mu_B$  per formula unit of  $\text{Fe}_{0.75}\text{Pt}_{0.25}$ . The MCS (magnetic Compton scattering) and VSM (vibrating sample magnetometer) experimental data stem from Taylor et al. [1].

tion to the total magnetic moment was  $2.009\mu_B/\text{FU}$ . Here FU means the formula unit, taken as  $\text{Fe}_{0.75}\text{Pt}_{0.25}$  in order to facilitate the comparison with the disordered alloy.

For the disordered alloy, the Fe spin moment was determined to be  $2.76\mu_B$  per atom, while the induced spin moment on the Pt atom was determined to be  $0.244\mu_B$ . This yields a net magnetic moment of  $2.202\mu_B/\text{FU}$  with a spin contribution of  $2.132\mu_B/\text{FU}$ .

The comparison with the experimental data of Taylor et al. [1] and with the results of other theoretical calculations is done in Tables 3.1 and 3.2. As can be seen, the different methods of calculation produce similar results, even if the lattice parameter used is slightly different. The calculations do not describe correctly the magnetic moments (Taylor et al. [1]). In particular, the spin magnetic moments are overestimated by all methods of calculation. As one notes, the spin magnetic moment on Fe at 15K ( $2.46\mu_B$ ) is higher than in pure Fe ( $\sim 2.1\mu_B$ ).

	Ordered sample	Disordered sample
15K MCS experiment [1]	2.46	2.18
300K MCS experiment[1]	2.056	1.97
KKR-CPA(Major) [110]	2.73	2.79
SPR-KKR(present work)	2.59	2.76
LMTO [1]	2.62	
FLAPW [16]	2.77	

Table 3.2: Spin magnetic moments per Fe atom in  $\text{Fe}_3\text{Pt}$  compound.

A possible explanation for the low temperature (15K) magnetic moment on Fe to be higher than that one may expect in pure Fe is a martensitic phase transition [111, 112] producing a *bct* distortion of the lattice below  $\approx 100$  K.

The magnetic Compton profile resolved along the [001] direction for ordered  $\text{Fe}_3\text{Pt}$  and

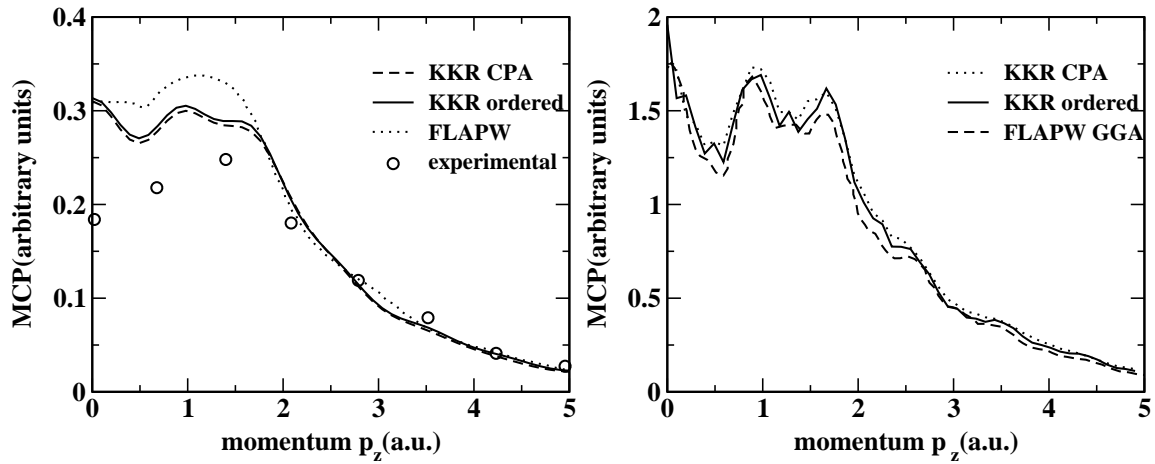


Figure 3.12: Left: The [001] directional MCP of  $\text{Fe}_3\text{Pt}$ . The experimental profile was measured at 305 K (Srajer et al. [15]) and normalized to the corresponding total spin moment. The SPR-KKR and FLAPW (Srajer et al. [15]) profiles have been broadened with a Gaussian of 0.8 a.u. FWHM. Right: The unbrodened [001] directional MCP of  $\text{Fe}_3\text{Pt}$  derived from SPR-KKR and FLAPW GGA (Wakoh et al. [16]) calculations, respectively.

$\text{Fe}_{0.75}\text{Pt}_{0.25}$  disordered alloy is shown in Fig. 3.12 (left). Our calculations are compared with experimental data of Srajer et al. [15] measured at 305 K within a momentum resolution of 0.8 a.u.. The theoretical profiles have been broadened with a Gaussian of FWHM corresponding to the experimental momentum resolution. The values of the experimental magnetic moment have been determined from the area of the measured profile, normalized to a

Fe standard with a known moment. The results of the FLAPW calculations of Srajer et al., with the appropriate broadening, have also been represented in the figure.

As can be seen, the broadening parameter that should be used to allow a comparison with the experiment smears out the fine structure of the spectra. Because of this, the KKR profiles for the ordered structure and the disordered alloy almost coincide.

Our calculation doesn't reproduce the behaviour at  $p_z \leq 0.5$  a.u. present in Srajer's FLAPW calculations. A dip around  $p_z = 0.5$  a.u. in the KKR calculation can be seen but it doesn't extend through  $p_z = 0$  a.u.. This is the main difference between our SPR-KKR calculations and the FLAPW calculations of Srajer et al.. Because experimental data with a better accuracy along [001] direction are not available, we compared our unbroadened spectra with the FLAPW calculations of Wakoh et al. [16].

As can be seen in Fig. 3.12 (right), the agreement between KKR and FLAPW-GGA [16] calculations is good. A dip at  $p_z = 0$  a.u. cannot be seen in any of the theoretical spectra. As a consequence, the dip at  $p_z \simeq 0$  a.u. in Srajer's FLAPW profile is questionable. The difference between theory and experiment should be ascribed to shortcomings of LSDA to deal with electron correlation.

As it has been shown before, the d-like and s-p like contributions to the MCP can be iso-

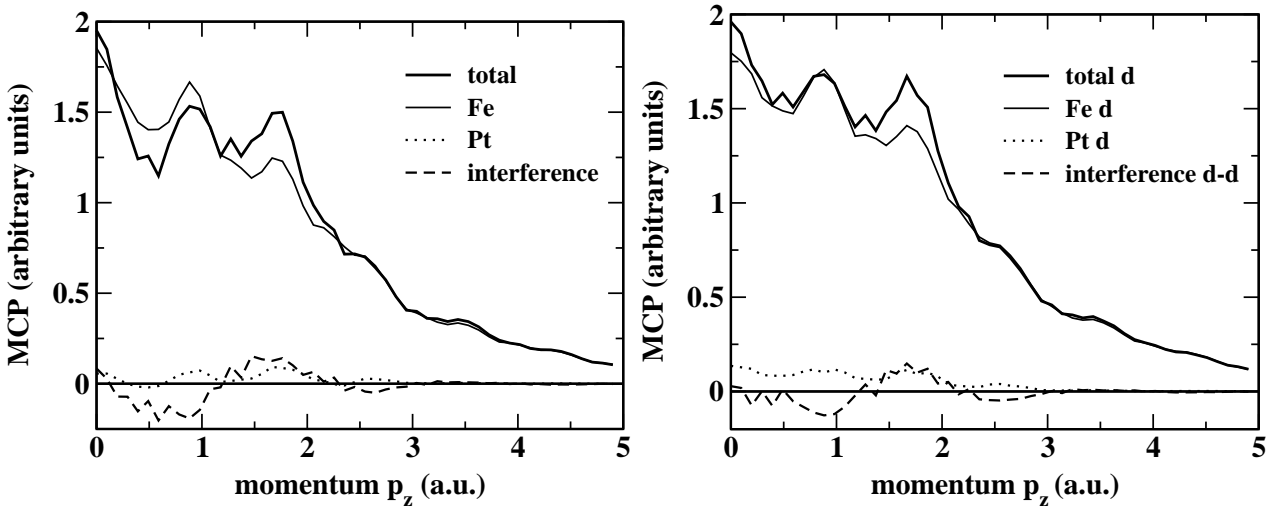


Figure 3.13: The SPR-KKR MCP along the [001] direction of  $\text{Fe}_3\text{Pt}$  decomposed into atomic type contributions (left). The d orbitals contributions at the MCP along the [001] direction of  $\text{Fe}_3\text{Pt}$ , decomposed into atomic type contributions (right), by SPR-KKR calculations.

lated by a corresponding setting of the quantum number  $\Lambda = (\kappa, \mu)$  in the calculation of the matrix elements  $M_{m_s, \Lambda}^{q\alpha}$  from Eq. (3.26). Also, a further decomposition of the MCP is possible in our SPR-KKR formalism. Considering the formula (3.26) of the Green's function, the MCP can be written as a sum over the atomic types, plus an additional so-called interference term which takes into account the contribution of pairs of atoms sitting on different sites.

The previous described decomposition has been performed for the MCP of ordered  $\text{Fe}_3\text{Pt}$  system. The decomposed spectra are presented in Fig. 3.13. On the left hand side one can see the total spectra decomposed into Fe and Pt contributions, plus the interference term. On the right hand side, the decomposition on the atomic types has been done for the d-like MCP of ordered  $\text{Fe}_3\text{Pt}$  system.

As can be seen in Fig. 3.13, the most significant contribution to the MCP comes from Fe. This result is expected, if one takes into account its spin magnetic moment (see Tables 3.2 and 3.1) which is responsible for the magnetic Compton effect. The very small spin moment on Pt is reflected by its minor contribution to the MCP. Most significant for the MCP shape is the oscillating interference term.

Comparing the d-like MCP and the total MCP of  $\text{Fe}_3\text{Pt}$  along the [001] direction, we can see that for  $p_z > 1$  a.u. there aren't major difference between the various spectras. This means that the major contribution on the MCP for  $p_z > 1$  a.u. comes from d orbitals of Fe and Pt.

The differences between d-like and total MCP spectras are visible at  $p_z \sim 0.7$  a.u., where the d-like dip of the MCP spectra is less pronounced. Responsible for this difference seems to be the negative polarization of s-p orbitals, as in the case of pure Fe, reflected in lowering of the Fe (total) profile compared with Fe(d) at  $p_z < 1$  a.u.. Also, the interference term gives a wider negative contribution at  $p_z < 1$  a.u. in the total profile compared with the d-d interference term. These combined influences seems to be decisive for the shape of the MCP of  $\text{Fe}_3\text{Pt}$ .

To allow for a more complete picture over the one dimensional projection of the spin momentum distribution in  $\text{Fe}_3\text{Pt}$  we performed calculations of the MCP along the [111] and [110] directions for the ordered system and the disordered alloy.

The experimental data of Taylor et al. [1] with a momentum resolution of 0.4 a.u. at 300K, normalized to an area of  $1.85 \mu_B$  have been used for comparison. The experiment performed on a single crystal and on chemically disordered sample, respectively, showed that the MCP is not sensitive to the degree of order in the sample. This result is in agreement with our calculations along the [001] direction which seems not to be affected by disorder.

The MCP for ordered  $\text{Fe}_3\text{Pt}$  is presented in Fig. 3.14. The FLAPW calculations of Wakoh et al. [16] and LMTO calculations of Major et al. [1] with the 0.4. a.u. FWHM gaussian parameter have been used for comparison.

The calculated MCP is in good overall agreement with the experimental profile, especially the high momentum components of the experimental profile are well reproduced by theory. As can be seen, our KKR calculations give a fit comparable with the FLAPW calculations, whereas the LMTO-calculated MCP is too large for  $p_z \leq 2$  a.u. along both crystallographic directions.

In Fig. 3.15 our KKR-CPA magnetic Compton profiles for disordered  $\text{Fe}_{0.75}\text{Pt}_{0.25}$  alloy are presented, together with the KKR-CPA calculations of Major et al. and experimental data [1]. The value of 0.4 FWHM for the gaussian broadening has been used for both KKR-CPA calculations, in accordance with the experimental momentum resolution.

The calculated MCPs are again in good overall agreement with that measured experimentally. Our fully-relativistic version of KKR-CPA leads to a more satisfying agreement with the experimental data in the momentum region below 2 a.u.. However, one should note that

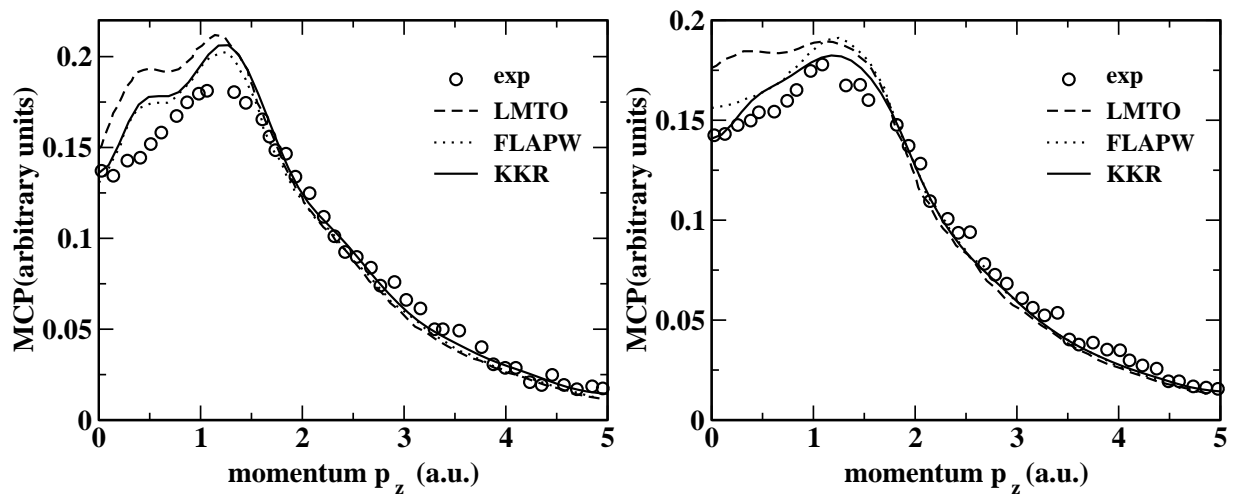


Figure 3.14: The [110] (left) and [111] (right) directional MCP of  $\text{Fe}_3\text{Pt}$ . The SPR-KKR profile (full line), the LMTO [1] and FLAPW [16] calculations are compared with experimental data [1].

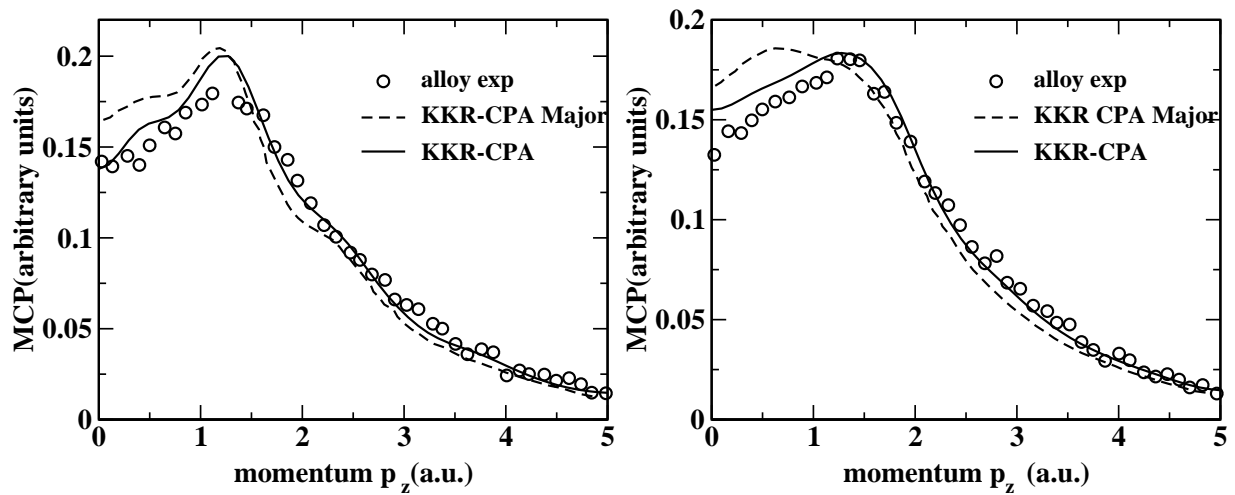


Figure 3.15: The [110] (left) and [111] (right) directional MCP for disordered  $\text{Fe}_{0.75}\text{Pt}_{0.25}$  alloy. The SPR-KKR calculations (full line) are compared with KKR-CPA calculations of Major et al. and experimental data [1]. Both KKR-CPA calculations have been broadened with a Gaussian of 0.4. a.u. FWHM, in accordance with the experimental momentum resolution.

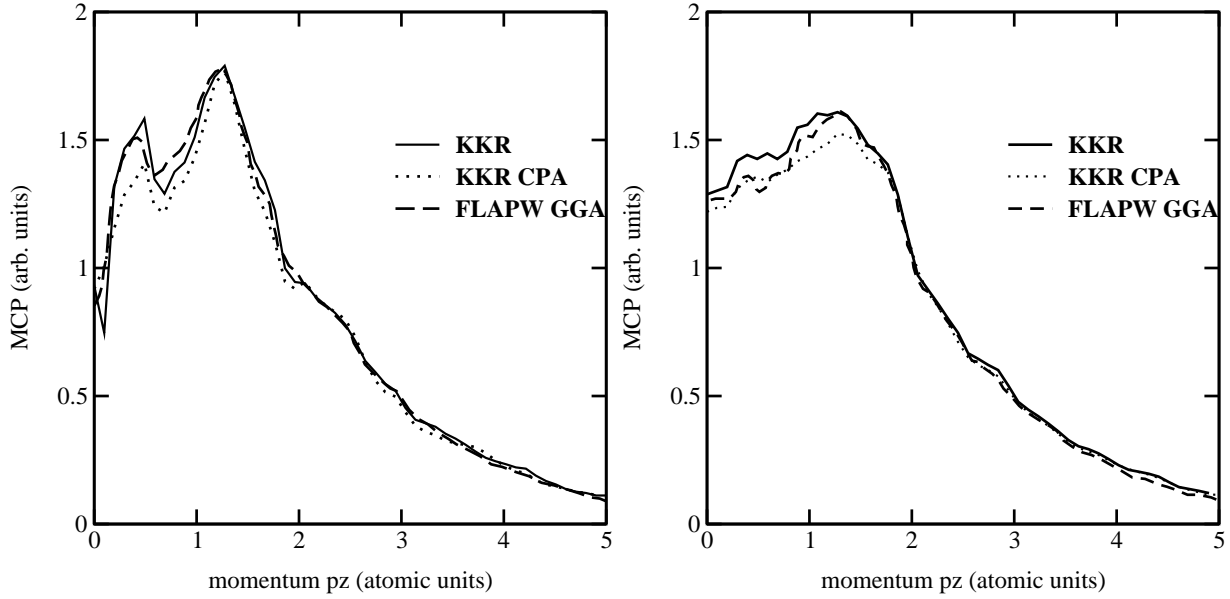


Figure 3.16: The unbroadered [110] (left) and [111] (right) directional MCP of  $\text{Fe}_3\text{Pt}$ . The SRR-KKR calculations for ordered and disordered compounds, respectively FLAPW-GGA calculations (Wakoh et al. [16]) are presented.

the calculated spin moments for each KKR-CPA version are very similar.

As the experimental measurements demonstrate [1], the directional magnetic Compton profiles for ordered and disordered compounds are almost identical, within the experimental resolution. We checked if from a theoretical point of view, one should notice some difference between the MCP for ordered and disordered sample. We investigated the disorder effect on the MCP along the [110] and the [111] direction using the KKR and CPA-KKR code and the same lattice parameters for  $\text{Cu}_3\text{Au}$  and *fcc* structure. The result can be seen in Fig. 3.16. The difference in the [110] profiles between the KKR and KKR-CPA appear at  $p_z \leq 2$  a.u., where the dip at  $\sim 0.7$  a.u. and the peak at  $\sim 0.5$  a.u. are lower for a disordered sample. This means that the negative polarisation in this momentum region is more pronounced for the ordered sample, supposing that between experimental spectra for ordered and disordered sample the difference is negligible.

For the [111] direction MCP, the fine structure of the spectra is reduced, so the information we can extract comparing the KKR, KKR-CPA and FLAPW spectra is limited. We notice the existence of a small hump around 0.7 - 0.9 a.u., present in the KKR spectra for the ordered system, which cannot be seen in the other spectra.

The very good overall agreement between KKR and FLAPW spectra must be emphasized.



## 3.6 Magnetic Compton profiles for rare earth systems

A fully relativistic study of the magnetic Compton profiles for the rare earth systems Gd and Y-Gd alloy is presented in this section. Because the relativistic effects cannot be neglected for the rare earth systems, this approach is expected to get a more appropriate description of the momentum distribution compared with the calculations which have been published until now [3].

There are several studies [113, 114, 115] about the applicability of the local spin-density approximation (LSDA) in the ground-state description of 4f-electronic systems. Because the LSDA will overestimate the extent of the 4f itineracy leading to an overestimation of the strength of the 4f bonding, the LSDA may produce poor agreement with experiment [116]. The investigation of Duffy et al. [3] concerning the validity of LSDA within the LMTO method for the description of the one-dimensional momentum densities of Gd showed very similar profile shapes for the LMTO-LSDA and LMTO-GGA calculations. Kubo and Asano calculated the MCP of Gd by the full-potential linear augmented-plane-wave (FLAPW) method on the basis of LSDA. They found a good agreement between their calculations and the experimental data of Sakai et al. [117], concluding that the spin polarization of the conduction electrons is satisfactorily reproduced by the band structure model based on the LSDA. Taking into account these studies, it is expected that the results of our calculations using LSDA will not suffer due to an inadequate treatment of exchange and correlation.

### 3.6.1 Magnetic Compton profile of Gd

Compared with the other rare earth systems, the magnetic order in Gd is relatively simple. Gd is a ferromagnetic system with a Curie-temperature of  $T_c = 293$  K. The magnetic moment lies parallel to the  $c$ -axis and remains so down to 232 K. At lower temperature the moment moves away from the  $c$ -axis, the maximum deviation of about  $65^\circ$  being achieved at 180 K, with the moments canted in a random cone structure.

The magnetic properties of the system originate predominantly from the exchange field of the localized 4f electrons, rather than that of the conduction electrons, as in the case of ferromagnetic transition metals. Due to the high localization of the 4f electrons, the exchange

Calculation method	Spin magnetic moment ( $\mu_B$ )
LMTO-LSDA [3]	7.65
LMTO-GGA [3]	7.52
FLAPW-LSDA [2]	7.70
KKR	7.53

Table 3.3: The theoretical spin magnetic moments in Gd . The SPR-KKR calculated magnetic moments are compared with FLAPW results of Kubo and Asano [2] respectively with LMTO magnetic moments of Duffy et al. [3].

interaction driving the magnetism is supposed to be indirectly mediated via the conduction electrons.

Before discussing the MCP results, it is interesting to examine the ground-state magnetic moments derived from self-consistent calculations. The magnetic moment comprises  $7 \mu_B$  from the half-filled 4f shell, plus an induced conduction electron moment. The experimental magnetic moment determined at 4.2 K is  $\mu_{total} = 7.62 \pm 0.01 \mu_B$  [118]. The spin magnetic moments obtained by different calculation methods are summarized in Table 3.3.

Many of the early MCP measurements were made at nitrogen temperature, but a higher

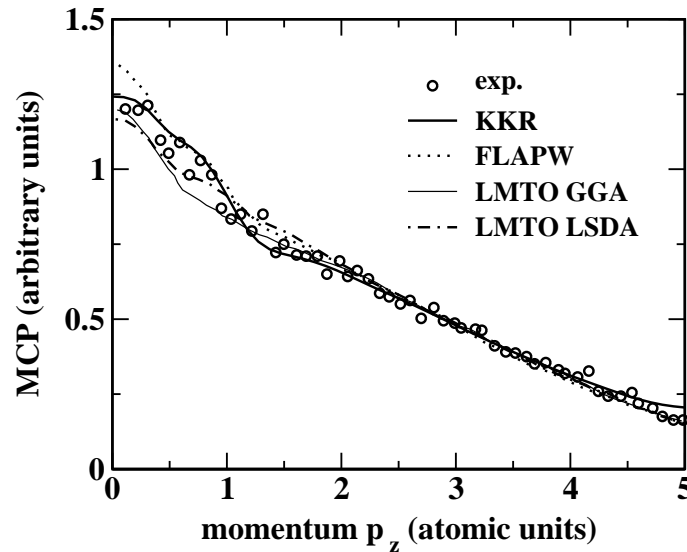


Figure 3.17: Magnetic Compton profile of Gd. Theoretical calculations are broadened with a Gaussian of FWHM 0.44 a.u.. The fully relativistic SPR-KKR profiles are compared with FLAPW [2], LMTO [3] MCP and experimental data [3].

temperature is needed to avoid the phase where the c-axis moments are canted. The experimental Compton profiles presented here were measured at ID15 X-Ray beam line at the ESRF. The temperature of the sample was  $235 \pm 2$  K, such that the moments of the sample are still parallel to the c-axis. The momentum resolution for the measured profiles was 0.44 atomic units.

The results of the previous FLAPW and LMTO calculations [3, 2] showed that (a) FLAPW theory doesn't produce any improvement compared to the LMTO calculation, in contrast to the situation in Ni and (b) GGA doesn't improve the results of LSDA, maybe due to the localized nature of the magnetisation.

The results of our KKR calculations are presented in Fig. 3.17, together with the results of LMTO and FLAPW calculations. All theoretical predictions were convoluted with the (Gaussian) experimental resolution function with width 0.44 atomic units. The experimental data were normalized, such that the area under the profile is equal with the spin magnetic moment determined by experiment [3]. After broadening, the calculated SPR-KKR

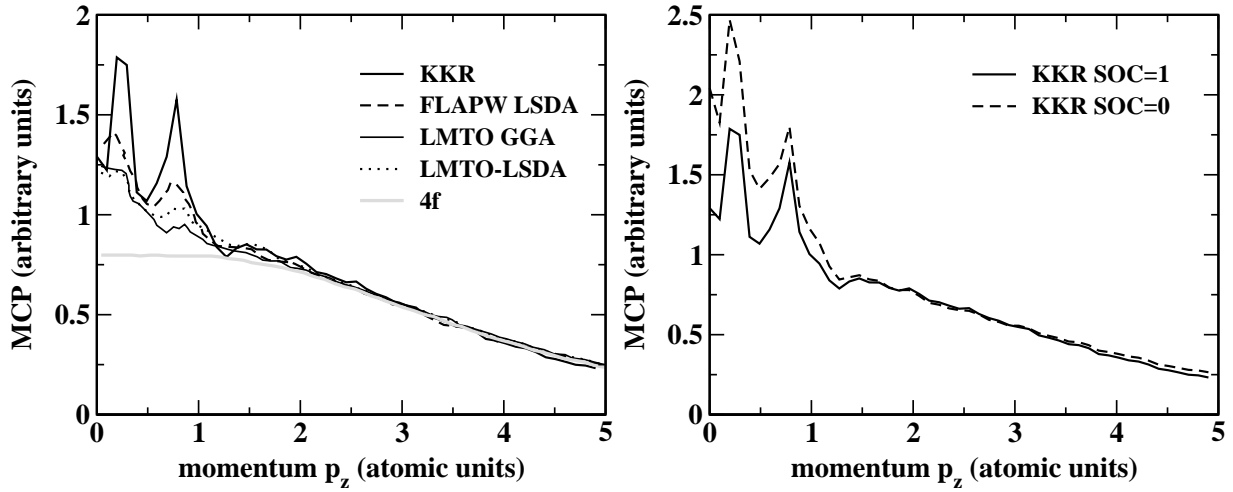


Figure 3.18: Theoretical predictions on the magnetic Compton scattering of Gd. Left: The SPR-KKR calculations (full line) together with FLAPW calculations of Kubo and Asano [2] and respectively LMTO calculations of Duffy et al. [3]. The gray line is the equivalent free-atom profile for Gd 4f, normalized to 7 electrons. Right: The effect of the spin-orbit coupling on the SPR-KKR MCP of Gd.

profile was normalized to the experimental MCP. The unbroadened theoretical predictions are represented in Fig. 3.18 (left) together with the equivalent free-atom profile for Gd 4f, normalized to seven electrons [3].

The 4f electrons contribution to the MCP of Gd is giving a broader profile compared with 3d ferromagnets, with an extension beyond 5 atomic units. At lower momenta ( $p_z \leq 1.5$  a.u.) there is a small contribution arising from the spin polarisation of the conduction electrons ( $6d^25d$ ) superimposed on the 4f electrons contribution, as can be seen in Fig. 3.18.

The results of KKR calculations are obtained fully relativistically as well as in scalar relativistic way, with the spin-orbit coupling switched off. The effect of the spin-orbit coupling on the SPR-KKR magnetic Compton profile (MCP) can be seen in Fig 3.18 (right). As expected, the spin-orbit coupling effect is important for the spin momentum density calculations. The scalar relativistic profile overestimates the profile at small momenta, whilst the fully relativistic calculations gives the best fit of the experimental data (see Fig. 3.17). In Fig. 3.18, the fine structure of the theoretical magnetic Compton profile can be seen. We note that the shape of the KKR profile is very similar to the FLAPW profile. The peaks at  $\simeq 0.4$  a.u. and  $\simeq 0.8$  a.u. are prominent in both calculations. The difference is the magnitude of the peaks and the behaviour at  $p_z = 0$  a.u., where the dip in the KKR profile is more pronounced. This behaviour around  $p_z = 0$  a.u. seems to be decisive, after broadening, for a better fit of the experimental data.

### 3.6.2 Magnetic Compton profile of $Y_{0.38}Gd_{0.62}$ alloy

Y has the same structure and similar atomic volume as Gd, and hence the  $Gd_{1-x}Y_x$  alloy readily form over the whole concentration range with only small changes in their lattice parameter.

The Gd-Y alloy series has been subject of investigations [119, 120] in view of the competition between ferromagnetic order favourable in Gd-rich alloy and the helical magnetism found in Y-rich alloy. The magnetic behaviour of the bulk alloy is complex; there are three different magnetic ordered phases in competition: for  $x \leq 0.3$  Y, the ferromagnetic order is present, for  $x \geq 0.4$  there is a helical antiferromagnetic phase and in between there is a delicate balance of the two phases at different temperatures.

Because Y is non magnetic, it might be thought that it will act like a diluent on the magnetic properties of Gd. This assumption was falsified by Thoburn et al. [119] through the evidence of a large additional total moment in the ferromagnetic phase of  $Gd_xY_{1-x}$  alloys. The behaviour of the total moment can be explained either through the appearance of an additional orbital moment due to the crystal field modification induced by the presence of Y, or an extra-spin moment induced by the hybridisation of the conduction bands in the alloy.

The magnetic Compton investigations of Duffy et al. [4] evidenced an additional spin moment of  $0.16 \pm 0.03 \mu_B$ . The magnetic moment was determined comparing the magnetic Compton profile of the alloy and of pure Gd, normalized to the same 4f electronic contribution in order to take into account the Gd dilution in the alloy. The area under the  $Y_{0.38}Gd_{0.62}$  MCP is higher than the corresponding area for pure Gd, the difference being attributed to the extra-spin moment on Y. LMTO calculations support the evidence of the extra-spin moment, supposed to arise from the polarisation of electrons on Y through a Ruderman-Kittel-Kasuya-Yoshida (RKKY) type of interaction.

Taking into account the previous work in the field, our purpose is to analyse the KKR predictions for the magnetic moments obtained from electronic band calculations and to compare them with experiment and with LMTO calculations. Also, the magnetic Compton profiles will be calculated and compared with the previous experimental data and theoretical predictions.

Fully relativistic KKR self-consistent band structure calculation have been performed for  $Y_{0.38}Gd_{0.62}$  alloy in a *hcp* structure with a lattice parameter  $a = 6.8758$  a.u. and  $c/a = 1.584$ . The Coherent Potential Approximation (CPA) was used for the treatment of the disordered alloy. The magnetic moments for Gd and Y are presented in Table 3.4, together with the

Calculation method	Gd (pure)	Gd (alloy)	Y (alloy)
LMTO-LSDA	7.64	7.56	0.35
KKR-LSDA	7.53 (7.44)	7.53 (7.42)	0.245 (0.24)

Table 3.4: LMTO [4] and SPR-KKR magnetic moments of  $Y_{0.38}Gd_{0.62}$  alloy. The SPR-KKR spin magnetic moments are presented in parenthesis.

LMTO based magnetic moments of Duffy et al. [4]. The KKR spin magnetic moments for each atom-type are presented in parenthesis. Both calculation methods predict a small magnetic moments induced by Y. KKR calculations show that the induced moment is associated with the spin, the orbital component being very small. This extra spin-moment has to be evidenced by the MCP calculations for  $Y_{0.38}Gd_{0.62}$  alloy, as will be shown in the following.

The experimental data of the [0001] MCP for  $Y_{0.38}Gd_{0.62}$  alloy were measured at the high

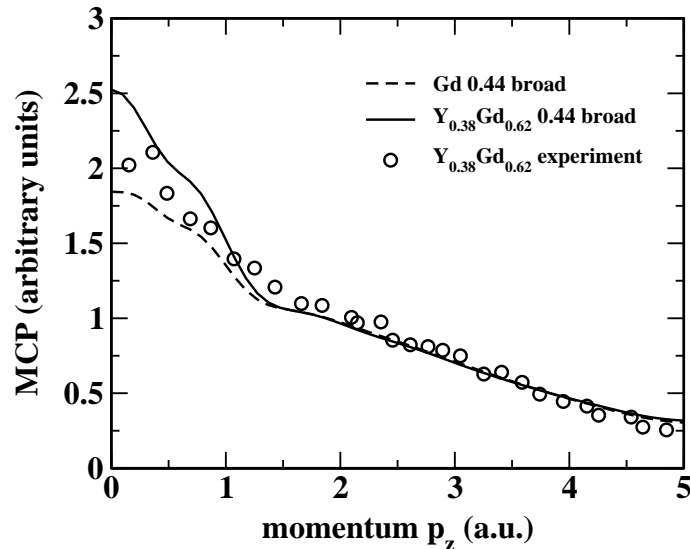


Figure 3.19: Magnetic Compton profile of  $Y_{0.38}Gd_{0.62}$  alloy. SPR-KKR profiles have been broadened with a Gaussian of FWHM 0.44 a.u. and normalized according to the 4f moment to be compared with experimental data of Duffy et al. [4].

energy beamline X-Ray beamline at the ESRF with an incident energy of 200 keV [4]. The temperature of the sample was maintained at  $70 \pm 2$  K. According to Thoburn et al.[120], for this temperature and concentration the alloy has a ferromagnetic order. The momentum resolution achieved during the measurements was 0.44 atomic units.

In Fig. 3.19 we present the theoretical KKR MCP of  $Y_{0.38}Gd_{0.62}$  convoluted with a Gaussian of FWHM 0.44 a.u. to simulate the experimental resolution and normalized according to the 4f moment. For normalization, the theoretical KKR MCP profile of pure Gd has been represented in the same figure in order to estimate the 4f contribution. The theoretical profile is compared with the experimental data of Duffy et. al [4]. The KKR MCP gives a new evidence of the extra-spin moment contribution of Y in the  $Y_{0.38}Gd_{0.62}$  alloy, compared with the pure Gd system. This extra spin contribution to the magnetic moments seems to be slightly overestimated by the KKR MCP calculations.

We performed KKR MCP calculations for ferromagnetically ordered  $Y_{0.50}Gd_{0.50}$  alloy, in order to investigate if the trend of the magnetic moments behaviour versus the concentration of Gd in the  $Gd_xY_{1-x}$  is reflected by the MCP calculations. According to Thoburn et al.

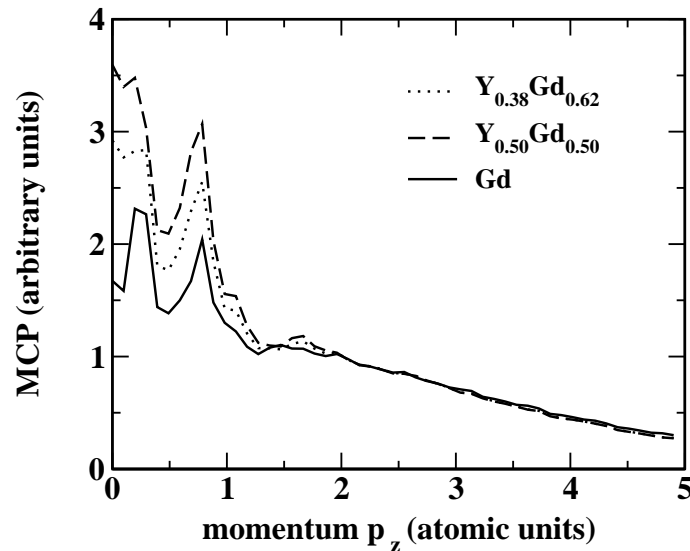


Figure 3.20: Magnetic Compton profiles of  $Y_{0.38}Gd_{0.62}$  and  $Gd_{0.50}Y_{0.50}$  alloys. The SPR-KKR profiles have been normalized to free atom-like 4f contribution.

[119], the magnetic moments in  $Gd_xY_{1-x}$  alloy increase with increasing the Y content, although pure Y is non-magnetic. The theoretical predictions for  $Y_{0.50}Gd_{0.50}$ ,  $Y_{0.38}Gd_{0.62}$  and pure Gd are presented in Fig. 3.20. The MCP for the alloys have been normalized to the same 4f contribution as in pure Gd. The results are in agreement with experimental magnetisation data [119], the spin magnetic moment in the  $Y_{0.50}Gd_{0.50}$  alloy being higher than in  $Y_{0.38}Gd_{0.62}$ .

### 3.7 Magnetic Compton profile of $UFe_2$

In recent years, the study of actinides and actinide compounds has attracted much interest because of great variety of magnetic behaviour, such as Pauli paramagnetism, localized/itinerant magnetism and heavy fermion behaviour. The complexity of the magnetic behaviour is connected with the spin-orbit coupling strength, which is rather large compared with the crystal field energy. The spin-orbit coupling induced orbital moment can be appreciable if the strength of the coupling is comparable to the f-band width.

Although f-electrons are usually treated as localized, there are some compounds for which the f-states are strongly coupled to the conduction band (s, p and d) giving rise to unusual properties. One consequence of delocalization is the formation in some compounds with ordered magnetic moments, much smaller than those anticipated from localized f-electrons [121]. This 5f electron delocalization has been reported in  $UFe_2$  compound [122].  $UFe_2$  is a soft ferromagnet with a Curie temperature of 160 K, which crystallize in the cubic *fcc* Laves phase and has low magnetic anisotropy. Neutron diffractions experiments [123, 124] found

a very small total moment in this system. The orbital and spin magnetic moments, which individually have a value of  $\sim 0.23\mu_B$ , almost completely cancel on the U sublattice.

The theoretical predictions based on spin-polarized LMTO calculations [122] found an 5f orbital moment on the U site  $\mu_l = 0.47\mu_B$  and an antiparallel spin component of  $\mu_s = -0.58\mu_B$ . Adding the small s, p and d contribution, the total U moment is  $-0.24\mu_B$  per atom, antiparallel to the larger ( $0.77\mu_B$ ) Fe moment. The spin and orbital moments on the uranium site in  $UFe_2$  deduced later from circular dichroism data by using the sum rules [125] confirmed the neutron diffraction data, but the spin and orbital contribution on U site are less than half ( $\mu_l \simeq \mu_s \simeq 0.23\mu_B$ ) of the values obtained from LMTO calculations.

Neutron experiments probe the total site magnetization, which for  $UFe_2$  is very small. Magnetic dichroism experiments are element specific, i.e. it doesn't show a complete picture of the  $UFe_2$  magnetism. For these reasons, magnetic Compton scattering experiments have been performed by Lawson et al. [17] in order to get information about the spin magnetization of this compound.

The measured profile is placed on an absolute scale by calibration with a measurement on pure metallic Fe whose moment is well known to be  $2.1\mu_B$ . This moment is almost entirely due to spin, while the orbital moment being negligible. The average momentum resolution achieved using an Ge solid state detector was 0.78 atomic units. The measured profile was fitted by using free-atom Compton profiles for Fe 3d, U 5f and a diffuse component, modeled as the sum of a U 6d free-atom profile and a free-electron parabola smeared with the experimental resolution function. Following this empirical procedure, Lawson et al. [17] obtained spin moments for 5f U and 3d Fe in agreement with those deduced from neutron measurements.

Our purpose is a direct KKR calculation of the magnetic Compton profile for  $UFe_2$  and a investigation concerning the role played by the spin-orbit coupling and by the interactions responsible for Hund's second rule.

### 3.7.1 The orbital polarization

Hund's first rule (concerning the exchange interaction between spins) is accounted for by the LSDA leading to the spin polarization. The second Hund rule (concerning the orbital exchange interaction between atomic orbital moments) is absent in LSDA because this theoretical approach is based on the properties of a spin polarized homogeneous electron gas. Although the interactions leading to Hund's second rule are usually neglected in an energy band calculations, they are crucial in atoms. Since we are dealing with a very narrow band system here, the atomic-like interactions play an important role. During the last years, the energy band calculations including the Hund's second rule have been applied with remarkably success to d- as well as f- electrons [122, 126].

The orbital polarization (OP) term added to the Hamiltonian is meant to account for Hund's second rule i.e. to maximize the orbital angular momentum. For f-electron systems Brooks'

OP-term has the form

$$\Delta\epsilon_{lm_l m_s} = -E_{m_s}^3 \langle \hat{l}_z \rangle_{m_s} m_l \delta_{l3} . \quad (3.27)$$

This term describes a shift in energy by  $\Delta\epsilon_{lm_l m_s}$  for an orbital with quantum numbers  $l = 3$ ,  $m_l$  and  $m_s$  that is proportional to  $\langle l_z \rangle_{m_s}$  for the  $m_s$ -spin subsystem and the Racah parameter  $E_{m_s}^3$ . The corresponding operator is given by

$$\mathcal{H}_{m_s}^{\text{OP}} = -E_{m_s}^3 (r) \langle \hat{l}_z \rangle_{m_s} \hat{l}_z \delta_{l3} \quad (3.28)$$

with

$$E_{m_s}^3 (r) = \frac{1}{3} \int \left[ \frac{5}{225} \frac{r_{<}^2}{r_{>}^3} + \frac{6}{1089} \frac{r_{<}^4}{r_{>}^5} - \frac{91}{7361} \frac{r_{<}^6}{r_{>}^7} \right] \rho_{f m_s}(r') 4\pi r'^2 dr' . \quad (3.29)$$

Introducing the vector potential function

$$A_{m_s}^{\text{OP}} = -E_{m_s}^3 (r) \langle l_z \rangle \quad (3.30)$$

one can get the Dirac Hamiltonian in the form

$$\mathcal{H} = \frac{\hbar c}{i} \vec{\alpha} \cdot \vec{\nabla} + \beta m c^2 + V_{eff}(\vec{r}) + \beta \vec{\sigma} \cdot \vec{B}_{eff}(\vec{r}) + A^{\text{OP}} \beta l_z . \quad (3.31)$$

The influence of the OP-term on the magnetic moments of  $\text{UFe}_2$  has been investigated. Self-consistent energy-band calculations were done, using the KKR band structure method within the local approximation to the density-functional theory (LSDA). The magnetic moments resulted from a fully-relativistic calculation, with and without the orbital polarization

	U		Fe	
	$\mathbf{m}_{spin}$	$\mathbf{m}_{orb}$	$\mathbf{m}_{spin}$	$\mathbf{m}_{orb}$
KKR	0.56	-0.29	-0.69	-0.06
KKR OP	0.62	-0.32	-0.74	-0.09
Experiment [123, 124]	0.22	-0.23	-0.59	-
LMTO [122]	0.71	-0.47	-0.75	-0.07
LMTO OP [122]	1.03	-0.88	-0.82	-0.07

Table 3.5: Magnetic moments of U and Fe in  $\text{UFe}_2$  compound.



term included in Hamiltonian, are presented in Table 3.5. These results are compared with the neutron diffraction experimental data [123, 124] and with results of LMTO calculations [126]. The theoretical KKR values for the spin and orbital moments compare rather well with LMTO calculations and with experimental data. Both KKR and LMTO calculated magnetic moments overestimate the moments, but the KKR results are closer to experiment. This result enable us to continue the investigations on the magnetic properties of this system.

### 3.7.2 Influence of spin-orbit coupling and orbital polarization on the MCP of $UFe_2$

The KKR-LSDA calculations of MCP with spin-orbit coupling switched on/off have been performed for  $UFe_2$ . The influence of the spin-orbit coupling on the magnetic Compton profile of  $UFe_2$  is presented in Fig. 3.21 (left). The theoretical KKR calculations have been convoluted with a Gaussian of 0.78 a.u., the same as the experimental resolution function. The experimental data stem from Lawson et al. [17].

As can be seen, in the high-momentum region ( $p_z \geq 2$  a.u.) the spin-orbit coupling doesn't

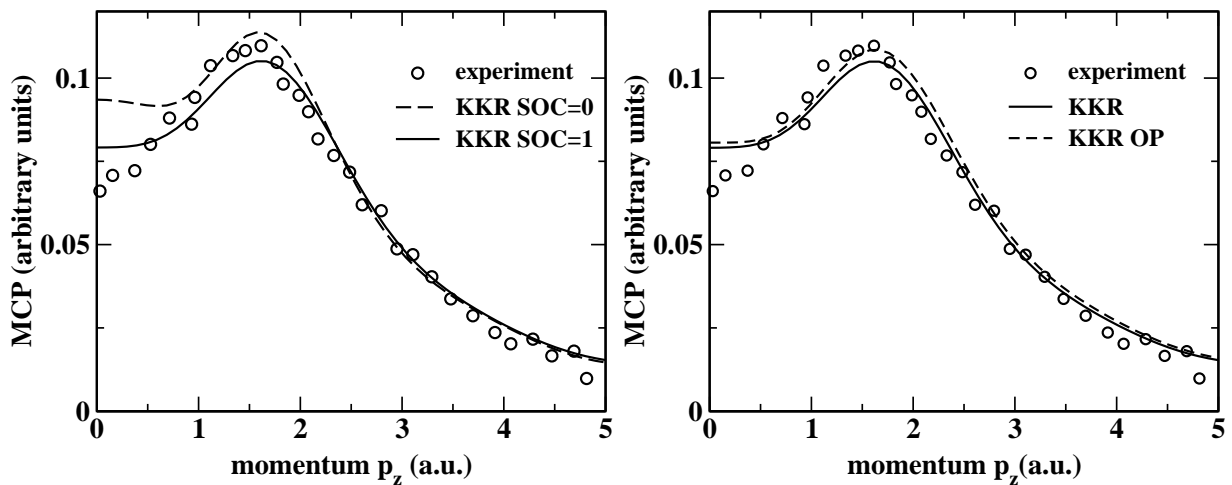


Figure 3.21: Influence of the spin orbit coupling (left) and orbital polarization (right) on the magnetic Compton profile of  $UFe_2$ . The theoretical spectra have been convoluted with a Gaussian of FWHM 0.78 a.u. to fit the experimental data of Lawson et al. [17]

influence the magnetic spin density. It is not the case for the low momentum region ( $p_z \leq 2$ ) a.u., where the calculation with spin-orbit switched off overestimates the magnetic Compton profile. This negative polarization of the profile in the low momentum region is almost correctly estimated by the fully relativistic calculations.

The MCP was calculated by the KKR-LSDA method, using the Hamiltonian from the Eq.

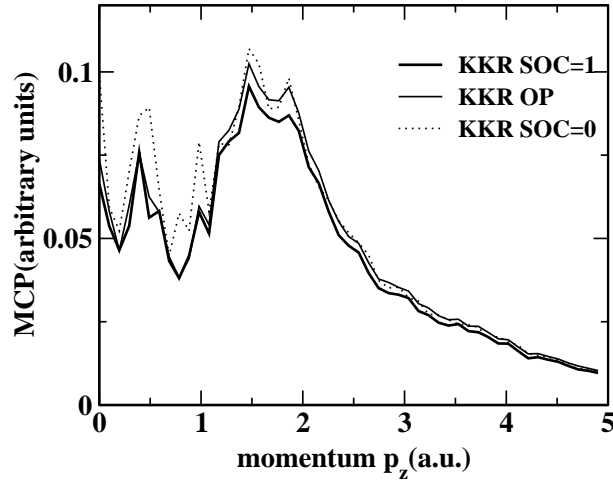


Figure 3.22: The theoretical magnetic Compton profile of  $\text{UFe}_2$ . The SOC = 0 labels the scalar-relativistic calculation and SOC labels the fully relativistic calculation. OP denotes the SPR-KKR calculation with orbital polarization included.

(3.31) in order to take into account the orbital polarization (KKR-OP mode). The profile calculated in the OP-mode is represented together with the fully relativistic profile, with the OP term missing from the Hamiltonian (KKR mode) and with the experimental data in Fig. 3.21 (right). The role played by the orbital polarization in the MCP of  $\text{UFe}_2$  is less obvious, but an improvement of the profile in the region of  $0.5 \leq p_z \leq 1.7$  a.u. is visible, the KKR-OP profile being closer to experiment. Because Compton scattering is driven by the spin magnetism, it is expected that changes in orbital interaction will affect it only if there are also changes in the spin polarization induced by spin-orbit interaction.

For a more detailed investigation of the role played by spin-orbit, and by the OP in different momentum regions of the MCP, the raw calculated spectra have not been convoluted and the fine structure of MCP is visible. As can be seen, the OP-mode of calculation enhances the peaks at 1.5 and 2.0, compared with the non-OP-mode. Inside the regions with  $p_z \leq 1.5$  a.u. and  $p_z \geq 2.5$  a.u., the OP and non-OP fully relativistic calculation coincide.

As expected, a non-relativistic band structure treatment is not adequate for this system, but one should note the big influence of the spin-orbit coupling in the MCP, compared with the smaller effect of the orbital polarization.

### 3.7.3 Individual atomic-type contributions on the magnetic Compton profile of $\text{UFe}_2$

We are interested to see which are the Fe and U contributions in the MCP of  $\text{UFe}_2$ . The MCP spectra can be decomposed into site contributions, making use on the Green's function formula (3.26). Further, if one associate the atomic type to each site into the unit cell, the

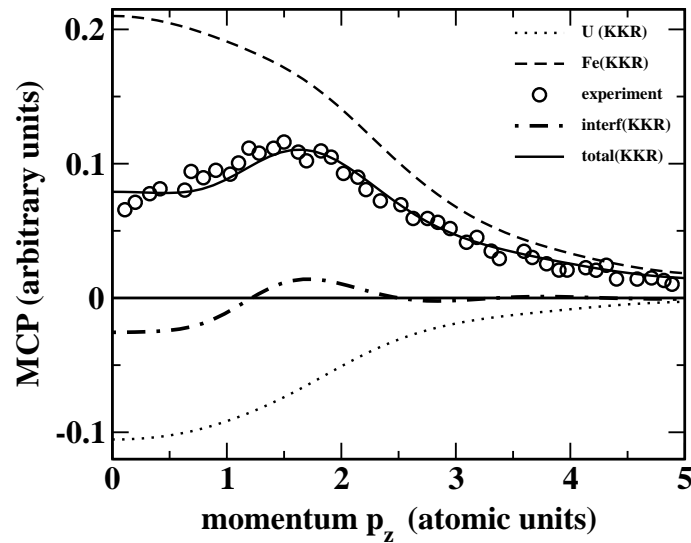


Figure 3.23: The magnetic Compton profile of  $UFe_2$  (full line) decomposed into U (dotted line), Fe (dashed line) and interference term (U-Fe) contribution (dashed-dotted line). The profiles have been broadened with a Gaussian of FWHM = 0.78 a.u., according to the experimental momentum resolution. The experimental data of Lawson et al. [17] are represented by circles.

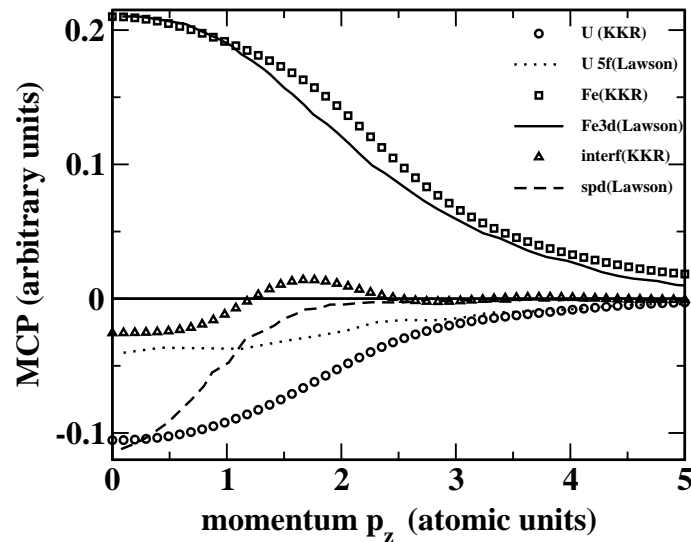


Figure 3.24: The partial components: U (circles), Fe (squares) and interference term (triangles) resulting from the SPR-KKR decomposition of the magnetic Compton profile, together with the 'Fe-3d' (full line), 'U-5f' (dotted line) and the 'spd' (dashed line) term used by Lawson et al. [17] to compose the best fit of the experimental data.

MCP spectra can be decomposed into distinct atomic-type contributions plus an interference term which takes into account the combined U-Fe contributions. The decomposition is presented in Fig. 3.23. As can be seen, Fe gives a positive free atom-like contribution, which is partially compensated by the negative free atom-like U contribution, in agreement with the antiparallel spin coupling determined by experiment [125] and confirmed by other theoretical calculations [122].

The decisive term for the final shape of the total profile is the interference term, which is negative for  $p_z \leq 1.2$  a.u. and positive for  $p_z \geq 1.2$  a.u.. It is obvious that this term is responsible for the negative polarization of the total profile at  $p_z \leq 1.2$  a.u. and for the maxima at  $p_z \simeq 1.7$  a.u..

Our decomposition, described below and presented in Fig. 3.23 is compared with the fitting of the experimental data performed by Lawson et al. [17]. They fitted the experimental profile by free-atom Compton profile for Fe  $3d$ , U  $5f$  and a diffuse component, labeled *spd*, which is modeled as the sum of a U  $6d$  free-atom profile and a free-electron parabola smeared with the experimental resolution function. The partial components of the MCP are presented for comparison in Fig. 3.24. The fitting realized by the total best-fit curve of Lawson et al. is comparable with the SPR-KKR fitting of the experimental data and it has not been represented in Fig. 3.24.

As can be seen in Fig. 3.24, the Fe contribution is similar in the SPR-KKR decomposition with the free atom profile for Fe  $3d$  [17]. Also, the shape of the U partial profile is similar with the free atom profile for U  $5f$  of Lawson et al.. This suggests a free atom-like contribution of Fe and U. The difference appears when the spin magnetic moment is estimated. If the Fe spin magnetic moment is comparable in the two cases, we conclude that the spin magnetic moment of U has been underestimated by the fitting of Lawson et al..

According to our direct calculation of the partial components, there is no reason of a possible representation of the interference term (or diffuse term) as a sum of U  $6d$  free atom profile and a free-electron parabola. Our SPR-KKR band structure calculations gives a spin moment on  $s$   $p$  and  $d$  orbitals of U  $\simeq 20$  % of the U- $f$  spin moment, so there is no evidence for such a big negative U- $6d$  contribution compared with the U- $5f$  one. As a consequence, the possibility of fitting the MCP by free atom-like profiles is questionable.

### 3.8 Conclusions

The SPR-KKR magnetic Compton profile calculated for Fe and Ni along [001], [110] and [111] directions show good agreement with the experimental data. The decomposition of the MCP [001] spectra of Fe into  $s$ -,  $p$ - and  $d$ -like contributions show a significant negative polarisation of  $s$ - and  $p$ - orbitals in the spin momentum density at small values of momentum.

The SPR-KKR two-dimensional projection of the spin momentum density for Fe perpendicular to the [001] direction crossing the  $\Gamma$  point is in good agreement with the FLAPW calculations and with the reconstruction from experimental spectra. This result demonstrates the

reliability of the SPR-KKR calculations of the MCP spectra.

The SPR-KKR calculations of the magnetic Compton profiles in Fe<sub>3</sub>Pt Invar alloys show that the ordering doesn't play a major role for the spin momentum density of the system. The decomposition of the MCP [001] spectra for Fe<sub>3</sub>Pt into Fe, Pt and interference terms show that Fe has the major contribution to MCP. Nevertheless, the shape of the profile is influenced by interference term which has a change in sign along the momentum axis.

The influence of the relativistic effects on the spin momentum density can be seen in the magnetic Compton profiles for Gd, Y<sub>0.38</sub>Gd<sub>0.62</sub> and UFe<sub>2</sub>. Also, the influence of the orbital polarisation (i.e the Hund's rule which describes the interaction between orbital moments) in UFe<sub>2</sub> systems is discussed. The decomposition of the MCP spectra of UFe<sub>2</sub> [001] into the U, Fe and interference terms show that the interference term cannot be neglected. Because of this, the atomic-like decomposition of the MCP spectra is questionable.



# Chapter 4

## Positron annihilation

### 4.1 Introduction to positron annihilation

There are only few experimental techniques for measuring directly wave-function-related quantities such as real-space electron density or momentum density. The positron annihilation experiment provide useful information on the electron momentum density and hence, on the electronic structure of solids. A short description of the positron annihilation experiment will be given in the following.

Solid state positron spectroscopy is based on the annihilation of positrons with electrons with the creation of, in general, pairs of high energy photons ( $\sim 0.5$  MeV) which carry information about both the energies and momenta of the annihilated electron-positron pair [127, 128]. The schematic process is presented in Fig 4.1. Positrons can be injected in the sample either directly from a radioactive source, in which case they have a continuous energy distribution from 0 to  $\sim 1$  MeV, or as monoenergetic beams with energy typically in the range 0 - 40 keV. The mean penetration depth depends on the target material. In the sample positrons rapidly lose their initial kinetic energy first via ionization processes, then via electron-hole excitations, and finally via phonon-scattering. After losing the excess energy positrons exist in thermal equilibrium with the ions and the electrons in the sample. The thermalization time of the positron is short compared with the life-time and can be ignored in most cases.

In thermal equilibrium the positron state develop according to a diffusion process in real space. The positrons scatters from phonons, electrons and defects of which the phonons give the dominant contribution. The average diffusion length is of the order of 1000 Å. In the case of periodic crystals and normal experimental conditions there is only one positron in the sample at a time. Due to Coulomb repulsion the positron wave function is mainly located in the interstitial region of the crystal, far from the positive nuclei. Localized positron states can be formed at open-volume crystal defects (vacancies, voids or dislocations). In the case of semiconductors and insulators, the positrons can be weakly bound by negative charged defects (impurity ions).

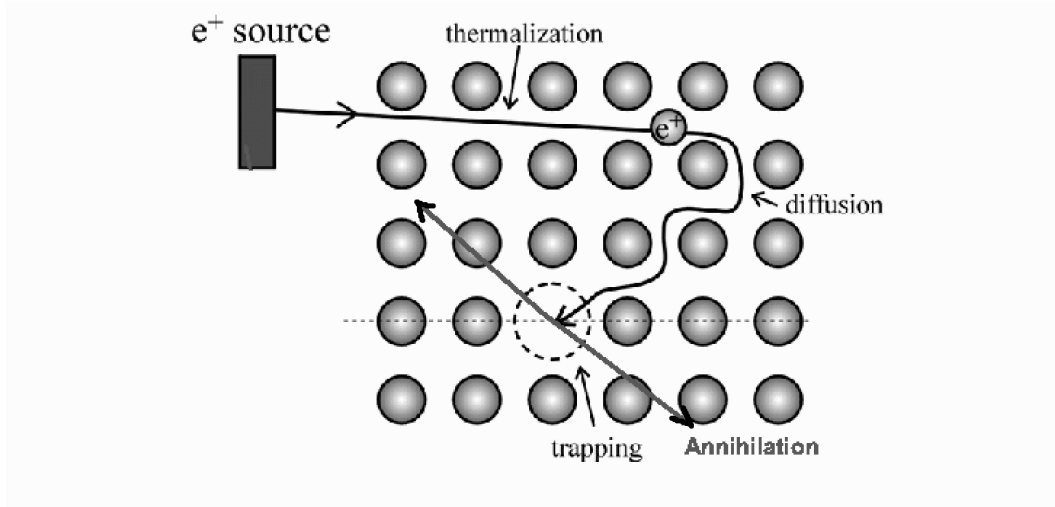


Figure 4.1: Positron annihilation in the solid gives rise to the  $\gamma$ -rays detected by experimental measurements.

In the center of the momentum frame of a low energy ( $p \ll m_0c$ ) electron-positron pair, the two photons are emitted in exactly opposite directions. However, in the laboratory frame, the momentum of the center-of-mass of annihilating pair produces small Doppler shifts ( $\leq 2$  keV) in the energies of the two photons and a small deviation from antiparallel alignment ( $\leq 0.5$  degrees). The deviation can be measured with the one- or two-dimensional angular correlation of the annihilation radiation (1D- or 2D-ACAR) methods.

The quantity measured in the 2D-ACAR experiment is usually identified with the 2D projections of the three-dimensional electron-positron momentum density distribution function  $n_{2\gamma}(\vec{p})$ , given by the formula:

$$n_{2\gamma}(\vec{p}) = \sum_{i_{occ}} \left| \int_{\Omega} e^{-i\vec{p}\vec{r}} \Psi_i^{ep}(\vec{r}, \vec{r}) d^3\vec{r} \right|^2 . \quad (4.1)$$

Here  $\Psi^{ep}(\vec{r}, \vec{r})$  is the two particle wave function when the positron and the electron of state  $i$  reside at the same point. The summation is done over all electronic occupied states,  $\vec{p}$  is the electron momentum and  $\Omega$  is the volume of the sample.

The two-particle wave function is usually written in a product form:

$$\Psi_i^{ep}(\vec{r}, \vec{r}) = \Psi^p(\vec{r}) \Psi_i^e(\vec{r}) \sqrt{\gamma_i(\vec{r})} , \quad (4.2)$$

where  $\Psi^p(\vec{r})$  and  $\Psi_i^e(\vec{r})$  are the positron and electron wave functions for the independent systems. The effects of the electron-positron interaction are included in the so-called enhancement factor  $\gamma_i(\vec{r})$ . The positron-electron correlation gives rise to an electronic cloud



around the positron which screens its positive charge, thereby greatly increasing the electron charge in its environment. This attraction strongly depends on the electron density. The enhancement factor  $\gamma_i(\vec{r})$  is defined as the ratio of perturbed to unperturbed electron densities in the initial  $i$  state at the positron position  $\vec{r}$ . If the electron-positron correlations are neglected, the value of the function  $\gamma_i(\vec{r})$  is approximated by 1. In this case, the positron annihilation is treated within the independent particle model (IPM). Apart from the IPM model, several models to determine the enhancement function have been developed [129, 130, 131, 132, 133, 134]. The electron-positron correlation is a complex many-body problem which will be not dealt within this work.

Instead, the quantity of interest from the electronic point of view is however the electron momentum distribution function  $n(\vec{p})$ , given by formula

$$n(\vec{p}) = \sum_{i_{occ}} \left| \int_{\Omega} e^{-i\vec{p}\vec{r}_e} \Psi_i^e(\vec{r}_e) d^3\vec{r}_e \right|^2. \quad (4.3)$$

To deduce features of  $n(\vec{p})$  from measurements of  $n_{2\gamma}(\vec{p})$  one has to understand the positron annihilation process and the states of the positron in a metal.

To first order in the positron-ion and electron-positron interactions, the most prominent feature of  $n_{2\gamma}(\vec{p})$  is the break that occurs when  $\vec{p}$  crosses the Fermi surface separating the filled and unfilled parts of  $\vec{p}$  space. The positions of these breaks define the Fermi surface. The effect of the interactions between positrons and ions and respectively between positrons and electrons is reflected in the differences between  $n_{2\gamma}(\vec{p})$  and  $n(\vec{p})$ . The importance of the electron-positron interaction becomes especially apparent when comparing ACAR spectra with Compton profiles.

## 4.2 The electron-positron momentum density

The purpose of this section is to present a general scheme to calculate  $n_{2\gamma}(\vec{p})$  such that it can be used in a practical determination of the two-dimensional angular correlation of the annihilation radiation (2D-ACAR) spectra and of the coincidence Doppler broadening (1D-ACAR) spectra.

One can relate the electron-positron momentum density  $n_{2\gamma}(\vec{p})$  to the two particle Green function  $G_{m_s m'_s}(\vec{p}_e, \vec{p}_p)$  in momentum representation, where  $m_s, \vec{p}_e, m'_s$  and  $\vec{p}_p$  are the spins and momenta of electron and positron, respectively. In the following calculations we will neglect the electron-positron correlations, breaking the system consisting of one positron and  $n$  electrons into two non-interacting subsystems: one subsystem consist on  $n$  fully interacting electrons and the other subsystem consists only in the positron. The Green's function of the electron-positron pair in momentum representation can be expressed using the multiple scattering Green's function given by formula (2.155) and the eigenfunctions of the momentum operator  $\Phi_{\vec{p}m_s}$  as:

$$G_{m_s m'_s}(\vec{p}_e, \vec{p}_p) = \frac{1}{N\Omega} \int d^3r \int d^3r' \phi_{\vec{p}_e m_s}^{e\dagger}(\vec{r}) \mathfrak{S} G^{e+}(\vec{r}, \vec{r}', E_e) \phi_{\vec{p}_p m'_s}^e(\vec{r}')$$

$$\phi_{\vec{p}_p m'_s}^{p\dagger}(\vec{r}) \Im G^{p+}(\vec{r}, \vec{r}', E_p) \phi_{\vec{p}_p m'_s}^p(\vec{r}') . \quad (4.4)$$

The eigenfunctions of the momentum operator can be written as  $\Phi_{\vec{p} m_s} = U(\vec{p}) e^{i\vec{p}\vec{r}} = U_{\vec{p} m_s} e^{i\vec{p}\vec{r}}$ , where  $U(\vec{p})$  is a four-component spinor (see Eq. (3.13)). This leads to the expression for the Green's function:

$$G_{m_s m'_s}(\vec{p}_e, \vec{p}_p) = \frac{1}{\Omega} \int d^3 r_0 \int d^3 r' U_{\vec{p}_e m_s}^{e\dagger} e^{-i\vec{p}_e \vec{r}_0} \Im G^{e+}(\vec{r}_0, \vec{r}', E_e) U_{\vec{p}_e m_s}^e e^{i\vec{p}_e \vec{r}'} \\ U_{\vec{p}_p m'_s}^{p\dagger} e^{-i\vec{p}_p \vec{r}_0} \Im G^{p+}(\vec{r}_0, \vec{r}', E_p) U_{\vec{p}_p m'_s}^p e^{i\vec{p}_p \vec{r}'} . \quad (4.5)$$

The space integral can be written as a summation over the cell-integrals:  $\int d^3 r = \sum_q \int dr_{0q}$  and  $\int d^3 r' = \sum_{n'q'} \int dr'_{n'q'}$ , where  $\vec{r}_0 = \vec{r}_{0q} + \vec{R}_q$  and  $\vec{r}' = \vec{r}'_{n'q'} + \vec{R}_{n'} + \vec{R}_{q'}$  as in Fig. A.1. With this, the Green's function reads as:

$$G_{m_s m'_s}(\vec{p}_e, \vec{p}_p) = \frac{1}{\Omega} \sum_q \sum_{n'q'} \int d^3 r_{0q} \int d^3 r'_{n'q'} \\ U_{\vec{p}_e m_s}^{e\dagger} e^{-i\vec{p}_e(\vec{r}_{0q} + \vec{R}_q)} \Im G^{e+}(\vec{r}_{0q}, \vec{r}'_{n'q'}, E_e) U_{\vec{p}_e m_s}^e e^{i\vec{p}_e(\vec{r}'_{n'q'} + \vec{R}_{n'} + \vec{R}_{q'})} \\ U_{\vec{p}_p m'_s}^{p\dagger} e^{-i\vec{p}_p(\vec{r}_{0q} + \vec{R}_q)} \Im G^{p+}(\vec{r}_{0q}, \vec{r}'_{n'q'}, E_p) U_{\vec{p}_p m'_s}^p e^{i\vec{p}_p(\vec{r}'_{n'q'} + \vec{R}_{n'} + \vec{R}_{q'})} . \quad (4.6)$$

Splitting the summation for  $q = q'$  and  $q \neq q'$ , one can write:

$$G_{m_s m'_s}(\vec{p}_e, \vec{p}_p) = \frac{1}{\Omega} \sum_q \int d^3 r_{0q} \int d^3 r'_{0q} \\ U_{\vec{p}_e m_s}^{e\dagger} e^{-i\vec{p}_e(\vec{r}_{0q} + \vec{R}_q)} \Im G^{e+}(\vec{r}_{0q}, \vec{r}'_{0q}, E_e) U_{\vec{p}_e m_s}^e e^{i\vec{p}_e(\vec{r}'_{0q} + \vec{R}_q)} \\ U_{\vec{p}_p m'_s}^{p\dagger} e^{-i\vec{p}_p(\vec{r}_{0q} + \vec{R}_q)} \Im G^{p+}(\vec{r}_{0q}, \vec{r}'_{0q}, E_p) U_{\vec{p}_p m'_s}^p e^{i\vec{p}_p(\vec{r}'_{0q} + \vec{R}_q)} \\ + \frac{1}{\Omega} \sum_q \sum'_{n'q'} \int d^3 r_{0q} \int d^3 r'_{n'q'} \\ U_{\vec{p}_e m_s}^{e\dagger} e^{-i\vec{p}_e(\vec{r}_{0q} + \vec{R}_q)} \Im G^{e+}(\vec{r}_{0q}, \vec{r}'_{n'q'}, E_e) U_{\vec{p}_e m_s}^e e^{i\vec{p}_e(\vec{r}'_{n'q'} + \vec{R}_{n'} + \vec{R}_{q'})} \\ U_{\vec{p}_p m'_s}^{p\dagger} e^{-i\vec{p}_p(\vec{r}_{0q} + \vec{R}_q)} \Im G^{p+}(\vec{r}_{0q}, \vec{r}'_{n'q'}, E_p) U_{\vec{p}_p m'_s}^p e^{i\vec{p}_p(\vec{r}'_{n'q'} + \vec{R}_{n'} + \vec{R}_{q'})} . \quad (4.7)$$

Taking into account that the sites  $q$  and  $q'$  ( $q \neq q'$ ) can be occupied with atoms of type  $\alpha$  or  $\beta$  with the probability  $x_{q\alpha}$  and  $x_{q'\beta}$ , respectively, one can write:

$$G_{m_s m'_s}(\vec{p}_e, \vec{p}_p) = \frac{1}{\Omega} \sum_q \sum_{\alpha} x_{q\alpha} \int d^3 r_{0q} \int d^3 r'_{0q}$$

$$\begin{aligned}
& U_{\vec{p}_e m_s}^{e\dagger} e^{-i\vec{p}_e \vec{r}_{0q}} \Im G^{e+\alpha}(\vec{r}_{0q}, \vec{r}'_{0q}, E_e) U_{\vec{p}_e m_s}^e e^{i\vec{p}_e \vec{r}'_{0q}} \\
& U_{\vec{p}_p m'_s}^{p\dagger} e^{-i\vec{p}_p \vec{r}_{0q}} \Im G^{p+\alpha}(\vec{r}_{0q}, \vec{r}'_{0q}, E_p) U_{\vec{p}_p m'_s}^p e^{i\vec{p}_p \vec{r}'_{0q}} \\
& + \frac{1}{\Omega} \sum_q \sum_{n'q'} \sum_{\alpha\beta} x_{q\alpha} x_{q'\beta} \int d^3 r_{0q} \int d^3 r'_{n'q'} \\
& U_{\vec{p}_e m_s}^{e\dagger} e^{-i\vec{p}_e(\vec{r}_{0q} + \vec{R}_q)} \Im G^{e+\alpha\beta}(\vec{r}_{0q}, \vec{r}'_{n'q'}, E_e) U_{\vec{p}_e m_s}^e e^{i\vec{p}_e(\vec{r}'_{n'q'} + \vec{R}_{n'} + \vec{R}_{q'})} \\
& U_{\vec{p}_p m'_s}^{p\dagger} e^{-i\vec{p}_p(\vec{r}_{0q} + \vec{R}_q)} \Im G^{p+\alpha\beta}(\vec{r}_{0q}, \vec{r}'_{n'q'}, E_p) U_{\vec{p}_p m'_s}^p e^{i\vec{p}_p(\vec{r}'_{n'q'} + \vec{R}_{n'} + \vec{R}_{q'})}. \quad (4.8)
\end{aligned}$$

Extending the summation for arbitrary  $q$  and  $q'$ , the Green's function reads:

$$\begin{aligned}
G_{m_s m'_s}(\vec{p}_e, \vec{p}_p) &= \frac{1}{\Omega} \sum_q \sum_{\alpha} x_{q\alpha} \int d^3 r_{0q} \int d^3 r'_{0q} \\
& U_{\vec{p}_e m_s}^{e\dagger} e^{-i\vec{p}_e \vec{r}_{0q}} \Im G^{e+\alpha}(\vec{r}_{0q}, \vec{r}'_{0q}, E_e) U_{\vec{p}_e m_s}^e e^{i\vec{p}_e \vec{r}'_{0q}} \\
& U_{\vec{p}_p m'_s}^{p\dagger} e^{-i\vec{p}_p \vec{r}_{0q}} \Im G^{p+\alpha}(\vec{r}_{0q}, \vec{r}'_{0q}, E_p) U_{\vec{p}_p m'_s}^p e^{i\vec{p}_p \vec{r}'_{0q}} \\
& - \frac{1}{\Omega} \sum_q \sum_{\alpha\beta} x_{q\alpha} x_{q\beta} \int d^3 r_{0q} \int d^3 r'_{0q} \\
& U_{\vec{p}_e m_s}^{e\dagger} e^{-i\vec{p}_e \vec{r}_{0q}} \Im G^{e+\alpha\beta}(\vec{r}_{0q}, \vec{r}'_{0q}, E_e) U_{\vec{p}_e m_s}^e e^{i\vec{p}_e \vec{r}'_{0q}} \\
& U_{\vec{p}_p m'_s}^{p\dagger} e^{-i\vec{p}_p \vec{r}_{0q}} \Im G^{p+\alpha\beta}(\vec{r}_{0q}, \vec{r}'_{0q}, E_p) U_{\vec{p}_p m'_s}^p e^{i\vec{p}_p \vec{r}'_{0q}} \\
& + \frac{1}{\Omega} \sum_q \sum_{n'q'} \sum_{\alpha\beta} x_{q\alpha} x_{q'\beta} \int d^3 r_{0q} \int d^3 r'_{n'q'} \\
& U_{\vec{p}_e m_s}^{e\dagger} e^{-i\vec{p}_e(\vec{r}_{0q} + \vec{R}_q)} \Im G^{e+\alpha\beta}(\vec{r}_{0q}, \vec{r}'_{n'q'}, E_e) U_{\vec{p}_e m_s}^e e^{i\vec{p}_e(\vec{r}'_{n'q'} + \vec{R}_{n'} + \vec{R}_{q'})} \\
& U_{\vec{p}_p m'_s}^{p\dagger} e^{-i\vec{p}_p(\vec{r}_{0q} + \vec{R}_q)} \Im G^{p+\alpha\beta}(\vec{r}_{0q}, \vec{r}'_{n'q'}, E_p) U_{\vec{p}_p m'_s}^p e^{i\vec{p}_p(\vec{r}'_{n'q'} + \vec{R}_{n'} + \vec{R}_{q'})}. \quad (4.9)
\end{aligned}$$

The calculation of the first and second term (so-called site-diagonal contribution) is presented in Appendix C.1, whilst the third term (site-off-diagonal contribution) is calculated in Appendix C.2. Using the matrix elements  $M_{m_s \Lambda m'_s \Lambda'}^{\mu\nu\alpha}$  and  $W^{p\nu q\alpha q'\beta}$  calculated in Appendix D and in Appendix C.3, respectively, the Green's function reads:

$$\begin{aligned}
G_{m_s m'_s}(\vec{p}_e, \vec{p}_p) &= \frac{1}{\Omega} \Im \sum_q \sum_{\alpha} x_{q\alpha} \left( \Im \tau_{\Lambda_s \Lambda_s}^{p+0q0q,\alpha}(E_p) \right) \sum_{\Lambda\Lambda'} M_{m_s \Lambda m'_s \Lambda_s}^{++\alpha} \tilde{M}_{m_s \Lambda' m'_s \Lambda_s}^{++\alpha} \tau_{\Lambda\Lambda'}^{e+0q0q,\alpha}(E_e) \\
& - \frac{1}{\Omega} \Im \sum_q \sum_{\alpha\beta} x_{q\alpha} x_{q\beta} \left( \Im \tau_{\Lambda_s \Lambda_s}^{p+0q\alpha 0q\beta}(E_p) \right) \\
& \sum_{\Lambda\Lambda'} M_{m_s \Lambda m'_s \Lambda_s}^{++\alpha} \tilde{M}_{m_s \Lambda' m'_s \Lambda_s}^{++\beta} \tau_{\Lambda\Lambda'}^{e+0q\alpha 0q\beta}(E_e) \\
& + \frac{1}{\Omega} \Im \sum_q \sum_{q'} e^{-i(\vec{p}_e + \vec{p}_p)(\vec{R}_q - \vec{R}_{q'})} \sum_{\alpha\beta} x_{q\alpha} x_{q'\beta} \left( \Im W^{p+q\alpha q'\beta} \right)
\end{aligned}$$

$$\sum_{\Lambda\Lambda'} M_{m_s\Lambda m'_s\Lambda_s}^{++\alpha} \tilde{M}_{m_s\Lambda' m'_s\Lambda_s}^{++\beta} \left( D^{e+\alpha} \tau^{e+qq'CPA}(\vec{p} - \vec{K}_m) \tilde{D}^{e+\beta} \right)_{\Lambda\Lambda'}. \quad (4.10)$$

In the previous calculation step we took into account the thermalization of the positron. This means that one may consider the positron to be in a state with  $\vec{k}_p = \vec{p}_p = 0$  with  $s$ -type symmetry, at the bottom of the positronic band [135, 128]. This implies for the orbital quantum number of the positron:  $l(\Lambda_p) = 0$ . Accordingly, the quantum number for the positron is given by  $\Lambda_p = \Lambda_s$ . Also, the positron energy  $E_p$  enters into the electron-positron Green's function as a parameter,  $E_p = E_p^0$ , where  $E_p^0$  is the energy of the bottom of the positronic band.

Introducing the single-site scattering matrix  $t_{\Lambda\Lambda'}^{e+q\alpha}$ , one can split the first term into the single-site and respectively backscattering contributions, as follows:

$$\begin{aligned} G_{m_s m'_s}(\vec{p}) &= \frac{1}{\Omega} \Im \sum_q \sum_{\alpha} x_{q\alpha} \left( \Im \tau_{\Lambda_s \Lambda_s}^{p+0q0q,\alpha}(E_p) \right) \sum_{\Lambda\Lambda'} M_{m_s\Lambda m'_s\Lambda_s}^{++\alpha} \tilde{M}_{m_s\Lambda' m'_s\Lambda_s}^{++\alpha} t_{\Lambda\Lambda'}^{e+q\alpha}(E_e) \\ &+ \frac{1}{\Omega} \Im \sum_q \sum_{\alpha} x_{q\alpha} \left( \Im \tau_{\Lambda_s \Lambda_s}^{p+0q0q,\alpha}(E_p) \right) \sum_{\Lambda\Lambda'} M_{m_s\Lambda m'_s\Lambda_s}^{++\alpha} \tilde{M}_{m_s\Lambda' m'_s\Lambda_s}^{++\alpha} \\ &\quad \left( \tau_{\Lambda\Lambda'}^{e+0q0q,\alpha}(E_e) - t_{\Lambda\Lambda'}^{e+q\alpha}(E_e) \right) \\ &- \frac{1}{\Omega} \Im \sum_q \sum_{\alpha\beta} x_{q\alpha} x_{q\beta} \left( \Im \tau_{\Lambda_s \Lambda_s}^{p+0q\alpha 0q\beta}(E_p) \right) \\ &\quad \sum_{\Lambda\Lambda'} M_{m_s\Lambda m'_s\Lambda_s}^{++\alpha} \tilde{M}_{m_s\Lambda' m'_s\Lambda_s}^{++\beta} \tau_{\Lambda\Lambda'}^{e+0q\alpha 0q\beta}(E_e) \\ &+ \frac{1}{\Omega} \Im \sum_q \sum_{q'} e^{-i(\vec{p}_e + \vec{p}_p)(\vec{R}_q - \vec{R}_{q'})} \sum_{\alpha\beta} x_{q\alpha} x_{q'\beta} \left( \Im W^{p+q\alpha q'\beta} \right) \\ &\quad \sum_{\Lambda\Lambda'} M_{m_s\Lambda m'_s\Lambda_s}^{++\alpha} \tilde{M}_{m_s\Lambda' m'_s\Lambda_s}^{++\beta} \left( D^{e+\alpha} \tau^{e+qq'CPA}(\vec{p} - \vec{K}_m) \tilde{D}^{e+\beta} \right)_{\Lambda\Lambda'}. \quad (4.11) \end{aligned}$$

The off-diagonal scattering path operator  $\tau^{e+qq'CPA}$  is defined in Eq. (2.189) and the matrices  $D^{e+\alpha}$  and  $\tilde{D}_{\Lambda\Lambda'}^{e+\beta}$  are defined in Eqs. (2.184) and (2.188), respectively. One has to note that the solutions of the Dirac equation  $Z_{\Lambda}^{p+q\alpha}$  for the positron which enters into the matrix elements  $M_{m_s\Lambda m'_s\Lambda_s}^{++\alpha}$  expression are calculated for a positron potential equal to the electronic Coulomb potential but with the opposite sign.

Based on the Feynman diagrams and the conservation of the spin angular momentum in the annihilation process [136] it was demonstrated that in a system where a positron can interact with electrons of both parallel and anti-parallel spin, it will almost always annihilate via two photons from an antiparallel positron-electron spin configuration. As consequence, the electron-positron pair has zero total spin angular momentum and  $m_s = -m'_s$  holds.

The electron-positron momentum density can be expressed using the electron-positron

Green's function as:

$$n_{2\gamma}^{m_s}(p) = -\frac{1}{\pi} \int_0^{E_F} G_{m_s}(p) dE_e . \quad (4.12)$$

The 2D angular correlation of annihilation radiation (2D-ACAR) spectra, which are usually identified with the 2D projections of the three-dimensional (3D) electron-positron momentum density is expressed as:

$$n^{2D-ACAR}(p_x, p_y) = \int (n_{2\gamma}^\uparrow + n_{2\gamma}^\downarrow) dp_z , \quad (4.13)$$

where the momentum components  $p_{x,y}$  are perpendicular to the photons propagation direction. The 1D-ACAR or the Doppler broadening spectrum is the one-dimensional momentum distribution:

$$n^{1D-ACAR}(p_z) = \int \int (n_{2\gamma}^\uparrow + n_{2\gamma}^\downarrow) dp_x dp_y , \quad (4.14)$$

where the integration is performed in a plane perpendicular to the photons propagation direction.

### 4.3 Electron-positron momentum density of V

The formalism described before is used to calculate 2D electron-positron momentum density projections and the results are compared with the two-dimensional angular correlation of the annihilation radiation (2D-ACAR) spectra determined by experiments. In order to see the impact of the electron-positron correlation on the electron-positron momentum density, we compare our calculations also with the LMTO spectra with electron-positron correlations included. The two dimensional projections of the electron-positron momentum density  $n_{2\gamma}(\vec{p})$  perpendicular to the [001] and [210] directions of *bcc* V have been calculated using the fully relativistic SPR-KKR package.

As a first step the electronic structure of V has been calculated self-consistently for the *bcc* structure with the lattice parameter  $a_{lat}=5.709$  a.u.. The band structure calculations for the positron have been performed using the same calculation code as for the electronic structure. The positron potential was taken as the inverse of the electron Coulomb potential. The integration (see Eq. (4.13)) along the  $p_z$  direction is done up to  $p_{z,max} = 6$  a.u. in a equidistant grid of 60 points. No significant change of the spectra appeared when  $p_{z,max}$  or the number of the grid points along  $p_z$  direction was increased.

The energy integration (see Eq. (4.12)) splits into an arc-like path of 30 points in a complex plane and a path parallel to the real axis consisting of 50 energy points. The arc-like

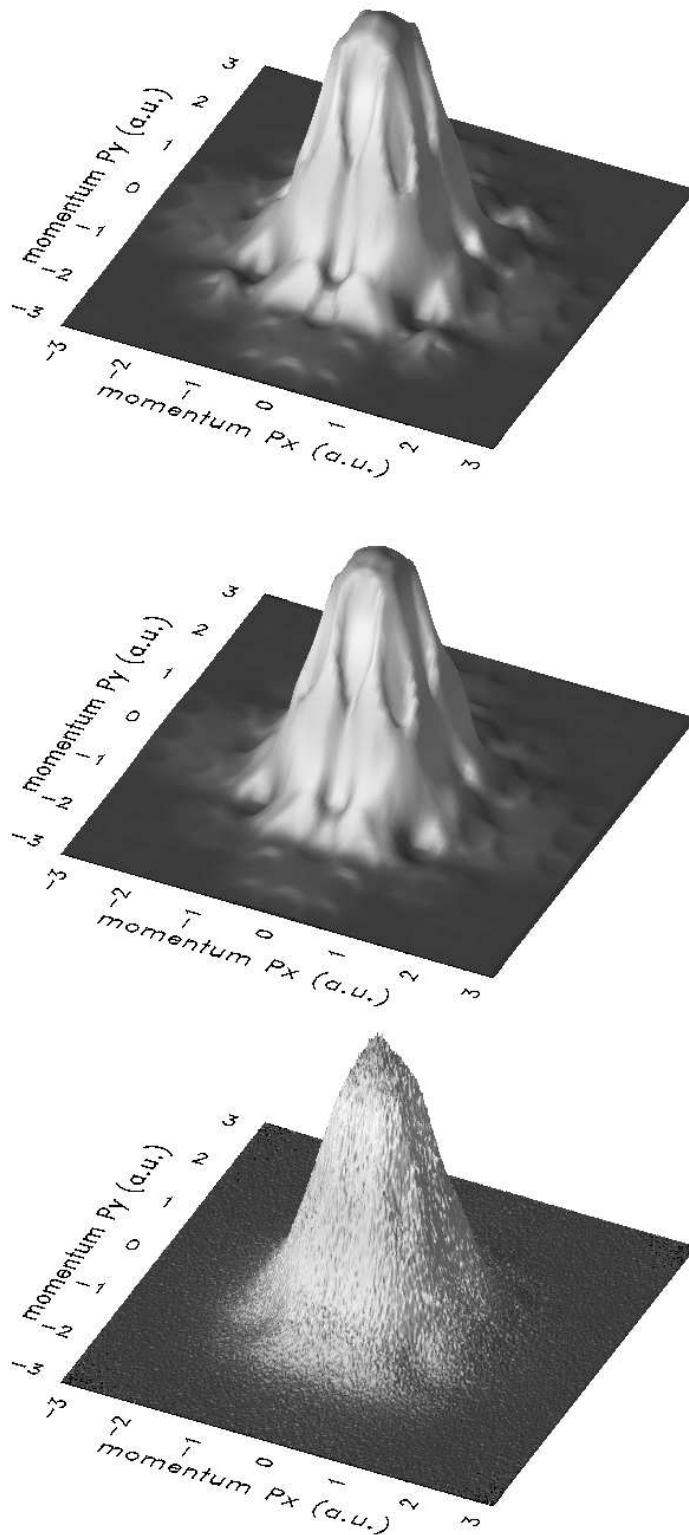


Figure 4.2: 2D-ACAR for V perpendicular to the [001] direction: SPR-KKR calculations (top), LMTO calculations [18] (middle), experiment [18] (bottom).

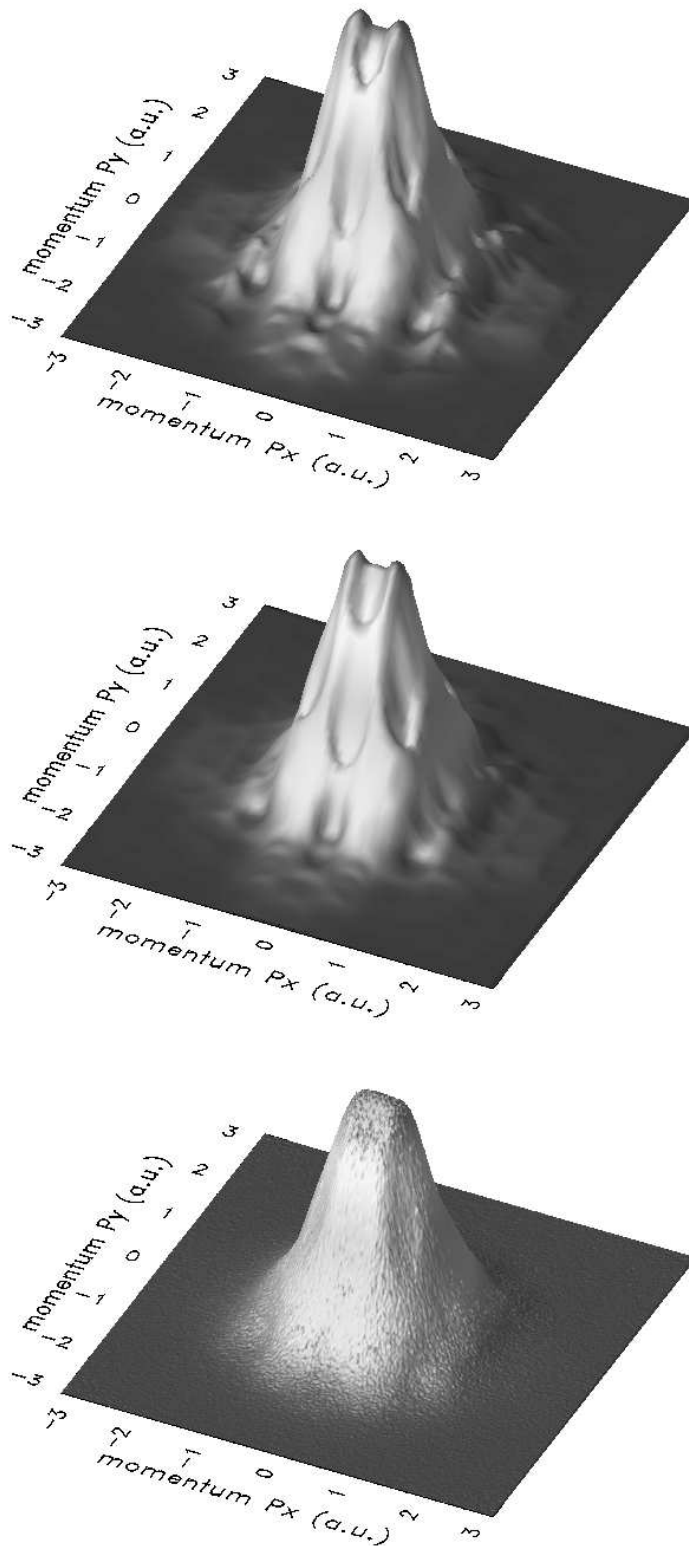


Figure 4.3: 2D-ACAR for V perpendicular to the [210] direction: SPR-KKR calculations (top), LMTO calculations [18] (middle) and experiment [18] (bottom).

energy path is used to evaluate the backscattering term and the off-diagonal contribution of electron-positron Green's function in Eq. (4.11), whilst the single-site term is evaluated through the energy integration path parallel to the real energy axis.

The SPR-KKR 2D electron-positron momentum density projected in the plane perpendicular to the [001] direction is presented in Fig. 4.2, together with the LMTO calculations [18] and the 2D-ACAR experimental data [18]. The resolution of the momenta for SPR-KKR spectra in the  $(p_x, p_y)$  plane is  $\Delta p = 0.04975$  a.u. whilst for the LMTO calculated spectra and for the experimental 2D-ACAR spectra is  $\Delta p = 0.05489$  and  $\Delta p = 0.01344$  respectively. The theoretical spectra are scaled to the same height as the experimental 2D-ACAR spectra.

As can be seen in both figures, the agreement between the SPR-KKR and LMTO calculations is very good. As the LMTO calculations include the electron-positron correlation effect, one should notice that this effect is minor in this case. The main features of the SPR-KKR and LMTO two-dimensional electron-positron momentum density can be traced back to the experimental spectra if one takes into account that the broadening is present in the experimental measurements.

## 4.4 Comparison with Compton scattering

As it was mentioned, the quantity of interest in Compton scattering is the electron momentum density given by Eq. (4.3), whilst the positron annihilation experiment is able to explore features of the electron-positron momentum density (see Eq. (4.1)). By the procedure described above one is able to determine both distribution functions. Between the expressions for  $n_{2\gamma}(\vec{p})$  and  $n(\vec{p})$  the difference appear mostly in the matrix elements which enter the expression for the  $G_{m_s}(\vec{p})$  (see the comparison of the matrix elements in Appendix D) and in the calculation of the t-matrix and the scattering path operators. The aim in the following is to demonstrate the difference between those two distribution functions. In other words, we want to see the impact of the positron wave function on the momentum distribution function in the case of pure Fe.

We will compare the magnetic Compton profile for Fe with the corresponding quantity, which is the one-dimensional projection of the  $(n_{2\gamma}^\uparrow - n_{2\gamma}^\downarrow)$  electron-positron momentum density (see Eq. (4.12)), given by:

$$J_{mag}^{2\gamma}(p_z) = \int \int (n_{2\gamma}^\uparrow - n_{2\gamma}^\downarrow) dp_x dp_y . \quad (4.15)$$

The SPR-KKR magnetic Compton profile (here denoted as  $J_{mag}(p_z)$ ) for Fe along the [001] and [110] scattering directions is represented in Fig 4.4, together with  $J_{mag}^{2\gamma}(p_z)$  constructed on the basis of the electron-positron momentum density. Also, the comparison between the SPR-KKR and LMTO calculations [18] of the magnetic Compton profile and the one dimensional projection of the  $(n_{2\gamma}^\uparrow - n_{2\gamma}^\downarrow)$  electron-positron momentum density is shown in Fig 4.4.



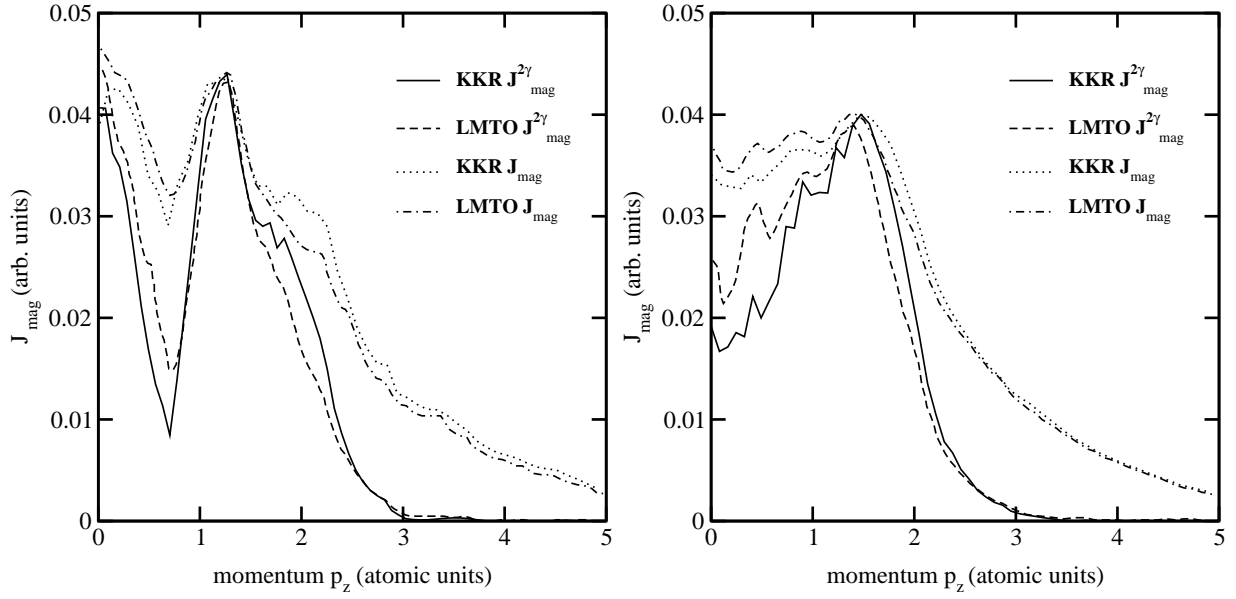


Figure 4.4: Left: The SPR-KKR and LMTO [18] calculated magnetic Compton profile  $J_{mag}(p_z)$  of Fe along the [001] (left) and the [110] direction (right) is compared with the positron annihilation spectra  $J_{mag}^{2\gamma}(p_z)$ .

One can see in Fig. 4.4 that the positron annihilation profile  $J_{mag}^{2\gamma}(p_z)$  decay more rapidly than the magnetic Compton profile  $J_{mag}(p_z)$  along the  $p_z$  direction for both scattering directions. The reason why the positron annihilation profile decays more rapidly in p-space is that the more localized states (at higher momentum) are not sampled by the positron, because the positron interact in a more pronounced way with the delocalized s and p-electrons from the interstitial region. Therefore the resulting profile is narrower for the positron annihilation spectra than for the Compton case.

Also, the dips at  $\sim 0.7$  a.u in the [001] spectra and at  $p_z \sim 0$  a.u. in the [110] spectra are deeper in the positron annihilation spectra. One can explain this feature due to a more pronounced contribution of the s- and p-orbitals for the positron annihilation spectra. The decomposition of the MCP spectra of Fe along the [001] direction into the s-, p- and d-like contributions has been presented in Fig. 3.3 and is given once more in Fig. 4.5 (right). As can be seen in Fig. 4.5, the s- and p-orbitals have a negative contribution at the MCP of Fe. Because the interaction between the positron and the s- and p-electrons is more pronounced in the positron annihilation experiment, one can expect that the negative contributions of the s- and p-electrons at the total positron annihilation spectra are increased compared with the Compton profile. The effect of this increased negative contribution is to generate deeper dips in the positron annihilation spectra compared with the Compton profile. In order to verify this effect, we performed a decomposition of the positron annihilation spectra  $J_{mag}^{2\gamma}(p_z)$  into s-, p- and d-like contributions. As expected, the s- and p-like contributions are negative and their

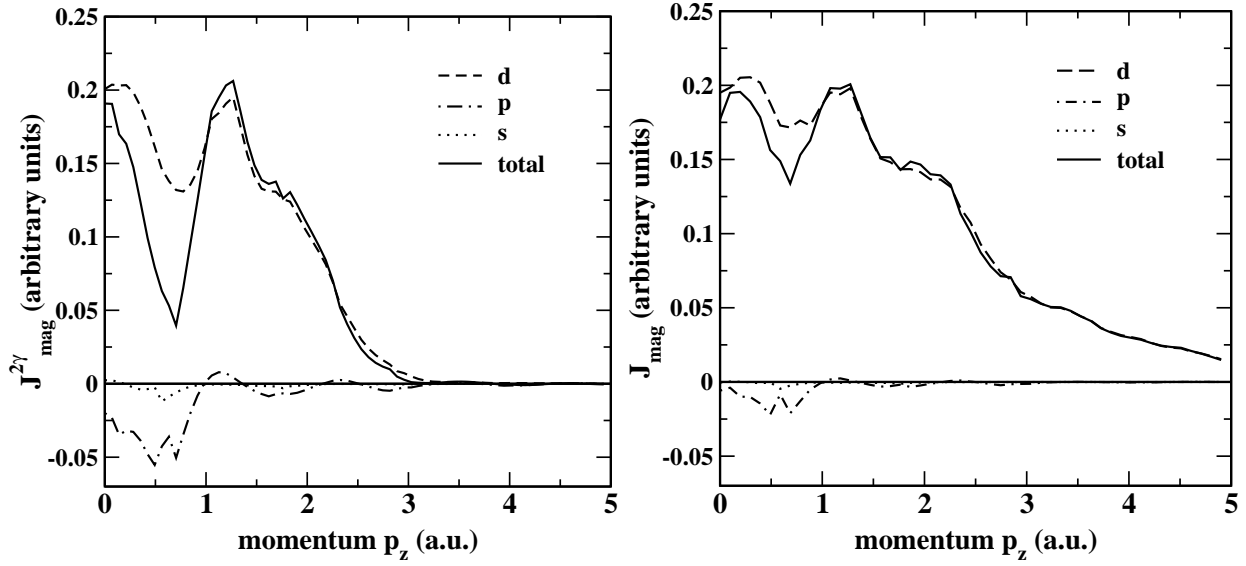


Figure 4.5: The SPR-KKR s, p and d- contribution to the positron annihilation spectra  $J_{mag}^{2\gamma}(p_z)$  of Fe along the [001] direction (left) compared with the decomposition of the corresponding magnetic Compton profile (right).

magnitude is increased compared with the s- and p-like contributions at the corresponding magnetic Compton profile. One also has to notice the very good agreement between the SPR-KKR and LMTO calculations, as can be seen in Fig. 4.4.

## 4.5 Conclusions

The SPR-KKR formalism for calculation of the electron-positron momentum density has been presented. This formalism was applied for the calculation of the two-dimensional momentum density of V perpendicular to the [001] and [211] directions, respectively. The very good agreement between the SPR-KKR and LMTO theoretical spectra and also with the experimental 2D-ACAR measurements should be emphasized. Also, the comparison of the magnetic Compton profile  $J_{mag}(p_z)$  and the positron annihilation spectra  $J_{mag}^{2\gamma}(p_z)$  for Fe along [001] and [110] directions is presented.

## Chapter 5

# Ground-state properties of Cr-chalcogenide systems

Transition-metal chalcogenides have attracted much interest in the past due to their large variety of physical properties, particularly concerning the relationship between the magnetic ordering and the combination of the metal and chalcogen atom. In this chapter we will summarize first the structural and magnetic properties of Cr-chalcogenides, as they are reflected in the investigations of several research groups. After the picture of the magnetism in CrX ( $X=S, Se, Te$ ) systems - as reflected in the literature - has been sketched, we will present and discuss new features of the magnetic properties in this systems found by our fully relativistic band-structure SPR-KKR calculations. The relationship between the crystalline structure, chemical composition and ground-state properties in CrX - CrX<sub>2</sub> ( $X = S, Se, Te$ ) systems will be investigated in the following section.

The binary CrX ( $X = S, Se, Te$ ) systems crystallize in the NiAs-type crystal structure. This structure (see below) consists of a hexagonal close packing of the metalloid atoms with the transition metal atoms located in the interstices in such a way as to form a simple hexagonal array. In all binary Cr-selenides, sulphides or tellurides magnetic moments - mainly localized on Cr - are present. The exchange interactions are predominantly antiferromagnetic in Cr-selenides and Cr-sulphides (Goodenough 1963 [137]), in contrast to the ferromagnetic Cr-tellurides [138].

NiAs-type Cr<sub>1-x</sub>S, which always has a few per cent Cr vacancies, exists only above 623 K. Below this temperature a Jan-Teller distortion around Cr<sup>2+</sup> (d<sup>4</sup>) results in a monoclinic lattice (Jellinek 1957 [139]). High temperature susceptibility data above 900 K give  $\theta = -1585$  K and  $\mu_{eff} = 5.24 \mu_B$  for CrS (Popma and Bruggen 1969 [140]). The extrapolated Curie-Weiss temperature  $\theta$  is a measure of the overall sign and magnitude of the exchange constants (positive  $\theta$  means ferromagnetic state, negative  $\theta$ , antiferromagnetic state). The sign of  $\theta$  gives the indication for an antiferromagnetic state in Cr<sub>1-x</sub>S below the Néel temperature at 450 K [141]. A metal-semiconductor transition is observed for Cr<sub>1-x</sub>S with  $x \leq 0.1$  at  $\sim 620$  K, while Cr<sub>1-x</sub>S with  $x \geq 0.1$  are metals.

The magnetic susceptibility measurements (Tsubokawa 1956 [142]) on NiAs-type compound

$\text{Cr}_{1-x}\text{Se}$  performed on single crystals show a Néel point close to 300 K and an effective magnetic moment of  $4.90 \mu_B$ . The extrapolated Curie-Weiss temperature determined by Lotgering and Gorter (1957) [143] is  $\theta = -185$  K, which gives an evidence of an antiferromagnetic state of this compound. Specific heat measurements (Tsubokawa 1960 [144]) locate the Néel temperature  $T_N$  at 320 K.

The anomalies present in both susceptibility data sets [143, 142] below 300 K have led these authors to suggest a magnetic phase transition and a non-collinear spin structure at lower temperature. The calculations of Hirone and Adachi [145], who considered the magnetic properties of the NiAs structures in the molecular-field approximation, showed that triangular spin configurations were stable over certain regions of the molecular-field coefficients of first, second and third nearest neighbours.

This theoretical result seems to be confirmed by the neutron diffraction measurements of the magnetic structure for CrSe performed by Corliss et al. [146] which show a umbrella-like antiferromagnetic spin structure.

The system  $\text{Cr}_{1-x}\text{Te}$  can be found in different phases, depending on the  $x$  value. According to the phase diagram determined by Ipser et al. [147], for  $x \leq 0.1$ , the system has the hexagonal NiAs structure. The monoclinic structure was found for the  $\text{Cr}_3\text{Te}_4$ , whilst the system  $\text{Cr}_2\text{Te}_3$  is trigonal. For the system  $\text{Cr}_5\text{Te}_8$ , both monoclinic and trigonal structures have been observed (Bensch et al. [148]). The monoclinic and trigonal structures are related to the NiAs structure type by successive removal of Cr in every second metal atom layer parallel to the  $c$  axis. The vacancy ordering within the layers can be influenced by thermal treatment. Also, a slight increase of the Te content leads to an order-disorder transition of the Cr vacancies from the monoclinic to trigonal phase [148].

$\text{Cr}_{1-x}\text{Te}$  with the hexagonal NiAs structure is a ferromagnet with the Curie temperature  $T_C \sim 340$  K, a saturation moment at 4.2 K of about  $2.4 - 2.7 \mu_B$  and an effective paramagnetic moment of  $\sim 4.0 - 4.5 \mu_B$  [143, 149, 150, 151].

There is a disagreement between the magnetic moments on Cr of  $4 \mu_B$  and higher determined by paramagnetic susceptibility measurements or the band structure calculations and respectively the low values of Cr magnetic moments from the saturation of the magnetisation at 4.2 K ( $\sim 2.4 \mu_B$ ). The ionic description in  $\text{Cr}^{+2}\text{Te}^{-2}$  would give for Cr the  $3d^4$  electronic configuration which corresponds to a magnetic moment of about  $4.8 \mu_B$  ( $\mu_{eff} = [q_c(q_c+2)]^{1/2}$ , where  $q_c$  is the number of unpaired electrons). This disagreement can be explained to some extent by non-collinear spin structures which may occur in this compound. Such structures are suggested by neutron diffraction studies (Bertaut et al. 1964 [152], Lambert-Andron et al. [153], Andresen 1963 [154], Makovetskii and Shakhlevich 1979 [155], Hamasaki et al. [156]) but the various investigations don't agree concerning the spin structure and magnitude of the Cr local magnetic moment. Most investigators conclude that the diffractograms of hexagonal  $\text{Cr}_{1-x}\text{Te}$  between 0 K and  $T_C$  can be described in terms of a collinear ferromagnetic structure. If the spin structure is collinear ferromagnetic, the ratio  $m_c/m_s$  (where  $m_c$  and  $m_s$  are the number of Bohr magnetons derived from the saturation magnetisation and from paramagnetic susceptibilities, respectively) is  $4.0/2.4 \sim 1.6$ . This value is bigger than 1, as expected for itinerant ferromagnets.

The band structure calculations performed for Cr-chalcogenide systems by Dijkstra et al.

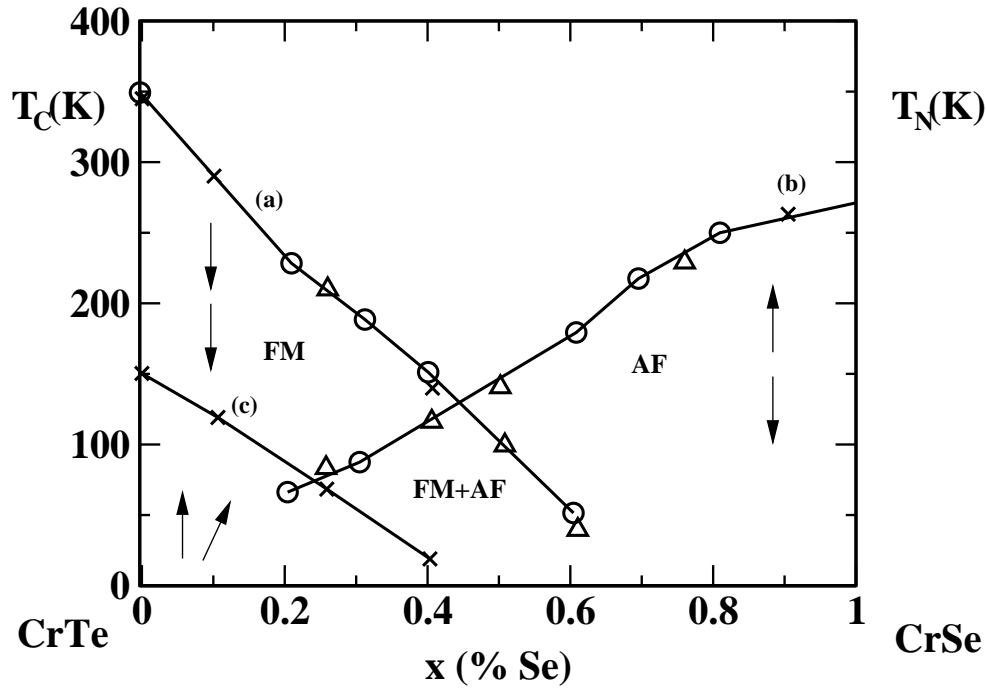


Figure 5.1: The magnetic phase diagram of  $\text{CrTe}_{1-x}\text{Se}_x$  [19] deduced from temperature dependence of magnetisation (crosses), neutron scattering measurements (triangles) and resistivity measurements (circles). The magnetic ordering (ferro-, antiferromagnetic and non-collinear) is indicated by arrows.

[8, 138] using the ASW method show for CrS and CrSe an antiferromagnetic ordering, apart from CrTe which is ferromagnet. This magnetic behaviour is confirmed by FLAPW band-structure calculations of Kawakami et al. [157].

There are studies which show that the magnetic ordering in CrX ( $X = \text{S}, \text{Se}, \text{Te}$ ) is influenced by the pressure. Kanomata et al. [158] found a giant magnetovolume effect for CrTe, which was suggested by the earlier FLAPW calculations of Takagaki et al. [159, 160]. From the total energy calculations as a function of lattice parameter it was found in addition that a pressure induced ferromagnetic  $\rightarrow$  antiferromagnetic transition is expected for CrTe at about 40 GPa. The complexity of the magnetic behaviour of Cr-chalcogenides is reflected in the magnetic phase diagram of the system  $\text{CrTe}_{1-x}\text{Se}_x$  (see Fig. 5.1). This phase diagram was suggested by Makovetskii (1986) [19]. The results of magnetic phase transition studies in the system  $\text{CrTe}_{1-x}\text{Se}_x$ , based on neutron diffraction measurements (triangles in Fig. 5.1), on analysis of the temperature dependence of magnetization (crosses) and electrical resistivity (circles) are used to obtain this phase diagram. In the region of Se concentration lower than 0.4, when the temperature is lower than line (a), the ferromagnetic ordering is observed with the arrangement of the magnetic moments within the basis plane. The Curie temperature

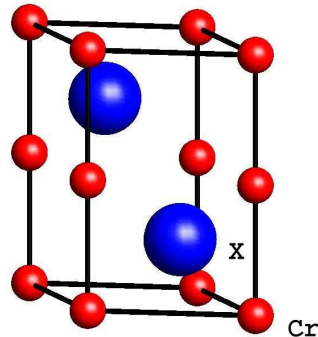


Figure 5.2: The NiAs structure for the CrX ( $X = \text{S}, \text{Se}, \text{Te}$ ) systems.

decreases nearly linear with the increasing of the Se content. Below the curve (c) the non-collinear magnetic structure occurs.

The alloys with Se concentration  $x$  between 0.7 and 1.0 have an antiferromagnetic order below the line (b), an umbrella-like non-collinear ordering of the magnetic moments being the most probable. The variation of the Néel temperature with increasing of the Se concentration of solid solutions deviates from a linear variation. In the region with Se concentration between 0.2 and 0.6 both ferromagnetic and antiferromagnetic ordering occurs, at the temperatures below lines (a) and (b).

## 5.1 Structural properties of binary CrX ( $X = \text{S}, \text{Se}, \text{Te}$ ) compounds

The systems CrX ( $X = \text{S}, \text{Se}, \text{Te}$ ) crystallize in the hexagonal NiAs structure (see Fig. 5.2). The space group of this structure is  $P6_3/mmc$  or  $D_{6h}^4$  (No. 194 in the *International Table of Crystallography*), with the Cr atoms at the  $(2a)$  sites  $(0, 0, 0)$  and  $(0, 0, \frac{1}{2})$  and the chalcogen atoms at the  $(2c)$  sites  $(\frac{1}{3}, \frac{2}{3}, \frac{1}{4})$  and  $(\frac{2}{3}, \frac{1}{3}, \frac{3}{4})$ .

The experimentally determined lattice parameters at room temperature are listed in the Table 5.1. The  $c_0/a_0$  ratio is smaller than the ideal value of 1.663 for CrTe and bigger than the ideal value for the other Cr-chalcogenides. Six chalcogen atoms form a trigonally distorted octahedron around Cr. A Cr atom is further surrounded by six other Cr atoms in the basal  $ab$  plane at the distance  $a_0$ . Much shorter metal-metal distances are present along the  $c$ -axis: a Cr atom has two Cr neighbours at  $c_0/2$ , as can be seen in the interatomic distances in the

	CrS	CrSe	CrTe
$a_0$ (Å)	3.456	3.684	3.997
$c_0$ (Å)	5.761	6.020	6.223
$c_0/a_0$	1.667	1.634	1.557

Table 5.1: The experimental [5, 6, 7] lattice parameters for CrX (X = S, Se, Te) systems.

	N		CrS	CrSe	CrTe
Cr-X (Å)	6		2.461	2.606	2.783
Cr-Cr (Å)	2	$c$	2.881	3.010	3.112
Cr-Cr (Å)	6	$ab$	3.456	3.684	3.997

Table 5.2: The interatomic distances in the NiAs structure for CrX (X = S, Se, Te) systems. N is the number of neighbours and  $c$  and  $ab$  distinguish Cr-neighbours along the  $c$ -axis and within the  $ab$  plane.

NiAs structure for the CrX (X = S, Se, Te) compounds presented in Table 5.2. One should note that the NiAs structure is not unique for the CrX (X = S, Se, Te) systems, the monoclinic distortion for the non-stoichiometric  $\text{Cr}_{1-x}\text{S}$  (Jellinek 1957 [139]) or the (partial) ordering of Cr vacancies in alternate metal layers of  $\text{Cr}_{1-x}\text{Te}$ , resulting in the trigonal space group  $P\bar{3}m1$  (or  $D_{3d}^3$ ) [138] are often mentioned as alternative crystal structure for these compounds.

## 5.2 Band-structure calculations of CrX (X = S, Se, Te) systems

Electronic band-structure calculations of CrX (X = S, Se, Te) have been performed for a collinear ferromagnetic and respectively antiferromagnetic arrangement of the Cr magnetic moments, as is shown in Fig. 5.6.

The band-structure calculations have been performed using the SPR – KKR method within the atomic sphere approximation (ASA). Exchange and correlation were treated in the local spin density approximation (LSDA). The parametrization of Vosko, Wilk and Nusair for exchange-correlation energy was used.

In the SPR-KKR-ASA, the Wigner-Seitz cells, located at the atomic sites are replaced by atomic spheres (AS) and the spherically symmetric potential within the spheres is extending to their boundaries. The sum of the volumes of those spheres is equal to the unit cell volume. This approximation completely neglects the interstitial part of the crystal. The coherent potential approximation (CPA) described in the section 2.3.1 is used to deal with disordered/non-stoichiometric compounds.

### 5.2.1 Density of states

The total density of states (DOS) of ferromagnetic CrS, CrSe and CrTe obtained by SPR-KKR calculations are shown in Figs. 5.3, 5.4 and 5.5. The density of states of CrS, CrSe and CrTe systems have similar features, which are listed in the following.

The band at around 12 eV binding energy has s-anion origin, whilst the higher energy

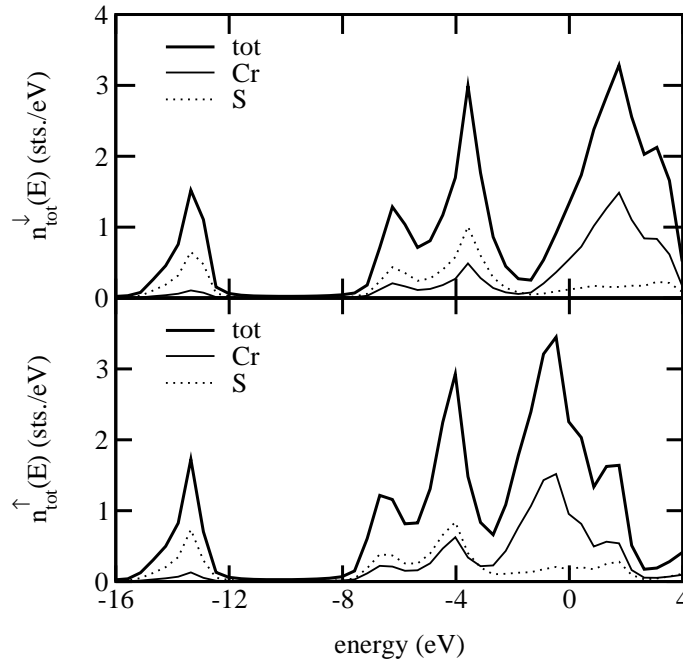


Figure 5.3: The spin-resolved KKR density of states of CrS.

band has Cr(3d)-X(p) character. In the lower part of the d-p band, the p-character is obvious and the influence of the exchange-splitting is minor. The higher part of the d-p band, having a Cr(3d) character show a clear exchange-splitting. The differences between the three compounds appear in the exchange-splitting and d-p peaks separation (in  $\uparrow$  and  $\downarrow$  bands), as can be seen in the Table 5.3. The SPR-KKR density of states (DOS) for CrX (X = S, Se, Te)

Exchange splitting Cr 3d (eV)	CrS	CrSe	CrTe
KKR	2.2	2.6	2.7
ASW [8]	2.5	2.7	2.9

Table 5.3: The exchange-splitting of the Cr(3d) states of CrX (X = S, Se, Te) systems in KKR and ASW calculations (Dijkstra et al. [8]).



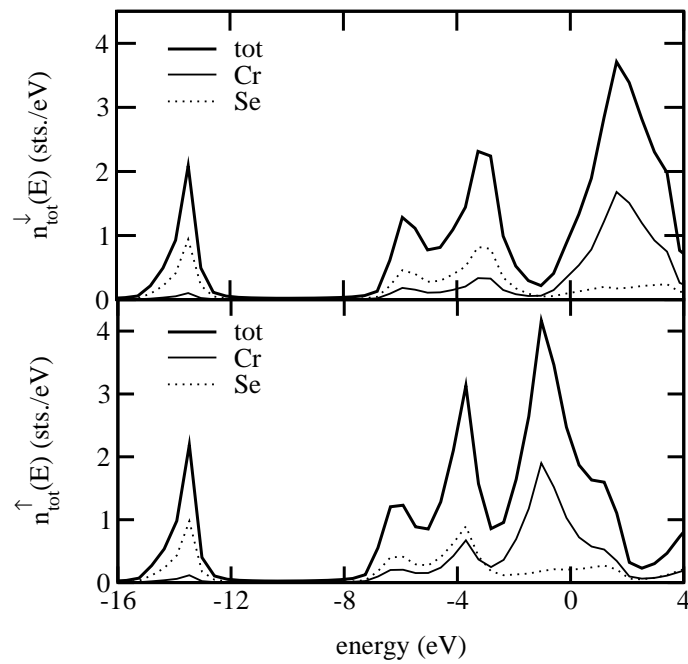


Figure 5.4: The spin-resolved KKR density of states of CrSe.

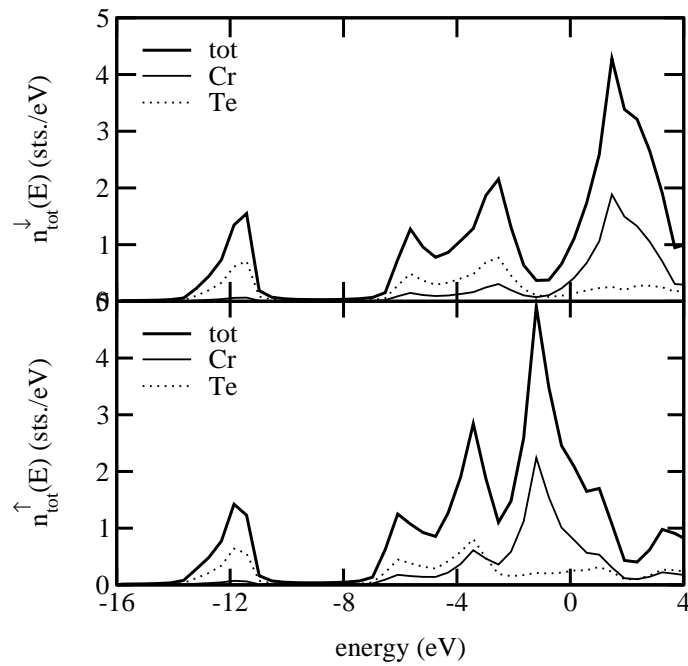


Figure 5.5: The spin-resolved KKR density of states of CrTe.

systems are similar with the ASW results of Dijkstra et al. [8] and LMTO calculations of Knecht [161].

## 5.2.2 Phase stability

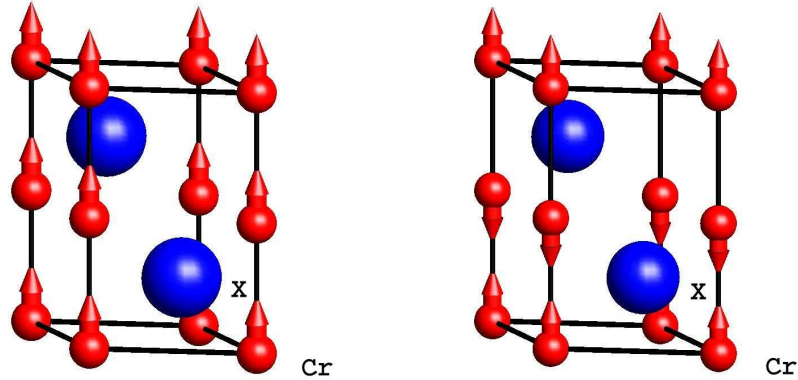


Figure 5.6: The spin configuration for ferromagnetic/antiferromagnetic calculation.

As it was suggested by the extrapolated Curie-Weiss temperature [140, 143], the ground state in the CrS and CrSe compounds is not ferromagnetic, but rather antiferromagnetic. For the CrTe compound, the ferromagnetic state is reported to be more stable [138, 159]. Having this in mind, we performed SPR-KKR calculations for the CrX (X = S, Se, Te) systems with a ferro- and antiferromagnetic spin configuration shown in Fig. 5.6. Comparing the total energies of the systems, as shown in Table 5.4, we found that the AF state of CrS and CrSe is indeed lower in energy than the FM state. For CrTe, the FM state is energetically more favourable. These trends confirm the previously cited experimental measurements and the ASW calculations of Dijkstra et al. [8], but doesn't exclude a possible non-collinear spin configuration as ground state of these systems.

	$E_{FM} - E_{AF}$ (mRy)	lower in energy
CrS	1.31	AF
CrSe	0.88	AF
CrTe	-3.91	FM

Table 5.4: Total energy difference  $E_{FM} - E_{AF}$  (mRy) in CrX (X = S, Se, Te) systems from SPR-KKR calculations.

### 5.2.3 Magnetic moments

The different number of occupied majority and minority states gives rise to a net magnetic moment per formula unit of CrX (X = S, Se, Te). The SPR-KKR calculated magnetic moments are presented in Table 5.5, together with the magnetic moments resulting from scalar-relativistic LMTO (Perlov [9]) and from ASW calculations (Dijkstra et al. [8]). As can be seen

	calculation mode	CrS	CrSe	CrTe
Cr magnetic moment ( $\mu_B$ )	SPR KKR	2.73	3.28	3.44
	LMTO	2.63	3.23	3.38
	ASW	2.84	3.40	3.51
X magnetic moment ( $\mu_B$ )	SPR KKR	0.001	0.002	-0.011
	LMTO	0.04	0.05	0.04
	ASW	0.20	0.24	0.22

Table 5.5: Magnetic moments in CrX (X = S, Se, Te) compounds resulting from SPR-KKR, LMTO [9] and ASW [8] calculations.

in Table 5.5, the Cr magnetic moments obtained by different calculation methods are comparable. The Cr magnetic moments increase from CrS to CrTe, this trend being present in all calculations. While the different band-structure calculation are in agreement concerning the Cr magnetic moment in CrX (X=S, Se, Te) systems, this does not apply for the chalcogen magnetic moment. The SPR-KKR finds the chalcogen atom almost non-magnetic, whilst the LMTO method predict magnetic moments  $\sim 0.04 \mu_B$ . The ASW predictions for the magnetic moment of chalcogen atom in those compounds give rather big values of  $\sim 0.2 \mu_B$ , but still small compared to Cr magnetic moments. Element specific magnetic measurements would be necessary to allow for a better description of these compounds.

Our fully relativistic SPR-KKR method allows for the calculations of orbital and spin magnetic moments, giving a more detailed picture of Cr-chalcogenide magnetism compared with the scalar-relativistic ASW (Dijkstra et al. [138]) or LMTO (Perlov [9]) methods. The spin and orbital magnetic moments for Cr, resulting from ferro- and antiferromagnetic calculations are shown in Table 5.6. As can be seen, the orbital magnetic moment in these compounds are about  $\sim 1\%$  of the value of spin magnetic moments. In the ground state, the spin and orbital magnetic moments are antiparallel for CrS and CrSe and parallel for CrTe. For all calculations, the spin magnetic moments of Cr in antiferromagnetic state is found to be  $\sim 5\%$  lower than in the ferromagnetic state. The same trend concerning the AF/FM Cr magnetic moments was reported by Dijkstra et al. [8] obtained from ASW calculations. They reported AF total magnetic moments for Cr to be about  $\sim 7-10\%$  lower than the FM magnetic moments.

The orbital magnetic moments are very small, antiparallel with the spin magnetic moment in Cr S and CrSe compounds and parallel in CrTe.

	FM		AF	
	$m_s$	$m_l$	$m_s$	$m_l$
CrS	2.736	-0.024	2.606	-0.032
CrSe	3.282	-0.013	3.066	-0.010
CrTe	3.439	0.007	3.284	0.022

Table 5.6: Magnetic moments of Cr in CrX (X = S, Se, Te) compounds resulted from FM/AF SPR-KKR calculations.

### 5.3 Non-collinear spin structures

A complementary approach to investigate the magnetic behaviour of solids is to consider particular microscopic models making use of magnetic interaction. One of the approaches widely used to consider magnetic properties of solids is the Heisenberg model that is normally used to describe the interaction of exchange coupled localised magnetic moments. An application of this model to metals requires some care because of the features related to the itinerant character of d-electrons [162, 163, 164, 165]. Nevertheless, this approach turned out to be very useful for the understanding of magnetic properties. Moreover, it is used very successfully in studies of magnetic metals and alloys. In line with these experiences, it is assumed in the following that the itinerant-electron system can be described (as is discussed in [162, 163]) by an effective classical Heisenberg Hamiltonian

$$H_{ex} = - \sum_{ij} J_{ij} \hat{e}_i \cdot \hat{e}_j, \quad (5.1)$$

where the summation is performed over all lattice sites  $i$  and  $j$ . Here  $\hat{e}_i$  and  $\hat{e}_j$  are the unit vectors along the directions of the magnetic moments on sites  $i$  and  $j$  respectively,  $J_{ij}$  is the exchange coupling parameter for the corresponding magnetic moments. A rigorous expression for the exchange parameters  $J_{ij}$  can be obtained using local spin density functional (LDSF) approach together with the KKR method. The approach described by Lichtenstein et al. [162, 163] is based on the calculation of the variation of the total energy with small deviations of two magnetic moments from their equilibrium directions. The exchange interaction parameter  $J_{ij}$  between the magnetic moments located on sites  $i$  and  $j$  is then given by the formula:

$$J_{ij} = \frac{1}{4\pi} \Im \int^{E_F} Tr_L (t_{i\uparrow}^{-1} - t_{i\downarrow}^{-1}) \hat{\tau}_{\uparrow}^{ij} (t_{j\uparrow}^{-1} - t_{j\downarrow}^{-1}) \hat{\tau}_{\downarrow}^{ji} dE. \quad (5.2)$$

Here  $t_{im_s}$  and  $\hat{\tau}_{m_s}^{ij}$  are the single-site scattering  $t$ -matrix and the scattering path operator for spin  $m_s$  and connected with the sites  $i$  and  $j$ .  $Tr_L$  means the trace over the orbital states labelled by the combined quantum number  $L = (l, m_l)$ .

Since these parameters are nothing else but the energy changes due to rotations of spin magnetic moments, they can be used to analyse the stability of a magnetic structure in a crystal. In particular, if negative values of  $J_{ij}$  parameters give the main contribution to the spin magnetic moment exchange interaction within a crystal implies that the underlying magnetic configuration is unstable because a small deviation results in an energy decrease. Thus analysing the  $J_{ij}$  values one can already draw some conclusions about the stability of a magnetic configuration.

### 5.3.1 Non-collinear spin structure in CrSe system

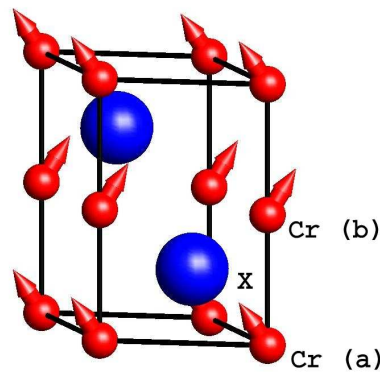


Figure 5.7: Non-collinear spin configuration in CrSe system. The spin orientation is shown for Cr atoms.

The KKR calculation of the exchange-coupling parameters  $J_{ij}$  in CrSe has been done by S. Mankovsky [20]. The exchange-coupling parameters are represented as a function of distance in Fig. 5.8 considering a ferromagnetic spin configuration of the system. The origin of the distance scale is the Cr(a) site at the position  $(0, 0, 0)$  (see Fig. 5.2). The Cr atom located at the position  $(0, 0, \frac{1}{2})$  will be denoted Cr(b). The chalcogen atoms are located at  $(\frac{2}{3}, \frac{2}{3}, \frac{1}{4})$  and  $(\frac{1}{3}, \frac{1}{3}, \frac{3}{4})$  in crystallographic units. The interatomic distances in the CrSe system can be seen in Table 5.2.

As have been discussed in section 5.2.3, the Se atoms have no own spontaneous magnetic moments, and the existing magnetic moments are induced on Se by the magnetic Cr atoms. For this reason their magnetic moments values are extremely sensitive to the neighbourhood. Therefore it will be more correct from our point of view if we will consider only Cr-Cr magnetic interactions and to neglect Cr-Se interactions. For the pair Cr(a)-Cr(b) a significant negative exchange coupling parameter has been obtained, but the energy introduced by the Heisenberg interaction (see Eq.(5.1)) is positive, which means that the relative spin orientation of the pair Cr(a)-Cr(b) is energetically not favourable.

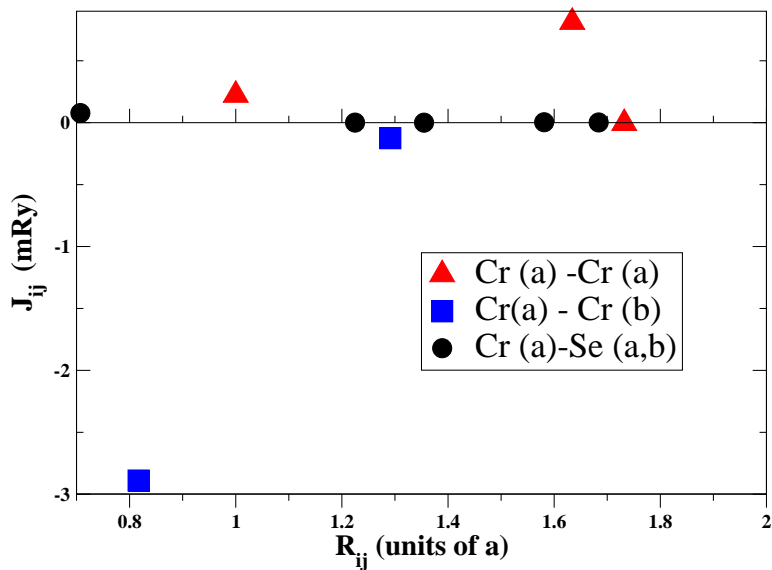


Figure 5.8: The exchange coupling parameters  $J_{ij}$  for ferromagnetic spin configuration in the system CrSe [20].

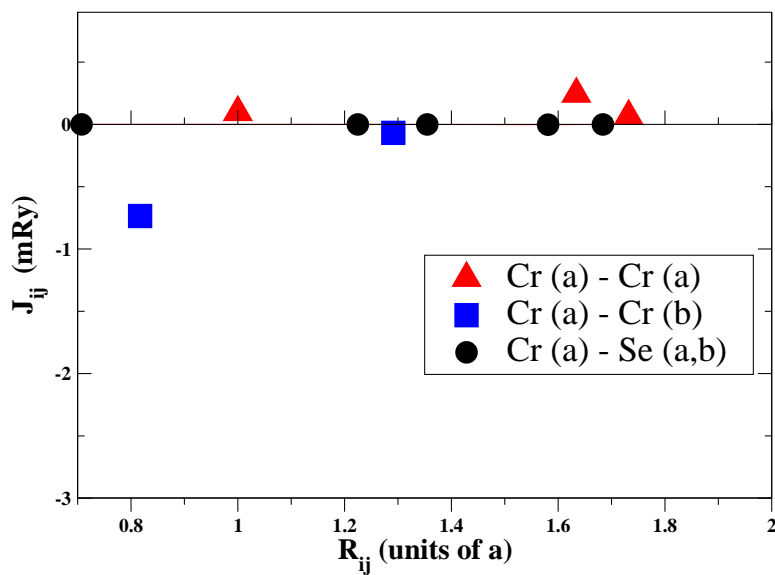


Figure 5.9: The exchange coupling parameters  $J_{ij}$  for antiferromagnetic spin configuration in the system CrSe [20].

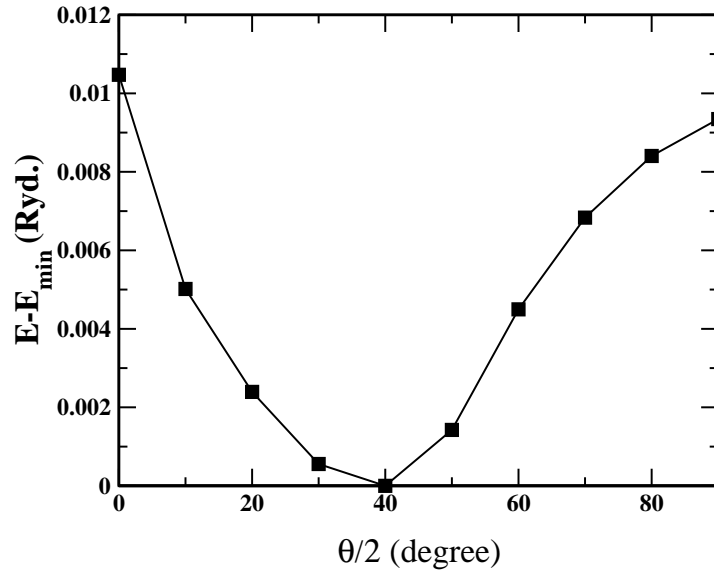


Figure 5.10: The total energy vs.  $\theta$  angle for the spin configuration from Fig. 5.7. SPR-KKR calculations for CrSe system.

The pair Cr(a)-Cr(a) has positive exchange-coupling parameter, but the magnitude of the exchange coupling parameter  $J_{ij}$  is  $\sim 12$  times smaller than the corresponding value of the parameter for the Cr(a)-Cr(b) pair. The ferromagnetic spin orientation of the Cr(a)-Cr(a) pair is energetically favourable, but the ordering energy is much smaller compared with the contribution of a Cr(a)-Cr(b) pair.

This consideration may give us a hint of a possible alternative spin configuration of the system. The conclusion from studying the nearest-neighbour spin interaction CrSe system is that the ferromagnetic spin arrangement is not energetically favourable and cannot be the ground state of this system.

The band-structure calculations are in agreement with this result, giving for a possible ground state an antiferromagnetic arrangement of spins. The calculation of the exchange coupling parameters has been done (Mankovsky [20]) also for an antiferromagnetic spin arrangement in CrSe system. The geometry is the same like in the ferromagnetic case. The exchange coupling parameters  $J_{ij}$  are represented in Fig. 5.9 as a function of the distance.

As can be seen, the main features in the spin-spin interaction between nearest neighbours seems to be unchanged. The Cr-Se magnetic coupling is negligible. The Cr(a)-Cr(a) magnetic interaction is smaller than in the ferromagnetic phase. The highest magnitude of the coupling occur for the Cr(a)-Cr(b) pairs. The sign of the exchange-coupling parameters shows us that in the antiferromagnetic phase, like in the ferromagnetic one discussed before the magnetic energy introduced by the spin-spin coupling destabilise the system. As a consequence we can expect that the magnetic ordering in the ground state of this system have to be a non-collinear one.

In order to prove this conclusion, we performed SPR-KKR calculations for a non-collinear

spin arrangement of the CrSe system. The spin configuration is shown in Fig. 5.7. The spins of Cr(a) and Cr(b) atoms are tilted, having a tilt angle  $\theta/2$  in respect to the  $c$  axis. Fig. 5.10 shows the total energy as a function of the tilt angle  $\theta/2$ . One can see in Fig. 5.10 that the spin configuration with  $\theta = 0^\circ$  (ferromagnetic phase) is not favourable. Also, the spin configuration for  $\theta = 180^\circ$  (antiferromagnetic phase) is not favourable, but is lower in energy compared with the ferromagnetic phase. The configuration lowest in energy and in consequence the most favourable one is the non-collinear spin arrangement having the  $\theta$  angle about  $80^\circ$ .

On the basis of this result, we conclude that a non-collinear spin arrangement in the CrSe is preferred. The SPR-KKR energy-band calculations and the calculations of the exchange coupling parameters are in full accordance concerning the ground-state spin configuration in CrSe system. One has to mention that the non-collinear spin configuration of the CrSe system may be more complex and the refinement of the spin configuration is possible in order to confirm a certain spin structure determined in experiment.

### 5.3.2 Non-collinear spin structure in CrTe system

The KKR calculation for the exchange-coupling parameters  $J_{ij}$  in CrTe has been done by S. Mankovsky [20]. The exchange-coupling parameters are represented as a function of distance in Fig. 5.11 for a ferromagnetic spin configuration and respectively in Fig. 5.12 for an antiferromagnetic spin configuration. Analysing the  $J_{ij}$  values for both spin configurations one can see similarities with the CrSe system. The Cr(a)-Cr(b) exchange parameters have considerably large negative values for the first coordination shell for both spin configurations. For shells farther away, the Cr(a)-Cr(b) exchange parameters indicate slight magnetic stabilities in the ferromagnetic case (Fig 5.11), while  $J_{ij}$  oscillates in the antiferromagnetic configurations (Fig. 5.12).

The energy of the exchange interaction between Cr(a) magnetic moments is negligible in the ferromagnetic configuration, only the second shell gives a small positive contribution. In the antiferromagnetic case, the Cr(a) - Cr(a) magnetic exchange interaction is positive for all coordination shells, but the energy of this interaction is significant smaller than the corresponding energy of Cr(a)-Cr(b) nearest neighbours.

Our analysis on the  $J_{ij}$  values cannot decide whether one of the ferro/antiferromagnetic phase of CrTe is more stable. The SPR-KKR calculation for a non-collinear spin arrangement in the CrTe system is required to give a clearer indication concerning the most stable spin configuration. Considering the spin configuration shown in Fig. 5.7, the total energy dependence on the half of the tilt angle between the spins is shown in Fig. 5.13.

As in the CrSe case, the spin configuration with  $\theta = 0^\circ$  (ferromagnetic phase) and  $\theta = 180^\circ$  (antiferromagnetic phase) are not favourable. The spin configuration with the highest stability is non-collinear, as in the CrSe case. This result (see also [166]) is in agreement with the phase diagram from Fig. 5.1 reproduced from Makovetskii [19]. Also, other experimental reports about non-collinear spin configuration in CrTe systems [152, 153, 154, 155, 156] support our result.



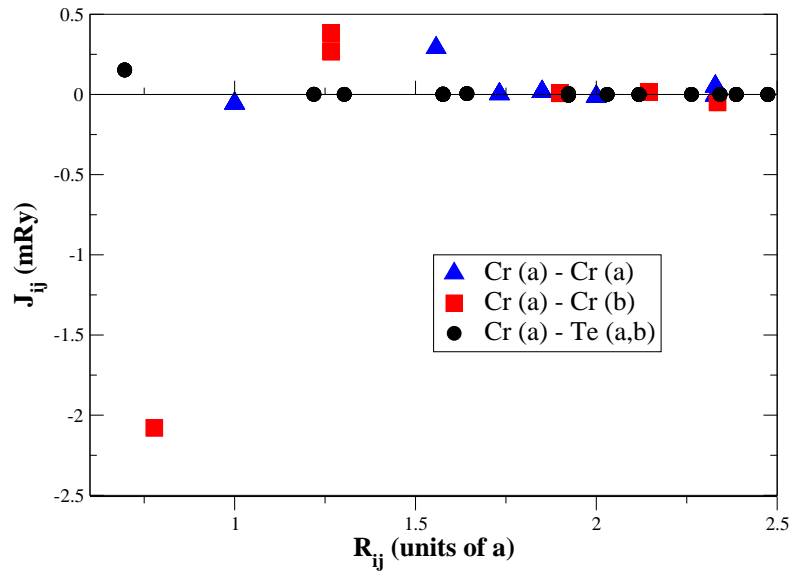


Figure 5.11: The exchange coupling parameters  $J_{ij}$  for ferromagnetic spin configuration in the system CrTe [20].

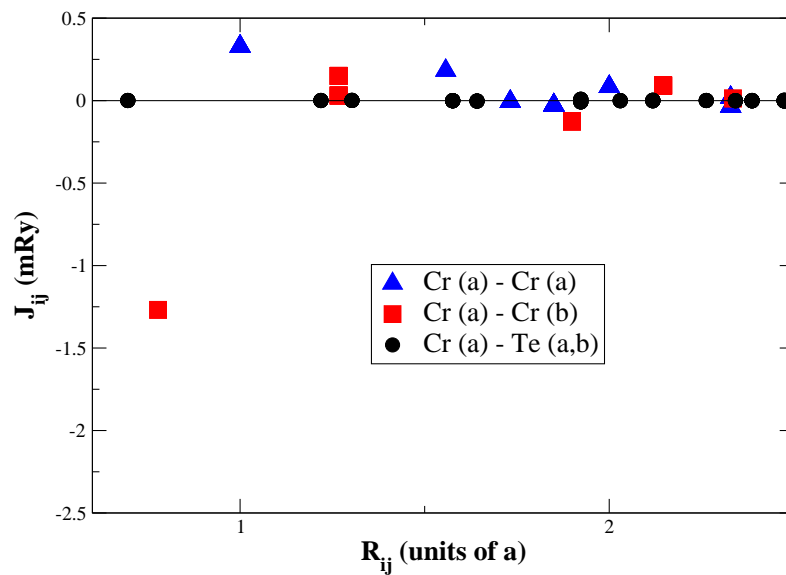


Figure 5.12: The exchange coupling parameters  $J_{ij}$  for antiferromagnetic spin configuration in the system CrTe [20].

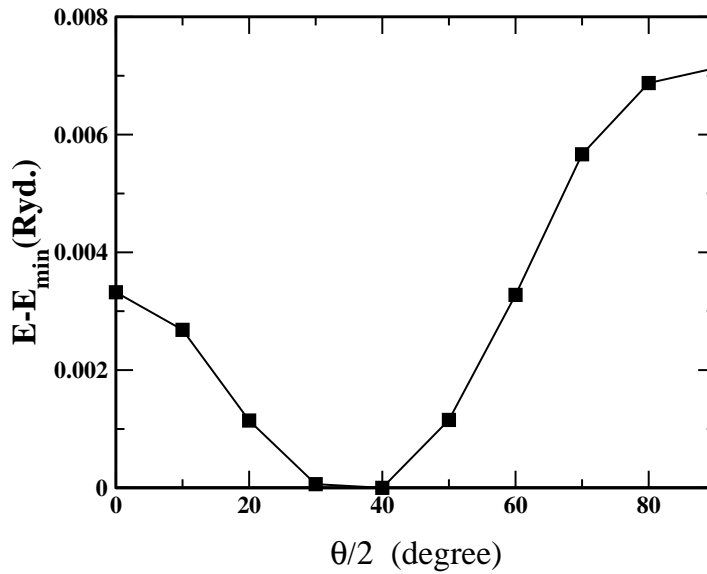


Figure 5.13: The total energy vs. tilt angle  $\theta$  for the spin configuration from Fig. 5.7. SPR-KKR calculations for the CrTe system.

## 5.4 Band-structure calculations for the system $\text{CrTe}_{1-x}\text{Se}_x$

### 5.4.1 Magnetic moments

In order to investigate the influence of the Se/Te content on the ground state properties of the  $\text{CrTe}_{1-x}\text{Se}_x$  system, we performed fully relativistic SPR-KKR calculations for the ferromagnetic phase of this system. The lattice parameters  $a$  and  $c$  used for band-structure calculations have been derived considering that they have linear dependence on the Se concentration.

The behaviour of the Cr magnetic moments as a function of the Se concentration is presented in Fig. 5.14. As expected from the results for the stoichiometric compounds, the total magnetic moments decrease with Se concentration, from  $3.42 \mu_B$  at 10% Se to  $3.28 \mu_B$  at 90% Se. The spin magnetic moment has a similar behaviour, decreasing with Se concentration. As a consequence of fully relativistic calculations, we can give separate predictions for the spin and orbital magnetic moments. As can be seen in Fig. 5.14, the orbital and spin magnetic moments of the compound  $\text{CrTe}_{1-x}\text{Se}_x$  are parallel for  $x$  lower than  $\sim 0.25$  % Se and antiparallel for higher Se concentrations. The absolute values of the orbital moment are lower than  $0.012 \mu_B$ .

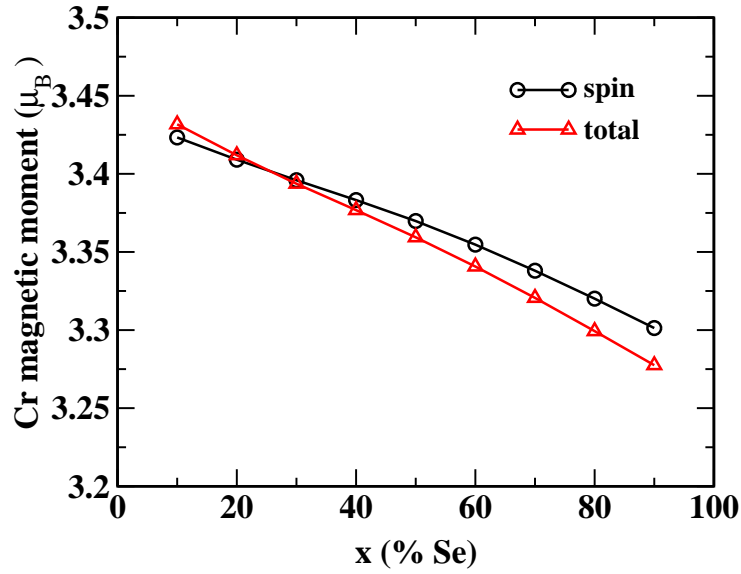


Figure 5.14: The behaviour of the magnetic moments in  $\text{CrTe}_{1-x}\text{Se}_x$  system with increasing Se concentration, as resulted from SPR-KKR calculations.

## 5.4.2 Magnetic ground state

As it was shown by Makovetskii [19], the magnetic ordering in the system  $\text{CrTe}_{1-x}\text{Se}_x$  is very complex. As can be seen in the phase diagram in Fig. 5.1, there are several spin configurations for this system for different temperature ranges and Se concentration.

We were interested to determine the magnetic ground state for the concentration points

	$a_{lat}$	$c_{lat}$	$c/a$
FM	3.559	5.775	1.622
AF	3.535	5.825	1.647
exp	3.777	6.080	1.609

Table 5.7: The SPR-KKR-LSDA equilibrium lattice parameters of  $\text{CrTe}_{0.30}\text{Se}_{0.70}$  system for AF and FM, compared with the experimental values ([5, 6, 7]).

close to the ferro- antiferromagnetic border, where the phase diagram didn't give a clear answer for the magnetic ground state of the system.

In order to establish the magnetic ground state, we have chosen the point with a concentration of 70 % Se and performed fully relativistic SPR-KKR calculation for the system  $\text{CrTe}_{0.30}\text{Se}_{0.70}$  with ferromagnetic and antiferromagnetic spin configuration. The exchange-correlation treatment was done within the local spin density approximation (LSDA) making

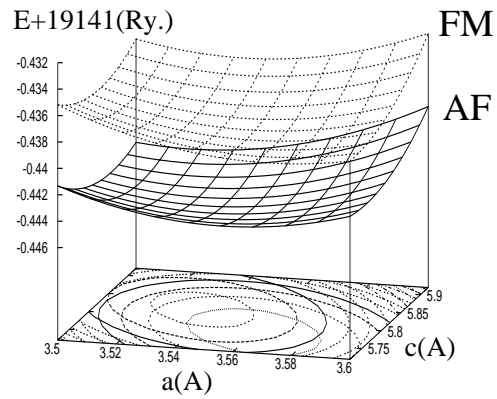


Figure 5.15: The total energy of the system  $\text{CrTe}_{0.30}\text{Se}_{0.70}$  as a function of lattice parameters, as resulted from SPR-KKR calculations, using LSDA to describe the exchange-correlation potential.

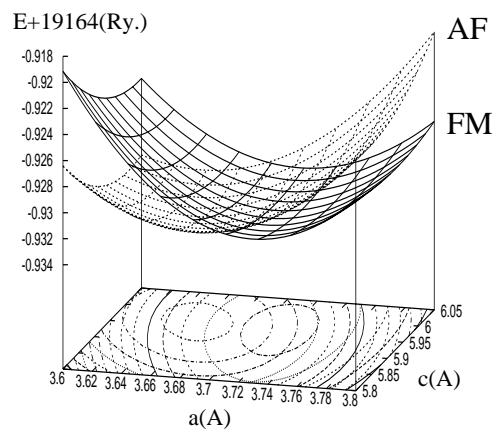


Figure 5.16: The total energy of the system  $\text{CrTe}_{0.30}\text{Se}_{0.70}$  as a function of lattice parameters, as resulted from SPR-KKR calculations using the GGA to describe the exchange-correlation potential.

use of the Voskow, Wilk and Nusair exchange-correlation energy. The band-structure calculation for both magnetic states have been done with variable lattice parameters  $a$  and  $c$ . The magnetic spin orientation within the unit cell is shown in Fig. 5.6.

Fig. 5.15 shows the total energy of the system in the ferro- and the antiferromagnetic states as a function of lattice parameters  $a$  and  $c$ . The energy-surface was reproduced from individual calculations, in such a way that the total energy fits the following equation:

$$E_T = \alpha_1 a^2 + \alpha_2 c^2 + \alpha_3 a^2 c^2 + \alpha_4 a^2 c + \alpha_5 a c^2 + \alpha_6 a c + \alpha_7 a + \alpha_8 c + E_0 \quad (5.3)$$

As can be seen, for both magnetic states, the total energy shows a minimum for a pair of  $(a_{min}, c_{min})$  lattice parameters. The antiferromagnetic state is lower in energy than the ferromagnetic state; the difference between the AF and the FM minimum energy of the energy-surface is 6.1 mRy. The result of our SPR-KKR calculations gives a clear indication for an antiferromagnetic ground state in this system.

The lattice parameters corresponding to the minima of this energy-surface, the so-called equilibrium lattice parameters are shown in Table 5.7. The calculated equilibrium lattice parameters are smaller by  $\sim 6\%$  than the experimental values. This disagreement between the experimental values and calculations is induced by the treatment of exchange-correlation within the local spin density approximation (LSDA) which overestimates the binding and lowers the equilibrium lattice parameters.

As a consequence, we repeated our calculations using the Perdew-Burke-Erzerhof (PBE) version of the general gradient approximation (GGA) for the exchange-correlation energy. The total energy surfaces have been constructed in the same way as for the SPR-KKR-LSDA calculations, fitting Eq. (5.3). Fig. 5.16 shows the total energy surfaces for ferro- and antiferromagnetic state as a function of the lattice parameters  $a$  and  $c$ . Different from the SPR-KKR-LSDA calculations, for certain ranges of the  $(a, c)$  lattice parameters, the ferromagnetic state is lower in energy. There is a crossing of the ferro- and antiferromagnetic energy surfaces, but the AF phase is still energetically favoured because the AF minimum is lower in energy with 0.96 mRy than the FM minimum. The equilibrium lattice parameters shown in Table 5.8 are closer to the experimental values, the difference to these values being smaller than 2%.

	$a_{lat}$	$c_{lat}$	$c/a$
FM	3.7132	5.9605	1.605
AF	3.6563	5.9653	1.631
exp	3.777	6.080	1.609

Table 5.8: The SPR-KKR-GGA equilibrium lattice parameters of  $\text{CrTe}_{0.30}\text{Se}_{0.70}$  system for AF and FM, compared with the experimental values ([5, 6, 7]).

## 5.5 Band-structure calculations for $\text{Cr}_{1+x}(\text{Te}_{1-y}\text{Se}_y)_2$ systems

### 5.5.1 Structural properties of $\text{Cr}_{1+x}(\text{Te}_{1-y}\text{Se}_y)_2$ compounds

The  $\text{Cr}_5\text{Te}_8$  compounds crystallise in a monoclinic or in a trigonal structure, depending on the actual composition [148, 167]. It is expected that the cation substitution in  $\text{Cr}_5\text{Te}_8$  will lead to new phases with distinct crystal structures and different physical properties.  $\text{Cr}_5\text{Te}_{8-x}\text{Se}_x$  samples were synthesised recently by Bensch et al. [10] directly from the elements via a high-temperature reaction with slowly cooling or quenching the products. Another approach was undertaken using the high-pressure high-temperature route [10]. The crystal structures were determined with Rietveld refinements.

The quenched samples crystallise in the  $\text{CdI}_2$  type of structure (space group  $P\bar{3}m1$  or  $D_{3d}^3$ )

	a(Å)	c(Å)	c/a	z
$\text{Cr}_{1.22}(\text{Te}_{0.88}\text{Se}_{0.12})_2$	3.8577	5.9876	1.551	0.2525
$\text{Cr}_{1.23}(\text{Te}_{0.88}\text{Se}_{0.12})_2$	3.8615	5.9894	1.551	0.2531
$\text{Cr}_{1.26}(\text{Te}_{0.88}\text{Se}_{0.12})_2$	3.8709	6.0113	1.553	0.2521
$\text{Cr}_{1.28}(\text{Te}_{0.75}\text{Se}_{0.25})_2$	3.8284	6.0087	1.569	0.2508
$\text{Cr}_{1.28}(\text{Te}_{0.88}\text{Se}_{0.12})_2$	3.8757	6.0355	1.557	0.2522
$\text{Cr}_{1.33}(\text{Te}_{0.88}\text{Se}_{0.12})_2$	3.8994	6.0546	1.552	0.2515

Table 5.9: The lattice parameters for  $\text{Cr}_{1+x}(\text{Se}/\text{Te})_2$  non-stoichiometric trigonal compounds [10].

shown in Fig. 5.17 (left), while a superstructure is identified for the samples  $\text{Cr}_{5+x}(\text{Te}/\text{Se})_8$  which were slowly cooled to room temperature. Both structures are related to the NiAs-type structure. In the quenched samples, the Cr atoms are completely disordered over the Cr sites, while in  $\text{Cr}_{5+x}(\text{Te}/\text{Se})_8$  the vacancies in the Cr layers are found partially ordered.

The trigonal symmetry of the quenched samples possess the following atom positions: Cr(a) at  $(0, 0, 0)$ , Cr(b) at  $(0, 0, 1/2)$  and Te/Se at  $(\frac{1}{3}, \frac{2}{3}, z)$  and  $(\frac{2}{3}, \frac{1}{3}, -z)$ . One can see in Fig. 5.17 that Cr(a), Cr(b) and Te/Se crystallographic positions define corresponding atom-layers along the  $c$  axis which alternate in the sequence Cr(a), Te/Se, Cr(b), Te/Se. The value of  $z$  is close to 0.25, which would correspond to equal distances between the Cr(a), Cr(b) and Te/Se layers.

The SPR-KKR band structure calculations have been performed for the quenched samples of type  $\text{Cr}_{1+x}(\text{Te}_{0.88}\text{Se}_{0.12})_2$  and  $\text{Cr}_{1+x}(\text{Te}_{0.75}\text{Se}_{0.25})_2$  with  $x$  between 0.21 and 0.33, prepared by Bensch et al. [10]. The lattice parameters and the  $z$  values are presented in Table 5.9.

The neutron diffraction measurements performed by Bensch et al. [10] show that the Cr(a) plane at  $z = 0$  and the Te/Se planes are fully occupied, whilst the Cr(b) plane at  $z = \frac{1}{2}$  is only partially occupied. The coherent potential approximation (CPA) described in section 2.3.1 is used to deal with these compounds. Using the CPA, a random distribution of Se/Te

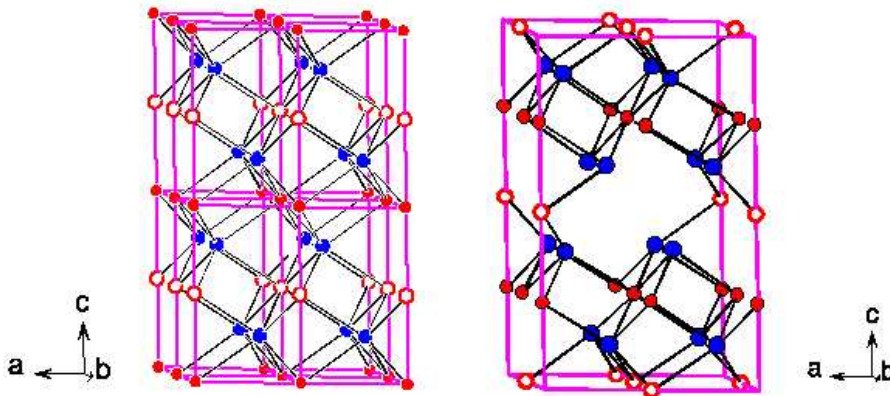


Figure 5.17: The structure of the non-stoichiometric  $Cr_{1+x}Q_2$  ( $Q=Te/Se$ ) compounds (left). The crystal structure of  $Cr_{5+x}Te_8$  (right) [10].

atoms within the chalcogen planes and a random distribution of the vacancies within the Cr(b) layer is considered.

## 5.5.2 Preferential site occupation

The neutron diffraction data (Bensch et al. [10]) concerning the site occupation in the systems  $Cr_{1+x}(Te/Se)_2$  systems was questioned. The layer of Cr at  $z = 0$  denoted by  $a$  (see Fig. 5.17, left) is fully occupied, whilst the plane of Cr(b) at  $z = 1/2$  is only partially occupied. The preference of Cr atoms for one of the layers must be energetically determined and it must be reflected in the variation of the total energy if a certain percentage of Cr is moved from Cr(a) to Cr(b) layer.

In order to verify this supposition, we performed SPR-KKR band-structure calculations to evaluate the variation of the total energy of the system, considering that  $x$  % of the Cr(a) atoms are moved into Cr(b) plane, according to the scheme:  $Cr_{1.0}Cr_{0.28}(Te_{0.88}Se_{0.12})_2 \rightarrow Cr_{1-x}^a Cr_{x+0.28}^b (Te_{0.88}Se_{0.12})_2$ . As can be seen in Fig. 5.18, a positive variation in the total energy of the  $Cr_{1.28}(Te_{0.88}Se_{0.12})_2$  system is produced by moving Cr atoms from Cr(a) to Cr(b) planes. This variation in the total energy increases almost linearly with  $x$ , the amount of the moved Cr atoms. The increasing of the total energy for this transformation shows clearly that the Cr(a) sites are preferential occupied by Cr atoms. If the Cr concentration would increase in this system, the Cr(a) plane would be occupied first. Only after the Cr(a) plane have been fully occupied, the Cr atoms start to populate the Cr(b) plane.

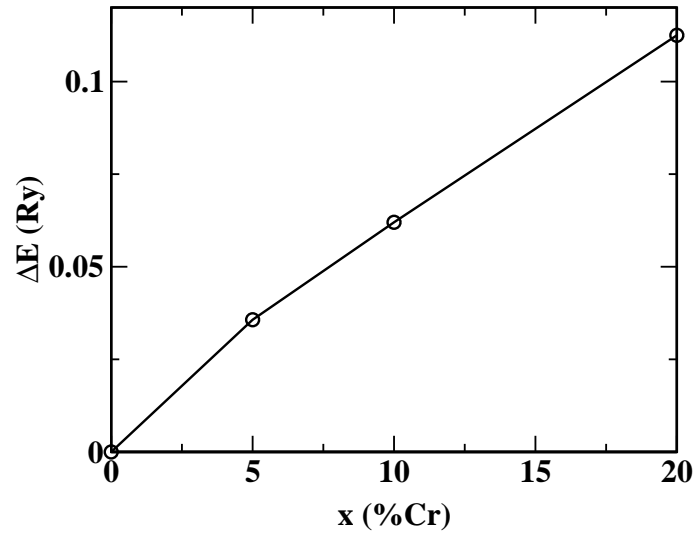


Figure 5.18: The SPR-KKR total energy variation of the system  $\text{Cr}_{1.28}(\text{Te}_{0.88}\text{Se}_{0.12})_2$  as a function of Cr concentration  $x$  moved from site  $a$  to site  $b$ , according to the scheme:  $\text{Cr}_{1.0}\text{Cr}_{0.28}(\text{Te}_{0.88}\text{Se}_{0.12})_2 \rightarrow \text{Cr}_{1-x}^a\text{Cr}_{x+0.28}^b(\text{Te}_{0.88}\text{Se}_{0.12})_2$ .

### 5.5.3 Density of states and magnetic moments

The spin-resolved density of states for three systems of  $\text{Cr}_{1+x}(\text{Te}/\text{Se})_2$  type are presented in Figs. 5.19, 5.21 and 5.20. The main features of the DOS for these compounds are the same as for the binary Cr chalcogenides, namely the s-band at lower energy and the d-p band crossing the Fermi level. The difference appear in exchange-splitting and in the separation of the p-like and d-like peaks in the d-p band. For both majority and minority states, the d-p separation is lower in these trigonal compounds than in the CrTe/CrSe of NiAs-type.

The magnetic moments for  $\text{Cr}_{1+x}(\text{Te}/\text{Se})_2$  obtained by SPR-KKR band-structure calculations are presented in Tables 5.10 and 5.11. As can be seen in Table 5.10, the magnetic moments of Cr on Cr(b) sites are about 25 % smaller than the magnetic moments on Cr(a) sites. We find an increase of the Cr(a)/Cr(b) magnetic moments with an increase of the Cr

	$x = 0.22$	$x = 0.23$	$x = 0.26$	$x = 0.28$	$x = 0.33$
Cr a	2.955	2.965	3.002	3.031	3.107
Cr b	2.199	2.199	2.343	2.43	2.458
Te	-0.200	-0.203	-0.202	-0.203	-0.206
Se	-0.282	-0.286	-0.283	-0.285	-0.283

Table 5.10: Magnetic moments in trigonal  $\text{Cr}_{1+x}(\text{Te}_{0.88}\text{Se}_{0.12})_2$  non-stoichiometric compounds (in  $\mu_B$ ).



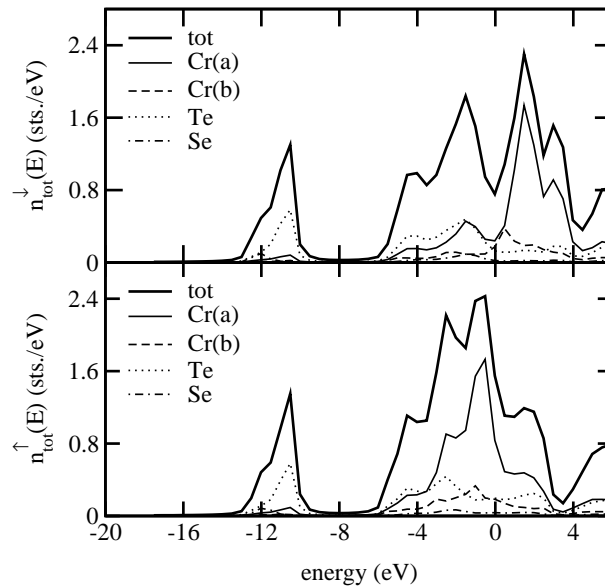


Figure 5.19: Spin-resolved DOS of the system  $Cr_{1.23}(Te_{0.88}Se_{0.12})_2$  obtained by SPR-KKR calculations.

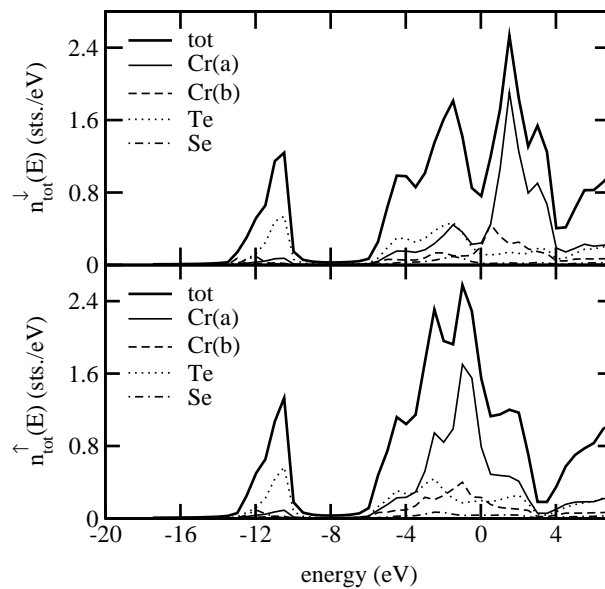


Figure 5.20: Spin-resolved DOS of the system  $Cr_{1.28}(Te_{0.88}Se_{0.12})_2$  obtained by SPR-KKR calculations.

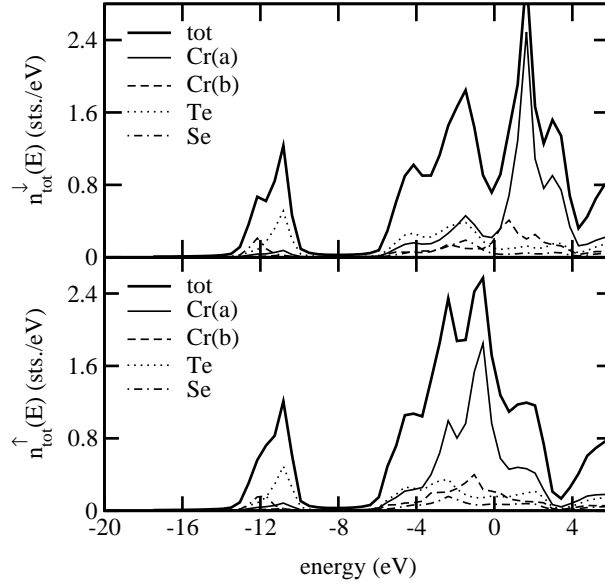


Figure 5.21: Spin-resolved DOS of the system  $\text{Cr}_{1.28}(\text{Te}_{0.75}\text{Se}_{0.25})_2$  obtained by SPR-KKR calculations.

	$\text{Cr}_{1.28}(\text{Te}_{0.88}\text{Se}_{0.12})_2$		$\text{Cr}_{1.28}(\text{Te}_{0.75}\text{Se}_{0.25})_2$	
	$m_{spin}(\mu_B)$	$m_{orb}(\mu_B)$	$m_{spin}(\mu_B)$	$m_{orb}(\mu_B)$
Cr(a)	3.019	0.011	2.962	0.007
Cr(b)	2.407	0.023	2.356	0.020
Te	-0.194	-0.008	-0.188	-0.008
Se	-0.281	-0.003	-0.270	-0.003

Table 5.11: Magnetic moments in trigonal  $\text{Cr}_{1.26}(\text{Te}_{0.88}\text{Se}_{0.12})_2$  and  $\text{Cr}_{1.26}(\text{Te}_{0.75}\text{Se}_{0.25})_2$  non-stoichiometric compounds (in  $\mu_B$ ).

content of the system. The average magnetic moments on Cr are in these  $\text{Cr}_{1+x}(\text{Te}_{0.88}\text{Se}_{0.12})_2$  non-stoichiometric compounds about 20 - 25 % smaller compared with the corresponding values in  $\text{CrTe}_{1-x}\text{Se}_x$  for  $x = 0.12$ .

We should note also the magnitude and the sign of the magnetic moment on the chalcogen atoms. Their magnetic moments are antiparallel with the Cr moments and their magnitude is significantly increased compared with the values of chalcogen atoms magnetic moments in  $\text{CrTe}_{1-x}\text{Se}_x$  (see Fig. 5.14). The chalcogen magnetic moment for non-stoichiometric compounds is almost independent on the Cr content. The negative magnetic polarisation of Te/Se atoms is explained by Dijkstra et al. [138] by a covalent mixing of Cr 3d and chalcogen p-bands. The calculated DOS of  $\text{Cr}_{1+x}(\text{Te}/\text{Se})_2$  systems is in agreement with this supposition [168].

For the compounds with the same Cr content ( $x = 0.28$ ) but different Te/Se ratio, the mag-

netic moments are presented in Table 5.11. The magnetic moments on Cr are slightly influenced by the chalcogen content. The enhancement of Cr magnetic moment with the Te content follows the general trend, as it was found for  $\text{CrTe}_{1-x}\text{Se}_x$  binary alloys.

## 5.6 Band-structure calculations for $(\text{Cr}_x\text{Ti}_{1-x})_5\text{Te}_8$ systems

Depending on the actual composition and the thermal treatment the binary Cr telluride  $\text{Cr}_5\text{Te}_8$  crystallizes in a monoclinic ( $m$ ) or trigonal ( $t$ ) structure [148]. Both structures are derived from the hexagonal NiAs structure type by successive removal of Cr atoms from every second metal atom layer parallel to the crystallographic  $c$  axis. The monoclinic ( $m$ ) phase is stable within the composition range  $\text{Cr}_{5.42}\text{Te}_8$  -  $\text{Cr}_{4.98}\text{Te}_8$ , whilst the stability of the trigonal phase covers the composition range  $\text{Cr}_{4.96}\text{Te}_8$  -  $\text{Cr}_{4.80}\text{Te}_8$ . Within the fully occupied metal atom layers the  $\text{CrTe}_6$  octahedra share common edges, the connection of the octahedra between full and metal deficient layers is achieved via common faces. The Cr - Cr distances within the full metal atom layers are longer than 3.8 Å excluding direct magnetic exchange interactions. In contrast, the Cr - Cr separation across the common faces are about 3 Å favouring direct magnetic exchange.

By magnetisation measurements on this system Bensch et al. [169] found out that the monoclinic to trigonal transition and the change of Cr content leads to important changes in the magnetic properties of this system. The system  $\text{Cr}_5\text{Te}_8$  is ferromagnetic, but a small change in the Cr content leads to important changes in the Curie temperature: if for the  $m$ - $\text{Cr}_{5.18}\text{Te}_8$  phase the Curie temperature is 180 K, for  $t$ - $\text{Cr}_{4.85}\text{Te}_8$  phase the Curie temperature is 240 K. Other experimental measurements [170] show for a monocrystalline sample of  $\text{Cr}_5\text{Te}_8$  a Curie temperature of 240 K. Also, the magnetisation measurements along different directions show a strong magnetocrystalline anisotropy of this system. Unfortunately, the crystalline structure characterisation of the samples used in these measurements are missing.

The pseudo-binary compounds  $(\text{Cr}_x\text{Ti}_{1-x})_5\text{Te}_8$  crystallize in the trigonal structure. According to the experimental measurements performed by Bensch et al. [171] for  $\text{CrTi}_4\text{Te}_8$  system, the substitution of Cr by Ti drastically alters the magnetic properties of the samples. A transition into the ferromagnetic state is observed at about 100 K. Susceptibility measurements performed in the zero field cooling (zfc) and field cooling (fc) mode show a divergence of the zfc and fc curves below about 100 K indicating spin glass behaviour. The magnetic moments on Cr are smaller than the reported values for binary CrTe compounds, showing a value of  $2.13 \mu_B$ .

The magnetic susceptibilities of CdI<sub>2</sub>-type  $(\text{Cr}_{1-x}\text{Ti}_x)_5\text{Te}_8$  have been measured by Hatakeyama et al. [172] for the range  $0 \leq x \leq 1$ . The Curie temperature deduced from susceptibility measurements steeply decreases with the increasing of  $x$ . The decreasing slope becomes smaller in the range of higher  $x$  ( $x \geq 0.3$ ).

A remarkable magnetovolume effect in  $(\text{Cr}_{1-x}\text{Ti}_x)_5\text{Te}_8$  systems has been reported [173]. The variation of Curie temperature with pressure have been studied for  $(\text{Cr}_{1-x}\text{Ti}_x)_5\text{Te}_8$  and  $(\text{Cr}_{1-x}\text{V}_x)_5\text{Te}_8$  system. The results show that the pressure needed to destroy the ferromag-

netic phase decrease with increasing  $x$  [173] more pronounced for  $(\text{Cr}_{1-x}\text{V}_x)_5\text{Te}_8$  than for  $(\text{Cr}_{1-x}\text{Ti}_x)_5\text{Te}_8$  systems. This is a second proof that Ti as well as V atoms alters the magnetic phase of the  $\text{Cr}_5\text{Te}_8$  system. Also, the measurements of magnetic moments of Cr deduced from saturation of magnetisation in  $(\text{Cr}_{1-x}\text{V}_x)_5\text{Te}_8$  systems [174] show a value of  $1.9 \mu_B/\text{Cr}$ . This value is remarkably lower than that ( $\sim 3.0 \mu_B$ ) expected on the localized moment for  $\text{Cr}^{3+}$ .

These arguments have been brought to underline the strong dependence of the magnetic properties of  $(\text{Cr}_x\text{Ti}_{1-x})_5\text{Te}_8$  systems into the composition and crystalline structure. The aim of the SPR-KKR calculations is to give a new insight on the properties of these systems. The interesting questions about the change of the magnetic moments with the Cr/Ti ratio in the systems and the preferential occupation of Cr and Ti atoms on different crystallographic sites can get good grounded answers by complementing the experimental work with calculations of the ground state properties.

### 5.6.1 Structural properties of $(\text{Cr}_x\text{Ti}_{1-x})_5\text{Te}_8$ compounds

The crystallographic structure of trigonal  $\text{Cr}_5\text{Te}_8$  is complex, being refined in the space group  $P\bar{3}m1$  with four crystallographically different sites for both Te and Cr. This phase contains two-dimensional planes of Cr and Te alternating along the  $c$  direction. The Te layers are fully occupied, whilst in the Cr layers there are vacancies. The crystallographic structure determined by Bensch et al. [148] takes into account the ordering of the vacancies in the metal layers. For the present calculations we will make use of the reduced model, denoted  $\text{Cr}_{1.25}\text{Te}_2$ . Within this model, the vacancy ordering in the metal layers is not taken into account and a random distribution of the vacancies in the metal layers is considered. In this reduced unit cell, the axes  $a$  and  $c$  are half as the values reported by Bensch et al. [148]. The same reduced model will be used for  $(\text{Cr}_x\text{Ti}_{1-x})_5\text{Te}_8$  systems, denoted now due to this simplification as  $(\text{Cr}_x\text{Ti}_{1-x})_{1.25}\text{Te}_2$  systems.

The Cr/Ti atoms are located on two crystallographically different sites, namely on  $(0, 0, 0)$  and  $(0, 0, 1/2)$ . The Te atoms occupy the sites  $(1/3, 2/3, z)$  and  $(2/3, 1/3, -z)$  where the parameter  $z$  govern the interlayer separation and is not determined by symmetry. This occupation leads to a  $\text{CdI}_2$  type of structure. In these  $\text{CdI}_2$ -like structures, the metal atoms are surrounded by the octahedral arrangement of Te atoms. For an ideal octahedral arrangement, the  $z$  value is  $1/4$  which is close to the observed value (see Table 5.12). The lattice parameters of the systems  $(\text{Cr}_x\text{Ti}_{1-x})_{1.25}\text{Te}_2$  are listed in Table 5.12.

The structure is similar to the non-stoichiometric  $\text{Cr}_{1+x}(\text{Te}/\text{Se})_2$  structure presented in Fig. 5.17. The Cr and Ti atoms are distributed into the metal-layers at  $z = 0$  and  $z = 1/2$ . From the experimental data it was determined that the layer at  $z = 0$  is fully occupied with atoms, whilst the vacancies appear into the  $z = 1/2$  layer. The position of Ti cannot be determined unambiguously making use of the experimental methods [171]. The neutron diffraction experiments performed in order to determine the Cr/Ti distribution in  $\text{TiCr}_4\text{Te}_8$  showed that a statistical distribution of Cr/Ti over the  $z = 0$  and  $z = 1/2$  layers has to be favoured.

	$x = 0$	$x = 0.2$	$x = 0.4$	$x = 0.6$	$x = 1.0$
$a_0$ (Å)	3.8309	3.8434	3.8508	3.8608	3.8735
$c_0$ (Å)	6.4076	6.3703	6.3186	6.2598	6.1266
$c_0/a_0$	1.6726	1.6575	1.6408	1.6214	1.579
$z$	0.2622	0.2606	0.2583	0.2547	0.2540

Table 5.12: The lattice parameters for  $(\text{Cr}_x\text{Ti}_{1-x})_{1.25}\text{Te}_2$  systems measured by Bensch et al. [10]. The value of  $z$  is given in units of  $c$ .

From the literature it is known [175, 169] that the magnetic properties of Cr-Te systems are not only influenced by the Cr:Ti ratio, but also that they are very sensitive to the interatomic distances and  $c/a$  ratio. In order to establish a possible dependence, the interatomic distances in  $(\text{Cr}_x\text{Ti}_{1-x})_{1.25}\text{Te}_2$  systems are presented in Table 5.13. The shortest dis-

	$x = 0.0$	$x = 0.2$	$x = 0.4$	$x = 0.6$	$x = 1.0$
$d_{M-M}$ (Å)	3.204	3.185	3.159	3.129	3.063
$d_{M-Te}$ (Å)	2.730	2.731	2.727	2.723	2.710
$d_{Te-Te}$ (Å)	3.893	3.882	3.863	3.843	3.793

Table 5.13: The average interatomic distances in  $(\text{Cr}_x\text{Ti}_{1-x})_{1.25}\text{Te}_2$  systems. The Cr/Ti atoms are denoted by M.

tance between the metal atoms is  $c/2$  followed by  $a$ . The average distance between the metal atoms (M=Cr/Ti) and Te atoms is calculated using the formula  $d_{M-Te} = \sqrt{(a/3)^2 + (c/4)^2}$ , whilst for the shortest distance between Te atoms the following formula is used:  $d_{Te-Te} = \sqrt{(a/3)^2 + (c/2)^2}$ . As it can be seen in Table 5.13, the metal-metal and metal-Te distances steeply decrease with Cr content. The interatomic distances presented here are in agreement with the interatomic distances ( $d_{Te-Te}$  between 3.79 and 3.90 Å and  $d_{M-Te}$  between 2.71 and 2.73 Å) in  $\text{Cr}_{1-x}\text{Ti}_x\text{Te}_2$  compounds reported by Hatakeyama et al. [173].

## 5.6.2 Preferential site occupation

As the position of Ti cannot be determined unambiguously by the experimental methods, we tried to determine it making use of energetic considerations. We performed SPR-KKR band structure calculations in order to determine the total energy of  $(\text{Cr}_x\text{Ti}_{1-x})_{1.25}\text{Te}_2$  systems. We used in our calculations the lattice parameters measured by Bensch et al. [10]. We started from the supposition that Cr and Ti are statistical distributed on the sites  $(0, 0, 0)$  and  $(0, 0, 1/2)$  within the trigonal unit cell described in the previous section. We will denote in

the following discussion the site  $(0, 0, 0)$  as site  $a$  and respectively the site  $(0, 0, 1/2)$  as site  $b$ . First we tried to determined if one of the crystallographic sites  $a$  or  $b$  is favoured when the metal content of the system is increased. The calculation was performed for  $\text{Cr}_{1.25}\text{Te}_2$  system, making the supposition that a certain percentage of Cr content is moved from site  $a$  to site  $b$ , according to the scheme:  $\text{Cr}_{1.25}\text{Te}_2 \rightarrow \text{Cr}_{1-x}^a \text{Cr}_{x+0.25}^b \text{Te}_2$ . The variation of the total energy as a function of Cr concentration moved from site  $b$  to site  $a$  is presented in Fig. 5.22. The total energy increase if the Cr atoms are moved from site  $a$  to site  $b$ , so we can conclude

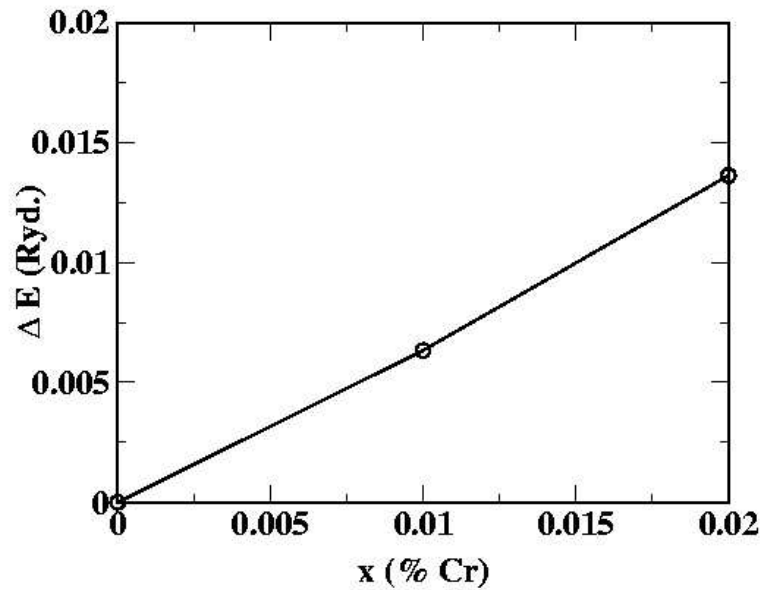


Figure 5.22: The SPR-KKR total energy variation of the system  $\text{Cr}_{1.25}\text{Te}_2$  as a function of Cr concentration  $x$  moved from site  $a$  to site  $b$ , according to the scheme:  $\text{Cr}_{1.25}\text{Te}_2 \rightarrow \text{Cr}_{1-x}^a \text{Cr}_{x+0.25}^b \text{Te}_2$ .

that the site  $a$  is occupied first. If the Cr concentration would increase in the system, only after the site  $a$  is fully occupied Cr atoms starts to populate the site  $b$ . This conclusion is supported by the experimental results showing the vacancies on the  $b$  sites of the  $\text{Cr}_{1.25}\text{Te}_2$  systems.

In order to determine the distribution of Cr and Ti atoms on the sites  $a$  and  $b$ , we started firstly from the supposition that site  $a$  is occupied with Cr and Ti. Secondly, we supposed that the distribution is statistical determined and the occupancy of a certain site ( $a$  or  $b$ ) is proportional with the concentration of Cr/Ti in the compound. This means that for the  $(\text{Cr}_{0.4}\text{Ti}_{0.6})_{1.25}\text{Te}_2$ , the occupation is given by the formula  $(\text{Cr}_{0.4}\text{Ti}_{0.6})^a (\text{Cr}_{0.1}\text{Ti}_{0.15})^b \text{Te}_2$ . We suppose now that a certain percentage (denoted by  $\delta$ ) of Cr atoms is moved from site  $b$  to site  $a$ , according to the scheme:  $(\text{Cr}_{0.4}\text{Ti}_{0.6})^a (\text{Cr}_{0.1}\text{Ti}_{0.15})^b \text{Te}_2 \rightarrow (\text{Cr}_{0.4+\delta}\text{Ti}_{0.6-\delta})^a (\text{Cr}_{0.1-\delta}\text{Ti}_{0.15+\delta})^b \text{Te}_2$ .

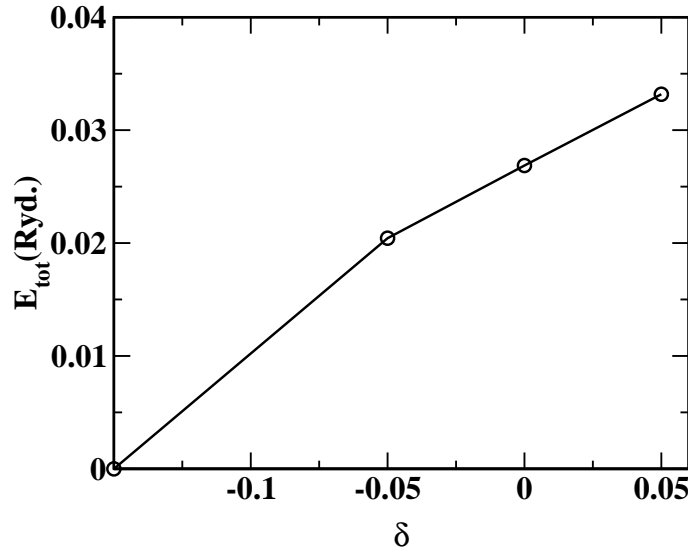


Figure 5.23: The SPR-KKR total energy variation of the system  $(\text{Cr}_{0.4}\text{Ti}_{0.6})_{1.25}\text{Te}_2$  as a function of Cr concentration  $\delta$  moved from site  $b$  to site  $a$ , according to the scheme:  $(\text{Cr}_{0.4}\text{Ti}_{0.6})^a(\text{Cr}_{0.1}\text{Ti}_{0.15})^b\text{Te}_2 \rightarrow (\text{Cr}_{0.4+\delta}\text{Ti}_{0.6-\delta})^a(\text{Cr}_{0.1-\delta}\text{Ti}_{0.15+\delta})^b\text{Te}_2$ .

The SPR-KKR calculations have been performed for the  $(\text{Cr}_{0.4}\text{Ti}_{0.6})_{1.25}\text{Te}_2$  system and the variation of the total energy as a function of  $\delta$  (the percentage of Cr moved from site  $b$  to site  $a$ ) is shown in Fig. 5.23.

The total energy of the system  $(\text{Cr}_{0.4}\text{Ti}_{0.6})_{1.25}\text{Te}_2$  increase if Cr is moved from site  $b$  to site  $a$ . The system with the lowest energy (for  $\delta = -0.15$ ) is described by the formula:  $(\text{Cr}_{0.25}\text{Ti}_{0.75})^a(\text{Cr}_{0.25})^b\text{Te}_2$ . This result reflects the preference of Ti atoms for site  $a$  and respectively of Cr atoms for site  $b$ . The SPR-KKR calculations performed for the other systems of  $(\text{Cr}_x\text{Ti}_{1-x})_{1.25}\text{Te}_2$  type with  $x = 0.2$  and  $x = 0.6$  give similar results.

These results allow us to conclude that the occupation rule in the system  $(\text{Cr}_x\text{Ti}_{1-x})_y\text{Te}_2$  are the following:

- a) increasing the  $y$  content, the Cr/Ti atoms occupy site  $a$  completely
- b) if site  $a$  is occupied, put Cr on site  $b$

### 5.6.3 Density of states and magnetic moments

The density of states for ferromagnetic  $(\text{Cr}_x\text{Ti}_{1-x})_{1.25}\text{Te}_2$  systems with  $0.2 \leq x \leq 1.0$  have been calculated using the SPR-KKR method. The spin-resolved density of states of the systems with  $x = 0.2$ ,  $x = 0.4$ ,  $x = 0.6$  and  $x = 1.0$  are presented in Figs. 5.24, 5.25, 5.26 and 5.27. One should note that the densities of states presented here have been calculated for the systems which obey the occupation rules derived in the previous section.

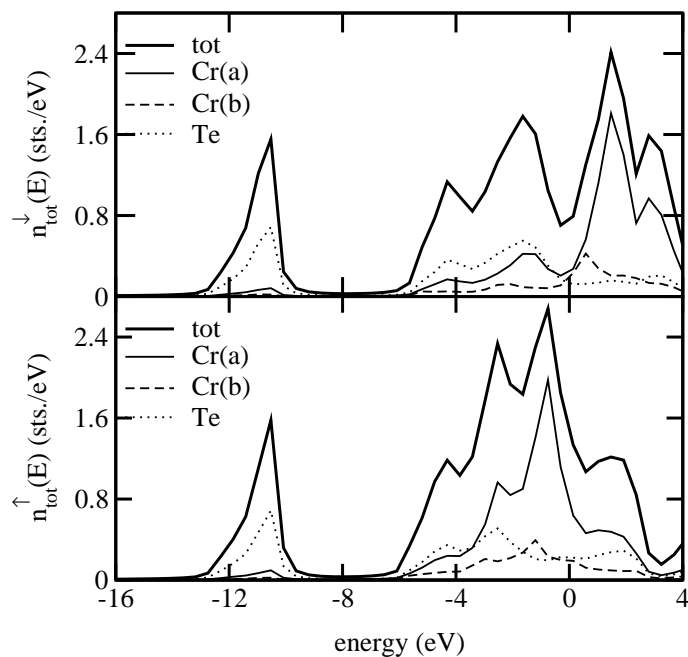


Figure 5.24: The spin-resolved KKR density of states of  $\text{Cr}_{1.25}\text{Te}_2$ .

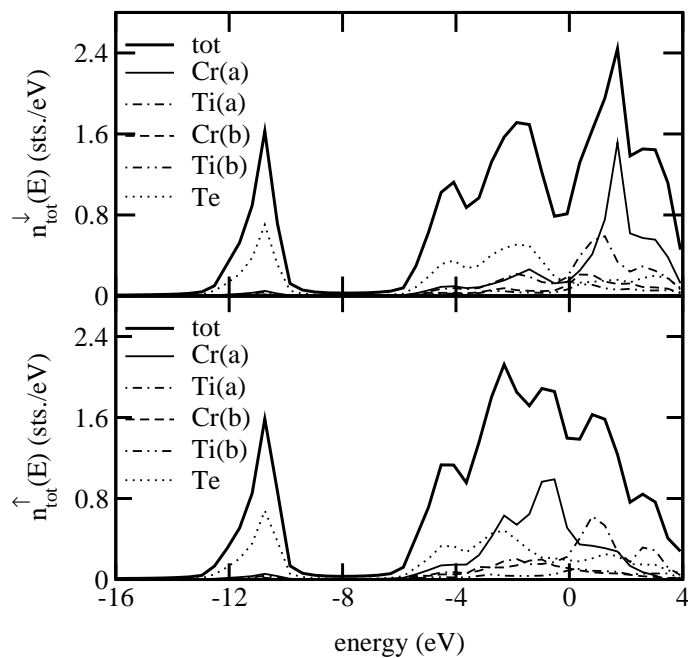


Figure 5.25: The spin-resolved KKR density of states of  $(\text{Cr}_{0.6}\text{Ti}_{0.4})_{1.25}\text{Te}_2$ .



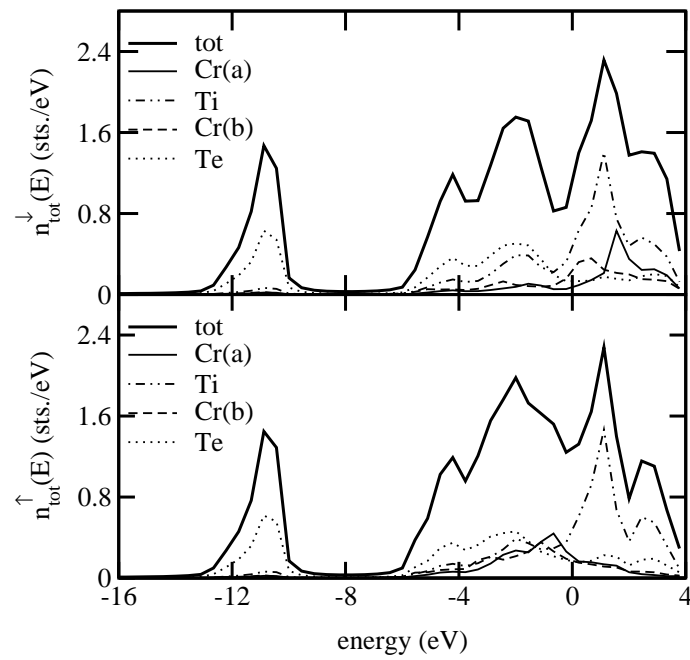


Figure 5.26: The spin-resolved KKR density of states of  $(\text{Cr}_{0.4}\text{Ti}_{0.6})_{1.25}\text{Te}_2$ .

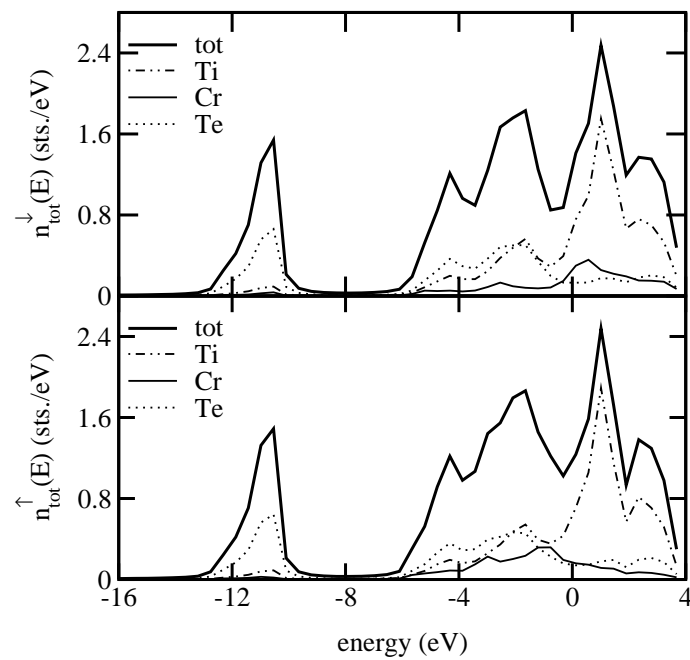


Figure 5.27: The spin-resolved KKR density of states of  $(\text{Cr}_{0.2}\text{Ti}_{0.8})_{1.25}\text{Te}_2$ .

	$x = 0.2$	$x = 0.4$	$x = 0.6$	$x = 1.0$
Exchange splitting Cr(a) (eV)	1.5	2.4	2.5	2.2
Exchange splitting Cr(b) (eV)	-	1.8	1.8	1.8

Table 5.14: The exchange splitting of Cr 3d in  $(\text{Cr}_x\text{Ti}_{1-x})_{1.25}\text{Te}_2$  compounds. Cr(a) and Cr(b) denote the two crystallographic sites of Cr in  $P\bar{3}m1$  trigonal symmetry.

A photoemission study (Shimada et al. [175]) has disclosed the electronic structure of  $\text{Cr}_5\text{Te}_8$ . If one assume the valence  $-2$  for Te atoms, the nominal number of  $d$  electrons in  $\text{Cr}_5\text{Te}_8$  system is 2.8 electrons per Cr atom. Because Cr atoms are octahedral surrounded by Te atoms, the Cr 3d orbitals split into threefold degenerated  $t_{2g}$  orbitals and respectively twofold degenerated  $e_g$  orbitals. If one assume a high spin configuration for Cr ions, the  $t_{2g\uparrow}$  orbitals are almost filled, whilst the orbital  $e_g \uparrow$  is empty. The  $t_{2g\downarrow}$  and  $e_{g\downarrow}$  orbitals are unoccupied. From the photoemission study of  $\text{Cr}_5\text{Te}_8$  system it was found that the electron correlation effect is very important in this system which means that electrons tend to localize on the atom rather to extend over all the crystal.

As one can see in the Figs. 5.24, 5.25, 5.26 and 5.27, the density of states of  $(\text{Cr}_x\text{Ti}_{1-x})_{1.25}\text{Te}_2$  systems keep the characteristics of the DOS of the Cr-Te systems. The contribution of Te is less affected by the Cr:Ti ratio. Also, the exchange-splitting is less visible in the case of Te minority/majority bands. A visible change appear due to the Cr contribution to the total DOS. One can see in particular changes into the position of the minority/majority d-like contribution of the Cr partial DOS. One can estimate that the splitting between the d-like majority/minority peaks of Cr increase when increasing the Cr concentration. The exchange splitting of Cr-3d estimated from the DOS calculations is listed in Table 5.14.

The Ti contribution is small in the occupied part of the valence band, the prominent peak of Ti partial DOS being located above the Fermi energy. The exchange splitting of the Ti contribution to the total DOS is weak and less affected by the Ti concentration. One should note that in Figs. 5.24, 5.25, 5.26 and 5.27 the partial DOS of each component is weighted by its concentration in order to get the total DOS.

If one considers the rigid band model, because Ti has less valence electrons like Cr, substitution of Ti in the  $\text{Cr}_{1.25}\text{Te}_2$  system would decrease the number of valence electrons and the Fermi level  $E_F$  would shift to lower energies in the  $t_{2g}$  band. If one compares the DOS of  $(\text{Cr}_x\text{Ti}_{1-x})_{1.25}\text{Te}_2$  systems with increased Ti content, the picture of band structure looks to be more complex than it is suggested in the rigid band model.

The SPR-KKR magnetic moments for  $(\text{Cr}_x\text{Ti}_{1-x})_{1.25}\text{Te}_2$  compounds are presented in Table 5.15. The calculation of the magnetic moments has been done respecting the preference of the Cr/Ti atoms for one of the two different metal sites into the unit cell. The calculations for  $\text{Ti}_{1.25}\text{Te}_2$  show that this system is non-magnetic.

The magnetic moments of Cr on site  $a$  are less influenced by the Ti content in the system, an increase of Ti content to 60 % in the system increase the magnetic moment of Cr on the site  $a$  by about 2%. The decrease of the magnetic moments of Cr with the increase of the Cr

	x=0.2	x=0.4	x=0.6	x=1.0
Cr a		3.114	3.080	3.043
Cr b	2.394	2.417	2.499	2.487
Te	-0.014	-0.080	-0.120	-0.206
Ti a	0.056	0.046	0.076	
Ti b		0.164	0.178	

Table 5.15: The SPR-KKR calculated magnetic moments in in  $(\text{Cr}_x\text{Ti}_{1-x})_{1.25}\text{Te}_2$  compounds.

content in the system (and implicit in the Cr(a) layer) is not unusual. The variation of the magnetic moment with the Cr:Te ratio in the systems  $\text{Cr}_x\text{TiSe}_2$  reported by Titov et al. [176] show a similar behaviour. The magnetic moment of Cr on site *b* is more sensitive to the Cr:Ti ratio in the system. For Cr(b), the magnetic moment increase with about 4 % with increasing of the Cr content in the system from  $x = 0.2$  to  $x = 1.0$ .

The magnetic moments induced on Ti atoms are rather small compared with the Cr magnetic moments. The magnetic moments of Ti atoms are depending very much on the crystallographic site occupied by those atoms. For the Ti atoms sitting on site *b*, the magnetic moments are about 2-3 times bigger than the Ti(a) magnetic moments.

As in the  $\text{Cr}_{1+x}(\text{Te/Se})_2$  systems, one can see also for the Te atoms in the  $(\text{Cr/Ti})_{1.25}\text{Te}_2$  systems a small negative magnetic moment. The Te magnetic moments are sensitive to the Cr:Ti ratio in the system, increasing about 14 times if the Cr content in the system is reduced with 60%. According to the scheme proposed by Dijkstra et al. [138] for the polarisation of Te 5p orbitals, one can say that the Cr-Te covalency is producing a negative magnetic polarisation of Te 5d orbitals, less pronounced with decreasing of the Cr content.

Concerning the magnetism of  $(\text{Cr}_x\text{Ti}_{1-x})_{1.25}\text{Te}_2$  systems, one can conclude that a) Cr magnetic moments are site-dependent, but the magnitude of the magnetic moment is less influenced by the Cr:Ti ratio and by the change of the lattice parameters in the system; b) The magnetism of Ti and Te atoms is negligible compared with Cr magnetic moments.

Our calculations invalidate the supposition that the substitution of Cr by Ti drastic alters the magnetism of  $(\text{Cr}_x\text{Ti}_{1-x})_{1.25}\text{Te}_2$  systems. The drastically decrease of the Curie temperature in those systems with increasing Ti content could have other sources. This could be a structural transition at  $T \leq T_C$  for example.

The rather big magnetic moments on Cr ( $\sim 3.0\mu_B$  and  $\sim 2.5\mu_B$ ) are not in agreement with the values obtained from magnetisation measurements ( $2.13\mu_B$ ) [171]. This disagreement has been often reported in the literature for Cr-Te systems ([156, 155, 154, 153]), suggesting a spin glass magnetic behaviour. We suppose that a non-collinear/spin glass magnetic structure in Cr-Ti-Te compounds would explain the disagreement between the measured and calculated magnetic moments.

## 5.7 Conclusions

The band structure calculations performed for Cr-chalcogenide systems show a variety of magnetic properties of these systems, depending on the composition and on the structure of the system. We found indications for a non-collinear spin structure in Cr-Se and Cr-Te systems. Our results are in agreement with the phase diagram of Makovetskii (1986) [19].

The Cr magnetic moments in the  $\text{CrSe}_x\text{Te}_{1-x}$  alloy show a strong dependence on the Se:Te ratio, in agreement with the individual magnetic moments of Cr in CrSe and CrTe compounds [8]. The phase stability of ferro-/ antiferromagnetic spin configuration of  $\text{CrTe}_{1-x}\text{Se}_x$  alloy was discussed for  $x = 70\%$  Se. The antiferromagnetic phase was found lower in energy.

The band structure calculations for non-stoichiometric  $\text{Cr}_{1+x}\text{Q}_2$  ( $\text{Q} = \text{Te/Se}$ ,  $\text{Te:Se} = 7:1$ ) with  $x$  between 0.21 and 0.33 show a site occupancy preference of Cr atoms within the trigonal structure. The magnetic moments of Cr depend on the crystallographic site occupied by Cr atoms and on the Cr content of the system.

Based on the SPR-KKR band structure calculations, we determined the occupation rules of Cr and Ti atoms on crystallographic sites inside the unit cell. The Ti substitution in  $\text{Cr}_{1.25}\text{Te}_2$  systems show a slight influence on the magnetic moments of Cr atoms despite the pronounced changes of the lattice parameters.

# Chapter 6

## Summary

Nowadays, the research aiming to discover new materials with technological applications needs to be supported by reliable theoretical descriptions. The subject of this work was to use the SPR-KKR formalism to investigate the ground state properties of materials from Cr-chalcogenide class and to describe the spectroscopic properties (Compton scattering and positron annihilation) of different metallic systems.

The fundamentals of the theoretical approach applied are presented in Chapter 2. In particular, the basics of the density functional theory (DFT) used to reduce the many-body electron-electron interaction to single electrons moving independently in an effective potential, together with the SPR-KKR formalism used to solve the electronic structure problem are discussed in detail.

This theoretical formalism is applied to get the description of the (magnetic) Compton profile, as it was shown in Chapter 3. The experimental MCP of Fe and Ni are very good described by the SPR-KKR theoretical spectra. If for Fe and Ni the accuracy of the KKR description of the experimental results is comparable with other theoretical descriptions (FLAPW, LMTO, APW), the quality of the KKR description of MCP spectra is evidenced when dealing with the systems that contain rare earth or actinide atoms. As can be seen for Gd, the KKR method gives better results compared with the full-potential method (FLAPW), showing that the fully relativistic treatment of this systems is decisive for the MCP description. The investigation of the influence of the spin-orbit coupling on the KKR MCP spectra of Gd,  $Y_{0.38}Gd_{0.62}$  and  $UFe_2$  show that the relativistic effects cannot be neglected in the study of these systems. Also, the agreement between theory and experiment in the case of the MCP spectra of  $UFe_2$  spectra is slightly enhanced when the orbital polarization is included.

The description of the 2D projection of the electron momentum density was derived. As it has been shown, the SPR-KKR 2D projection perpendicular to the [001] direction of *bcc* Fe gives a good description of the experimental reconstructed spectra.

The KKR formalism allows us to decompose the MCP spectra into partial contributions of the orbitals, as it was shown for Fe and  $Fe_3Pt$ . As the overall shape of the MCP is characteristic of the particular localization of each orbital, this is a useful method to get informations about the orbital localizations and the spin polarization of the orbitals. For the systems with

many atoms per unit cell, the decomposition of the MCP spectra into the atomic-like partial contributions and an interference term show that the contribution coming from interference term is crucial for the MCP analysis.

The formalism which describe the positron annihilation is presented in Chapter 4. The 2D projection of the electron-positron momentum density allows to analyse the experimental 2D-ACAR spectra, as it was shown in the case of V. A further extension of this formalism can be done in order to determine the topology of the Fermi surface of metals, which in practice is reconstructed from 2D-ACAR data.

The experimental work performed by the group of Prof. Bensch on the preparation and determination of the structure and the magnetic properties of Cr-chalcogenide systems was completed by theoretical calculations of the ground-state properties, as it was shown in Chapter 5. The SPR-KKR method was used with success to determine the density of states, the magnetic moments and the occupation rules of the crystallographic sites for the compounds of type  $\text{Cr}_{1+x}(\text{Te}_{1-y}\text{Se}_y)_2$  and  $(\text{Cr}_x\text{Ti}_{1-x})_5\text{Te}_8$ .

A complementary approach to investigate the magnetic behaviour of solids using a microscopic model of the magnetic interaction was combined with the SPR-KKR band structure calculations in order to determine the magnetic ground state of the CrSe and CrTe systems. According to this investigation, the magnetic ground state of CrSe and CrTe systems was found to have a non-collinear spin configuration, in agreement with the phase diagram determined by Makovetskii [19]. Nevertheless, combining this method with the neutron diffraction data suggesting a certain type of spin arrangement can be a useful tool to establish the full spin configuration of the magnetic systems with non-collinear spin configuration.

The influence of the exchange-correlation treatment on the equilibrium lattice parameters for  $\text{CrSe}_x\text{Te}_{1-x}$  alloy was investigated. Using the GGA treatment of the exchange-coupling energy, the equilibrium lattice parameters differ from the experimental values by less than 2%, whilst the LSDA give an error of about 6%. The antiferromagnetic spin configuration found was lowest in energy for the equilibrium lattice parameters for both exchange-coupling treatments. Further extension for non-collinear spin configurations could give more information about the stability of the magnetic phase.

# Appendix A

## Green's function in momentum representation (Compton)

In order to calculate the Green's function in momentum representation, one has to introduce the site-diagonal and non-site diagonal expression for the Green's function in the coordinate representation, together with the formula describing the eigenfunction in the momentum representation:

$$G_{m_s m'_s}(\vec{p}, \vec{p}', E) = \frac{1}{N\Omega} \int d^3 r \int d^3 r' \Phi_{\vec{p} m_s}^\times(\vec{r}) \Im G^+(\vec{r}, \vec{r}', E) \Phi_{\vec{p}' m'_s}(\vec{r}'). \quad (\text{A.1})$$

Fig. A.1 shows the vectors used, with the Bravais vector  $\vec{R}_n$  giving the position of the  $n$ th cell origin and the basis vector  $\vec{R}_q$  giving the position of the  $q$ th site inside the  $n$ th cell. According to this notation and considering that the origin of the reference system is the origin of the  $n$ th cell, the momentum representation Green's function reads as:

$$\begin{aligned} G_{m_s m'_s}(\vec{p}, \vec{p}', E) &= \frac{1}{\Omega} \sum_q \sum_{n'q'} \int d^3 r_{0q} \int d^3 r'_{n'q'} U_{\vec{p} m_s}^\times e^{-i\vec{p}(\vec{r}_{0q} + \vec{R}_q)} \Im G^+(\vec{r}_{0q}, \vec{r}'_{n'q'}, E) \\ &\quad \times U_{\vec{p}' m'_s} e^{i\vec{p}'(\vec{r}'_{n'q'} + \vec{R}_{n'} + \vec{R}_{q'})} \\ &= \frac{1}{\Omega} \sum_q \int d^3 r_{0q} \int d^3 r'_{0q} U_{\vec{p} m_s}^\times e^{-i\vec{p}(\vec{r}_{0q} + \vec{R}_q)} \\ &\quad \Im \left[ \sum_\alpha x_{q\alpha} \sum_{\Lambda\Lambda'} Z_\Lambda^{q\alpha}(\vec{r}_{0q}, E) \tau_{\Lambda\Lambda'}^{0q0q,\alpha}(E) Z_{\Lambda'}^{q\alpha\times}(\vec{r}'_{0q}, E) \right. \\ &\quad \left. - \sum_\Lambda Z_\Lambda^{q\alpha}(\vec{r}_{nq<}, E) J_\Lambda^{q\alpha\times}(\vec{r}_{nq>}, E) \right] U_{\vec{p}' m'_s} e^{i\vec{p}'(\vec{r}'_{0q} + \vec{R}_q)} \\ &+ \frac{1}{\Omega} \sum_q \sum_{n'q'}' \int d^3 r_{0q} \int d^3 r'_{n'q'} U_{\vec{p} m_s}^\times e^{-i\vec{p}(\vec{r}_{0q} + \vec{R}_q)} \end{aligned}$$

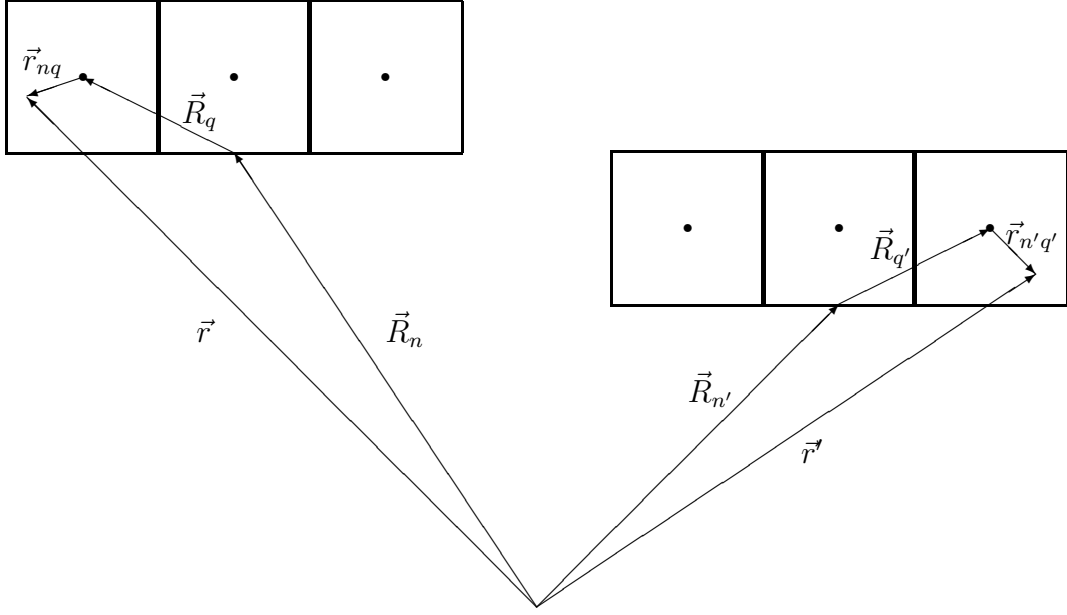


Figure A.1: The vectorial configuration for the Green's function formula A.1

$$\begin{aligned}
& \Im \left[ \sum_{\alpha\beta, \alpha \neq \beta} x_{q\alpha} x_{q'\beta} \sum_{\Lambda\Lambda'} Z_{\Lambda}^{nq\alpha}(\vec{r}_{nq}, E) \tau_{\Lambda\Lambda'}^{nq\alpha n'q'\beta}(E) Z_{\Lambda'}^{n'q'\beta}(\vec{r}'_{n'q'}, E) \right] \times \\
& \quad \times U_{\vec{p}m'_s} e^{i\vec{p}(\vec{r}'_{n'q'} + \vec{R}_{n'} + \vec{R}_{q'})} \\
& \text{introduce matrix elements (see Appendix B)} \\
& = \frac{1}{\Omega} \sum_q \Im \sum_{\alpha} x_{q\alpha} \left[ \sum_{\Lambda\Lambda'} M_{m_s\Lambda}^{q\alpha} \tau_{\Lambda\Lambda'}^{0q0q, \alpha} M_{m'_s\Lambda'}^{q\alpha*} - \sum_{\Lambda} \tilde{M}_{m_s\Lambda m'_s}^{q\alpha} \right] \\
& + \frac{1}{\Omega} \Im \sum_q \sum_{n'q'} e^{-i\vec{p}(\vec{R}_q - \vec{R}_{q'})} e^{i\vec{p}\vec{R}_{n'}} \sum_{\alpha\beta, \alpha \neq \beta} x_{q\alpha} x_{q'\beta} \sum_{\Lambda\Lambda'} M_{m_s\Lambda}^{q\alpha} \tau_{\Lambda\Lambda'}^{nq\alpha n'q'\beta} M_{m'_s\Lambda'}^{q'\beta*} \\
& \text{subtract non-site diagonal contribution coming from the same atom-type} \\
& = \frac{1}{\Omega} \Im \sum_q \sum_{\alpha} x_{q\alpha} \left[ \sum_{\Lambda\Lambda'} M_{m_s\Lambda}^{q\alpha} \tau_{\Lambda\Lambda'}^{0q0q, \alpha} M_{m'_s\Lambda'}^{q\alpha*} - \sum_{\Lambda} \tilde{M}_{m_s\Lambda m'_s}^{q\alpha} \right] \\
& - \frac{1}{\Omega} \Im \sum_q \sum_{\alpha\beta} x_{q\alpha} x_{q\beta} \sum_{\Lambda\Lambda'} M_{m_s\Lambda}^{q\alpha} \tau_{\Lambda\Lambda'}^{0q\alpha 0q\alpha} M_{m'_s\Lambda'}^{q\alpha*} \\
& + \frac{1}{\Omega} \Im \sum_q \sum_{q'} e^{-i\vec{p}(\vec{R}_q - \vec{R}_{q'})} \sum_{n'} e^{i\vec{p}\vec{R}_{n'}} \\
& \quad \sum_{\alpha\beta} x_{q\alpha} x_{q'\beta} \sum_{\Lambda\Lambda'} M_{m_s\Lambda}^{q\alpha} (D^{q\alpha} \tau^{nqn'q'CPA} \tilde{D}^{q'\beta})_{\Lambda\Lambda'} M_{m'_s\Lambda'}^{q'\beta*}
\end{aligned}$$



$$\begin{aligned}
&= \frac{1}{\Omega} \Im \sum_q \sum_\alpha x_{q\alpha} \left[ \sum_{\Lambda\Lambda'} M_{m_s\Lambda}^{q\alpha} \tau_{\Lambda\Lambda'}^{0q0q,\alpha} M_{m'_s\Lambda'}^{q\alpha*} - \sum_\Lambda \tilde{M}_{m_s\Lambda m'_s}^{q\alpha} \right] \\
&- \frac{1}{\Omega} \Im \sum_q \sum_{\alpha\beta} x_{q\alpha} x_{q\alpha} \sum_{\Lambda\Lambda'} M_{m_s\Lambda}^{q\alpha} \tau_{\Lambda\Lambda'}^{0q\alpha 0q\alpha} M_{m'_s\Lambda'}^{q\alpha*} \\
&+ \frac{1}{\Omega} \Im \sum_q \sum_{q'} e^{-i\vec{p}(\vec{R}_q - \vec{R}_{q'})} \sum_{\alpha\beta} x_{q\alpha} x_{q'\beta} \\
&\quad \sum_{\Lambda\Lambda'} M_{m_s\Lambda}^{q\alpha} \left( D^{q\alpha} \left[ \sum_{n'} e^{i\vec{p}\vec{R}_{n'}} \tau^{nqn'q'CPA} \right] \tilde{D}^{q'\beta} \right)_{\Lambda\Lambda'} M_{m'_s\Lambda'}^{q'\beta*}
\end{aligned}$$

introduce the scattering path operators

$$\begin{aligned}
&= \frac{1}{\Omega} \Im \sum_q \sum_\alpha x_{q\alpha} \left[ \sum_{\Lambda\Lambda'} M_{m_s\Lambda}^{q\alpha} \left( D^{q\alpha} \tau^{0q0qCPA} \right)_{\Lambda\Lambda'} M_{m'_s\Lambda'}^{q\alpha*} - \sum_\Lambda \tilde{M}_{m_s\Lambda m'_s}^{q\alpha} \right] \\
&- \frac{1}{\Omega} \Im \sum_q \sum_{\alpha\beta} x_{q\alpha} x_{q\alpha} \sum_{\Lambda\Lambda'} M_{m_s\Lambda}^{q\alpha} \left( D^{q\alpha} \tau^{0q0qCPA} \tilde{D}^{q\alpha} \right)_{\Lambda\Lambda'} M_{m'_s\Lambda'}^{q\alpha*} \\
&+ \frac{1}{\Omega} \Im \sum_q \sum_{q'} e^{-i\vec{p}(\vec{R}_q - \vec{R}_{q'})} \sum_{\alpha\beta} x_{q\alpha} x_{q'\beta} \\
&\quad \sum_{\Lambda\Lambda'} M_{m_s\Lambda}^{q\alpha} \left( D^{q\alpha} \tau^{qq'CPA}(\vec{p}) \tilde{D}^{q'\beta} \right)_{\Lambda\Lambda'} M_{m'_s\Lambda'}^{q'\beta*}
\end{aligned}$$

split the single site part

$$\begin{aligned}
&= \frac{1}{\Omega} \Im \sum_q \sum_\alpha x_{q\alpha} \left[ \sum_{\Lambda\Lambda'} M_{m_s\Lambda}^{q\alpha} t_{\Lambda\Lambda'}^{q\alpha} M_{m'_s\Lambda'}^{q\alpha*} - \sum_\Lambda \tilde{M}_{m_s\Lambda m'_s}^{q\alpha} \right] \\
&+ \frac{1}{\Omega} \Im \sum_q \sum_\alpha x_{q\alpha} \sum_{\Lambda\Lambda'} M_{m_s\Lambda}^{q\alpha} \left( D^{q\alpha} \tau^{0q0qCPA} - t^{q\alpha} \right)_{\Lambda\Lambda'} M_{m'_s\Lambda'}^{q\alpha*} \\
&- \frac{1}{\Omega} \Im \sum_q \sum_{\alpha\beta} x_{q\alpha} x_{q\alpha} \sum_{\Lambda\Lambda'} M_{m_s\Lambda}^{q\alpha} \left( D^{q\alpha} \tau^{0q0qCPA} \tilde{D}^{q\alpha} \right)_{\Lambda\Lambda'} M_{m'_s\Lambda'}^{q\alpha*} \\
&+ \frac{1}{\Omega} \Im \sum_q \sum_{q'} e^{-i\vec{p}(\vec{R}_q - \vec{R}_{q'})} \sum_{\alpha\beta} x_{q\alpha} x_{q'\beta} \\
&\quad \sum_{\Lambda\Lambda'} M_{m_s\Lambda}^{q\alpha} \left( D^{q\alpha} \tau^{qq'CPA}(\vec{p}) \tilde{D}^{q'\beta} \right)_{\Lambda\Lambda'} M_{m'_s\Lambda'}^{q'\beta*}
\end{aligned}$$

The formulation presented allows a direct application to disordered system, in which case the resulting expression represents the corresponding configurational average. In addition one should note that the final expression has been split into four terms: a pure single-site term, two site diagonal terms and a additional site-off-diagonal term.



## Appendix B

### Matrix elements (Compton)

The calculations of the matrix elements which enter in Eq. (3.23) is based on the expression for the momentum eigenfunction  $\Phi_{\vec{p}m_s}$ :

$$\begin{aligned}\phi_{\vec{p}m_s}(\vec{r}) &= U_{\vec{p}m_s} e^{i\vec{p}\vec{r}} \\ &= \left( \frac{E_p + c^2}{2E_p + c^2} \right)^{1/2} \left( \frac{c\vec{\sigma}\vec{p}}{E_p + c^2} \chi_{m_s} \right) e^{i\vec{p}\vec{r}} \\ &= 4\pi \left( \frac{E_p + c^2}{2E_p + c^2} \right)^{1/2} \sum_{\Lambda} i^l C_{\Lambda}^{m_s} Y_l^{\mu - m_s^*}(\hat{p}) \left( \begin{array}{c} j_l(pr) \chi_{\Lambda}(\hat{r}) \\ \frac{icpS_{\kappa}}{E_p + c^2} j_{\bar{l}}(pr) \chi_{-\Lambda}(\hat{r}) \end{array} \right)\end{aligned}$$

with

$$E_p = \frac{c^2}{2} \left( \sqrt{1 + 4\frac{p^2}{c^2}} - 1 \right)$$

Using the previous expression of the momentum eigenfunction and the regular solutions of the Dirac equation for a spherical symmetric potential (see Eq. (2.106)), the matrix elements occurring in the expression for the momentum representation of the Green's function are given by:

$$\begin{aligned}M_{m_s\Lambda} &= M_{m_s\Lambda}(\vec{p}, E) \\ &= \langle \phi_{\vec{p}m_s} | Z_{\Lambda'} \rangle \\ &= \langle \epsilon_p \sum_{\Lambda} i^l C_{\Lambda}^{m_s} Y_l^{\mu - m_s^*}(\hat{p}) \left( \begin{array}{c} j_l(pr) \chi_{\Lambda}(\hat{r}) \\ \frac{icpS_{\kappa}}{E_p + c^2} j_{\bar{l}}(pr) \chi_{-\Lambda}(\hat{r}) \end{array} \right) | \sum_{\Lambda''} \left( \begin{array}{c} g_{\Lambda''\Lambda'}(r) \chi_{\Lambda''}(\hat{r}) \\ i f_{\Lambda''\Lambda'}(r) \chi_{-\Lambda''}(\hat{r}) \end{array} \right) \rangle \\ &= \epsilon_p \sum_{\Lambda\Lambda''} i^{-l} C_{\Lambda}^{m_s} Y_l^{\mu - m_s^*}(\hat{p}) \left( \langle j_l(pr) | g_{\Lambda''\Lambda'}(r) \rangle \langle \chi_{\Lambda}(\hat{r}) | \chi_{\Lambda''}(\hat{r}) \rangle \right. \\ &\quad \left. + \frac{cpS_{\kappa}}{E_p + c^2} \langle j_{\bar{l}}(pr) | f_{\Lambda''\Lambda'}(r) \rangle \langle \chi_{-\Lambda}(\hat{r}) | \chi_{-\Lambda''}(\hat{r}) \rangle \right)\end{aligned}$$

$$= \epsilon_p \sum_{\Lambda} i^{-l} C_{\Lambda}^{m_s} Y_l^{\mu-m_s}(\hat{p}) \left( \langle j_l(pr) | g_{\Lambda\Lambda'}(r) \rangle + \frac{cpS_{\kappa}}{E_p + c^2} \langle j_{\bar{l}}(pr) | f_{\Lambda\Lambda'}(r) \rangle \right)$$

with

$$\epsilon_p = 4\pi \left( \frac{E_p + c^2}{2E_p + c^2} \right)^{1/2}$$

Using the orthogonality of the spin-angular functions, ( $\langle \chi_{\Lambda}(\hat{r}) | \chi_{\Lambda''}(\hat{r}) \rangle = \delta_{\Lambda, \Lambda''}$ ), one has:

$$\begin{aligned} M_{m_s \Lambda'' m'_s} &= M_{m_s \Lambda'' m'_s}(\vec{p}, E) \\ &= \langle \phi_{\vec{p} m_s}(\vec{r}) | \left( Z_{\Lambda''}(\vec{r}) J_{\Lambda''}^{\times}(\vec{r}') \Theta(r' - r) \right. \\ &\quad \left. J_{\Lambda''}(\vec{r}) Z_{\Lambda''}^{\times}(\vec{r}') \Theta(r - r') \right) | \phi_{\vec{p} m'_s}(\vec{r}') \rangle \\ &= \epsilon_p^2 \sum_{\Lambda \Lambda'} \sum_{\Lambda_1 \Lambda_2} i^{-l+l'} C_{\Lambda}^{m_s} C_{\Lambda'}^{m'_s} Y_l^{\mu-m_s}(\hat{p}) Y_{l'}^{\mu'-m'_s}(\hat{p}) \\ &\quad \left\langle \left( \begin{array}{c} j_l(pr) \chi_{\Lambda}(\hat{r}) \\ w_{\kappa p} j_{\bar{l}}(pr) \chi_{-\Lambda}(\hat{r}) \end{array} \right) \middle| \left( Z_{\Lambda_1 \Lambda''}(\vec{r}) J_{\Lambda_2 \Lambda''}^{\times}(\vec{r}') \Theta(r' - r) \right. \right. \\ &\quad \left. \left. J_{\Lambda_1 \Lambda''}(\vec{r}) Z_{\Lambda_2 \Lambda''}^{\times}(\vec{r}') \Theta(r - r') \right) \middle| \left( \begin{array}{c} j_{l'}(pr) \chi_{\Lambda'}(\hat{r}) \\ w_{\kappa' p} j_{\bar{l}'}(pr) \chi_{-\Lambda'}(\hat{r}) \end{array} \right) \right\rangle \\ &= \epsilon_p^2 \sum_{\Lambda \Lambda'} \sum_{\Lambda_1 \Lambda_2} i^{-l+l'} C_{\Lambda}^{m_s} C_{\Lambda'}^{m'_s} Y_l^{\mu-m_s}(\hat{p}) Y_{l'}^{\mu'-m'_s}(\hat{p}) \int r^2 dr \int r'^2 dr' \\ &\quad \left( j_l(pr) g_{\Lambda_1 \Lambda''}(r) \tilde{g}_{\Lambda_2 \Lambda''}(r') j_{l'}(pr) \Theta(r' - r) \langle \chi_{\Lambda} | \chi_{\Lambda_1} \rangle \langle \chi_{\Lambda_2} | \chi_{\Lambda'} \rangle \right. \\ &\quad + j_l(pr) \tilde{g}_{\Lambda_1 \Lambda''}(r) g_{\Lambda_2 \Lambda''}(r') j_{l'}(pr) \Theta(r - r') \langle \chi_{\Lambda} | \chi_{\Lambda_1} \rangle \langle \chi_{\Lambda_2} | \chi_{\Lambda'} \rangle \\ &\quad + w_{\kappa p} j_{\bar{l}}(pr) w_{\kappa_1 p} f_{\Lambda_1 \Lambda''}(r) w_{\kappa_2 p} \tilde{f}_{\Lambda_2 \Lambda''}(r') w_{\kappa' p} j_{\bar{l}'}(pr) \Theta(r' - r) \langle \chi_{-\Lambda} | \chi_{-\Lambda_1} \rangle \langle \chi_{-\Lambda_2} | \chi_{-\Lambda'} \rangle \\ &\quad \left. + w_{\kappa p} j_l(pr) w_{\kappa_1 p} \tilde{f}_{\Lambda_1 \Lambda''}(r) w_{\kappa_2 p} f_{\Lambda_2 \Lambda''}(r') w_{\kappa' p} j_{\bar{l}'}(pr) \Theta(r - r') \langle \chi_{-\Lambda} | \chi_{-\Lambda_1} \rangle \langle \chi_{-\Lambda_2} | \chi_{-\Lambda'} \rangle \right) \\ &= \epsilon_p^2 \sum_{\Lambda \Lambda'} i^{-l+l'} C_{\Lambda}^{m_s} C_{\Lambda'}^{m'_s} Y_l^{\mu-m_s}(\hat{p}) Y_{l'}^{\mu'-m'_s}(\hat{p}) \\ &\quad \left( \int_0^{r_{ws}} r^2 dr j_l(pr) g_{\Lambda\Lambda''}(r) \int_r^{r_{ws}} r'^2 dr' \tilde{g}_{\Lambda'\Lambda''}(r') j_{l'}(pr) \right. \\ &\quad + \int_0^{r_{ws}} r^2 dr j_l(pr) \tilde{g}_{\Lambda\Lambda''}(r) \int_0^r r'^2 dr' g_{\Lambda'\Lambda''}(r') j_{l'}(pr) \\ &\quad + w_{\kappa p}^2 w_{\kappa' p}^2 \int_0^{r_{ws}} r^2 dr j_{\bar{l}}(pr) f_{\Lambda\Lambda''}(r) \int_r^{r_{ws}} r'^2 dr' \tilde{f}_{\Lambda'\Lambda''}(r') j_{\bar{l}'}(pr) \\ &\quad \left. + w_{\kappa p}^2 w_{\kappa' p}^2 \int_0^{r_{ws}} r^2 dr j_l(pr) \tilde{f}_{\Lambda\Lambda''}(r) \int_0^r r'^2 dr' f_{\Lambda'\Lambda''}(r') j_{\bar{l}'}(pr) \right) \end{aligned}$$

with

$$w_{\kappa p} = \frac{cpS_{\kappa}}{E_p + c^2}.$$



# Appendix C

## Green's function in momentum representation (Positron Annihilation)

### C.1 Site-diagonal contribution

The following section gives the various steps to transform the site-diagonal contribution in the first two terms of Eq. (4.8).

$$\begin{aligned}
& \frac{1}{\Omega} \sum_q \sum_{\alpha} x_{q\alpha} \int d^3 r_{0q} \int d^3 r'_{0q} U_{\vec{p}_e m_s}^{e\dagger} e^{-i\vec{p}_e \vec{r}_{0q}} \Im G^{e+\alpha}(\vec{r}_{0q}, \vec{r}'_{0q}, E_e) U_{\vec{p}_e m_s}^e e^{i\vec{p}_e \vec{r}'_{0q}} \\
& \quad U_{\vec{p}_p m'_s}^{p\dagger} e^{-i\vec{p}_p \vec{r}_{0q}} \Im G^{p+\alpha}(\vec{r}_{0q}, \vec{r}'_{0q}, E_p) U_{\vec{p}_p m'_s}^p e^{i\vec{p}_p \vec{r}'_{0q}} \\
- & \frac{1}{\Omega} \sum_q \sum_{\alpha\beta} x_{q\alpha} x_{q\beta} \int d^3 r_{0q} \int d^3 r'_{0q} U_{\vec{p}_e m_s}^{e\dagger} e^{-i\vec{p}_e \vec{r}_{0q}} \Im G^{e+\alpha\beta}(\vec{r}_{0q}, \vec{r}'_{0q}, E_e) U_{\vec{p}_e m_s}^e e^{i\vec{p}_e \vec{r}'_{0q}} \\
& \quad U_{\vec{p}_p m'_s}^{p\dagger} e^{-i\vec{p}_p \vec{r}_{0q}} \Im G^{p+\alpha\beta}(\vec{r}_{0q}, \vec{r}'_{0q}, E_p) U_{\vec{p}_p m'_s}^p e^{i\vec{p}_p \vec{r}'_{0q}} \\
= & \frac{-1}{4\Omega} \sum_q \sum_{\alpha} x_{q\alpha} \int d^3 r_{0q} \int d^3 r'_{0q} \\
& \quad U_{\vec{p}_e m_s}^{e\dagger} e^{-i\vec{p}_e \vec{r}_{0q}} \left( G^{e+\alpha}(\vec{r}_{0q}, \vec{r}'_{0q}, E_e) - G^{e-\alpha}(\vec{r}_{0q}, \vec{r}'_{0q}, E_e) \right) U_{\vec{p}_e m_s}^e e^{i\vec{p}_e \vec{r}'_{0q}} \\
& \quad U_{\vec{p}_p m'_s}^{p\dagger} e^{-i\vec{p}_p \vec{r}_{0q}} \left( G^{p+\alpha}(\vec{r}_{0q}, \vec{r}'_{0q}, E_p) - G^{p-\alpha}(\vec{r}_{0q}, \vec{r}'_{0q}, E_p) \right) U_{\vec{p}_p m'_s}^p e^{i\vec{p}_p \vec{r}'_{0q}} \\
- & \frac{-1}{4\Omega} \sum_q \sum_{\alpha\beta} x_{q\alpha} x_{q\beta} \int d^3 r_{0q} \int d^3 r'_{0q} \\
& \quad U_{\vec{p}_e m_s}^{e\dagger} e^{-i\vec{p}_e \vec{r}_{0q}} \left( G^{e+\alpha\beta}(\vec{r}_{0q}, \vec{r}'_{0q}, E_e) - G^{e-\alpha\beta}(\vec{r}_{0q}, \vec{r}'_{0q}, E_e) \right) U_{\vec{p}_e m_s}^e e^{i\vec{p}_e \vec{r}'_{0q}} \\
& \quad U_{\vec{p}_p m'_s}^{p\dagger} e^{-i\vec{p}_p \vec{r}_{0q}} \left( G^{p+\alpha\beta}(\vec{r}_{0q}, \vec{r}'_{0q}, E_p) - G^{p-\alpha\beta}(\vec{r}_{0q}, \vec{r}'_{0q}, E_p) \right) U_{\vec{p}_p m'_s}^p e^{i\vec{p}_p \vec{r}'_{0q}}
\end{aligned}$$

$$\begin{aligned}
&= \frac{-1}{4\Omega} \sum_q \sum_\alpha x_{q\alpha} \int d^3 r_{0q} \int d^3 r'_{0q} \\
&\quad U_{\vec{p}_e m_s}^{e\dagger} e^{-i\vec{p}_e \vec{r}'_{0q}} \left( \sum_{\Lambda\Lambda'} Z_\Lambda^{e+q\alpha}(\vec{r}'_{0q}) \tau_{\Lambda\Lambda'}^{e+0q0q,\alpha}(E_e) Z_{\Lambda'}^{e+q\alpha \times}(\vec{r}'_{0q}) \right. \\
&\quad \quad \left. - \sum_{\Lambda\Lambda'} Z_\Lambda^{e-q\alpha}(\vec{r}'_{0q}) \tau_{\Lambda\Lambda'}^{e-0q0q,\alpha}(E_e) Z_{\Lambda'}^{e-q\alpha \times}(\vec{r}'_{0q}) \right) U_{\vec{p}_e m_s}^e e^{i\vec{p}_e \vec{r}'_{0q}} \\
&\quad U_{\vec{p}_p m'_s}^{p\dagger} e^{-i\vec{p}_p \vec{r}'_{0q}} \left( \sum_{\Lambda''\Lambda'''} Z_{\Lambda''}^{p+q\alpha}(\vec{r}'_{0q}) \tau_{\Lambda''\Lambda'''}^{p+0q0q,\alpha}(E_p) Z_{\Lambda'''}^{p+q\alpha \times}(\vec{r}'_{0q}) \right. \\
&\quad \quad \left. - \sum_{\Lambda''\Lambda'''} Z_{\Lambda''}^{p-q\alpha}(\vec{r}'_{0q}) \tau_{\Lambda''\Lambda'''}^{p-0q0q,\alpha}(E_p) Z_{\Lambda'''}^{p-q\alpha \times}(\vec{r}'_{0q}) \right) U_{\vec{p}_p m'_s}^p e^{i\vec{p}_p \vec{r}'_{0q}} \\
&- \frac{-1}{4\Omega} \sum_q \sum_{\alpha\beta} x_{q\alpha} x_{q\beta} \int d^3 r_{0q} \int d^3 r'_{0q} \\
&\quad U_{\vec{p}_e m_s}^{e\dagger} e^{-i\vec{p}_e \vec{r}'_{0q}} \left( \sum_{\Lambda\Lambda'} Z_\Lambda^{e+q\alpha}(\vec{r}'_{0q}) \tau_{\Lambda\Lambda'}^{e+0q\alpha 0q\beta}(E_e) Z_{\Lambda'}^{e+q\beta \times}(\vec{r}'_{0q}) \right. \\
&\quad \quad \left. - \sum_{\Lambda\Lambda'} Z_\Lambda^{e-q\alpha}(\vec{r}'_{0q}) \tau_{\Lambda\Lambda'}^{e-0q\alpha 0q\beta}(E_e) Z_{\Lambda'}^{e-q\beta \times}(\vec{r}'_{0q}) \right) U_{\vec{p}_e m_s}^e e^{i\vec{p}_e \vec{r}'_{0q}} \\
&\quad U_{\vec{p}_p m'_s}^{p\dagger} e^{-i\vec{p}_p \vec{r}'_{0q}} \left( \sum_{\Lambda''\Lambda'''} Z_{\Lambda''}^{p+q\alpha}(\vec{r}'_{0q}) \tau_{\Lambda''\Lambda'''}^{p+0q\alpha 0q\beta}(E_p) Z_{\Lambda'''}^{p+q\beta \times}(\vec{r}'_{0q}) \right. \\
&\quad \quad \left. - \sum_{\Lambda''\Lambda'''} Z_{\Lambda''}^{p-q\alpha}(\vec{r}'_{0q}) \tau_{\Lambda''\Lambda'''}^{p-0q\alpha 0q\beta}(E_p) Z_{\Lambda'''}^{p-q\beta \times}(\vec{r}'_{0q}) \right) U_{\vec{p}_p m'_s}^p e^{i\vec{p}_p \vec{r}'_{0q}} \\
&= \frac{-1}{4\Omega} \sum_q \sum_\alpha x_{q\alpha} \sum_{\Lambda\Lambda'} \sum_{\Lambda''\Lambda'''} M_{m_s \Lambda m'_s \Lambda''}^{++\alpha} \tilde{M}_{m_s \Lambda' m'_s \Lambda'''}^{++\alpha} \tau_{\Lambda\Lambda'}^{e+0q0q,\alpha}(E_e) \tau_{\Lambda''\Lambda'''}^{p+0q0q,\alpha}(E_p) \\
&\quad - M_{m_s \Lambda m'_s \Lambda''}^{+-\alpha} \tilde{M}_{m_s \Lambda' m'_s \Lambda'''}^{+-\alpha} \tau_{\Lambda\Lambda'}^{e+0q0q,\alpha}(E_e) \tau_{\Lambda''\Lambda'''}^{p-0q0q,\alpha}(E_p) \\
&\quad - M_{m_s \Lambda m'_s \Lambda''}^{-+\alpha} \tilde{M}_{m_s \Lambda' m'_s \Lambda'''}^{-+\alpha} \tau_{\Lambda\Lambda'}^{e-0q0q,\alpha}(E_e) \tau_{\Lambda''\Lambda'''}^{p+0q0q,\alpha}(E_p) \\
&\quad + M_{m_s \Lambda m'_s \Lambda''}^{--\alpha} \tilde{M}_{m_s \Lambda' m'_s \Lambda'''}^{--\alpha} \tau_{\Lambda\Lambda'}^{e-0q0q,\alpha}(E_e) \tau_{\Lambda''\Lambda'''}^{p-0q0q,\alpha}(E_p) \\
&- \frac{-1}{4\Omega} \sum_q \sum_{\alpha\beta} x_{q\alpha} x_{q\beta} \sum_{\Lambda\Lambda'} \sum_{\Lambda''\Lambda'''} M_{m_s \Lambda m'_s \Lambda''}^{++\alpha} \tilde{M}_{m_s \Lambda' m'_s \Lambda'''}^{++\beta} \tau_{\Lambda\Lambda'}^{e+0q\alpha 0q\beta}(E_e) \tau_{\Lambda''\Lambda'''}^{p+0q\alpha 0q\beta}(E_p) \\
&\quad - M_{m_s \Lambda m'_s \Lambda''}^{+-\alpha} \tilde{M}_{m_s \Lambda' m'_s \Lambda'''}^{+-\beta} \tau_{\Lambda\Lambda'}^{e+0q\alpha 0q\beta}(E_e) \tau_{\Lambda''\Lambda'''}^{p-0q\alpha 0q\beta}(E_p) \\
&\quad - M_{m_s \Lambda m'_s \Lambda''}^{-+\alpha} \tilde{M}_{m_s \Lambda' m'_s \Lambda'''}^{-+\beta} \tau_{\Lambda\Lambda'}^{e-0q\alpha 0q\beta}(E_e) \tau_{\Lambda''\Lambda'''}^{p+0q\alpha 0q\beta}(E_p) \\
&\quad + M_{m_s \Lambda m'_s \Lambda''}^{--\alpha} \tilde{M}_{m_s \Lambda' m'_s \Lambda'''}^{--\beta} \tau_{\Lambda\Lambda'}^{e-0q\alpha 0q\beta}(E_e) \tau_{\Lambda''\Lambda'''}^{p-0q\alpha 0q\beta}(E_p)
\end{aligned}$$

assume the positron to be in a state with  $\vec{k}_p = \vec{p}_p = 0$  at bottom of the band  
this implies:  $l(\Lambda_p) = 0$  and  $\mu(\Lambda_p) = m'_s$        $\Lambda'' = \Lambda''' = \Lambda_s$



$$\begin{aligned}
&= \frac{-1}{4\Omega} \sum_q \sum_\alpha x_{q\alpha} \sum_{\Lambda\Lambda'} M_{m_s\Lambda m'_s\Lambda_s}^{++\alpha} \tilde{M}_{m_s\Lambda' m'_s\Lambda_s}^{++\alpha} \tau_{\Lambda\Lambda'}^{e+0q0q,\alpha}(E_e) \tau_{\Lambda_s\Lambda_s}^{p+0q0q,\alpha}(E_p) \\
&\quad - M_{m_s\Lambda m'_s\Lambda_s}^{+-\alpha} \tilde{M}_{m_s\Lambda' m'_s\Lambda_s}^{+-\alpha} \tau_{\Lambda\Lambda'}^{e+0q0q,\alpha}(E_e) \tau_{\Lambda_s\Lambda_s}^{p-0q0q,\alpha}(E_p) \\
&\quad - M_{m_s\Lambda m'_s\Lambda_s}^{-+\alpha} \tilde{M}_{m_s\Lambda' m'_s\Lambda_s}^{-+\alpha} \tau_{\Lambda\Lambda'}^{e-0q0q,\alpha}(E_e) \tau_{\Lambda_s\Lambda_s}^{p+0q0q,\alpha}(E_p) \\
&\quad + M_{m_s\Lambda m'_s\Lambda_s}^{--\alpha} \tilde{M}_{m_s\Lambda' m'_s\Lambda_s}^{--\alpha} \tau_{\Lambda\Lambda'}^{e-0q0q,\alpha}(E_e) \tau_{\Lambda_s\Lambda_s}^{p-0q0q,\alpha}(E_p) \\
&- \frac{-1}{4\Omega} \sum_q \sum_{\alpha\beta} x_{q\alpha} x_{q\beta} \sum_{\Lambda\Lambda'} M_{m_s\Lambda m'_s\Lambda_s}^{++\alpha} \tilde{M}_{m_s\Lambda' m'_s\Lambda_s}^{++\beta} \tau_{\Lambda\Lambda'}^{e+0q\alpha 0q\beta}(E_e) \tau_{\Lambda_s\Lambda_s}^{p+0q\alpha 0q\beta}(E_p) \\
&\quad - M_{m_s\Lambda m'_s\Lambda_s}^{+-\alpha} \tilde{M}_{m_s\Lambda' m'_s\Lambda_s}^{+-\beta} \tau_{\Lambda\Lambda'}^{e+0q\alpha 0q\beta}(E_e) \tau_{\Lambda_s\Lambda_s}^{p-0q\alpha 0q\beta}(E_p) \\
&\quad - M_{m_s\Lambda m'_s\Lambda_s}^{-+\alpha} \tilde{M}_{m_s\Lambda' m'_s\Lambda_s}^{-+\beta} \tau_{\Lambda\Lambda'}^{e-0q\alpha 0q\beta}(E_e) \tau_{\Lambda_s\Lambda_s}^{p+0q\alpha 0q\beta}(E_p) \\
&\quad + M_{m_s\Lambda m'_s\Lambda_s}^{--\alpha} \tilde{M}_{m_s\Lambda' m'_s\Lambda_s}^{--\beta} \tau_{\Lambda\Lambda'}^{e-0q\alpha 0q\beta}(E_e) \tau_{\Lambda_s\Lambda_s}^{p-0q\alpha 0q\beta}(E_p)
\end{aligned}$$

evaluate  $G^{p\pm}$  for  $\Im E_p \rightarrow 0$

this implies:  $\Im G^{p+} \rightarrow \sum_{\Lambda_s} Z_{\Lambda_s}^{p+} \Im \tau_{\Lambda_s\Lambda_s}^{p+} Z_{\Lambda_s}^{p+ \times}$

$$\begin{aligned}
&= \frac{1}{2i\Omega} \sum_q \sum_\alpha x_{q\alpha} \left( \Im \tau_{\Lambda_s\Lambda_s}^{p+0q0q,\alpha}(E_p) \right) \sum_{\Lambda\Lambda'} M_{m_s\Lambda m'_s\Lambda_s}^{++\alpha} \tilde{M}_{m_s\Lambda' m'_s\Lambda_s}^{++\alpha} \tau_{\Lambda\Lambda'}^{e+0q0q,\alpha}(E_e) \\
&\quad - M_{m_s\Lambda m'_s\Lambda_s}^{-+\alpha} \tilde{M}_{m_s\Lambda' m'_s\Lambda_s}^{-+\alpha} \tau_{\Lambda\Lambda'}^{e-0q0q,\alpha}(E_e) \\
&- \frac{1}{2i\Omega} \sum_q \sum_{\alpha\beta} x_{q\alpha} x_{q\beta} \left( \Im \tau_{\Lambda_s\Lambda_s}^{p+0q\alpha 0q\beta}(E_p) \right) \sum_{\Lambda\Lambda'} M_{m_s\Lambda m'_s\Lambda_s}^{++\alpha} \tilde{M}_{m_s\Lambda' m'_s\Lambda_s}^{++\beta} \tau_{\Lambda\Lambda'}^{e+0q\alpha 0q\beta}(E_e) \\
&\quad - M_{m_s\Lambda m'_s\Lambda_s}^{-+\alpha} \tilde{M}_{m_s\Lambda' m'_s\Lambda_s}^{-+\beta} \tau_{\Lambda\Lambda'}^{e-0q\alpha 0q\beta}(E_e)
\end{aligned}$$

replace ...  $\frac{1}{2i}(G^{e+} - G^{e-})$  ... by:  $\Im \dots G^{e+} \dots$

$$\begin{aligned}
&= \frac{1}{\Omega} \Im \sum_q \sum_\alpha x_{q\alpha} \left( \Im \tau_{\Lambda_s\Lambda_s}^{p+0q0q,\alpha}(E_p) \right) \sum_{\Lambda\Lambda'} M_{m_s\Lambda m'_s\Lambda_s}^{++\alpha} \tilde{M}_{m_s\Lambda' m'_s\Lambda_s}^{++\alpha} \tau_{\Lambda\Lambda'}^{e+0q0q,\alpha}(E_e) \\
&- \frac{1}{\Omega} \Im \sum_q \sum_{\alpha\beta} x_{q\alpha} x_{q\beta} \left( \Im \tau_{\Lambda_s\Lambda_s}^{p+0q\alpha 0q\beta}(E_p) \right) \sum_{\Lambda\Lambda'} M_{m_s\Lambda m'_s\Lambda_s}^{++\alpha} \tilde{M}_{m_s\Lambda' m'_s\Lambda_s}^{++\beta} \tau_{\Lambda\Lambda'}^{e+0q\alpha 0q\beta}(E_e)
\end{aligned}$$

## C.2 Site-off-diagonal contribution

This section describes in detail the transformation of the site-off-diagonal (third) term of Eq. (4.8).

$$\begin{aligned}
& \frac{1}{\Omega} \sum_q \sum_{n'q'} \sum_{\alpha\beta} x_{q\alpha} x_{q'\beta} \int d^3 r_{0q} \int d^3 r'_{n'q'} \\
& \quad U_{\vec{p}_e m_s}^{e\dagger} e^{-i\vec{p}_e(\vec{r}_{0q} + \vec{R}_q)} \Im G^{e+\alpha\beta}(\vec{r}_{0q}, \vec{r}'_{n'q'}, E_e) U_{\vec{p}_e m_s}^e e^{i\vec{p}_e(\vec{r}'_{n'q'} + \vec{R}_{n'} + \vec{R}_{q'})} \\
& \quad U_{\vec{p}_p m'_s}^{p\dagger} e^{-i\vec{p}_p(\vec{r}_{0q} + \vec{R}_q)} \Im G^{p+\alpha\beta}(\vec{r}_{0q}, \vec{r}'_{n'q'}, E_p) U_{\vec{p}_p m'_s}^p e^{i\vec{p}_p(\vec{r}'_{n'q'} + \vec{R}_{n'} + \vec{R}_{q'})} \\
&= \frac{1}{\Omega} \sum_q \sum_{n'q'} \sum_{\alpha\beta} x_{q\alpha} x_{q'\beta} \int d^3 r_{0q} \int d^3 r'_{n'q'} \\
& \quad U_{\vec{p}_e m_s}^{e\dagger} e^{-i\vec{p}_e(\vec{r}_{0q} + \vec{R}_q)} \left( G^{e+\alpha\beta}(\vec{r}_{0q}, \vec{r}'_{n'q'}, E_e) - G^{e-\alpha\beta}(\vec{r}_{0q}, \vec{r}'_{n'q'}, E_e) \right) U_{\vec{p}_e m_s}^e e^{i\vec{p}_e(\vec{r}'_{n'q'} + \vec{R}_{n'} + \vec{R}_{q'})} \\
& \quad U_{\vec{p}_p m'_s}^{p\dagger} e^{-i\vec{p}_p(\vec{r}_{0q} + \vec{R}_q)} \left( G^{p+\alpha\beta}(\vec{r}_{0q}, \vec{r}'_{n'q'}, E_p) - G^{p-\alpha\beta}(\vec{r}_{0q}, \vec{r}'_{n'q'}, E_p) \right) U_{\vec{p}_p m'_s}^p e^{i\vec{p}_p(\vec{r}'_{n'q'} + \vec{R}_{n'} + \vec{R}_{q'})} \\
&= \frac{1}{\Omega} \sum_q \sum_{n'q'} \sum_{\alpha\beta} x_{q\alpha} x_{q'\beta} \int d^3 r_{0q} \int d^3 r'_{n'q'} \\
& \quad U_{\vec{p}_e m_s}^{e\dagger} e^{-i\vec{p}_e(\vec{r}_{0q} + \vec{R}_q)} \left( \sum_{\Lambda\Lambda'} Z_{\Lambda}^{e+q\alpha}(\vec{r}_{0q}) \tau_{\Lambda\Lambda'}^{e+0q\alpha n'q'\beta}(E_e) Z_{\Lambda'}^{e+q\beta\times}(\vec{r}'_{0q}) \right. \\
& \quad \left. - \sum_{\Lambda\Lambda'} Z_{\Lambda}^{e-q\alpha}(\vec{r}_{0q}) \tau_{\Lambda\Lambda'}^{e-0q\alpha n'q'\beta}(E_e) Z_{\Lambda'}^{e-q\beta\times}(\vec{r}'_{0q}) \right) U_{\vec{p}_e m_s}^e e^{i\vec{p}_e(\vec{r}'_{n'q'} + \vec{R}_{n'} + \vec{R}_{q'})} \\
& \quad U_{\vec{p}_p m'_s}^{p\dagger} e^{-i\vec{p}_p(\vec{r}_{0q} + \vec{R}_q)} \left( \sum_{\Lambda''\Lambda'''} Z_{\Lambda''}^{p+q\alpha}(\vec{r}_{0q}) \tau_{\Lambda''\Lambda'''}^{p+0q\alpha n'q'\beta}(E_p) Z_{\Lambda'''}^{p+q\beta\times}(\vec{r}'_{0q}) \right. \\
& \quad \left. - \sum_{\Lambda''\Lambda'''} Z_{\Lambda''}^{p-q\alpha}(\vec{r}_{0q}) \tau_{\Lambda''\Lambda'''}^{p-0q\alpha n'q'\beta}(E_p) Z_{\Lambda'''}^{p-q\beta\times}(\vec{r}'_{0q}) \right) U_{\vec{p}_p m'_s}^p e^{i\vec{p}_p(\vec{r}'_{n'q'} + \vec{R}_{n'} + \vec{R}_{q'})} \\
&= \frac{-1}{4\Omega} \sum_q \sum_{q'} e^{-i(\vec{p}_e + \vec{p}_p)(\vec{R}_q - \vec{R}_{q'})} \sum_{\alpha\beta} x_{q\alpha} x_{q'\beta} \sum_{\Lambda\Lambda'} \sum_{\Lambda''\Lambda'''} \\
& \quad M_{m_s \Lambda m'_s \Lambda''}^{++\alpha} \tilde{M}_{m_s \Lambda' m'_s \Lambda'''}^{++\beta} \sum_{n'} e^{i(\vec{p}_e + \vec{p}_p)\vec{R}_{n'}} \tau_{\Lambda\Lambda'}^{e+0q\alpha n'q'\beta}(E_e) \tau_{\Lambda''\Lambda'''}^{p+0q\alpha n'q'\beta}(E_p) \\
& \quad - M_{m_s \Lambda m'_s \Lambda''}^{+-\alpha} \tilde{M}_{m_s \Lambda' m'_s \Lambda'''}^{+-\beta} \sum_{n'} e^{i(\vec{p}_e + \vec{p}_p)\vec{R}_{n'}} \tau_{\Lambda\Lambda'}^{e+0q\alpha n'q'\beta}(E_e) \tau_{\Lambda''\Lambda'''}^{p-0q\alpha n'q'\beta}(E_p) \\
& \quad - M_{m_s \Lambda m'_s \Lambda''}^{-+\alpha} \tilde{M}_{m_s \Lambda' m'_s \Lambda'''}^{-+\beta} \sum_{n'} e^{i(\vec{p}_e + \vec{p}_p)\vec{R}_{n'}} \tau_{\Lambda\Lambda'}^{e-0q\alpha n'q'\beta}(E_e) \tau_{\Lambda''\Lambda'''}^{p+0q\alpha n'q'\beta}(E_p) \\
& \quad + M_{m_s \Lambda m'_s \Lambda''}^{--\alpha} \tilde{M}_{m_s \Lambda' m'_s \Lambda'''}^{--\beta} \sum_{n'} e^{i(\vec{p}_e + \vec{p}_p)\vec{R}_{n'}} \tau_{\Lambda\Lambda'}^{e-0q\alpha n'q'\beta}(E_e) \tau_{\Lambda''\Lambda'''}^{p-0q\alpha n'q'\beta}(E_p)
\end{aligned}$$

assume the positron to be in a state with  $\vec{k}_p = \vec{p}_p = 0$  at bottom of the band

this implies:  $l(\Lambda_p) = 0$  and  $\mu(\Lambda_p) = m'_s$        $\Lambda'' = \Lambda''' = \Lambda_s$   
see evaluation of lattice sum below

$$\begin{aligned}
&= \frac{-1}{4\Omega} \sum_q \sum_{q'} e^{-i(\vec{p}_e + \vec{p}_p)(\vec{R}_q - \vec{R}_{q'})} \sum_{\alpha\beta} x_{q\alpha} x_{q'\beta} \sum_{\Lambda\Lambda'} \\
&\quad M_{m_s\Lambda m'_s\Lambda_s}^{++\alpha} \tilde{M}_{m_s\Lambda' m'_s\Lambda_s}^{++\beta} \left( D^{e+\alpha} \tau^{e+qq'CPA}(\vec{p} - \vec{K}_m) \tilde{D}^{e+\beta} \right)_{\Lambda\Lambda'} W^{p+q\alpha q'\beta} \\
&\quad - M_{m_s\Lambda m'_s\Lambda_s}^{+-\alpha} \tilde{M}_{m_s\Lambda' m'_s\Lambda_s}^{+-\beta} \left( D^{e+\alpha} \tau^{e+qq'CPA}(\vec{p} - \vec{K}_m) \tilde{D}^{e+\beta} \right)_{\Lambda\Lambda'} W^{p-q\alpha q'\beta} \\
&\quad - M_{m_s\Lambda m'_s\Lambda_s}^{-+\alpha} \tilde{M}_{m_s\Lambda' m'_s\Lambda_s}^{-+\beta} \left( D^{e-\alpha} \tau^{e-qq'CPA}(\vec{p} - \vec{K}_m) \tilde{D}^{e-\beta} \right)_{\Lambda\Lambda'} W^{p+q\alpha q'\beta} \\
&\quad + M_{m_s\Lambda m'_s\Lambda_s}^{--\alpha} \tilde{M}_{m_s\Lambda' m'_s\Lambda_s}^{--\beta} \left( D^{e-\alpha} \tau^{e-qq'CPA}(\vec{p} - \vec{K}_m) \tilde{D}^{e-\beta} \right)_{\Lambda\Lambda'} W^{p-q\alpha q'\beta}
\end{aligned}$$

evaluate  $G^{p\pm}$  for  $\Im E_p \rightarrow 0$

this implies:  $\Im G^{p+} \rightarrow \sum_{\Lambda_s} Z_{\Lambda_s}^{p+} \Im \tau_{\Lambda_s\Lambda_s}^{p+} Z_{\Lambda_s}^{p+\times}$

$$\begin{aligned}
&= \frac{1}{2i\Omega} \sum_q \sum_{q'} e^{-i(\vec{p}_e + \vec{p}_p)(\vec{R}_q - \vec{R}_{q'})} \sum_{\alpha\beta} x_{q\alpha} x_{q'\beta} \left( \Im W^{p+q\alpha q'\beta} \right) \sum_{\Lambda\Lambda'} \\
&\quad M_{m_s\Lambda m'_s\Lambda_s}^{++\alpha} \tilde{M}_{m_s\Lambda' m'_s\Lambda_s}^{++\beta} \left( D^{e+\alpha} \tau^{e+qq'CPA}(\vec{p} - \vec{K}_m) \tilde{D}^{e+\beta} \right)_{\Lambda\Lambda'} \\
&\quad - M_{m_s\Lambda m'_s\Lambda_s}^{-+\alpha} \tilde{M}_{m_s\Lambda' m'_s\Lambda_s}^{-+\beta} \left( D^{e-\alpha} \tau^{e-qq'CPA}(\vec{p} - \vec{K}_m) \tilde{D}^{e-\beta} \right)_{\Lambda\Lambda'}
\end{aligned}$$

replace ...  $\frac{1}{2i}(G^{e+} - G^{e-})$  ... by:  $\Im \dots G^{e+} \dots$

$$\begin{aligned}
&= \frac{1}{\Omega} \Im \sum_q \sum_{q'} e^{-i(\vec{p}_e + \vec{p}_p)(\vec{R}_q - \vec{R}_{q'})} \sum_{\alpha\beta} x_{q\alpha} x_{q'\beta} \left( \Im W^{p+q\alpha q'\beta} \right) \\
&\quad \sum_{\Lambda\Lambda'} M_{m_s\Lambda m'_s\Lambda_s}^{++\alpha} \tilde{M}_{m_s\Lambda' m'_s\Lambda_s}^{++\beta} \left( D^{e+\alpha} \tau^{e+qq'CPA}(\vec{p} - \vec{K}_m) \tilde{D}^{e+\beta} \right)_{\Lambda\Lambda'}
\end{aligned}$$

### C.3 Lattice sum

Evaluation of the lattice sum occurring in the positron annihilation (see Eq. (4.8)):

$$\begin{aligned}
& \sum_{n'} e^{i(\vec{p}_e + \vec{p}_p) \vec{R}_{n'}} \tau_{\Lambda \Lambda'}^{e\mu 0q\alpha n' q' \beta}(E_e) \tau_{\Lambda'' \Lambda'''}^{p\nu 0q\alpha n' q' \beta}(E_p) \\
&= \sum_{n'} e^{i(\vec{p}_e + \vec{p}_p) \vec{R}_{n'}} (D^{\epsilon\mu \alpha} \tau^{\epsilon\mu 0q n' q' CPA} \tilde{D}^{\epsilon\mu \beta})_{\Lambda \Lambda'} (D^{p\nu \alpha} \tau^{p\nu 0q n' q' CPA} \tilde{D}^{p\nu \beta})_{\Lambda'' \Lambda'''} \\
&= \sum_{\Lambda_a \Lambda_b} \sum_{\Lambda_c \Lambda_d} D_{\Lambda \Lambda_a}^{\epsilon\mu \alpha} \tilde{D}_{\Lambda_b \Lambda'}^{\epsilon\mu \beta} D_{\Lambda'' \Lambda_c}^{p\nu \alpha} \tilde{D}_{\Lambda_c \Lambda'''}^{p\nu \beta} \sum_{n'} e^{i(\vec{p}_e + \vec{p}_p) \vec{R}_{n'}} \tau_{\Lambda_a \Lambda_b}^{\epsilon\mu 0q n' q' CPA} \tau_{\Lambda_c \Lambda_d}^{p\nu 0q n' q' CPA} \\
&= \sum_{\Lambda_a \Lambda_b} \sum_{\Lambda_c \Lambda_d} D_{\Lambda \Lambda_a}^{\epsilon\mu \alpha} \tilde{D}_{\Lambda_b \Lambda'}^{\epsilon\mu \beta} D_{\Lambda'' \Lambda_c}^{p\nu \alpha} \tilde{D}_{\Lambda_c \Lambda'''}^{p\nu \beta} \\
&\quad \sum_{n'} e^{i(\vec{p}_e + \vec{p}_p) \vec{R}_{n'}} \tau_{\Lambda_a \Lambda_b}^{\epsilon\mu 0q n' q' CPA} \frac{1}{\Omega_{BZ}} \int_{\Omega_{BZ}} d^3 k_p \tau_{\Lambda_c \Lambda_d}^{p\nu q q' CPA}(\vec{k}_p) e^{-i\vec{k}_p \vec{R}_{n'}} \\
&= \sum_{\Lambda_a \Lambda_b} \sum_{\Lambda_c \Lambda_d} D_{\Lambda \Lambda_a}^{\epsilon\mu \alpha} \tilde{D}_{\Lambda_b \Lambda'}^{\epsilon\mu \beta} D_{\Lambda'' \Lambda_c}^{p\nu \alpha} \tilde{D}_{\Lambda_c \Lambda'''}^{p\nu \beta} \\
&\quad \frac{1}{\Omega_{BZ}} \int_{\Omega_{BZ}} d^3 k_p \left( \sum_{n'} e^{i(\vec{p}_e + \vec{p}_p - \vec{k}_p) \vec{R}_{n'}} \tau_{\Lambda_a \Lambda_b}^{\epsilon\mu 0q n' q' CPA} \right) \tau_{\Lambda_c \Lambda_d}^{p\nu q q' CPA}(\vec{k}_p) \\
&= \sum_{\Lambda_a \Lambda_b} \sum_{\Lambda_c \Lambda_d} D_{\Lambda \Lambda_a}^{\epsilon\mu \alpha} \tilde{D}_{\Lambda_b \Lambda'}^{\epsilon\mu \beta} D_{\Lambda'' \Lambda_c}^{p\nu \alpha} \tilde{D}_{\Lambda_c \Lambda'''}^{p\nu \beta} \\
&\quad \frac{1}{\Omega_{BZ}} \int_{\Omega_{BZ}} d^3 k_p \left( \sum_{n'} e^{i(\vec{k}_e + \vec{K}_m) \vec{R}_{n'}} \tau_{\Lambda_a \Lambda_b}^{\epsilon\mu 0q n' q' CPA} \right) \tau_{\Lambda_c \Lambda_d}^{p\nu q q' CPA}(\vec{k}_p) \\
&= \sum_{\Lambda_a \Lambda_b} \sum_{\Lambda_c \Lambda_d} D_{\Lambda \Lambda_a}^{\epsilon\mu \alpha} \tilde{D}_{\Lambda_b \Lambda'}^{\epsilon\mu \beta} D_{\Lambda'' \Lambda_c}^{p\nu \alpha} \tilde{D}_{\Lambda_c \Lambda'''}^{p\nu \beta} \\
&\quad \frac{1}{\Omega_{BZ}} \int_{\Omega_{BZ}} d^3 k_p \tau_{\Lambda_a \Lambda_b}^{\epsilon\mu q q' CPA}(\vec{p}_e + \vec{p}_p - \vec{k}_p - \vec{K}_m) \tau_{\Lambda_c \Lambda_d}^{p\nu q q' CPA}(\vec{k}_p)
\end{aligned}$$

assume the positron to be in a state with  $\vec{k}_p = \vec{p}_p = 0$  at bottom of the band

this implies:  $l(\Lambda_p) = 0$  and  $\mu(\Lambda_p) = m'_s$

$$\tau_{\Lambda_c \Lambda_d}^{p\nu q q' CPA}(\vec{k}_p) = \xi_{\Lambda_s}^{p\nu q q'} \delta(E_p - E_p^0) \delta(\vec{k}_p - \vec{0}) \quad \text{and} \quad \Lambda_c = \Lambda_d = \Lambda'' = \Lambda''' = \Lambda_s$$

$$\begin{aligned}
&= \delta_{\Lambda'' \Lambda_s} \delta_{\Lambda''' \Lambda_s} D_{\Lambda_s \Lambda_s}^{p\nu \alpha} \tilde{D}_{\Lambda_s \Lambda_s}^{p\nu \beta} \sum_{\Lambda_a \Lambda_b} D_{\Lambda \Lambda_a}^{\epsilon\mu \alpha} \tilde{D}_{\Lambda_b \Lambda'}^{\epsilon\mu \beta} \tau_{\Lambda_a \Lambda_b}^{\epsilon\mu q q' CPA}(\vec{p} - \vec{K}_m) \frac{1}{\Omega_{BZ}} \xi_{\Lambda_s}^{p\nu q q'} \delta(E_p - E_p^0) \\
&= \delta_{\Lambda'' \Lambda_s} \delta_{\Lambda''' \Lambda_s} D_{\Lambda_s \Lambda_s}^{p\nu \alpha} \xi_{\Lambda_s}^{p\nu q q'} \tilde{D}_{\Lambda_s \Lambda_s}^{p\nu \beta} \frac{1}{\Omega_{BZ}} \delta(E_p - E_p^0) \left( D^{\epsilon\mu \alpha} \tau^{\epsilon\mu q q' CPA}(\vec{p} - \vec{K}_m) \tilde{D}^{\epsilon\mu \beta} \right)_{\Lambda \Lambda'}
\end{aligned}$$

$$\begin{aligned}
&= \delta_{\Lambda''\Lambda_s} \delta_{\Lambda'''\Lambda_s} W^{p\nu q\alpha q'\beta} \left( D^{e\mu\alpha} \tau^{e\mu qq'CPA} (\vec{p} - \vec{K}_m) \tilde{D}^{e\mu\beta} \right)_{\Lambda\Lambda'} \\
&\text{with } W^{p\nu q\alpha q'\beta} = D_{\Lambda_s\Lambda_s}^{p\nu\alpha} \xi_{\Lambda_s}^{p\nu qq'} \tilde{D}_{\Lambda_s\Lambda_s}^{p\nu\beta} \frac{1}{\Omega_{BZ}} \delta(E_p - E_p^0)
\end{aligned}$$



# Appendix D

## Matrix elements (Positron Annihilation)

The matrix elements entering in Eq. (4.10) are worked out in this section:

$$\begin{aligned}
 M_{m_s \Lambda m'_s \Lambda''}^{\mu\nu\alpha} &= \int d^3r U_{\vec{p}_e m_s}^{e\dagger} e^{-i\vec{p}_e \vec{r}} Z_{\Lambda}^{e\mu q\alpha}(\vec{r}) U_{\vec{p}_p m'_s}^{p\dagger} e^{-i\vec{p}_p \vec{r}} Z_{\Lambda''}^{p\nu q\alpha}(\vec{r}) \\
 &= \int d^3r e^{-i(\vec{p}_e + \vec{p}_p) \vec{r}} U_{\vec{p}_e m_s}^{e\dagger} Z_{\Lambda}^{e\mu q\alpha}(\vec{r}) U_{\vec{p}_p m'_s}^{p\dagger} Z_{\Lambda''}^{p\nu q\alpha}(\vec{r})
 \end{aligned}$$

assume the positron to be in a state with  $\vec{k}_p = \vec{p}_p = 0$  at bottom of the band  
this implies:  $l(\Lambda_p) = 0$  and  $\mu(\Lambda_p) = m'_s$

$$\begin{aligned}
 &= \int d^3r e^{-i\vec{p} \vec{r}} U_{\vec{p} m_s}^{e\dagger} Z_{\Lambda}^{e\mu q\alpha}(\vec{r}) U_{0 m'_s}^{p\dagger} Z_{\Lambda''}^{p\nu q\alpha}(\vec{r}) \\
 &= \int d^3r \epsilon_{p_e} \sum_{\Lambda_a} i^{-l_a} C_{\Lambda_a}^{m_s} Y_l^{\mu_a - m_s}(\hat{p}) \left( \begin{array}{c} j_{l_a}(pr) \chi_{\Lambda_a}(\hat{r}) \\ \frac{icpS_{\kappa_a}}{E_p + c^2} \bar{j}_{l_a}(pr) \chi_{-\Lambda_a}(\hat{r}) \end{array} \right)^\dagger \\
 &\quad \sum_{\Lambda_e} \left( \begin{array}{c} g_{\Lambda_e \Lambda}^{e\mu}(r) \chi_{\Lambda_e}(\hat{r}) \\ i f_{\Lambda_e \Lambda}^{e\mu}(r) \chi_{-\Lambda_e}(\hat{r}) \end{array} \right) \times \left( \begin{array}{c} \chi_{m'_s} \\ 0 \end{array} \right)^\dagger \sum_{\Lambda_p} \left( \begin{array}{c} g_{\Lambda_p \Lambda''}^{p\nu}(r) \chi_{\Lambda_p}(\hat{r}) \\ i f_{\Lambda_p \Lambda''}^{p\nu}(r) \chi_{-\Lambda_p}(\hat{r}) \end{array} \right) \\
 &= \int d^3r \epsilon_{p_e} \sum_{\Lambda_a} i^{-l_a} C_{\Lambda_a}^{m_s} Y_l^{\mu_a - m_s}(\hat{p}) \left( \begin{array}{c} j_{l_a}(pr) \chi_{\Lambda_a}(\hat{r}) \\ \frac{icpS_{\kappa_a}}{E_p + c^2} \bar{j}_{l_a}(pr) \chi_{-\Lambda_a}(\hat{r}) \end{array} \right)^\dagger \\
 &\quad \sum_{\Lambda_e} \left( \begin{array}{c} g_{\Lambda_e \Lambda}^{e\mu}(r) \chi_{\Lambda_e}(\hat{r}) \\ i f_{\Lambda_e \Lambda}^{e\mu}(r) \chi_{-\Lambda_e}(\hat{r}) \end{array} \right) \underbrace{\left( \begin{array}{c} \chi_{m'_s} \\ 0 \end{array} \right)^\dagger \sum_{\Lambda_p} \left( \begin{array}{c} g_{\Lambda_p \Lambda''}^{p\nu}(r) \chi_{\Lambda_p}(\hat{r}) \\ i f_{\Lambda_p \Lambda''}^{p\nu}(r) \chi_{-\Lambda_p}(\hat{r}) \end{array} \right)}_{g_{\Lambda_s \Lambda_s}^{p\nu}(r) Y_{00}}
 \end{aligned}$$

$$\begin{aligned}
&= \epsilon_{p_e} Y_{00} \sum_{\Lambda_a \Lambda_e} i^{-l_a} C_{\Lambda_a}^{m_s} Y_l^{\mu_a - m_s}(\hat{p}) \left( \int r^2 dr j_{l_a}(pr) g_{\Lambda_e \Lambda}^{e\mu}(r) g_{\Lambda_s \Lambda_s}^{p\nu}(r) \langle \chi_{\Lambda_a}(\hat{r}) | \chi_{\Lambda_e}(\hat{r}) \rangle \right. \\
&\quad \left. + \frac{cpS_{\kappa_a}}{E_p + c^2} \int r^2 dr j_{\bar{l}_a}(pr) f_{\Lambda_e \Lambda}^{e\mu}(r) g_{\Lambda_s \Lambda_s}^{p\nu}(r) \langle \chi_{-\Lambda_a}(\hat{r}) | \chi_{-\Lambda_e}(\hat{r}) \rangle \right) \\
&= \epsilon_{p_e} Y_{00} \sum_{\Lambda_a} i^{-l_a} C_{\Lambda_a}^{m_s} Y_l^{\mu_a - m_s}(\hat{p}) \left( \int r^2 dr j_{l_a}(pr) g_{\Lambda_a \Lambda}^{e\mu}(r) g_{\Lambda_s \Lambda_s}^{p\nu}(r) \right. \\
&\quad \left. + \frac{cpS_{\kappa_a}}{E_p + c^2} \int r^2 dr j_{\bar{l}_a}(pr) f_{\Lambda_a \Lambda}^{e\mu}(r) g_{\Lambda_s \Lambda_s}^{p\nu}(r) \right)
\end{aligned}$$

$$\tilde{M}_{m_s \Lambda' m'_s \Lambda''}^{\mu\nu\alpha} = \int d^3r Z_{\Lambda'}^{e\mu q\alpha \times}(\vec{r}) U_{\vec{p}_e m_s}^e e^{i\vec{p}_e \vec{r}} Z_{\Lambda''}^{p\nu q\alpha \times}(\vec{r}) U_{\vec{p}_p m'_s}^p e^{i\vec{p}_p \vec{r}}$$

Comparison of the positron-annihilation matrix elements with those of Compton scattering:

$$\begin{aligned}
M_{m_s \Lambda' m'_s \Lambda''}^{\mu\nu\alpha} &= \epsilon_{p_e} Y_{00} \sum_{\Lambda_a} i^{-l_a} C_{\Lambda_a}^{m_s} Y_l^{\mu_a - m_s}(\hat{p}) \left( \int r^2 dr j_{l_a}(pr) g_{\Lambda_a \Lambda}^{e\mu}(r) \mathbf{g}_{\Lambda_s \Lambda_s}^{p\nu}(\mathbf{r}) \right. \\
&\quad \left. + \frac{cpS_{\kappa_a}}{E_p + c^2} \int r^2 dr j_{\bar{l}_a}(pr) f_{\Lambda_a \Lambda}^{e\mu}(r) \mathbf{g}_{\Lambda_s \Lambda_s}^{p\nu}(\mathbf{r}) \right) \\
M_{m_s \Lambda'} &= \epsilon_p \sum_{\Lambda} i^{-l} C_{\Lambda}^{m_s} Y_l^{\mu - m_s}(\hat{p}) \left( \langle j_l(pr) | g_{\Lambda \Lambda'}(r) \rangle + \frac{cpS_{\kappa}}{E_p + c^2} \langle j_{\bar{l}}(pr) | f_{\Lambda \Lambda'}(r) \rangle \right) \\
&\text{with } \epsilon_p = 4\pi \left( \frac{E_p + c^2}{2E_p + c^2} \right)^{1/2}
\end{aligned}$$



# Bibliography

- [1] J. W. Taylor, J. A. Duffy, A. M. Bebb, J. E. McCarthy, M. R. Lees, M. J. Cooper, and D. N. Timms, in press (2002).
- [2] Y. Kubo and S. Asano, *J. Magn. Magn. Materials* **115**, 177 (1992).
- [3] J. A. Duffy, J. E. McCarthy, S. B. Dugdale, V. Honkimäki, M. J. Cooper, M. A. Alam, T. Jarlborg, and S. B. Palmer, *J. Phys.: Condensed Matter* **10**, 10391 (1998).
- [4] J. A. Duffy, S. B. Dugdale, J. E. McCarthy, M. A. Alam, M. J. Cooper, S. B. Palmer, and T. Jarlborg, *Phys. Rev. B* **61**(21), 14331 (2000).
- [5] M. Chevreton, E. F. Bertaut, and F. Jellinek, *Acta Cryst.* **16**, 431 (1963).
- [6] M. Chevreton, M. Murat, C. Eyraud, and E. F. Bertaut, *J. Phys. (Paris)* **24**, 443 (1963).
- [7] G. I. Makovetskii and G. M. Shakhlevich, *phys. stat. sol. (a)* **47**, 219 (1978).
- [8] J. Dijkstra, C. F. Bruggen, C. Haas, and R. A. de Groot, *J. Phys.: Condensed Matter* **1**, 9163 (1989).
- [9] A. Perlov, unpublished.
- [10] W. Bensch and Z. Huang, unpublished.
- [11] Y. Kubo and S. Asano, *Phys. Rev. B* **42**, 4431 (1990).
- [12] M. A. G. Dixon, J. A. Duffy, S. Gardelis, J. E. McCarthy, M. J. Cooper, S. B. Dugdale, T. Jarlborg, and D. N. Timms, *J. Phys.: Condensed Matter* **10**, 2759 (1998).
- [13] Y. Tanaka, N. Sakai, Y. Kubo, and H. Kawata, *Phys. Rev. Letters* (1993).
- [14] A. Bansil, S. Kaprzyk, A. Andrejczuk, L. Dobrzynski, J. Kwiatkowska, F. Maniawski, and E. Zukowski, *Phys. Rev. B* **57**(1), 314 (1998).
- [15] G. Srajer, C. Yahnke, D. Haeffner, D. Mills, L. Assoufid, B. Harmon, and Z. Zuo, *J. Phys.: Condensed Matter* **11**(23), 253 (1999).

- [16] S. Wakoh, M. Tokii, M. Matsumoto, and I. Matsumoto, J. Phys. Soc. Japan **71**(5), 1393 (2002).
- [17] P. K. Lawson, M. J. Cooper, M. A. G. Dixon, D. N. Timms, E. Zukowski, F. Itoh, and H. Sakurai, Phys. Rev. B **56**(6), 3239 (1997).
- [18] Z. Major, unpublished.
- [19] M. I. Makovetskii, Soviet Physics - Solid State **28**, 447 (1986).
- [20] S. Mankovsky, unpublished.
- [21] M. Faraday, Phil. Trans. Roy. Soc. (London) **136**, 1 (1846).
- [22] M. Faraday, Trans. Roy. Soc. (London) **5** (1846).
- [23] P. A. M. Dirac, Proc. Roy. Soc. (London) A **117**, 610 (1928).
- [24] P. A. M. Dirac, Proc. Roy. Soc. (London) A **118**, 351 (1928).
- [25] A. H. Compton, Phys. Rev. **21**, 483 (1923).
- [26] A. H. Compton, Phys. Rev. **22**, 409 (1923).
- [27] C. E. M. Jauncey, Phys. Rev. **25**, 723 (1925).
- [28] J. W. M. DuMond, Phys. Rev. **33**, 643 (1929).
- [29] J. W. M. DuMond, Phys. Rev. **36**, 1685 (1930).
- [30] M. J. Cooper, Rep. Prog. Phys. **48**, 415 (1985).
- [31] W. Schülke, phys. stat. sol. (b) **82**, 229 (1977).
- [32] P. Hohenberg and W. Kohn, Phys. Rev. B **136**, 864 (1964).
- [33] W. Kohn and J. Sham, Phys. Rev. **A**(140), 1133 (1965).
- [34] L. J. Sham and W. Kohn, Phys. Rev. **145**, 561 (1966).
- [35] M. Ernzerhof, Chem. Phys. Lett. **263**, 499 (1996).
- [36] Y. A. Wang, Phys. Rev. A **56**(2), 1646 (1997).
- [37] P. Strange, *Relativistic Quantum Mechanics* (Cambridge University Press, 1998).
- [38] U. von Barth and L. Hedin, J. Phys. C: Solid State Phys. **5**, 1629 (1972).
- [39] O. Gunnarson and B. I. Lundqvist, Phys. Rev. B **13**, 4274 (1976).
- [40] S. H. Vosko, L. Wilk, and M. Nusair, Can. J. Phys. **58**, 1200 (1980).

- [41] J. P. Perdew and A. Zunger, *Phys. Rev. B* **23**, 5048 (1981).
- [42] D. C. Langreth and M. J. Mehl, *Phys. Rev. B* **28**, 1809 (1983).
- [43] D. C. Langreth and M. J. Mehl, *Phys. Rev. B* **29**, 2310 (1983).
- [44] J. P. Perdew and W. Yue, *Phys. Rev. B* **33**, 8800 (1986).
- [45] J. P. Perdew, *Phys. Rev. B* **33**, 8822 (1986).
- [46] C. Lee, W. Yang, and R. G. Parr, *Phys. Rev. B* **37**, 785 (1988).
- [47] J. P. Perdew, *Electronic Structure of Solids* (Akademie Verlag, Berlin, 1991), chap. Unified Theory of Exchange and Correlation Beyond the Local Density Approximation, pp. 11–20.
- [48] J. P. Perdew and Y. Wang, *Phys. Rev. B* **45** (1992).
- [49] J. P. Perdew, K. Burke, and M. Ernzerhof, *Phys. Rev. Letters* **77**, 3865 (1996).
- [50] J. P. Perdew, K. Burke, and M. Ernzerhof, *Phys. Rev. Letters* **78**, 1396 (1997).
- [51] E. H. Lieb and S. Oxford, *Intern. J. Quantum. Chem.* **XIX**, 427 (1981).
- [52] A. K. Rajagopal and J. Callaway, *Phys. Rev. B* **7**, 1912 (1973).
- [53] A. K. Rajagopal, *J. Phys. C: Solid State Phys.* **11**, L943 (1978).
- [54] M. V. Ramana and A. K. Rajagopal, *J. Phys. C: Solid State Phys.* **12**, L845 (1979).
- [55] A. H. M. Donald and S. H. Vosko, *J. Phys. C: Solid State Phys.* **12**, 2977 (1979).
- [56] J. Korryng, *Physica* **XIII**, 392 (1947).
- [57] J. Korryng, *Physica* **16**, 601 (1950).
- [58] W. Kohn and N. Rostoker, *Phys. Rev.* **94**, 1111 (1954).
- [59] J. S. Faulkner, *J. Phys. C: Solid State Phys.* **10**, 4661 (1977).
- [60] J. S. Faulkner, *Phys. Rev. B* **19**, 6186 (1979).
- [61] J. S. Faulkner and G. M. Stocks, *Phys. Rev. B* (1980).
- [62] B. L. Gyorffy and G. M. Stocks, *J. Phys. F: Met. Phys.* (1980).
- [63] G. M. Stocks, W. Temmerman, and B. L. Györffy, *Phys. Rev. Letters* **41**, 339 (1978).
- [64] A. Gonis, *Phys. Rev. B* **33**, 5914 (1986).
- [65] A. Gonis, *Phys. Rev. B* **34**, 1290 (1986).

- [66] A. Gonis, *Green functions for ordered and disordered systems* (North-Holland, Amsterdam, 1992).
- [67] P. H. Dederichs, B. Drittler, and R. Zeller, *Mat. Res. Soc. Symp. Proc.* **253**, 185 (1992).
- [68] P. Strange, H. Ebert, J. B. Staunton, and B. L. Györfy, *J. Phys.: Condensed Matter* **1**, 2959 (1989).
- [69] P. Weinberger, *Electron Scattering Theory for Ordered and Disordered Matter* (Oxford University Press, 1990).
- [70] H. Ebert, *Phys. Rev. B* **38**, 9390 (1988).
- [71] H. Ebert, *J. Phys.: Condensed Matter* **1**, 9111 (1989).
- [72] H. Ebert, in *Electronic Structure and Physical Properties of Solids*, edited by H. Dreyssé (Springer, Berlin, 2000), vol. 535, p. 191.
- [73] H. Ebert et al., *The Munich SPR-KKR package*, version 2.1.1, <http://olymp.cup.uni-muenchen.de/ak/ebert/SPRKKR> (2002).
- [74] P. Strange, J. B. Staunton, and B. L. Györfy, *J. Phys. C: Solid State Phys.* **17**, 3355 (1984).
- [75] R. Feder, F. Rosicky, and B. Ackermann, *Z. Physik B* **52**, 31 (1983).
- [76] A. C. Jenkins and P. Strange, *J. Phys.: Condensed Matter* **6**, 3499 (1994).
- [77] E. Tamura, *Phys. Rev. B* **45**(7), 3271 (1992).
- [78] H. Ebert and B. L. Györfy, *J. Phys. F: Met. Phys.* **18**, 451 (1988).
- [79] B. L. Györfy and M. J. Stott, *Band Structure Spectroscopy of Metals and Alloys* (Academic Press, New York, 1972).
- [80] A. Bansil, L. Schwartz, and H. Ehrenreich, *Phys. Rev. B* **12**, 2893 (1975).
- [81] W. M. Temmerman, B. L. Györfy, and G. M. Stocks, *J. Phys. F: Met. Phys.* **8**, 2461 (1978).
- [82] J. S. Faulkner, in *Progress in Materials Science*, edited by J. W. Christian, P. Haasen, and T. B. Massalsky (Pergamon Press, 1982), vol. 27, p. 1.
- [83] P. Soven, *Phys. Rev.* **156**, 809 (1967).
- [84] Taylor, *Scattering theory: the quantum theory of scattering* (Academic Press, 1972).
- [85] O. Klein and Y. Nishina, *Z. Physik* **52**, 853 (1929).
- [86] F. W. Lipps and H. A. Tolhoek, *Physica* **20**, 395 (1954).

- [87] P. M. Platzman and N. Tzoar, *Phys. Rev. B* **2**, 3556 (1970).
- [88] S. Wakoh and Y. Kubo, *J. Magn. Magn. Materials* **5**, 202 (1977).
- [89] B. Williams, *Compton Scattering* (McGraw-Hill New York, 1977).
- [90] D. Mills, *Phys. Rev. B* **36**(11), 6178 (1987).
- [91] S. P. Collins, M. J. Cooper, D. Timms, A. Brahmia, D. Laundry, and P. Kane, *J. Phys.: Condensed Matter* **1**, 9009 (1989).
- [92] Y. Sakurai, Y. Tanaka, T. Ohata, Y. Watanabe, S. Nanao, Y. Ushigami, T. Iwazumi, H. Kawata, and N. Shiotani, *J. Phys.: Condensed Matter* (1994).
- [93] M. Cooper, D. Laundry, D. Cardwell, D. Timms, R. Holt, and G. Clark, *Phys. Rev. B* **34**(8), 5984 (1986).
- [94] D. A. Cardwell and M. J. Cooper, *J. Phys.: Condensed Matter* **1**, 9357 (1989).
- [95] N. Sakai and K. Ono, *Phys. Rev. Letters* **37**, 351 (1976).
- [96] R. Ribberfors, *Phys. Rev. B* **12**, 2067 (1975).
- [97] P. Holm and R. Ribberfors, *Phys. Rev. A* **40**, 6251 (1989).
- [98] P. Eisenberg and P. Platzman, *Phys. Rev. A* **2**, 415 (1970).
- [99] M. Cooper, *Physica B* **159**, 137 (1989).
- [100] *X-Ray Scattering and Absorption by Magnetic Materials* (Clarendon Press, Oxford, 1996), chap. 7.
- [101] M. E. Rose, *Relativistic Electron Theory* (Wiley, 1961).
- [102] M. J. Cooper and J. A. Duffy, *J. Phys. Chem. Solids* **61**, 345 (2000).
- [103] T. Baruah, R. R. Zope, and A. Kshirsagar, *Phys. Rev. B* **62**(24), 16435 (2000).
- [104] W. B. Pearson, *Handbook of the Lattice Spacing and Structures of Metals and Alloys* (Pergamon London, 1958).
- [105] M. van Schlifgaarde, I. A. Abrikisov, and B. Johansson, *Nature* **400**, 46 (1999).
- [106] R. J. Weiss, *Proc. Phys. Soc.* **82**, 281 (1963).
- [107] P. J. Brown, K. R. A. Zeibeck, and K. U. Neumann, *J. Phys.: Condensed Matter* **13**, 1563 (2001).
- [108] Y. Kakehashi, *Phys. Rev. B* **38**, 12051R (1988).

- [109] A. Wildes and A. Cowlam, unpublished.
- [110] Z. Major, S. B. Dugdale, T. Jarlborg, E. Bruno, B. Ginatempo, J. B. Staunton, and J. Poulter, *J. Phys.: Condensed Matter* **15**, 3619 (2003).
- [111] K. Tajima, V. Endoh, Y. Ishikawa, and W. G. Stirling, *Phys. Rev. Letters* **37**, 519 (1976).
- [112] J. Kästner, J. Neuhaus, E. F. Wassermann, W. Petry, B. Hennion, and H. Bach, *Eur. Phys. J. B* **11**, 75 (1999).
- [113] D. J. Singh, *Phys. Rev. B* **44**, 7451 (1994).
- [114] D. M. Bylander and L. Kleinmann, *Phys. Rev. B* (1994).
- [115] D. M. Bylander and L. Kleinmann, *Phys. Rev. B* **50**, 1363 (1994).
- [116] B. I. Min, H. J. F. Jansen, T. Oguchi, and A. J. Freeman, *J. Magn. Magn. Materials* **59**, 277 (1986).
- [117] N. Sakai, Y. Tanaka, F. Ytoh, H. Sakurai, M. Ito, H. Kawata, and T. Iwazumi, *J. Phys. Soc. Japan* **60**, 1201 (1991).
- [118] L. W. Roeland, G. J. Cock, F. A. Mueller, A. C. Moleman, K. A. McKewen, R. G. Jordan, and D. W. Jones, *J. Phys. F: Met. Phys.* **5**, L233 (1975).
- [119] W. C. Thoburn, S. Legvold, and F. H. Spedding, *Phys. Rev.* **110**(6), 1298 (1958).
- [120] S. Bates, S. B. Palmer, J. B. Sousa, G. J. McIntire, D. Fort, S. Legvold, B. J. Beaudry, and W. C. Koehler, *Phys. Rev. Letters* **55**, 2968 (1985).
- [121] M. S. S. Brooks and P. J. Kelly, *Phys. Rev. Letters* **51**(18), 1708 (1983).
- [122] O. Eriksson, M. S. S. Brooks, and B. Johansson, *Phys. Rev. B* **41**(13), 9087 (1990).
- [123] M. Wulff, G. H. Lander, B. Lebech, and A. Delapalme, *Phys. Rev. B* **39**, 4719 (1989).
- [124] M. Wulff, B. Lebech, A. Delapalme, G. H. Lander, J. Rebizant, and J. C. Spirlet, *Physica B* **156-157**, 836 (1989).
- [125] M. Finazzi, P. Sainctavit, A. M. Dias, J. P. Kappler, G. Krill, J. P. Sanchez, P. D. de Reótier, A. Yaouanc, A. Rogalev, and J. Goulon, *Phys. Rev. B* **55**(5), 3010 (1997).
- [126] L. Severin, M. S. S. Brooks, and B. Johansson, *Phys. Rev. Letters* **71**(19), 3214 (1993).
- [127] M. J. Puska and R. M. Nieminen, *Rev. Mod. Phys.* **66**(3), 841 (1994).
- [128] J. H. Kaiser, *Positron-electron Momentum Densities in Metals*, Ph.D. thesis, University of East Anglia Norwich (1984).

- [129] S. Daniuk, *J. Phys.: Condensed Matter* p. 5561 (1989).
- [130] T. Jarlborg and A. K. Singh, *Phys. Rev. B* **36**, 4660 (1987).
- [131] B. Barbellini, M. J. Puska, T. Torsti, and R. M. Nieminen, *Phys. Rev. B* **51**, 7341 (1995).
- [132] B. Barbellini, M. Hakala, M. J. Puska, and R. M. Nieminen, *Phys. Rev. B* **56**, 7136 (1997).
- [133] A. Rubaszek, Z. Szotek, and W. M. Temmerman, *Phys. Rev. B* **63**, 165115 (2001).
- [134] A. Rubaszek, Z. Szotek, and W. M. Temmerman, *Phys. Rev. B* **65**, 125104 (2002).
- [135] Z. Szotek, B. L. Gyorffy, G. M. Stocks, and W. M. Temmerman, *J. Phys. F: Met. Phys.* **14**, 2571 (1984).
- [136] V. B. Beretetskii, E. M. Lifshitz, and L. P. Pitaevskii, *Relativistic Quantum Theory* (Oxford: Pergamon Press, 1971).
- [137] J. B. Goodenough, *Magnetism and the Chemical Bond* (Interscience Pub., 1963).
- [138] J. Dijkstra, H. H. Weitering, C. F. Bruggen, C. Haas, and R. A. de Groot, *J. Phys.: Condensed Matter* **1**, 9141 (1989).
- [139] F. Jellinek, *Acta Cryst.* **10**, 620 (1957).
- [140] T. J. A. Popma and C. F. Bruggen, *J. Inorg. Nucl. Chem.* **31**, 73 (1969).
- [141] T. Kamigaichi, *J. Sci. Hiroshima Univ.* **A24**, 371 (1960).
- [142] I. Tsubokawa, *J. Phys. Soc. Japan* **11**, 662 (1956).
- [143] F. K. Lotgering and E. W. Gorter, *J. Phys. Chem. Solids* **3**, 238 (1957).
- [144] I. Tsubokawa, *J. Phys. Soc. Japan* **15**, 2243 (1960).
- [145] T. Hirone and K. Adachi, *J. Phys. Soc. Japan* **12**, 156 (1957).
- [146] L. M. Corliss, N. Elliott, J. M. Hastings, and R. L. Sass, *Phys. Rev.* **122**, 1402 (1961).
- [147] H. Ipsier, K. L. Komarek, and K. O. Klepp, *J. Less-Common Met.* **92**, 265 (1983).
- [148] W. Bensch, O. Helmer, and C. Näther, *Mat. Res. Bull.* **32**(3), 305 (1997).
- [149] A. Oshawa, Y. Yamaguchi, N. Kazama, H. Yamaguchi, and H. Watanabe, *J. Phys. Soc. Japan* **33**, 1303 (1972).
- [150] T. Hirone and S. Chiba, *J. Phys. Soc. Japan* **15**, 1991 (1960).
- [151] S. Ohta, *J. Phys. Soc. Japan* **54**, 1076 (1985).

- [152] E. F. Bertaut, G. Roult, R. Aleonard, R. Pauthenet, M. Chevreton, and R. Jansen, *J. Phys. (Paris)* **25**, 582 (1964).
- [153] B. Lambert-Andron, N. P. Grazhdankina, and C. Vettier, *J. Phys. (Paris)* **39**, L43 (1979).
- [154] A. F. Andresen, *Acta Chem. Scand.* **17**, 1335 (1963).
- [155] G. I. Makovetskii and G. M. Shakhlevich, *Kristall Technik* **14**, 97 (1979).
- [156] T. Hamasaki, T. Hashimoto, Y. Yamaguchi, and H. Watanabe, *Solid State Commun.* **16**, 895 (1975).
- [157] T. Kawakami, N. Tanaka, and K. Motizuki, *J. Magn. Magn. Materials* **196-197**, 629 (1999).
- [158] T. Kanomata, Y. Sugawara, T. Kaneko, K. Kamishima, H. A. Katori, and T. Goto, *J. Appl. Cryst.* **297**, 5 (2000).
- [159] M. Takagaki, T. Kawakami, N. Tanaka, M. Shirai, and K. Motizuki, *J. Phys. Soc. Japan* **67**(3), 1014 (1998).
- [160] M. Takagaki, T. Kawakami, M. Shirai, and K. Motizuki, *J. Magn. Magn. Materials* **177-181**, 1385 (1998).
- [161] M. Knecht, Ph.D. thesis, Ludwig-Maximilians Universität München (1999).
- [162] A. I. Liechtenstein, M. I. Katsnelson, V. P. Antropov, and V. A. Gubanov, *J. Magn. Magn. Materials* **67**, 65 (1987).
- [163] A. I. Liechtenstein, M. I. Katsnelson, and V. A. Gubanov, *J. Phys. F: Met. Phys.* **14**, L125 (1984).
- [164] M. Pajda, J. Kudrnovsky, I. Turek, V. Drchal, and P. Bruno, *Phys. Rev. B* **64**, 174402 (2001).
- [165] S. V. Halilov, H. Eschring, A. Y. Perlov, and P. M. Oppeneer, *Phys. Rev. B* **58**, 293 (1998).
- [166] D. Benea, S. Mankovsky, A. Perlov, and H. Ebert, *J. Phys.: Condensed Matter* (2004), submitted.
- [167] G. Chattopadhyay, *J. Phase Equilibria* **15**(4), 1 (1994).
- [168] Z. L. Huang, W. Bensch, D. Benea, and H. Ebert, *J. Solid State Chem.* (2004), submitted.
- [169] *11. Vortragstagung f"ur Festk"orperchemie und Materialforschung.*
- [170] M. Akram and F. M. Nazar, *J. Mat. Sci. Lett.* **2**, 441 (1983).
- [171] W. Bensch and B. Sander, unpublished.



- [172] K. Hatakeyama, A. Takase, S. Anzai, H. Yoshida, T. Kaneko, S. Abe, and S. Ohta, *Jap. J. Appl. Phys. Suppl.* **39**(1), 507 (2000).
- [173] K. Hatakeyama, S. Anzai, H. Yoshida, T. Kaneko, S. Abe, and S. Ohta, *J. Phys. Soc. Japan* (2002).
- [174] K. Hatakeyama, T. Kaneko, S. Abe, H. Yoshida, Y. Nakagawa, S. Anzai, and S. Ohta, *J. Phys. Soc. Japan* **71**(6), 1605 (2002).
- [175] K. Shimada, T. Saitoh, H. Natame, A. Fujimori, S. Ishida, S. Asano, M. Matoba, and S. Anzai, *Phys. Rev. B* **53**(12), 7673 (1996).
- [176] A. N. Titov, A. V. Kuranov, V. G. Pleschev, Y. M. Yaroschenko, M. V. Yablonskikh, A. V. Postnikov, S. Plogmann, M. Neumann, A. V. Ezhov, and E. Z. Kurmaev, *Phys. Rev. B* **63**, 035106 (2001).

## Publications and presentations

### Publications

1. Layer-resolved magnetic moments in Ni/Pt multilayers  
F. Wilhelm, P. Pouloupoulos, G. Ceballos, H. Wende, K. Baberschke, P. Srivastava, D. Benea, H. Ebert, M. Angelakeris, N. K. Flevaris, D. Niarchos, A. Rogalev and N. B. Brookes  
*Phys. Rev. Letters* **85**, 413 (2000).
2. X-ray magnetic circular dichroic magnetometry on Ni/Pt multilayers  
P. Pouloupoulos, F. Wilhelm, H. Wende, G. Ceballos, K. Baberschke, D. Benea, H. Ebert, M. Angelakeris, N. K. Flevaris, A. Rogalev and N. B. Brookes  
*J. Appl. Physics* **89**, 3874 (2001).
3. Relation between  $L_{2,3}$  XMCD and the magnetic ground-state properties for the early 3d element V  
A. Scherz, H. Wende, K. Baberschke, J. Minar, D. Benea and H. Ebert  
*Phys. Rev. B* **66**, 184402 (2002).
4. Direct observation of the multisheet Fermi surface in the strongly correlated transition metal compound  $ZrZn_2$   
Zs. Major, S. B. Dugdale, R. J. Watts, G. Santi, M. A. Alam, S. M. Hayden, J. A. Duffy, J. W. Taylor, T. Jarlborg, E. Bruno, D. Benea and H. Ebert  
*Phys. Rev. Lett.*, accepted.
5. Substitution Effects on Structure and Magnetism in Chromium Chalcogenide  $Cr_5Te_8$ . Part one: Cluster Glass Behaviour in Trigonal  $Cr_{1+x}Q_2$  with Basic Cell (Q=Te, Se; Te:Se=7:1)  
Z. L. Huang, W. Bensch, D. Benea and H. Ebert  
*J. Solid State Chem.*, submitted.
6. Magnetic structure of CrTe  
D. Benea, S. Mankovsky, A. Perlov and H. Ebert  
*J. Phys.: Condensed Matter*, submitted.

### Posters and Presentations

1. A relativistic description of magnetic Compton scattering for metals  
Poster  
DPG-Frühjahrstagung, Regensburg, 27. - 31. März 2000

2. A relativistic description of magnetic Compton scattering for metals  
Poster  
 $\Psi_k$  Conference, Schwäbisch Gmünd, 22.-26.08 2000
3. A relativistic description of magnetic Compton scattering for metals  
Poster  
International Workshop on X-ray Spectroscopies for Magnetic Solids, Berlin, 9. 12. 2000
4. A relativistic description of magnetic Compton scattering for metals  
Poster  
DPG-Frühjahrstagung, Hamburg, 26. - 30. März 2001
5. A relativistic description of magnetic Compton scattering of solids  
Talk  
1<sup>st</sup> Annual Meeting of the Research Training Network  
**Computational Magnetoelectronics**, September 21-30, 2001, Budapest
6. Disorder-induced magnetism in  $\text{TiFe}_x\text{Co}_{1-x}$   
Poster  
DPG-Frühjahrstagung, Regensburg 11-15.03.2002
7. Magnetic Compton profile of  $\text{UFe}_2$   
Poster  
DPG-Frühjahrstagung, Regensburg 11-15.03.2002
8. Disorder-induced magnetism in  $\text{TiFe}_x\text{Co}_{1-x}$   
Poster  
19<sup>th</sup> General Conference of the EPS Condensed Matter Division/  
CMMP 2002 Condensed Matter and Materials Physics,  
Brighton UK, 7-11 April, 2002
9. Disorder-induced magnetism in  $\text{TiFe}_x\text{Co}_{1-x}$   
Poster  
2<sup>nd</sup> Annual Meeting of the Research Training Network  
**Computational Magnetoelectronics**, 5-9 October 2002, Oléron, France
10. Magnetic properties in chromium-chalcogenide systems  
Talk  
Substitutionseffekte in ionischen Festkörpern, Rauischholzhausen, 24-26 Feb. 2003

11. Magnetic properties in chromium-chalcogenide systems  
Poster  
DPG-Frühjahrstagung, Dresden 24-28.03.2003
12. Magnetic properties in chromium-chalcogenide systems  
Poster  
The 9<sup>th</sup> European Conference on Solid State Chemistry, Stuttgart, 3-6.09.2003
13. Magnetic properties in chromium-chalcogenide systems  
Poster  
DPG-Frühjahrstagung, Regensburg 8-12.03.2004

## ACKNOWLEDGEMENTS

I would like to thank Prof. Dr. H. Ebert, my research supervisor, for all encouragement, guidance and support he gave me during my research stage in Munich.

I would also like to express my appreciation to Dr. A. Perlov and Dr. A. Mankovsky for their help, advice and helpful comments made during my research stage. For many helpful discussions and the fruitful collaboration within the spectroscopy part of my work, it is pleasant for me to thank here Zsuzsanna Major and Dr. S.B. Dugdale. Also, for a very good collaboration during the development of the common scientific project, I am grateful to Prof. Dr. W. Bensch and Dr. Z.L. Huang.

I would like to thank people who influenced my scientific formation: Prof. Dr. G. Ilonca, Prof. Dr. V. Crisan and Dr. C. Corega.

For their support and friendship from the first days of my experience 'abroad', I want to thank Voicu and Andrea Popescu.

For assistance in the computer area, thanks to H. Freyer, T. Huhne and J. Minár. Special thanks to Jan for providing a stimulating and friendly atmosphere in the office.

For the pleasant hours I shared with them, thank to my colleagues and friends Dr. I. Cabria, M. Kosuth and S. Chadov.

To my parents, for all their love and support is dedicated this thesis.

# LEBENS LAUF

## PERSÖNLICHE ANGABEN

- Name: Diana-Ancuța Benea
- Geburtsdatum: 8 Januar 1970
- Geburtsort: Cluj-Napoca, Rumänien
- Staatsangehörigkeit: rumänisch
- Familienstand: ledig

## SCHULBILDUNG

- 1976 – 1980: Grundschule in Poieni, Kreis Cluj, Rumänien
- 1980 – 1988: Gymnasium in Poieni, Kreis Cluj und Cluj-Napoca, Rumänien / Abitur

## STUDIUM

- 1988 – 1993: Studium der Physik an der Universität Babeş-Bolyai, Cluj-Napoca, Rumänien. Diplomarbeit zum Thema "Magnetische und Transporteigenschaften des Supraleiters  $\text{YBa}_2\text{Cu}_{1-x}\text{M}_x\text{O}_{7-8}$ " unter der Leitung von Prof. Dr. Gh. Ilonca und Assist. Dr. A. V. Pop.
- Juni 1993: Diplomprüfung mit Note 10.

## BERUF

- 1993 – 1996: Physiklehrerin in Gymnasien in Cluj-Napoca, Rumänien
- 1995: Definitiver Titel eines Professors für die mittlere Schulausbildung
- Oktober 1996 -Februar 1999: Universitätsassistentin am Lehrstuhl für Mechanik, Molekularphysik und Physik des kondensierten Zustandes der Fakultät für Physik der Universität Babeş-Bolyai, Cluj-Napoca, Rumänien.
- Seit Februar 1999: Wissenschaftlicher Angestellter und Doktorand am Institut für Physikalische Chemie an der Ludwig-Maximilians Universität München.